Development of clinical instruments for traumatic brain injury patients: design, realisation, and performance

Chu Wang

Supervised by Prof. Martyn G Boutelle

SUBMITTED IN PARTIAL FULFILMENT OF THE REQUIREMENTS FOR THE DEGREE OF DOCTOR OF PHILOSOPHY (Ph. D.) AND THE DIPLOMA OF IMPERIAL COLLEGE LONDON

Department of Bioengineering

Imperial College London

September 2015

I certify that all work presented in this thesis is the product of my own original work unless otherwise referenced.

Chu Wang

Acknowledgement

Martyn Boutelle: You are not only a PhD supervisor, but also my good mentor. Over the past four years, you have guided me to the right path, and taught me how to be an excellent engineer as well as a good person. I'm simply grateful for working with you. Without your kind help and demonstrations, it is impossible for me to finish this thesis.

Manos Drakakis: We got to know each other 3 year ago, when you examined my early-stage report. Since then, you have been offering me great help. Thank you so much for the opportunity to work in your lab for most of my PhD period. Your intelligence and generosity greatly inspires me, and it is really my honour to have the chance to work with you.

Konstantinos Papadimitriou: Thanks for sharing the time and experience with me in the lab. Three years ago, you lead me into the project, and got me started with all the essential electronics. I also gained a lot from your focus, consistency, and hardworking. You are always a good accompany. Our experience of debugging the circuit board during 2013 Ester holiday is one of the most unforgettable memories in my research career.

The sensor group: Agnes, Sally, Michelle, Prang, Sahir, Rob, and Isabelle – It has been a great pleasure to work with you. Thank you all for your help with my project, and your patience and intelligence when we have any problem in the experiments. We share so much happy experience during the past four years. I will never forget the badminton, bowling, the NBA games, the extreme cold weather in Chicago, and so much more.

The COSBID group: Toby, Sharon, and Professor Strong – It has been a great time to work with you in the clinical monitoring. The traumatic brain injury project has given me the opportunity to grow from an electronic graduate to a professional medical device engineer. Your practical thinking and extensive experience has helped me build a practical understanding of the clinical environment, which is invaluable for my future career.

My family: I am so blessed to have you all, my parents, parents-in-law, and my wife. Thanks for all your unconditional supports and accompanies throughout my PhD period. I owe you everything, and you are always my fundamental career motivations. Thanks are from the bottom of the list, but from the bottom of my heart.

This thesis is dedicated to my wife, Xiangning (Fiona) Liu. Your support, kindness, companion, and optimism are indispensable for me to accomplish the thesis. This is for you.

Chu Wang

Abstract

This thesis focuses on designing and developing both wired and wireless multimodal clinical monitoring electronic instruments for traumatic brain injury (TBI) patients.

Potentiostats using both a transimpedance resistive design and a novel switched-capacitor based design have been developed to support amperometric sensors and biosensors in detecting concentrations of important biomolecules, such as glucose and lactate in the injured brain tissue. The performance and relevant advantages/disadvantages of these two potentiostat designs have been also discussed.

A high-resolution low-noise bio-potential acquisition system has been developed, to monitor the electroencephalography and electrocorticography of TBI patients. To optimise the monitoring performance, the system has been separated into two functional parts: a battery-powered head-stage box that records, amplifies, and digitalises the biopotentials; a bed-side digital unit that integrates with a new patient monitoring instrument. A commercial device has been used as a comparison, and the new design shows better electrical interference elimination.

I have also designed an intelligent multimodal TBI instrumentation box to simultaneously monitor chemical, electrical, and physical parameters from a TBI patient. The instrumentation box has been carefully designed and evaluated to meet IEC60601 (3rd edition) safety regulation and it has passed local hospital test for clinical uses.

The thesis then concentrates on developing different wireless solutions for the TBI instruments, and aims at eliminating clinical cable congestion and practical issues in intensive care units. By integrating with TBI-related electronics, different wireless modules have been evaluated and compared.

Finally, to enable the device to display real-time tissue concentrations to the clinical team, a wireless control of a sensor auto-calibration system has been developed. Relevant graphic user interfaces have been designed on both PC and android-based smart phones or tablets.

Contents

List of Figures

List of Tables

List of Abbreviations

a_X	Activity of Spice X
ABP	Arterial Blood Pressure
ABS	Acrylonitrile Butadiene Styrene
AC	Alternative Current
aCSF	Artificial CerebroSpinal Fluid
ADC	Analog-to-Digital Converter
Ag	Silver
Ag/AgCl	Silver/silver chloride
A_{OL}	Open-Loop Gain
API	Application Programming Interface
ATP	Adenosine Triphosphate
BER	Bit Error Rate
BNC	Bayonet Neill-Concelman
BOM	Billing of Materials
BP	Blood Pressure
BPS	Bits per Second
BT	Bluetooth
Ca^{2+}	Calcium
$CaCl_2$	Calcium Chloride
CAD	Computer Aid Drawing
CE	Counter Electrode
CISC	Complex Instruction Set Computer
CMOS	Complementary Metal Oxide Semiconductor
CMRR	Common-Mode Rejection Ratio
COM	Communication
CPP	Cerebral Perfusion Pressure
CS	Chip Select
CV	Cycle Voltammetry
DAC	Digital-to-Analog Converter
DAQ	Data Acquisition Device
DC	Direct Current
DTR	Data Terminal Ready
DUT	Device under Test
ECF	Extracellular Fluid
ECG	Electrocardiography
ECoG	Electrocorticography
EDTA	Ethylenediaminetetraacetic Aacid
EEG	Electroencephalography
EEPROM	Electrically Erasable Programmable Read-Only Memory
EMC	Electrical Magnetic Compatibility
EMG	Electromyography
EMI	Electromagnetic Inference
ESD	Electrical Static Discharge
ESR	Equivalent Series Resistor
EIB	Electrical Interface Board
Fc	Ferrocene Monocarboxylate
FPGA	Field-Programming Gate Array
FSCV	Fast-Scan Cycling Voltammetry
G	Gain

GND	Ground
GUI	Graphic User Interface
HDL	Hardware Description Languages
HRP	Horseradish Peroxide
IC	Integrated Circuit
I^2C	Inter-Integrated Circuit
ICP	Intracranial Pressure
ICU	Intensive Care Unit
ID	Identification
IDE	Integrated Development Environment
IEC	International Electro technical Commission
IEEE	Institute of Electrical and Electronics Engineers
INA	Instrumentation Amplifier
IO	Input/Output
ISE	Ion Selective Electrode
ISM	Industrial Scientific and Medical
K^+	Potassium
KCL	Potassium Chloride
LDO	Low Dropout
LCD	Liquid Crystal Display
LED	Light Emitting Diode
M	Inductance
MAC	Medium Access Control
MD	Microdialysis
$MgCl_2$	Magnesium Chloride
MISO	Master Input Salve Output
MOSI	Master Output Salve Input
MRI	Magnetic Resonance Imaging
Na^+	Sodium
NaCl	Sodium Chloride
NC	Normal Conditions
Opamp	Operational Amplifier
PbO_2	Tissue Oxygen Partial Pressure
PC	Personal Computer
PCB	Printed Circuit Board
PCIe	Peripheral Component Interconnect Express
PDMS	Polydimethylsiloxane
PHY	Physical layer
PIC	Peripheral Interface Controller
PPM	Parts Per Million
PSRR	Power Supply Rejection Ratio
PTFE	Polytetrafluoroethylene
PVC	Polyvinyl Chloride
PWM	Pulse Width Modulation
RAM	Random Access Memory
RE	Reference Electrode
RF	Radio Frequency
RISC	Reduced Instruction Set Computer
RMS	Root Mean Square
RTS	Request to Send
RuHex	Hexamine Ruthenium Chloride, $Ru(NH_3)_6Cl_3$

RX	Receiver Line
SAH	Sub-Arachnoid Hemorrhage
SCLK	SPI clock
SCL	Serial Clock
SD	Spreading Depolarisation
SDA	Serial Data
SELV	Safety Extra Low Voltage
SFC	Signal Fault Conditions
SMA	Sub Miniature version A
SMB	Sub Miniature version B
SNR	Signal-to-Noise Ratio
SoC	System on Chip
SPI	Serial Peripheral Interface
SPS	Sample per Second
TBI	Traumatic Brain Injury
TTL	Transistor-Transistor Logic
TX	Transmission Line
UART	Universal Asynchronous Receiver/Transmitter
UL	Underwriters Laboratories
USB	Universal Serial Bus
UPS	Uninterruptable Power Supply
VHDL	VHSIC (Very High Speed Integrated Circuit) Hardware Description Language
WE	Working Electrode

Chapter 1: Introduction and Literature Review

1.1. Traumatic Brain Injury

Traumatic Brain Injury (TBI) is one of the key causes of mortality and morbidity in the world, especially for young adults [1, 2]. It occurs when rapid external forces apply to the skull, caused by accidents, such as traffic accidents, violence, and accidental falls. There are possible outcomes: the skull fractures causing a penetrative injury; a blood vessel on the surface of the brain is ruptured causing a sub-dural bleed; or the brain is violently ruptured against the skull causing either bruising (sub-dural haematoma) or sheering of nerve cells (diffuse axonal injury). Brain injuries should not be treated as single events, but as complex and subsequential processes, which contain multiple interplays of different effects, such as structural damage, regional ischemia, inflammation, and metabolic crisis (failure of energy supply) [3, 4]. Without effective treatment, the pathological features of TBI are likely to cause patients to suffer from secondary brain injuries, which will be even more damaging. To develop effective treatments, the understanding of the pathological mechanisms of TBI is required.

Primary brain injury happens at the moment of trauma rapidly, and it is very unpredictable. Based on the severity of the injury, blood vessels, axonal shearing, blood brain barrier and meninges may be damaged (Figure 1.1).

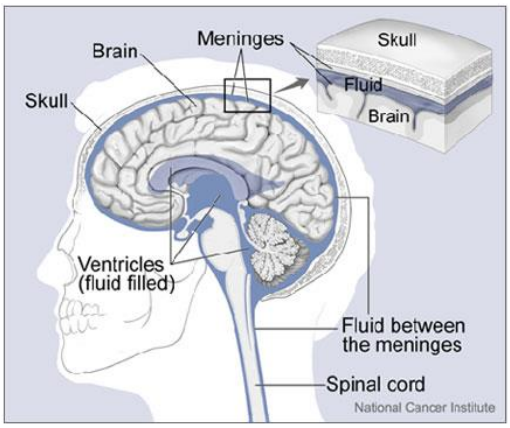

Figure 1.1: The structure of the brain and surroundings

The human brain is a soft and jelly-like tissue, which is protected by the bones of the skull and the intermediate membrane layers, which are called as meninges. Ventricles are filled with the extracellular fluid (ECF), which flows through the spaces between the meninges and cushions the brain. The picture is extracted from [5].

Different regions in the brain have different sensitivities to mechanical loading, due to their structures and makeups. Therefore, some tissues in the brain may experience more force and become more injured in the primary injury. However, little can be done to interact with the event of primary brain injury, other than preventing the trauma itself, for example use of cycle helmets and air bags in cars.

Sauaia et al.[6] reported that a large percentage of the people who die from traumatic brain injury do not die straight away, but days to weeks later after the event. Furthermore, unlike patients with other types of injuries, around 40% of TBI patients deteriorate after being hospitalised [7]. These situations are due to the effect of secondary brain injury, which is able to damage uninjured tissue or neurons after the primary injury. Secondary brain injury is an indirect result of the initial trauma. It occurs in hours and days after the primary brain injury, and can have a much larger impact on the brain and hence the outcome from the patient.

1.1.1 Causes of secondary brain injury

Secondary brain injury is thought to have a number of causes that can be slowly acting or dynamic. These can be included as either failure of energy supply/blood flow or abnormal brain activities.

Failure of energy supply/blood flow

Cerebral blood flow delivers essential energy substrates (glucose and oxygen) to neurons and is locally regulated. Secondary brain injury can cause ischemia due to bleeding or blood clotting, which causes insufficient blood flow in the brain. Without sufficient blood flow, cells rapidly consume local adenosine triphosphate (ATP) and hence the local glucose, either from free tissue glucose or the small glycogen reserves. Once ATP is completely depleted, cells will die within minutes [8].

As the injured tissues swell and the skull confines the brain to a limited volume, the intracranial pressure (ICP), the pressure within the skull, is likely to increase. If there is no hole in the skull, the brain tissue will become pressurised. This results in two problems:

a. The ICP counteracts the arterial blood pressure (ABP), which reduces the blood flow to the brain, leading to a reduction in cerebral perfusion pressure (CPP), defined as

$$CPP = ABP - ICP \tag{1.1}$$

This in turn can reduce blood flow to the brain.

b. The brain tissue tries to leave the skull by the only hole available, at the bottom of the skull. This is known as “coning”.

If there is a hole in the skull, for example from surgery, the brain is extruded through the hole to release ICP, causing herniation at the edge of the hole (Figure 1.2).

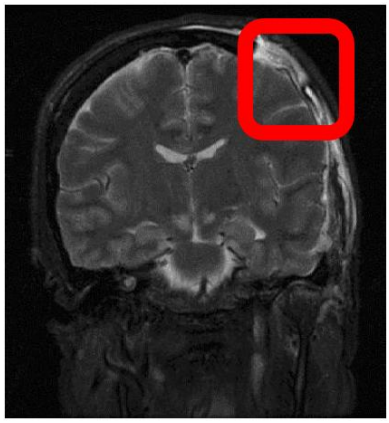

Figure 1.2: MRI scan of brain herniation

The red block indicates extrusion of the brain through a craniotomy with associated herniation. The skull was removed either for surgery or releasing. This figure is extracted from [9].

Hypotension, either constant or dynamic falls in arterial blood pressure (ABP) will cause a drop in cerebral perfusion pressure (CPP), which means it has the same impact as a high ICP does. The human brain under normal conditions has a cerebral auto-regulation mechanism, which maintains a stable blood flow, with an ABP between 50-150mmHg (the solid line in Figure 1.3). An injured brain may lose this ability. The flow becomes pressure passive with the problem that local blood flow is no longer being conditioned by the local energy demand (the dotted line in Figure 1.3). A major way in which TBI patients are treated is to maintain CPP more than 70mmHg initially by increasing ABP, but for severe cases, by removing the skull (known as craniectomy) and hence reduce the ICP.

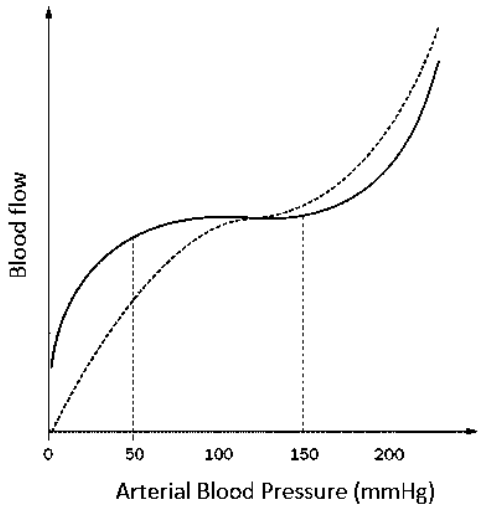

Figure 1.3: The relationship between the blood flow and the blood pressure

The solid line indicates auto-regulation under the normal brain condition, and the dot line the response when the auto-regulation fails and the flow becomes pressure-passive (analogues to Ohm law). The figure is extracted from [10].

Abnormal brain activities

Cortical spreading depolarisation (SD) and seizures are also associated with secondary brain injuries [11]. SD waves are consisted of mass neuronal and astrocytic depolarisation, which are originally generated from ischemic brain injury and propagate across the cerebral cortex, often cycling around the site of injury for a period of 10-20 minutes [12]. These waves happen frequently in patients who have undergone the craniotomy, such as sub-arachnoid hemorrhage (SAH), TBI, malignant hemispheric stroke, and spontaneous intra-cerebral hematoma [13-16]. SD waves temporarily silence the electrical activity of the cortex (Figure 1.4). The occurrence of spreading depolarisation has been proved to be associated with poor patient's outcome in a recent clinical study [17].

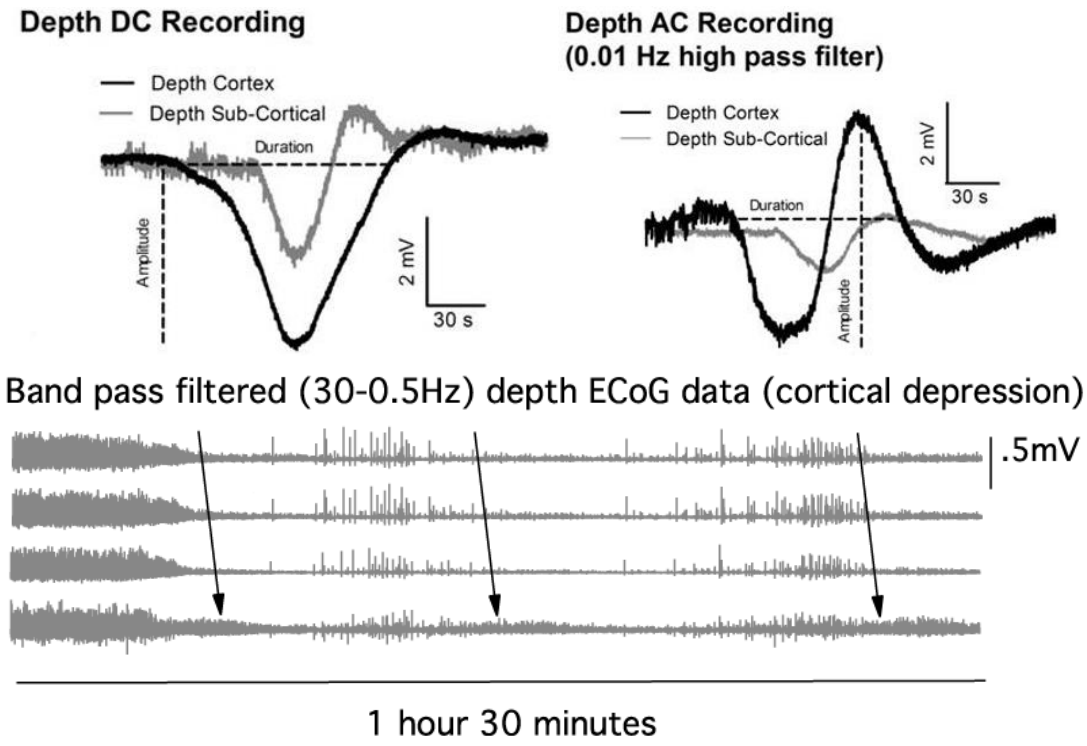

Figure 1.4: Classic electrocorticography (ECoG) signal patterns

The upper two Figures are respectively DC and AC recording of the SD waves from depth electrodes. The black traces are recorded from the cortex while the grey ones are from sub-cortical area. The lower traces is processed by a band-pass (30-0.5Hz) filter, which shows the reduction of cortical activities. The figures are extracted from [18].

1.1.2 Key parameters of measuring secondary brain injury

Secondary brain injury occurs after intensive care unit (ICU) admission, which means that potentially it could be monitored and prevented by measuring the key parameters discussed above and taking actions when any of these parameters become abnormal.

As a surrogate for blood flow, CPP is calculated by direct measurements of ICP and ABP. As for the energy supply, different chemical sensors can be applied to measure the concentration of tissue oxygen, glucose, lactate, and potassium. To investigate the effects of SD waves, they are characterized using electrocorticography (ECoG) by a slow large negative potential drop (Figure 1.4). Clinically, both electroencephalography (EEG) (mainly for seizures) and ECoG measurements can be applied for monitoring brain activities (Table 1.1).

Causes of secondary brain injury	Associated parameters (detection method)
Failure of blood flow	ICP, blood pressure, temperature (Licox monitor)
Failure of energy supply	Tissue oxygen, glucose, lactate concentration (Licox monitor and on-line microdialysis)
Abnormal brain activities	ECoG, potassium/sodium concentration (for SD), and EEG (for seizures)

Table 1.1: Causes of secondary brain injury and the relevant monitoring parameters

1.2 Clinical instrumentation system design

As outlined in Table 1.1, multiple monitoring parameters are required for a TBI patient. Therefore, a multimodal clinical instrumentation is needed to measure all the parameters simultaneously, and provide real-time feedback to the clinical team.

The main difference in monitoring a patient compared with a bench-test signal is that the patient signal can change unpredictably and can be noisy, due to either the electrical noise in ICU, or the noise triggered by nursing actions/patient movements [19]. Furthermore, the system must guarantee patient safety, limiting the amount of leakage current flowing into the patient [20]. In a standard biomedical information acquisition system, a transducer is used to convert a biological parameter from the patient to an electrical signal. The signal is then processed, stored, and displayed, so that the clinical team can perceive the information. In some cases, the sensor requires external applied energy, such as a bias voltage and an excitation current, to function accurately. Both the sensing elements and the processing electronics require regular calibrations, but the sensing elements need to be calibrated more frequent than the electronics.

1.3 Transducer techniques for TBI monitoring

A transducer is a device that can convert energy from one form to another. Specifically, a transducer, converting an electric parameter to a physical output, is named as an actuator, and a transducer, converting a physical parameter or concentration to an electric output, is a sensor. In TBI monitoring, sensors are preferable, as they produce electric output, which allows further signal processing [21]. In this section, the essential sensor techniques of detecting relevant changes in TBI patients will be discussed.

1.3.1 Chemical Sensors

The main chemical sensing techniques used for measuring these neurotransmitters are microdialysis [22], in vivo implanted sensors [23] and voltammetry [24, 25]. Different techniques have their own advantages and disadvantages:

Implanted sensors

Implanted sensors can be placed into the targeted sites, which allows them to detect subtle changes without any measurement delay. However, as the sensors are implanted and measured in vivo, sensitivity can be degraded quickly due to biofouling. In addition, the sensor cannot be calibrated in situ, which makes the loss of sensitivity and drifts difficult to track. Therefore, it is not suitable for long-term monitoring. The only exception is the Licox devices, which utilise gas-permeable membrane to reduce the bio-fouling effects.

In vivo voltammetry applies a voltage waveform to an implanted microelectrode and measure the output current. This is typically at a very high scanning speed in fast-scan cycling voltammetry (FSCV). It has widespread uses for measuring dopamine in animals, yielding a sub-second temporal resolution [24]. Pioneering work has recently begun to use FSCV in the human brain [26, 27]. The issue of applying this technique is that the output signals are generally very small, which also requires further processing to subtract the background current. Moreover, the fragility of the implanted carbon fibers makes it difficult to apply to the human brain.

Microdialysis

An alternative approach for clinical monitoring that has found widespread use is microdialysis [28-30]. It is a sampling method, allowing the sensors to be placed outside the patient. This technique has been widely used in vivo chemical collection. Here a 300-micrometer sampling probe is placed in the tissue of interest. All molecules that not present in the perfusion fluid diffuse from the extracellular space into the probe, and then are carried out of the probe for ex vivo analysis, using a wide range of analytical methods (Figure 1.5). Microdialysis is an established clinical sampling method that allows continuous monitoring of the chemical changes occurring within tissue extracellular fluid over time. Many good reviews are available, explaining microdialysis [31, 32] and its clinical applications [33]. This method normally presents high sensitivity due to the wide range of the possible analytical methods.

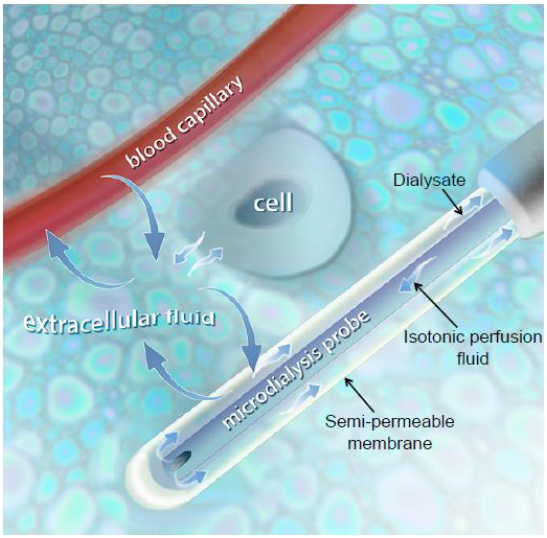

Figure 1.5: Schematic of microdialysis sampling

Microdialysis samples chemical species from the extracellular space via an implanted microdialysis probe and the semi-permeable membrane. The figure is extracted from [22].

Traditionally, dialysate samples are not analysed in real time. Samples are collected hourly and analysed offline, showing an average of the dialysate levels over that measuring time [34]. This therefore leads to an information delay with respect to the condition of the patient [28]. Recently, a novel online technique has been developed, which allows for sampling of metabolites at high temporal resolution without the need for separate sample collection and analysis [28, 34, 35]. This rapid sampling microdialysis technique has been used to monitor changes in glucose and lactate levels in the brain and bowel during surgery and postoperatively [28-30]. The clinical experiments described in the thesis were conducted on the basis of the on-line microdialysis technique.

1.3.2 Amperometry and three-electrode system

The most common chemical species can be oxidized or reduced beyond a certain applied potential, to give an oxidation or reduction current. The simplest and most common amperometric detection is single-potential DC Amperometry. A known potential (compared to a reference electrode) is applied to the working electrode to switch on an oxidation or reduction reaction, such that it takes place under the mass-transport control. The resulting current depends on the flux of species to the electrode surface. This in turn depends on species concentration, diffusion coefficient, electrode size, and the mass-transport regime.

To conduct an amperometric experiment described above, at least two electrodes are required. The working electrode (WE) collects the charge generated from, or passes the

electrons required for, the chemical reaction. The other electrode, which is known as reference electrode (RE), must hold a constant potential with respect to the working electrode, such that the chemical reaction can be continuously performed under the same applied voltage. In addition, the reference electrode is also required to balance the charge added or removed by the working electrode. However, it is very difficult for an electrode to maintain the desired constant potential as well as pass current. Therefore, another electrode is added to the system, particularly for supplying electrons, which is named as counter (or auxiliary) electrode (CE). The simplified schematic is shown in Figure 1.6.

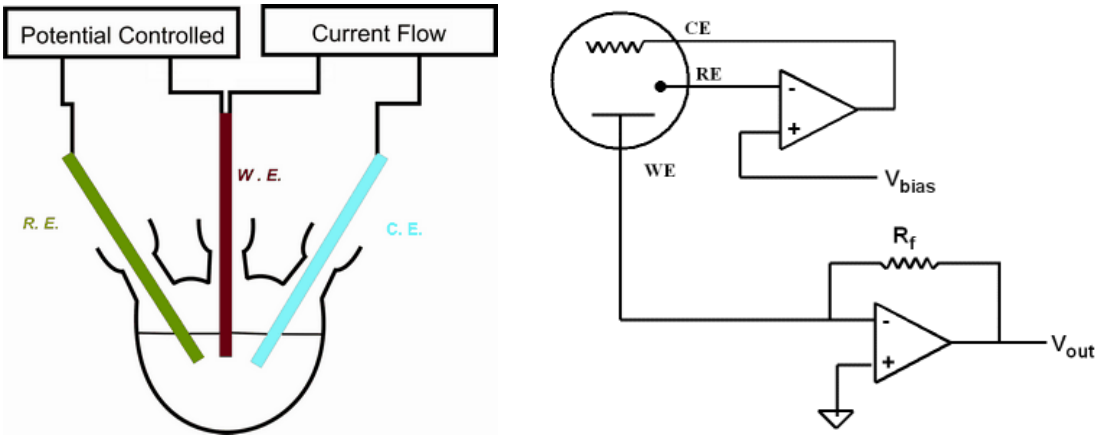

Figure 1.6: Simplified schematic of a three-electrode system

A working electrode, a reference electrode, and a counter electrode are involved in the system. In electrochemistry, the potential of the working electrode is normally virtually grounded for relatively easy output voltage calculations. The voltage is measured by passing through the output current through the resistor, R_f. This is called as transimpedance circuit, which will be discussed in Chapter 4. The overall bias potential on the electrochemical reaction is then regulated by the reference electrode, which is connected with the external bias voltage source, V_{bias}. The counter electrode is connected to the output of the op-amp, which provides the essential current to the system.

Glucose and lactate sensors, developed in Prof. Butelle's lab for TBI monitoring, operate on the basis of the three-electrode system, and the detailed working principle and relevant electronic considerations will be discussed in Chapter 4.

1.3.3 Potentiometry and ion-selective electrode

Potentiometry is the field of electroanalytical chemistry in which potential is measured under the condition of no current flow. The measured potential is related to the concentration of some components of the analyte solution, like potassium ion. The transducer, which is able to convert the activity of a specific ion in the solution into an electrical potential, is named an ion-selective electrode (ISE) that was originally described by Cremer in 1906 [36]. According to the Nernst Equation (1.2), the output voltage is dependent on the logarithm of the ionic

activity. By mounting different ion-selective membranes, different ISEs maintain different ionic selectivities.

$$E = 2.303\frac{RT}{zF}\log_{10}\frac{extracellular\ ion\ activity}{intracellular\ ion\ activity} = 2.303\frac{RT}{zF}\log_{10}\frac{[ion\ outside\ cell]}{[ion\ inside\ cell]} \quad (1.2)$$

E is the potential across the membrane (in volts, equivalent to joules per coulomb), R is the universal gas constant, 8.314 $JK^{-1}mol^{-1}$, T is the absolute temperature (in Kelvin), Z is the number of electrons each ion carries, F is the Faraday constant, 9.649 × 10^4 C mol^{-1}, [ion outside cell] is the extracellular ionic concentration, and [ion inside cell] is the intracellular ionic concentration. The activity a_x is proportional to the concentration [x], $a_x = [x] \times \delta$, where δ is the coefficient, ranging from 0 – 1.

To simplify the equation, at room temperature (25 ˚C), the potential difference across the ion-selective membrane for a univalent ion, such as sodium, potassium or chloride, is

$$\Delta E = 59.16\log_{10}\frac{[ion\ outside\ cell]}{[ion\ inside\ cell]}\ mV \quad (1.3)$$

An ISE selectively binds with the ion of interest, and its output potential is proportional to the activities (or concentration) of the ion, as shown in Equation (1.3). A miniaturised potassium ISE has been developed and optimised in Prof. Boutelle's group and used in this work, as the potassium concentration change in the local injured brain tissue is associated with spreading depolarisation events.

Experimentally, the output voltage of the ISE was measured against an external Ag/AgCl reference electrode. The behaviour of the Ag/AgCl electrode is governed by Equation (1.4), and a comparison between two Ag/AgCl electrodes generates the voltage in Equation (1.5).

$$\mathrm{AgCl(s)} + e^- \rightleftharpoons Ag^+ + Cl^- \quad (1.4)$$

$$\Delta E = \frac{59.16}{z}\log_{10}\frac{[a_{AgCl}]}{[a_{Ag}][a_{cl-}]}\ mV \quad (1.5)$$

AgCl is only very slightly soluble in water, a solubility product of $10^{-10}mol^2dm^{-3}$. In other words, the equilibrium in Equation (1.4) lies on the left. Based on these characteristics, an Ag/AgCl electrode is very chemically stable, and normally used as a practical reference electrode, especially in biological applications. In addition, the Ag/AgCl electrode also exhibits less electrical noise than the equivalent metallic Ag electrode. Studies [37] has showed that the electrode with AgCl coating yielded far less noise than that when the coating was removed. Moreover, the majority of the noise components for the purely metallic electrodes was at low frequency, which would become large noise interference for most low-frequency and low-

voltage applications. An ISE also features very large impedance due to poor conductivity of ions across the selective membrane, the interfacing electronics require sufficient input impedance to fully load the sensing voltage from the ISE.

1.3.4 Essential bio-signals in TBI monitoring

Bio-electrical signals

A bio-electrical signal refers to the change of the electrical potential across a specific tissue. Three different bio-signals, electrocardiography (ECG), electroencephalography (EEG), and electrocorticography (ECoG), were measured in the thesis to verify the functionalities of the system discussed in Chapter 5.

Each heart muscle cell maintains a negative potential, due to the ionic concentration difference, and this is called as membrane potential, which spreads across the membrane. In the electronic aspect, during each heartbeat process, two major events occur, depolarisation and repolarisation. During depolarisation, the membrane potential increases and goes towards to zero, which is caused by the influx of positive ions, mainly from Na^+ and Ca^{2+}. This event yields a rise in the voltage. After the depolarisation, repolarisation occurs, which indicates that the heart is recharging itself.

Electrocardiography (ECG) records the process of the electrical activity of the heart. As the polarisation and depolarisation of cardiac tissue are able to generate electrical impulses, these impulses can be sensed as a waveform over a period of time. In general, the waveform can be used to measure the heartbeat rate and its regularity. By further analysis, the size and the position of the chambers, as well as the presence of any weakness of the heart, can be detected.

3-, 5-, and 12-lead methods are widely used in clinical measurement, to spontaneously detect ECG signals at different positions. Each lead detects the ECG from a different angle, the combination of different leads can offer a better understanding of the cardiac condition of the patient. A standard ECG signal of a cardiac cycle contains 6 different main components (Figure 1.7), and the relevant characteristics are summarised in Table 1.2 [38].

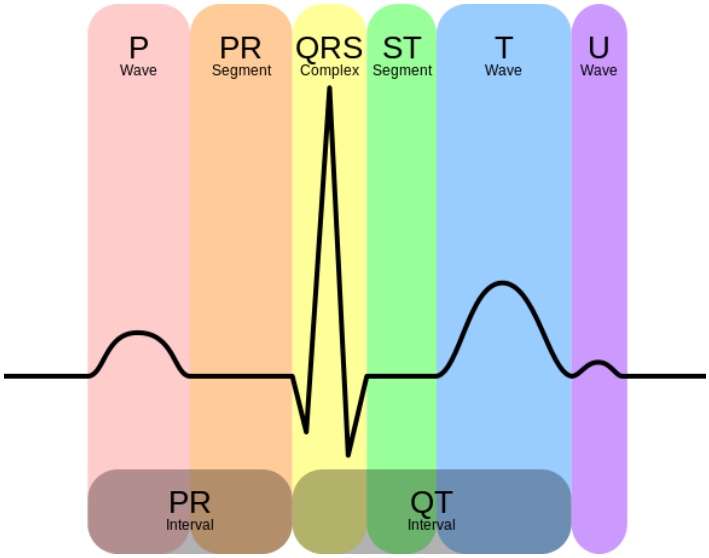

Figure 1.7: Schematic of an ECG signal

The figure presents a classic ECG signal pattern, which contains 6 different feature waves discussed in Table 1.2. The figure is extracted from [15].

Feature	Description	Duration/frequency
P wave	Formed when the atria contract to pump blood into the ventricles	80ms
PR interval	Time measured between the P wave and the QRS complex, which indicates the time electrical impulse takes to travel from the sinus node to the ventricles	120 - 200ms
QRS complex	The rapid depolarisation of the left and right ventricles, which has larger muscle mass than the atria, and therefore the magnitude is much larger than the P wave	80 – 100ms
ST segment	Represents the period when the ventricles are depolarised and isoelectric.	80 – 120ms
T wave	Represents the repolarisation of the ventricles. The interval from the beginning of the QRS complex to the apex of the T wave	160ms
U wave	Hypothesised to be caused by the repolarization of the interventricular septum. Normally low amplitude, and sometimes completely absent.	

Table 1.2: Characteristics of different waves in ECG signal

As the table and the figure indicates, an ECG signal contains a few different components with different amplitudes and frequencies. The amplitudes ranges from 0.2mV (T wave) to 3mV (QRS wave), and the frequency spreads between 0.5Hz to 100Hz.

EEG is the external monitoring of brain electrical activity across the scalp, which is due to the ionic current flows within the neurons of the brain. EEG signal is the main clinical electrical reference of brain activities, and EEG recording is extremely useful of diagnosing epilepsy, sleep disorders, coma, and brain death. The detailed EEG components, relevant frequencies, and locations are summarised in Table 1.3 [39].

Band	Frequency (Hz)	Location
Delta	<4	Frontally in adults and posteriorly in children[40]
Theta	4-7	Found in locations not related to task at hand[40]
Alpha	8-15	Both sides of posterior regions
Beta	16-31	Both sides of frontal region[41]
Gamma	32+	Somatosensory cortex

Table 1.3: Comparison table of EEG signal components over frequencies

EEG measurement is non-invasive, which directly applies electrodes to the surface of the scalp. The number of electrodes can vary from 8 up to 256. As EEG is non-invasive, it has widely clinical applications, including long-term continuous monitoring for TBI patients [42]. However, the major problem of EEG signal is that it has extra signal attenuation when it travels through skull and scalp, coupled to muscle potential generated in the scalp. The main effect is that low-frequency components that can be clearly observed in ECoG signals can no longer be seen on the brain itself. In addition, EEG has a worse spatial localisation of the electrical activity source [11], which indicates that it is difficult to use EEG to distinguish the electrical activities of injured tissue from those of healthy tissues.

ECoG monitors brain activity inside the skull. Two different types of electrodes have been reported to detect and monitor ECoG signals in literature: the strip electrode [43] and the depth electrode [18] (Figure 1.8). The strip electrodes are placed directly onto the cortex of the brain when the patient undergoes the craniotomy. However, this technique is restricted to certain number of patients who require craniotomy. Whereas applying the depth electrode array, SD waves can be detected and monitored via a burr hole on the cortex. This technique does not require patients with the craniotomy, which potentially facilitates the monitoring process and the number of available patient samples.

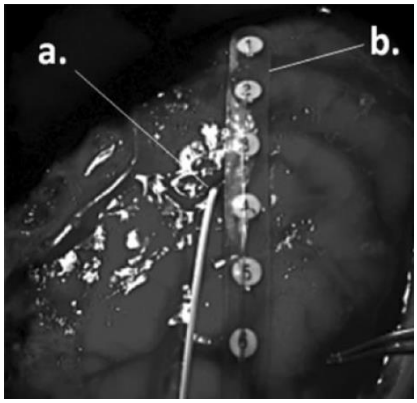

Figure 1.8: ECoG electrodes on the surface of the cortex

Depth electrode (a) vs. strip electrodes (b). Clinically, the separation between a and b is not well defined. The clinical team tries to place the depth electrode as close as possible to the strip electrode, right underneath the strip electrode. Currently, they are investigating and validating the performance of the depth electrode, as they consider it as the replacement of the strip electrode in the future. The figure is extracted from [18].

In this thesis, a novel electronic instrument has been developed for bio-electrical signal detections. The device has programmable measurement gains, therefore ECG, EEG, and ECoG can all be measured. The signal quality has been compared with a commercial bio-amplifier, which will be further discussed in Chapter 5.

Non-electrical bio-signals

Apart from the bio-electrical signals described above, several non-electrical bio-signals, such as intracranial pressure (ICP), blood pressure (BP), tissue oxygen partial pressure (PbO_2), and tissue temperature, are also of great importance in TBI monitoring. In the thesis, these parameters have been measured by external commercial devices. Each device provides an analog output, which can be recorded from the central data recorder. The TBI instrumentation box, discussed in Chapter 6, provides relevant connections on the back panel. These devices are well developed to fit the current TBI monitoring, and critically are used as “standards of clinical care”. Therefore further optimisations are beyond the scope of this thesis.

1.4 Key electronics requirement

1.4.1 Biopotential amplifier

A biopotential amplifier is an amplifier specifically designed to measure biopotentials. Its fundamental function is to safely measure a small electrical signal from a biological origin and amplify it for further data processing. This indicates that a biopotential amplifier should be able to increase signal strength while maintaining high signal fidelity. In addition, a

biopotential amplifier should have enough precision to measure low-level signals and feature high input impedance to overwhelm high source impedance from measurement electrodes. Furthermore, a biopotential amplifier can also provide necessary protection to the patient/organism being studied, as any electrical leakage current from the input terminals of a biopotential amplifier can cause microhazard or macrohazard of the patient. The details will be further discussed in Chapter 6.

Very frequently, biopotentials are measured from bipolar electrodes with respect to ground. In practice, such an electrode normally presents a background (offset) voltage, due to the electrode-tissue interface, together with the desired biopotential. In addition, the biopotential is normally much smaller than the background voltage, which makes the following processing electronics unable to extract the real signal from the background. This background voltage on every electrode is called as common-mode signal. To tackle this problem, the most appropriate biopotential amplifier is a differential one, which can ideally remove all the common-mode voltage and only amplify the voltage difference between two electrodes. Therefore, a biopotential amplifier is required to have high common-mode rejection ratio (CMRR) at all frequencies down to DC, to minimise the interference from the common-mode signal. Generally, an instrumentation amplifier (3 op-amp based) maintains better CMRR (more than 110dB) than a single op-amp (60-80dB), and the details will be discussed in Chapter 2.

As mentioned, the high input impedance, R_L, is also of great importance for a biopotential amplifier, as it can minimise the voltage loading of the signal from an electrode/sensor being measured, for example, the ion selective electrode (ISE) described in 1.3.3. Practically, the impedance ranges from hundreds of MΩ to several GΩ. Therefore, an ISE should be treated as a DC voltage source (V_S) with a large resistor (R_S) in series. It creates a resistor-based voltage divider circuit, with the biopotential amplifier (Figure 1.9). The actual voltage that arrives at the input terminal, V_L, is based on the ratio of these resistors:

$$V_L = \frac{R_L}{R_S + R_L} V_S \tag{1.6}$$

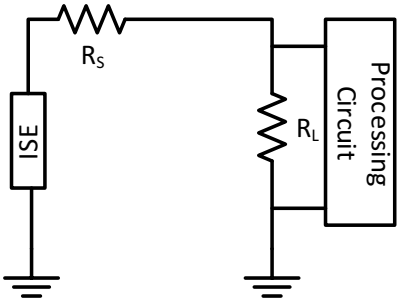

Figure 1.9: Schematic of a high-impedance ISE interface

Therefore, the input impedance of the amplifier, to which the electrodes are connected, must be much higher than the source impedance of the electrodes, to avoid attenuation of signal amplitude and significant distortions [37].

In addition to these factors, other essential factors of a biopotential amplifier are the bandwidth and signal-to-noise ratio (SNR). As most bioelectrical signals appear at low frequencies (DC to 250Hz), a biopotential amplifier should be trimmed to operate at the specific frequency range, where the measured bioelectrical signal may exist. By limiting the operating bandwidth, the noise from other bandwidths can be eliminated, and therefore optimal SNR can be obtained.

1.4.2 Potentiostat

A potentiostat is a fundamental electronic hardware, which is utilised to control the three-electrode system and run most electroanalytical experiments. In order to successfully activate desired electrochemical reactions, a potentiostat is required to meet three requirements:

- Maintain a required constant positive/negative excitation voltage between the working electrode and the reference electrode, with the excitation voltage being selectable for users.
- Convert the current generated from the working electrode to a relatively large and clear voltage for further processing.
- Prevent current passage through the reference electrode

There are many potentiostat manufactures in the market, and the price for a potentiostat can vary from hundreds pounds to twenty thousand pounds [44]. In addition, the applications for

a certain potentiostat can vary significantly. For a chemical detection in the human tissue, the potentiostat is generally required to maintain pA sensitivity. Potentiostats to handle 10A current with 100V compliance voltage are needed in studies on axle rod corrosion.

Commercial potentiostats tend to have multiple functions to meet as many consumers as possible. The performance in general is associated with the price. Some complex potentiostats may also involve internal data converter, microcontroller, and display/analysis software, like BI-PG 100 [45]. However, as most of commercial potentiostats are designed to meet universal purposes, they always have some unwanted features in some levels. In addition, the size of such a potentiostat is normally relatively large, which is not suitable for high-integration limited-space applications. Therefore, in the thesis, custom miniaturised high-precision potentiostats have been developed, which are particularly suitable for TBI and other clinical monitoring.

1.4.3 Microcontroller

A microcontroller is a compact microcomputer on a highly integrated circuit, designed for embedded systems, using on-chip embedded flash memory in which to store and execute its program. It is a self-contained system, which normally contains a core processor, programmable input, and output peripherals, timers, and on-chip analog-to-digital converters (ADCs). It is normally designed using complementary metal oxide semiconductor (CMOS) technology, which is less vulnerable to power spikes and uses less power than other fabrication techniques. The predominant architecture for a microcontroller is Complex Instruction Set Computer (CISC), which enables the chip to execute multiple control instructions with a single macro function. In some cases, a microcontroller is designed on the basis of a Reduced Instruction Set Computer (RISC) architecture, which offers fewer instructions, but consumes less power [46].

Microcontrollers need to be programmed and the relevant code needs to be stored, in order to function correctly. They were initially programmed in assembly languages, but various high-level programming languages, such as C and JAVA, have been developed to facilitate the coding process. Nowadays, microcontrollers are widely used in the electronics market, and the major vendors including Atmel, Microchip Technology, Texas Instruments, and NXP Semiconductors. Based on the functionalities, cost, size, power consumptions, and IO pins, different microcontrollers have their own application fields. One single chip cannot be a

universal fit to every application. In this thesis, 8-bit AVR-based and 32-bit ARM-based controllers were mainly used to implement certain applications.

1.4.4 FPGA

A field-programmable gate array (FPGA) is also an integrated circuit, whose internal logic gates can be configured by users. Unlike standard microcontrollers, with internal built-in logics and registers, FPGA maintains large resources of logic gates and random-access memory (RAM) blocks to implement complicated digital computations. By using hardware description languages (HDL), internal gate logics of a FPGA can be then configured. A FPGA normally maintains multiple programmable logic blocks, which feature reconfigurable interconnections that allows different blocks to be "wired up". In addition, these logic blocks are able to function independently, which means a FPGA is capable of communicating with multiple digital devices simultaneously. By contrast, a standard single-core microcontroller can only perform one task at a specific time.

Currently, Xilinx and Altera are the main FPGA manufactures, which jointly control more than 80% of the market [47, 48]. The size and capability of a FPGA also vary over different series. It can be as small as 3 × 3 mm, with 2μW power consumption, while it can also be a 50 × 50 mm large-scale unit, with more than 1 million internal logic gates. The detailed implementation of the FPGA will be discussed in Chapter 4 and 5.

1.5 Design process for clinical instruments

Unlike purely implementing ideas and proving concepts in the lab, designing a practical clinical instrument is much more complicated, which is also an expensive and lengthy process. The design involves idea inventions, prototype design, debugging, final product development, clinical regulatory approvals, clinical tests, casing, and manufacturing. If the design is going to be commercialised, it also requires marketing and sale phases (Figure 1.10).

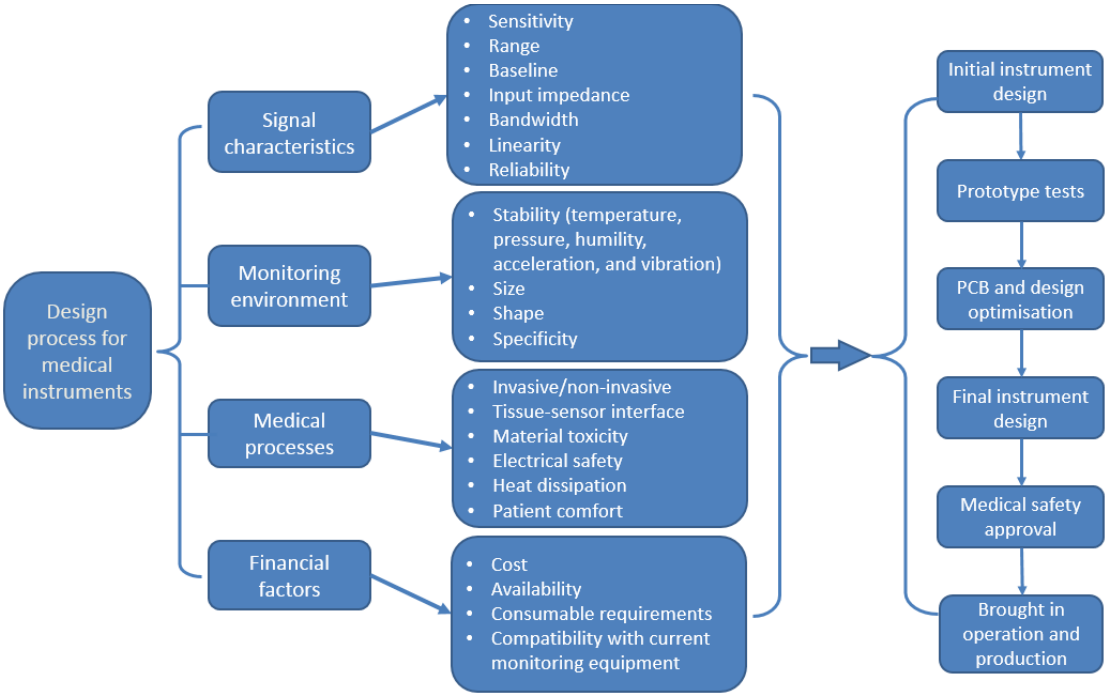

Figure 1.10: Design process and consideration for medical instruments

The factors in the list (Figure 1.10) are those of great importance in designing a clinical instrument, whereas some processes may be overlooked by only implementing a lab-based device or a coursework. These are my major design processes and considerations when working on the thesis, and all the factors will be discussed on specific applications in following chapters.

1.6 The outline of the thesis

There are ten chapters in the thesis, discussing about various novel wired and wireless electronic system designs and development for clinical uses, especially for traumatic brain injury (TBI) monitoring (Figure 1.11). The introduction, common materials, and design considerations have been discussed from Chapter 1-3, and the main chapters of the thesis are from Chapter 4 to 9.

Figure 1.11: The outline of the thesis

More specifically, Chapter 1 describes the background, transducing techniques, and relevant electronic requirement of the TBI monitoring system.

Chapter 2 mainly contains common materials, technical terms, analysis methodologies, communication protocols, and different amplifier types.

In Chapter 3, I will discuss my experience on PCB routing, layout, and relevant system design. The interfacing considerations when working with practical sensors and clinical human-contact electrodes will also be considered. In addition, the considerations of different experimental set-up and the methods of avoiding unnecessary resistive/capacitive/inductive noise will be illustrated.

In Chapter 4 and 5, different electronic monitoring systems will be designed and developed to measure the relevant key parameters in a TBI patient. More specifically, Chapter 4 discusses two different (resistive and capacitive) potentiostat designs to support and operate

amperometric sensors, converting extra-low current from a sensor to a voltage output for further signal processing, while maintaining a desired voltage between the working and reference electrode. The performance tests of both designs and the relevant comparison tests will be discussed. In Chapter 5, a voltage-input analog front-end chip will be demonstrated for bioelectrical potential acquisition. By employing the same central processor and extra analog output digital-to-analog converters (DACs), the system can achieve very low noise and detection limit. By trimming the internal programmable gain, the system is capable of monitoring different bioelectrical signals.

Chapter 6 focuses on developing a multimodal monitoring instrumentation system for TBI patients, which integrates the designs discussed in Chapter 4 and 5. The electrical and mechanical considerations of the system will also be demonstrated. As the TBI box is designed for clinical monitoring, relevant patient safety, IEC60601 standard, and isolation methods will also be discussed.

In Chapter 7, I will demonstrate the needs and benefits of applying wireless technologies into the current monitoring electronics. Different wireless solutions will be compared in this chapter. The designs discussed in Chapter 4 and 5 will be implemented wireless solutions. Both lab-based and clinical data will be discussed at the end of the chapter.

In Chapter 8, a stackable modular system will be introduced. The design, development, and benefits of the stackable system will be illustrated, and the comparative performance against a standard spreading layout design will be also analysed. In addition, the comparison between the Bluetooth and the Zigbee wireless solution will be discussed as well.

In Chapter 9, a wireless microfluidic-based sensor auto-calibration system will be introduced, which allows the sensor monitoring system to display real-time biological concentration changes. The system developed in this chapter will involve sensor excitation circuitry, ADCs, digital controlling system, feedback circuit, and DAC outputs. At the end of the chapter, a graphic user interface operated on either a PC or a smart phone/tablet will be also illustrated.

In Chapter 10, I will summarise all the electronic systems and relevant achievements in the thesis. The future research and potential developments will be discussed at the end of the chapter.

In general, this thesis involves all the essential steps of designing a clinical instrumentation system. One instrumentation does not necessarily contain all the steps, due to individual applications and functionalities, but at least it should have some of the functional parts. A generalised designing block for a clinical electronic system is demonstrated in Figure 1.12, and every individual functional block will be discussed in specific chapters (indicated with red dot rectangular).

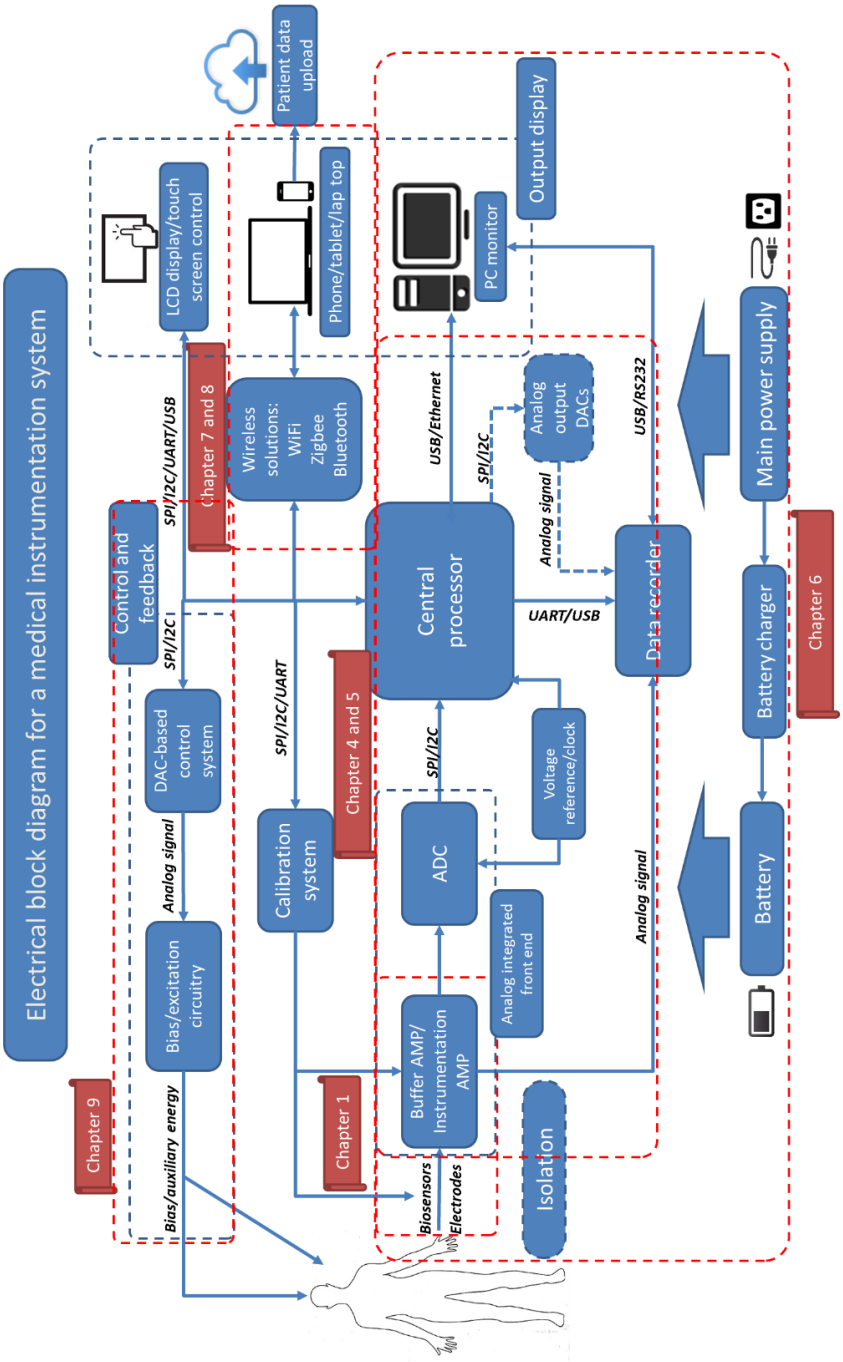

Figure 1.12: Electrical block diagram for medical instrument design

1.7 Publications and patents

Most design and development discussed in the thesis has been submitted or in preparation to publications or patents:

1. The TBI instrumentation design, development, and results discussed in Chapter 4-6 have been submitted for publication in the Journal of the Royal Society Interface *("High-Performance Bioinstrumentation for Real-Time Neuroelectrochemical Traumatic Brain Injury Monitoring"), and demonstrated at science TV series "Bang Goes the Theory" on BBC1.*
2. The wireless stackable system discussed in Chapter 8 has been published in the Journal of Analytical Chemistry *("A 3D printed microfluidic device with integrated biosensors for online analysis of subcutaneous human microdialysate")*.
3. The contents in Chapter 9 has been prepared to submit to the Journal of the Analyst, Royal Society of Chemistry *("Wireless Microfluidic-Based Biosensor Auto-calibration System Development for Real-time Concentration Display") and it has also been submitted together with the on-line microdialysis technique for a know-how patent.*
4. The wireless implementation discussed in Chapter 7 is being integrated with miniaturised biosensors and the clinical results are in preparation to publish in the Journal of Analytical Chemistry.
5. The electronic systems described in Chapter 4, 5, 6 have been also involved in other literatures published in the group.

Chapter 2: Common Materials and Test Methodologies

This section describes the common chemical and clinical materials used in the thesis, technical terms, electronic programming and testing devices, and statistical tools for analysing data.

2.1 Transducers used in this thesis

2.1.1 Microfluidic analysis system

As mentioned, a microfluidic system is used for TBI patient monitoring. A standard microdialysis system contains serveral essential parts (Figure 2.1), and each part will be discussed in the following section.

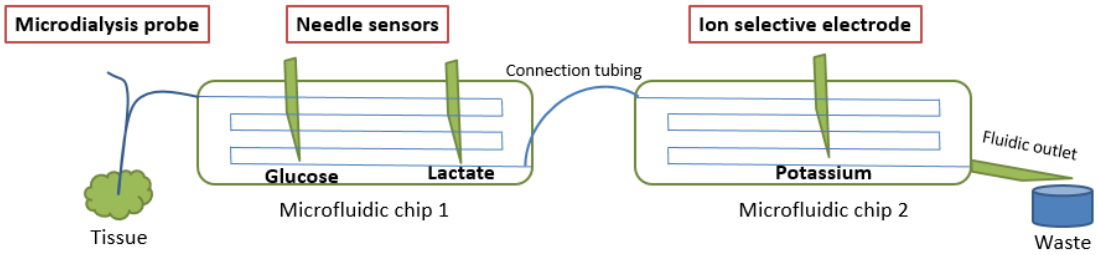

Figure 2.1: Simplified schematic of a microfluidic analysis system

Microdialysis probe

In clinical monitoring, an FDA-approved brain MD probe (CMA 70, Sweden) was used. It has a gold tip to locate the probe on CT scans. In the thesis, we have used artificial cerebro-spinal fluid (aCSF, discussed in Section 2.2.3) at 2 µL/min.

Microfluidic chip

The microfluidic chips used in the thesis have been developed based on Polydimethylsiloxane (PDMS) (Figure 2.2). All the chips used in the thesis were fabricated in Prof. Boutelle's group.

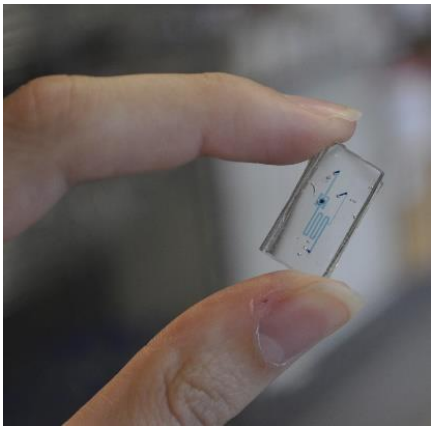

Figure 2.2: Appearance of a microfluidic chip

The chip itself is transparent, and the one in this figure is filled with a colour dye to show the internal traces.

2.1.2 Amperometric sensor - needle electrode

Needle electrodes used in this thesis have been miniaturised to place in microfluidic chips. They incorporate all the three electrodes required for an electrochemical reaction. Figure 2.3 shows the appearance of the combined needle electrode, which features a working electrode (WE), a reference electrode (RE), and a counter/auxiliary electrode (CE or AE). All sensors were made by Dr. Michelle Rogers and Dr. Sally Gowers in Prof. Boutelle group.

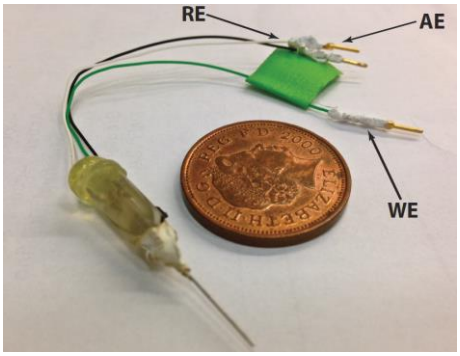

Figure 2.3: The appearance of a needle electrode

2.1.3 Ion selective electrode (ISE)

The miniaturised potassium ISEs used in this work were made by Dr. Chi Leong in Prof. Boutelle group. Each ISE consists of a polymer membrane casted at one end of a polymer electrode body, an internal silver/ silver chloride (Ag/AgCl) reference electrode and an internal filling solution of physiological saline. The membrane consists of 0.2 mg potassium tetrakis borate,

150 mg Bis sebacate, 66 mg polyvinyl chloride, and 2.0 mg of potassium ionophore. All the chemicals are obtained from Sigma-Aldrich (UK), and the appearance of the assembled ISE is shown in Figure 2.4. The ISEs are stored in aCSF at 4 degree Celsius when not in use.

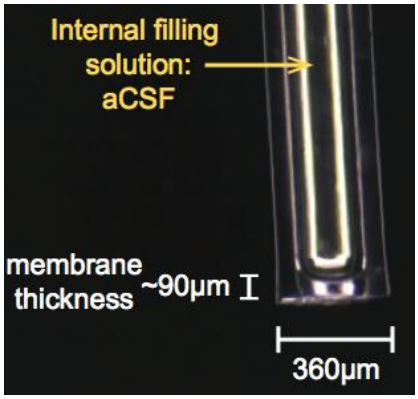

Figure 2.4: ISE appearance

The picture is captured under a microscope. The ion-selective membrane is 90µm thick, and the tip is 360µm wide.

Experimentally, the output voltage of the ISE was measured against an external Ag/AgCl reference electrode (saturated at 3M KCl). The ISEs were calibrated at 25 degrees Celsius and had a Nernstian sensitivity of approximately 59 mV/dec and good temporal response for the physiological range of interest.

2.1.4 EEG/ECG electrode and gel

The EEG/ECG electrodes were surface Ag/AgCl electrodes, bought from Unimed. They are the standard EEG electrodes used in clinical practice. To remove any motion artefact and reduce skin impedance when performing ECG or EEG tests, a conductive gel is normally applied. The one used in the thesis was Nuprep EEG & ECG Skin Prep Gel, from Weaver and Company.

2.1.5 ECoG electrodes

Two types of sterile ECoG electrodes, strip electrodes and depth electrodes, were involved in the thesis, and both were purchased from AD-TECH, USA. The part number for the strip electrode is TS06R-AP10X-0W6, and that for the depth electrode is SD08R-AP58X-000. They are made of platinum, and both designed for long-term clinical monitoring.

AD-TECH also provides an electrode-electronics cable adaptor, called as Cabrio connection system (Figure 2.5), which features a secure clip on the electrode cable. Each gold pin in the connector corresponds to one electrode, and signals from different electrodes will be converted and transferred to the electronics, via the while multicore cable.

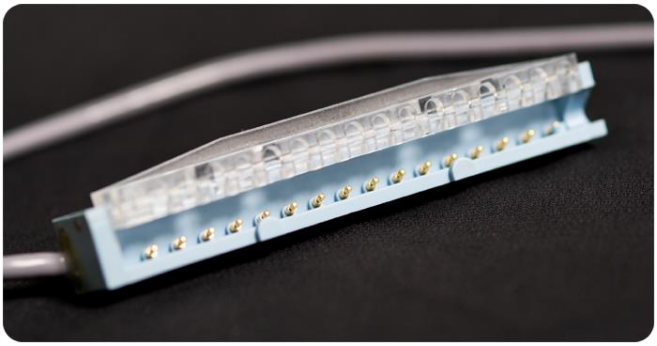

Figure 2.5: Cabrio connection system

Different types of Carbio connectors are available on the website. The figure is extracted from [49].

2.2 Chemical and clinical material preparation

All solutions were made of extra-high purity (de-ionised) water, whose resistivity is approximately 18MΩ-cm.

2.2.1 Hexamine ruthenium (III) chloride (RuHex)

The RuHex solution used in the thesis was prepared by applying 1 mM RuHex, $Ru(NH_3)_6Cl_3$, into 0.1M potassium chloride (from Sigma). Other concentrations between 0 to 1mM were diluted from the 1mM RuHex solution. Before using the solution, it was de-oxygenated by purging with nitrogen gas for 20 minutes.

2.2.2 Ferrocene buffer

Ferrocene (Fc) buffer used in the thesis was consisted of ferrocene carboxylic acid, EDTA, sodium chloride, and sodium citrate. The detailed concentrations are shown in the Table 2.1. Fc buffer was filtered with 0.1µm and 0.02µm membranes to remove undissolved particles before use.

Chemical	Concentration (mM)
Ferrocene carboxylic acid	1.5
EDTA	1.0
Sodium chloride	150
Sodium citrate	100

Table 2.1: Composition of Fc buffer

2.2.3 Artificial cerebro-spinal fluid (aCSF)

Different compositions of aCSF are available, but to be consistent with all the clinical results and relevant sensor calibrations, the same aCSF composition (Table 2.2) is used for all the experiment demonstrated in this thesis. The solution is filtered with 0.02µm membrane to eliminate any undissolved particles interference.

Chemical	Concentration (mM)
Magnesium chloride ($MgCl_2$)	0.85
Calcium chloride (CaCl2)	1.2
Potassium chloride (KCl)	2.7
Sodium chloride (NaCl)	147

Table 2.2: Composition of aCSF buffer

All the calibration experiments were prepared on the basis of the aCSF background, unless stated otherwise.

2.3 Electronic testing device and relevant software

2.3.1 Current source and picometer

The current source used in this thesis is 6221 AC/DC precision current source (Keithley Instruments), which provides current in a wide range, from 100fA to 100mA. High output impedance (10^{14} Ω) ensures the device to provide stable current into various loads. The blue LED on the panel indicates the status of the device (Table 2.3). The device is also able to source AC current in a wide frequency range, however, in this thesis the current source was only used for providing DC current to evaluate the device under test (DUT).

LED Status	Indication
Off	Device is not outputting any current
Constantly on	Device is output a pre-set current
Flashing	Device is configured to output a current, but no load is detected

Table 2.3: Status of the current source

The picometer used in the thesis is Model 6485 5-1/2 picometer, from Keithey, which guarantees 10fA resolution. The detection range is from 20fA to 20mA, with up to 1000 readings per second. The picometer was applied to justify the accuracy of the current source, and eliminate any artefact or electrical interference from the current input side.

2.3.2 Signal generator

The signal generator used in the thesis is 33220A, single-channel 20MHz function/arbitrary waveform generator, from Agilent. It has two different working modes: local mode and remote mode. In the local mode, different output signal types, such as sine, square, pulse, ramp, triangle and DC waveform, can be configured from the front panel of the device. In addition, the amplitude of the signal can be selected from $10mV_{P-P}$ to $10V_{p-p}$, with a frequency of up to 20MHz. In the remote mode, the signal can be downloaded from the host computer via USB. The software used to edit and download the waveform is *wrapper*, and it allows users to import customised data from various formats. For example, the simulated ECoG data, discussed in Chapter 5, was generated from this software.

2.3.3 Digital signal analyser

All the digital data analysis in the thesis have been conducted with a digital oscilloscope, InfiniiVision MSO-X 2002A from Agilent. It has 2 analog channels and 8 digital channels, which scans up to 70MHz. When recording digital transmission waveforms, a logic analyser, Saleae logic 8 USB logic analyser, from Microchip has been used. With its processing software, the analyser is capable of recording 8-channel logic status for a certain time period, and it supports both 3.3V and 5V logic voltage levels.

2.3.4 Data recorder

The main data acquisition device (DAQ) used in this thesis is *PowerLab 16/35*, from ADInstruments (Figure 2.6). The main reason for applying PowerLab in the thesis is the associated data acquisition and analysis software, LabChart 7. All the settings of a PowerLab can be configured from this software. In addition, the software allows users to do real-time or post data processing, such as signal scaling, digital filters, and power spectrums. The recorded data can be stored and exported in various format, such as txt, IGOR, and Matlab, which offers the possibilities of further data processing.

Figure 2.6: Appearance of the latest PowerLab

It is a 16-channel DAQ with 16-bit resolution in each channel, and the scanning rate is up to 200k sample/s. The detection range can be selected between ±2mV and ±10V by the uses of internal amplifiers. The device also features two analog output channels, which allows users to simulate a waveform or generate a constant voltage to activate a certain electrochemical reaction. The figure is extracted from [50].

2.3.5 PCB design software

Two printed-circuit board (PCB) computer aid drawing (CAD) packages have been used for the circuit designs discussed in the thesis. When working on simple single or double-layer circuit board, I use CadSoft EAGLE 7.1.0, as it provides easy user interface and provides free light version to design up to 2 signal layers with limited dimension 100mm × 80mm. However, the schematic editor can create only one sheet. Apart from the size and function limitations, the software is good and efficient to design small-scale circuit boards, like potentiostat descried in Chapter 4 and Xbee-based wireless potentiostat described in Chapter 7. In addition, one of the largest electronic distributors, Farnell, provides various component libraries in EAGLE format, which significantly reduce the design time.

When certain projects require complex mixed-signal designs with multiple (4 or more) signal layers, such as wireless LabSmith controller described in Chapter 8, and the stacking data acquisition system described in Chapter 7, I use Altium Design 14, which is a professional CAD designing software. It supports up to 16 signal layers in the PCB layout editor, and supports up to 999 sheets in the schematic editors. In addition, it provides native 3D design of the PCB, which allows users to visualise the board and integrate other mechanical designs into Altium. The latest Altium is also able to import EAGLE files and libraries, which allows users to keep their previous EAGLE-based designs.

2.3.6 FPGA Programming software

As for FPGA programming, such as DDC controller described in Chapter 4 and the monitor-side digital board described in Chapter 5, the coding language is VHDL, which is written in Xilinx ISE Design Suite 13.1, and the code debugging process is performed in Xilinx ISE Simulator (ISim). After compiling the code, ISE Design Suite generates a bit file, which can be then downloaded to the FPGA via a code downloader, FPGAconf.

2.3.7 Arduino programming

The thesis also contains some programming of Arduino products, such as Arduino DUE described in Chapter 4 and 7, and Arduino UNO described in Chapter 8. The code for these projects is written in Arduino IDE 1.5.2.

2.4 Common electronic components, terms and considerations

2.4.1 Op-amp selection considerations

Each op-amp has its own specifications and limitations, and there is no universal op-amp that can fill in every application. There are always trade-offs among various specifications of an op-amp.

Chopper-stabilised amplifier

When working as a standard front buffer, the input offset voltage should be minimised to maintain a “zero” baseline. Normally, a chopper-stabilised amplifier, such as AD8629 from Analog Devices, can be utilised, as the offset voltage, V_{OS}, is normally less than 1μV, while a general-purpose precision amplifier has a V_{OS} between 50 – 500μV.

A chopper-stabilised amplifier applies an internal oscillator to control the internal chopper switches. The standard schematic of a chopper amplifier is shown in Figure 2.7, and it works in 2 different modes, which are controlled by the chopper switches. When the switches are placed to “Z”, which indicates as the auto-zero mode, C2 is charged by the input offset voltage while C3 is charged by the output offset voltage. This mode eliminates any appearing offset. When the switches are placed to “S”, the op-amp works in the sampling mode, which takes the new offset on the input nodes. By switching between these two modes, the offset can be continuously cancelled out [51-53]. Another advantage of applying chopper amplifier is that

it samples at a certain frequency from hundreds of Hz to several kHz, which makes it effective to remove the flicker (1/f) noise, the main noise source in low-frequency applications.

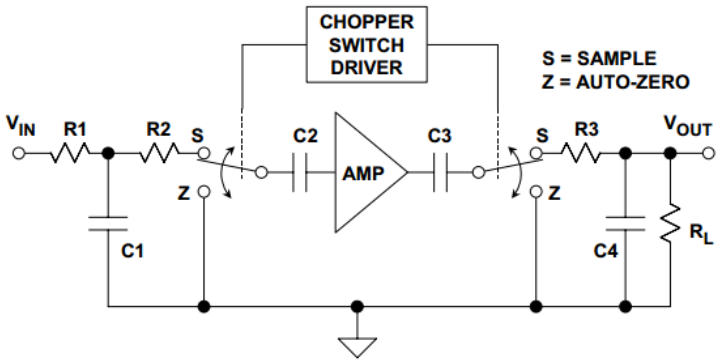

Figure 2.7: Standard schematic of a chopper amplifier

The internal chopper switch controls different states of the amplifier. The figure is extracted from [53].

A potential drawback of a chopper amplifier is that the internal sampling frequency potentially limits the input signal frequency range. The input frequency should not exceed half of the chopping frequency, based on the aliasing theory. As Figure 2.7 shows, R1 and C1 in the circuit serve as an anti-aliasing filter, to limit the input frequency within the working range.

High-impedance amplifier

As discussed, a chopper amplifier can be a “perfect” buffer selection for low-frequency applications. However it is not always applicable due to the mismatch of the impedance. As discussed in Section 1.3.2, when working as an interface of an external high-impedance (≥ 100MΩ) source, such as a PH electrode or a general ISE, the impedance of the electrode makes a chopper amplifier unable to load in the transferring voltage. Therefore, a high-impedance (10 - 100GΩ) application-specific amplifier is required.

Instrumentation amplifier

When working in a relatively noisy environment, like monitoring biosensors in a clinical ward, a very high CMRR is desired, as it can effectively reduce common noise on the inputs. In addition, an op-amp with high input impedance is also desired, due to the high impedance of some sensors. To deal with these issues, an instrumentation amplifier (INA) (Figure 2.8) becomes one of the best options. An INA is a type of differential amplifier with internal buffers, which meets the need of input impedance matching. It normally contains three

internal op-amps, where 2 op-amp work as buffers to the inputs and one is utilised for producing the desired output.

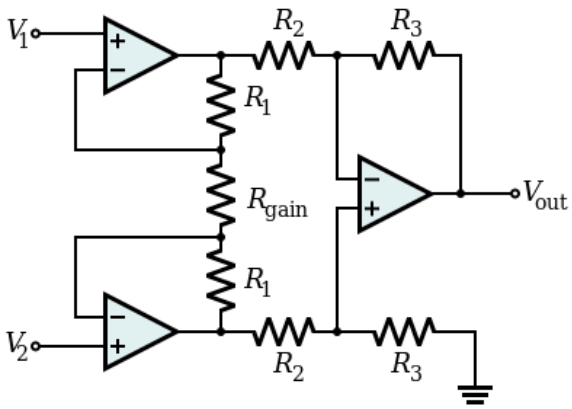

Figure 2.8: The schematic of an INA

The two front buffers are manufactured in the same micro-fabrication process, which makes them to maintain the same properties, such as offset and input bias current. This significantly increases its ability to reject common-mode signals on the input terminals, and therefore yields a much higher CMRR than a standard op-amp does. The figure is extracted from [54].

In terms of the amplification, three resistor-pairs and a gain resistor are involved in the schematic, which generates the overall gain, G, as:

$$G = \frac{V_{out}}{V_2 - V_1} = \left(1 + \frac{2R_1}{R_{gain}}\right)\frac{R_3}{R_2} \tag{2.1}$$

The rightmost circuit, involving R_2 and R_3, is a standard differential amplifier, and the resistance of R_2 and R_3 is normally trimmed to the exactly the same, which generates a unit gain. In addition, R_1 is also pre-set during manufacture, and only a gain resistor, R_{gain} is left for users to tune the gain.

Such a schematic is not too difficult to be implemented on a circuit board with a few op-amps and resistors. However it is highly recommended to apply a complete INA chip. As an INA chip, such as INA116 from TI, has trimmed all the internal resistor-pairs to maintain the same resistance, tolerance, and temperature coefficient. Its internal op-amps also feature the same characteristics, which makes the output much more accurate and reliable than a self-assemble INA.

In addition to the application-specific op-amps discussed above, Table 2.4 shows several other features and considerations when sourcing a suitable op-amp for a specific application.

Function	Performance	Package	Market
Numbers of op-amps (single, dual, or quad)	Low bias/offset current	Type (surface mount or through-hole)	Availability
Single or dual supply	High speed	Size	Cost
Operating voltages	Low power/High precision	Footprint	

Table 2.4: Op-amp selection criteria

2.4.2 Power regulator

Two common DC/DC converters are commonly used in electronic circuit designs, linear regulators and switched-mode converters. Each type has its own features and can be utilised in certain applications.

Linear regulator

A linear regulator can only output a voltage that is lower than its input. This type of regulator is relatively cheap and reliable, due to its architecture and circuitry (Figure 2.9). As the figure indicates, it effectively works as a PNP transistor in series with a voltage reference through an op-amp. However, as the regulator dissipates heat, which equals to the product of the output current and the voltage drop, it is very power inefficient for applications that require a large voltage drop. In addition, the unwanted heat dissipation can cause the circuit board and relevant components malfunction.

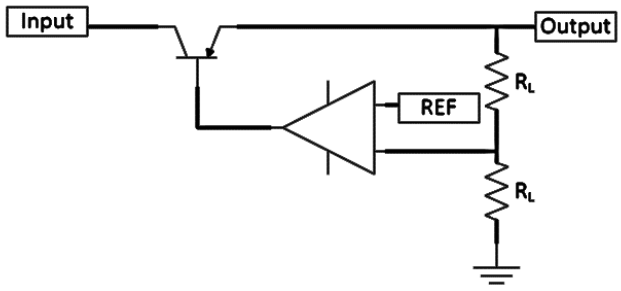

Figure 2.9: Simplified schematic of a linear regulator

A low dropout (LDO) voltage regulator is the most common linear regulator. The dropout voltage is the minimum voltage difference between its input and output, which indicates the properties of the internal transistor as well as the overall regulator performance (Figure 2.10). As the name indicates, a LDO has a low dropout range, making the chip relatively more efficient.

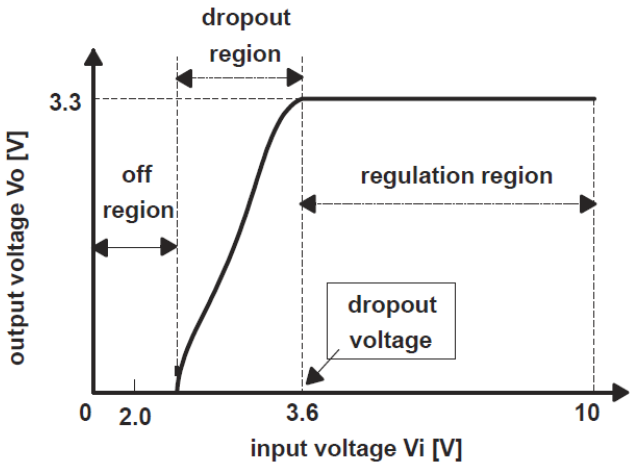

Figure 2.10: Voltage response between LDO's input and output.

This figure is extracted from TPS76733-3.3 LDO data sheet [55]. As the figure shows, the dropout voltage for this LDO is 3.6V.

Switched-mode converter

Another commonly used voltage regulator is the switched-mode converter. The internal circuitry is slightly more complex than a linear regulator, and the simplified version is shown in Figure 2.11 for demonstration purpose. Compared with a standard linear regulator, a switched-mode converter features an internal oscillator, as well as an energy storage circuit. The oscillator periodically controls on/off state of the internal switch between the PNP and the voltage reference. Due to this circuit architecture, switched-mode converter is able to make most of the input voltage, which provides high conversion efficiency (75% to 98%). However, this type of DC/DC converter has its own drawbacks. The major issue is the noise, generated from its internal switching circuitry and potentially the harmonic noise [56]. The noise can severely interfere measurements, if reasonable care is not taken during PCB layout and experimental set-up.

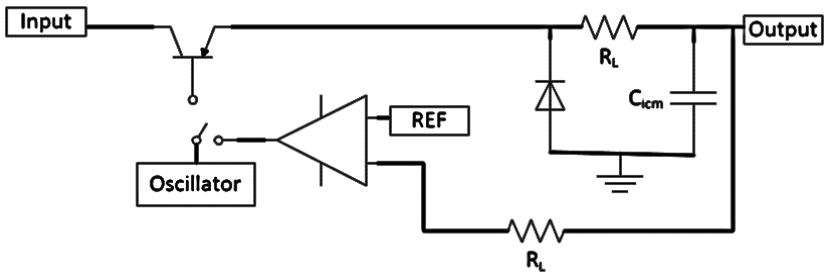

Figure 2.11: Simplified schematic of a linear regulator

2.5 Digital communication protocols

Three different digital serial communication protocols, serial peripheral interface (SPI), inter-integrated circuit (I^2C), and universal asynchronous receiver/transmitter (UART), are worldwide used, and all of them have been applied to different designs in the thesis.

2.5.1 SPI

SPI bus is a synchronous serial data link, which operates in full duplex mode. It is widely used in short-distance and single-master applications. During a SPI transmission, a master device, normally a microcontroller, is defined to initialise the data frame. A single master is able to communicate with multiple slaves. A standard single-master and single-slave SPI configuration contains 4 data wires: chip select (CS), master input slave output (MISO), master output slave input (MOSI), and SPI clock (SCLK). When connecting to additional slaves, only the number of CS pins increases and the number of other SPI pins remain the same. Every CS pin is used for controlling its corresponding slave device.

After initialising a SPI transmission by activating (normally active-low) the CS pin of a certain slave, the master is ready to communicate with this slave. As SPI is a duplex communication, both MOSI and MISO lines are used during the SCLK cycles. In the beginning of the transmission, the master issues SCLK, which determines the speed of this SPI transmission. Following each falling/rising edge of the SCLK, the master sends a bit data on the MOSI line to the slave, and the slave sends a bit data on the MISO line to the master. Based on the certain requirement of the device, the master issues a certain number of SCLK cycles to complete a full set of data transmission. After issuing the last SCLK and accomplishing the last data transmission, the CS pin is deactivated (normally tied high). It indicates that the SPI communication is complete, and then the master is capable of communicating with other slaves. Each device has its own SPI data format and the timing requirement.

In addition to setting the clock frequency, the master is also required to configure the clock polarity (CPOL) and phase (CPHA), which yields 4 different operation modes (Table 2.5). When communicating with a certain device, the SPI mode needs to be clarified, to ensure successful data transmission. It varies between devices, and the modes for writing and reading data can be different for the same device.

Mode	CPOL	CPHA	Operation
0	0	0	Clock is normally low and data is sampled on rising edges
1	0	1	Clock is normally low and data is sampled on falling edges
2	1	0	Clock is normally high and data is sampled on rising edges
3	1	1	Clock is normally high and data is sampled on falling edges

Table 2.5: SPI operation modes

2.5.2 I²C interface

I²C is a two-wire serial communication protocol used for low-speed peripherals to embed systems, and it is invented by Philips Semiconductors, which is known as NXP Semiconductors today [57]. Unlike SPI communication protocol, I²C only requires 2 wires: SCL (Serial Clock Line) and SDA (Serial Data Line). SCL is in charge of synchronising all data transfers over the I²C bus, while SDA contains all the data that need to be transmitted. As a standard setting, both lines are "open drain", which means that the chip can only drive its output low but it is not able to drive it high. In order to make the lines capable of going high, 2 pull-up resistors connected to the power supply are required. For robust communications, the resistance can be calculated, with normal varies from 1kΩ to 10kΩ [58]. All the devices in the I²C bus share the same SCL and SDA, and the transmitting data will be distinguished by device addresses (Figure 2.12).

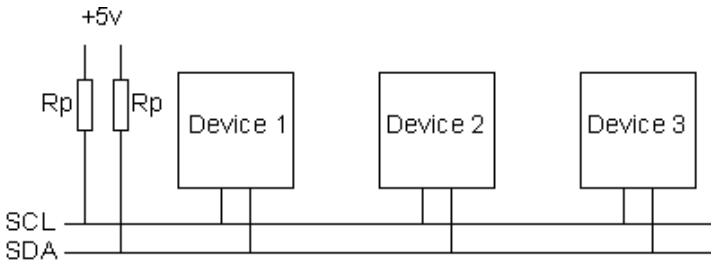

Figure 2.12: Schematic of a standard I²C peripheral

R_P is the pull-up resistor. Devices 1-3 are able to communicate on the I²C buses. The power supply in this schematic is +5V.

The devices on the I²C bus can be either masters or slaves, and SCL clock line is always driven by the master device. When the master tries to communicate to a slave, it issues a start sequence, which is one of the two pre-defined sequences on the I²C bus. The other one is stop sequence, which will be issued from the master when it finishes the data transmission (Figure 2.13). The two sequences are special, since the SDA line is allowed to change while the SCL line is high. In normal data-transferred process, SDA must be kept stable when SCL is high, which means that data will be acquired when SCL is high.

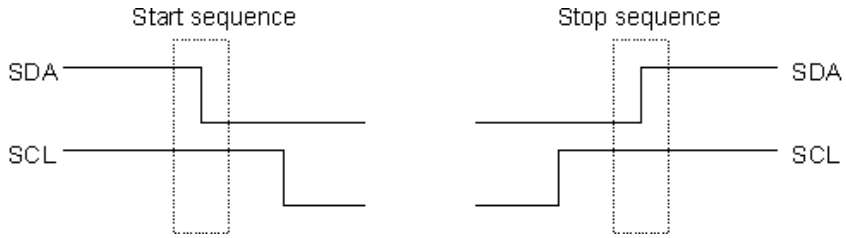

Figure 2.13: Timing for start/stop sequence on I^2C bus

The start sequence is SDA going from high to low when SCL stays high (left), while the stop sequence is SDA going from low to high when SCL stays high (right).

As for data transmission, the master sends/receives one byte (8 bits) each time, following by an acknowledgement bit, which indicates that every transmission has 9-bit data and SCL issues 9 clock pulses. If the slave sends back a low acknowledgement bit ("0"), then it indicates that it has received the data and is ready to receive another byte. Whereas if it sends a high acknowledgement bit ("1"), it indicates that the slave is not able to accept any more data, at which point the master should terminate the transmission, by issuing the stop sequence.

A standard I^2C device has 7-bit address, and therefore up to 128 (or 2^7) different devices can be implemented on the same I^2C bus. Recent devices, such as stm32L053 microcontroller, start to support 11-bit addressing, which makes it capable of communicating with more devices. The address byte is always the first data byte needed to send, since all the following commands or data need to be sent/received to/from the addressed slave. A read/write bit will be placed after these 7 address bits, to indicate whether reading or receiving the following data. More specifically, to tie the last bit low ("0") means writing to the slave, and high ("1") means reading from the slave. The standard data format of addressing is shown in Figure 2.14.

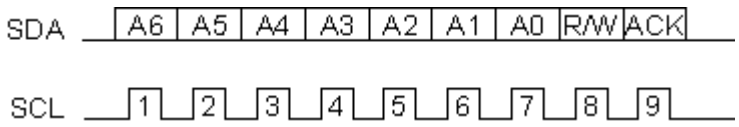

Figure 2.14: Data format when sending the address byte

A6-A0 are the 7-bit device address. "0" at R/W bit means writing to the slave and "1" indicates reading from it. An acknowledgement bit is always attached at the end of a one-byte data block.

2.5.3 UART

UART is one for the most used serial protocols, and most microcontrollers or integrated modules have one or multiple hardware UARTs on board. Normally hardware UART contains two pins: transmission line (TX) and receiver line (RX). Most often 1-byte (8-bit) data is

transferred each time, together with start and stop bits. The data block for 1-byte data is shown in Table 2.6.

Bit 1	Bit 2	Bit 3	Bit 4	Bit 5	Bit 6	Bit 7	Bit 8	Bit9	Bit 10
Start	Data 0	Data 1	Data 2	Data 3	Data 4	Data 5	Data 6	Data 7	Stop

Table 2.6: UART data format

The start bit is low and the stop bit is high, which indicates there is always a falling edge (stop "1" – start "0") to initialise the communication. In this communication, only the protocol is defined, so any voltage level, like 3.3V or 5V, can be used for UART communication. This is called as transistor-transistor logic (TTL). However for long-distance communication, 3.3 or 5V TTL logic is not reliable as the voltage fluctuation may be larger than the digital voltage threshold. Therefore, it requires to be converted in higher voltages. For example, RS-232 applies +12V as "0" and -12V as "1". Therefore, TTL and RS232 can transmit the same digital information with different analog voltage levels. Regardless the voltage difference, the data rates for both protocols remain the same.

When setting up a UART communication, both devices should agree on transmission speed, the bit rate, as they only have the start bit's falling edge to synchronise the whole transmission. That is why UART is called as asynchronous communication. In addition, each UART contains a shift register, which is used for converting the transmitting/receiving data between serial and parallel. When attempting to communicate with the host computer, an UART-to-USB adaptor/chip is required, to convert a RS232/TTL serial signal to a USB signal.

2.6 Data analysis methodology and relevant software

All analog experimental data presented in this thesis were acquired initially from LabChart 7. The data were imported into Igor pro 6 for further data processing. The digital data analysis and relevant graphic user interfaces, discussed in Chapter 9, were generated from Matlab.

2.6.1 Time-domain analysis

Several key parameters are used in the thesis to analyse the performance of the devices and relevant output data.

Central value and spread

The central value of a Gaussian distribution with n observations, x_i and $1 \leq i \leq n$, can be estimated by the mean value, m_x, which is defined as:

$$m_x = \frac{\sum_{i=1}^{n} x_i}{n} \tag{2.2}$$

The distribution of the data within these n observations around the mean value is defined as the standard deviation, σ_x, which can be estimated as:

$$SD = \sqrt{\sum_{i=1}^{n} \frac{(x_i - m_x)^2}{n-1}} \tag{2.3}$$

Root mean square (rms)

The rms is an equivalent DC value of a time-varying sinusoidal waveform, commonly used to characterise the noise level, which can be noise voltage, $v_n(t)$, or noise current, $i_n(t)$. With a suitable averaging time interval, T, the rms voltage value, $V_{n(rms)}$ is defined as:

$$V_{n\,(rms)} = \sqrt{\left[\frac{1}{T_2 - T_1}\int_{T_1}^{T_2} v_n^2(t)\,dt\right]} \tag{2.4}$$

The rms current value, $I_{n(rms)}$ is defined as:

$$I_{n\,(rms)} = \sqrt{\left[\frac{1}{T_2 - T_1}\int_{T_1}^{T_2} i_n^2(t)\,dt\right]} \tag{2.5}$$

The summation of multiple signal sources, $V_{no\,(rms)}$, can be expressed as:

$$V_{no\,(rms)}^2 = \sum_{i=1}^{n} V_{ni\,(rms)}^2 \tag{2.6}$$

The rms value is beneficial, as it indicates the normalised power of the signal. If the signal is applied to a 1Ω resistor, the average power dissipation, P_{diss}, can be expressed as:

$$P_{diss} = \frac{V_{n\,(rms)}^2}{1\Omega} = I_{n\,(rms)}^2 \times 1\Omega \tag{2.7}$$

Signal-to-noise ratio (SNR)

The SNR can be simply presented as the ratio between the signal rms value and the noise rms value. More commonly, SNR is presented in decibels, which is defined as:

$$\text{SNR (dB)} = 10\log_{10}(\frac{signal\ power}{noise\ power}) = 10\log_{10}[\frac{V_{x\,(rms)}^2}{V_{n\,(rms)}^2}] = 20\log_{10}[\frac{V_{x\,(rms)}}{V_{n\,(rms)}}] \quad (2.8)$$

2.6.2 Frequency domain analysis

In addition to time-domain analysis, frequency analysis, such as (root) spectral density or power spectrum, is also of great importance in analysing different frequency compositions in a signal. For example, the data sheet of an op-amp often provides the input noise voltage density as one of the primary characteristics.

As the spectral density is associated with frequency, the actual noise level needs to be estimated across the operating frequency range. For example, the input noise voltage density, e_n, is expressed in units of nano volts per root-hertz ($\text{nV}/\sqrt{Hz}$) in an op-amp's datasheet. If the e_n of an op-amp is $10\text{nV}/\sqrt{Hz}$ and the operating frequency ranges from DC to 1kHz, the rms value should be calculated as:

$$V_{n\,(rms)}(F_H, F_L) \approx e_n\sqrt{F_H - F_L} = 10\,nV/\sqrt{Hz} \times \sqrt{1kHz} = 316.2\,nV \quad (2.9)$$

Where F_H and F_L are the high and low frequency limit, respectively.

The nominal peak-to-peak voltage level, $V_{P\text{-}P}$, can be deducted from the rms value, on the basis of the probability theory. Commonly, the probability threshold is set as 99.9%, which means only 0.1% of the time that the signal will exceed the calculated peak-to-peak value [59], and this threshold yields:

$$V_{P-P} = 6.6 \times V_{n\,(rms)} = 2.1mV \quad (2.10)$$

Therefore, the corresponding nominal peak-to-peak noise from the op-amp, within 1kHz range, is 2.1mV.

A common misunderstanding in a data sheet is due to another parameter, input noise voltage, which is expressed in volts within a certain frequency range, normally from 0.1 to 10Hz. Both input noise voltage and input noise voltage density describe the noise characteristic of the op-amp. However, they have different focuses. As both flicker (1/f) noise and white noise are inevitable in measurement, the flicker noise is more significant than the white noise in low

frequencies, and it becomes less significant when working in high frequencies [60]. Therefore, manufactures often test and release these two different parameters. The input noise voltage (0.1 – 10Hz) is used for characterising the flicker noise, while the input noise voltage density focuses on the full frequency range, aiming at the white noise interference.

2.7 Summary

This chapter has introduced all the common materials used in the thesis, such as chemicals, amperometric sensors, and ion-selective electrodes. All the testing equipment, electronic components, relevant digital communication protocols, and data analysis methodology have been also demonstrated.

Chapter 3: PCB Routing and Practical Experimental Considerations

As a hardware application engineer, in this chapter, I will mainly discuss my experience on designing different types of PCB and developing relevant systems. As the thesis primarily deals with practical lab-based and clinical monitoring, I will also demonstrate the relevant practical experimental considerations and optimisation methods.

3.1 PCB routing considerations

Careful PCB routing is an indispensable process of building a high-performance circuit board. Component placement, relevant trace selection, and PCB layer management can play significant roles in the circuit performance, especially for low-level signal detection and mixed-signal processing. Every trace on a circuit board should be placed thoughtfully, as each one is inherently a resistor and an inductor [61]. The resistance is determined by the trace width, length, thickness, and operating temperature. In addition, close traces/planes on the same layer or between different layers can work as capacitors, which make the PCB vulnerable high-frequency interference. Each signal in the circuit requires its optimal trace width and length. High-speed and large-current signals require short and wide traces, whereas routing low-speed logic signals, longer and thinner traces are acceptable to minimize the board size.

Furthermore, right-angle sharp corners should be avoided due to the following reasons:

a. When working on high-frequency digital circuitry (more than 100MHz), like USB3.0 and Peripheral Component Interconnect Express (PCIe) bus standards, the signal gets attenuated when it hits the sharp corner and reflects back.
b. 90˚ or more than 90˚ angles yields sharp corner, which cause longer traces, therefore higher impedance and more copper are required.
c. Visually, a PCB with all 45˚ corner traces looks much neater and cleaner than one with 90˚ corner.
d. Gentle angles are less likely to have etching problems during manufacturing.

Apart from general routing principles, several special PCB layout techniques for specific applications will be further discussed.

3.1.1 Guard ring

When working on sensitive signal measurements, guard rings on input nodes of the PCB are of great importance. A guard ring is an enclosed circular trace on the PCB, which normally confines both input nodes of an op-amp and should be placed on both top and bottom layer of the PCB. An example is shown in Figure 3.1, which is the recommendation layout for the op-amp LMP7721. The guard ring is driven by the same potential as the guarding nodes, normally buffered by an op-amp. It can eliminate any surface current leakage from high-potential pins (e.g. power pins V+ and V-) to sensitive pins (e.g. input pins IN- and IN+). The leakage current cannot flow from power pins to the susceptible input pins, as it needs to first reach the guard ring, which then consumes this leakage current from the driving source. In addition, the guard ring itself does not generate any leakage current to the susceptible nodes, as they have very similar potential.

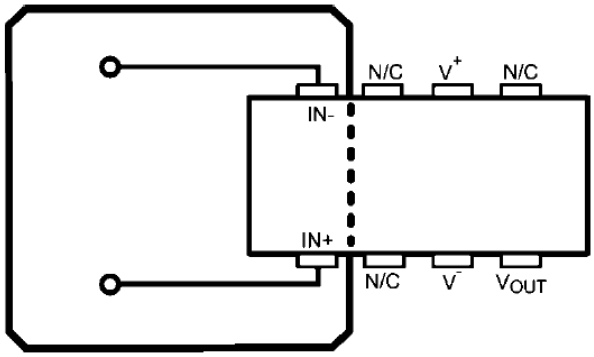

Figure 3.1: Guard ring demonstration in LMP7721

The figure is extracted from LMP7721 datasheet [62]

Such guard rings have been largely used in the thesis, as most of my electronic systems have been designed to work with real-world chemical sensors, which can be very vulnerable to surrounding electrical interferences. For example, such designs can be found in the transimpedance circuit discussed in Chapter 4, 7, 8, and 9.

3.1.2 Mixed-signal PCB design

When working on mixed-signal PCB design, sensitive analog circuitry should be generally placed away from high-speed digital circuitry. This is because they maintain different

electronic features and can interfere each other. Analog circuits normally work with signals varying in a continuous and smooth range, for which small changes in voltage or current are critical. However, digital signals have a wide window of voltages to map a single digital state, based on certain thresholds. In addition, when digital signals transmit abruptly from one state to another, they generate pulse current. Relatively large and sharp digital pulse current during state transitions can overwhelm the precise analog signals if they are not adequately separated. The analog circuit in turn may operate at high voltages, which is likely to introduce leakage to the digital circuitry.

Ground Plane

A general approach of dealing with the cross talk and managing mixed-signal design is to add ground planes. A ground plane is a large copper area, which is electronically connected to the ground terminal, working as a current-return path. As a general principle, a ground plane should be made as large as possible, such that it maintains minimal resistance, which efficiently conducts large return currents from many components without introducing a significant voltage drop, and therefore maintain the same ground potential among the components. In addition, a large ground plane also facilitates designers, as it allows grounding any component without adding additional traces.

In a digital circuit design, employing a ground plane is able to reduce electrical state-switching noise and pulse current. Without applying a ground plane, the current pluses are likely to be converted to significant voltages via the relatively high-impedance trace between the power and ground pins. The voltage fluctuation therefore creates noise on the ground line, which interferes all other circuitry. Comparatively, a ground plane is able to minimise the trace impedance, and therefore cause less disturbance.

Another advantage of utilising ground planes is to minimise crosstalk between adjacent traces. When two traces run in parallel, the electrical signal from one trace may be interfered by the other via electromagnetic coupling. When a ground plane is placed underneath, the return current is oppositely directional, which exactly follows the pattern of the trace [61]. This confines the electromagnetic distribution of the traces, and therefore reduces the crosstalk.

In a single/double-layer PCB design, to maximise the functionalities of the ground plane, a ground plane often covers most of the PCB area that is not occupied by other signal traces. As for a multi-layer PCB design, a completely separate layer can be used as the ground plane. When designing a mixed-signal circuit, the ground plane can also be split into an analog ground plane and a digital ground plane, which works better to minimise the crosstalk. In addition to ground plane, a power plane is often utilised in a multiple-layer mixed design, to distinguish analog and digital power supplies. The detailed distribution of the power/ground planes varies among applications, and the specific arrangement will be discussed in the circuit design sections of each project.

In some cases, a ground plane is not preferable as it changes the local capacitance and alters the antenna radiation pattern. For example, no ground place should be placed under a RF chip/PCB-trace antenna to optimise its radiation efficiency. Moreover, no ground plane should be placed under a capacitive touch pad, as the sensor relies on the local capacitance change to detect a touch event.

Current return path

A common misunderstanding of routing PCB traces is to treat each trace as a separate and complete unit. Actually, every trace should be analysed together with its return path. The return path is practically even more critical than the trace itself. In practice, if the return path of the signal has not been carefully considered, it may result in circuit under-performance or even malfunctioning.

After applying ground and power planes, the circuit might be considered as “optimised”. However, the planes are not the universal keys to every design. If considering current return path, issues can still remain if reasonable care is not taken when placing components. Following by the principle that current travels through the least-impedance trace, the return current path for DC and AC components are described in Figure 3.2. Integrated circuit (IC) 1 and 2 are placed on top of a ground plane, and the red line from IC1 to IC2 is the signal trace. As for the return current path, the DC current will flow via the least-resistance path, shown as the blue line. However, the AC current return follows the lease-impedance path. It is oppositely directional, and flows back to IC1 via the same pattern of the signal trace [61].

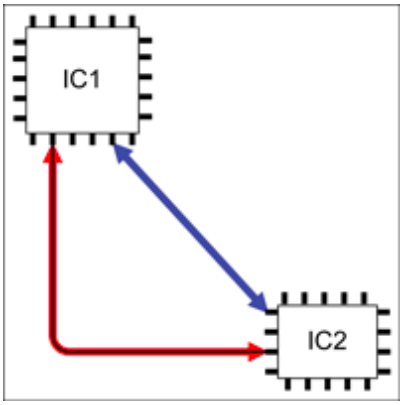

Figure 3.2: Signal trace and relevant return paths

This simplified circuit above is used for demonstration only, and Figure 3.3 shows a more practical issue when overlooking the return path. The white line in the figure is used for separating the digital and analog grounds. The upper area is the analog part, and the lower field is the digital circuitry. An ADC has been placed in the middle, because part of the internal circuitry belongs to analog and the other belongs to digital. In addition, another digital IC has been placed in the digital side. As shown, a red trace for a digital connection is routed cross the analog part from the digital IC to the ADC. As discussed, the common issue for this trace placement is to make a digital trace travel in the analog area, which can therefore contaminate analog signals. However, this is only a small part of the problem. The main issue occurs when plotting the return path of the signal trace, which is shown in Figure 3.3b.

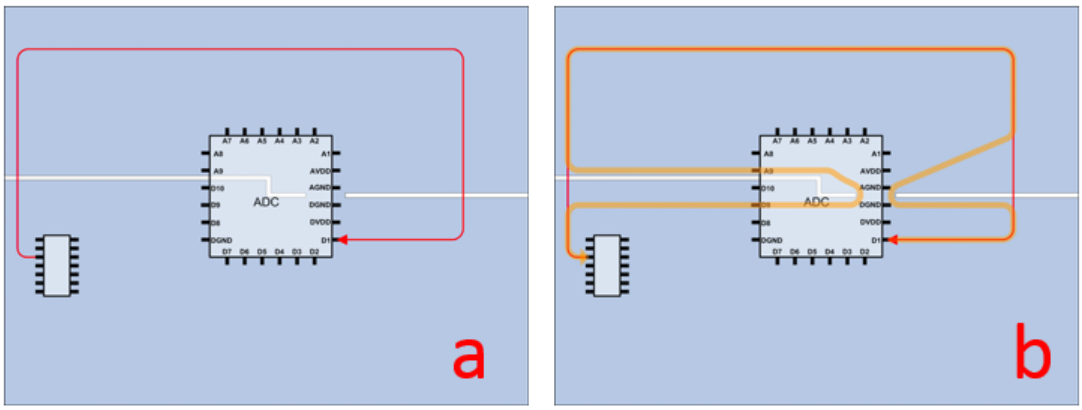

Figure 3.3: An example of signal trace and its return path

The signal trace across ground planes is shown on the left, and its return path is shown on the right. The figures are extracted from [61].

The return path in Figure 3.3b is highlighted in the orange colour. Following the least-impedance principle, the return path tends to travel from pin D1 on the ADC back to the digital

IC via the same signal trace. It follows the trace nicely until encounters the plane cut. At the edge of the cut, the current can only return to the single joint ground point to get to the other side of the cut. Consequently, in addition to running digital current through analog circuitry's ground, two loop antennas have been created and started to radiate these signals. As a conclusion, rather than only introducing ground planes, the ground planes should also be cut carefully. Digital and analog components/traces should stay at their respective side of the cut.

In practice, if components have been placed in appropriate area of traces and return paths being well regulated without any crossover, the ground plane cuts can be removed. Since no currents are crossing the ground cuts, the cuts play no roles on the circuit board. It indicates that a separation of ground planes is not always necessary, as long as all the traces and their return paths have been carefully designed and regulated.

3.1.3 Decoupling/bypass capacitor

A decoupling capacitor is normally used to either bypass unwanted high-frequency AC signals superimposed on the DC power lines or provide local energy to compensate fast changing current demands in digital circuitry. Normally, a decoupling capacitor is placed between the power (VCC) and ground (GND) pins of an IC. The decoupling capacitor should always be placed as close as possible to the circuitry (or ICs) that requires decoupled. As each PCB trace has certain amount of line inductances and resistances, minimising the length of the PCB trace can improve the decoupling performance. In addition, as a capacitor effectively works as a resistor, a capacitor, and an inductor in series (Figure 3.4 and table3.1), a single capacitor does not work efficiently to remove all the high-frequency AC components.

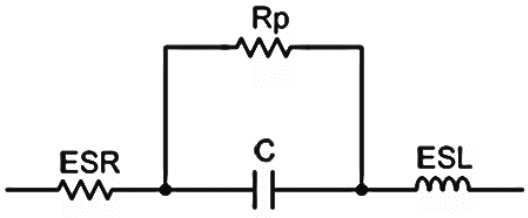

Figure 3.4: Model of a practical capacitor

Parameter	Description
C	The nominal value of the capacitance
ESR	Equivalent series resistance, which is ideally zero. It varies between different materials. Ceramic capacitors have the best ESR in mΩ, tantalum electrolytic capacitors have ESR in hundreds of mΩ, and aluminium electrolytic capacitors have ESR in Ω.
ESL	Equivalent series inductance, which is ideally zero. Practically, it ranges from 100pH to 10nH.
R_P	Parallel leakage resistance (or insulation resistance), which is ideally infinite. Practically, it ranges from tens of MΩ for some electrolytic capacitors to tens of GΩ for ceramic capacitors.
Voltage rating	The maximum voltage that can be applied to the capacitor. The capacitor may be damaged if exceeding the rating.
Voltage coefficient	The changes in capacitance with applied voltage (ppm/V). A high voltage coefficient can cause distortion.
Temperature coefficient	The changes in capacitance with operating temperature (ppm/˚C), which is ideally zero. Practically, it ranges from 10 to 100ppm/˚C.

Table 3.1: Capacitor specifications

Different types of capacitors can be used in different applications. C0G and NP0 (type 1 ceramic) have lowest temperature and voltage coefficient with good tolerance. Therefore, they are normally used for filtering and precise signal processing. X7R (type 2 ceramic) has substantial voltage coefficient with a large capacitance range (10pF to 47μF). Therefore, it is normally used for decoupling and other applications, where accuracy and low distortion are not required. Tantalum electrolytic capacitors normally have larger capacitance (1μF to 150μF), which can be used for bulk decoupling and other applications where large capacitances are required. This type of capacitor is polarised, and it can be damaged if the reserved-polarity connection is made.

At lower frequencies, the capacitor offers a low-impedance path to ground. However, when the capacitor reaches its self-resonance, the capacitive feature diminishes and becomes inductive. As Figure 3.5 shows, initially the impedance of a capacitor decreases as the frequency rises. However after passing a certain frequency, the impedance starts to increase again due to the ESL. The turning frequency is determined by its capacitance, and the lowest impedance is determined by the ESR. Different capacitors have different impedance-frequency responses. This is the reason why multiple de-coupling capacitors may be required in some critical low-noise design, like the ADS1298 design discussed in Chapter 5. When a capacitor's frequency response is rolling off, another one is becoming significant, which helps the device maintain low-AC impedance over a wide range of frequencies.

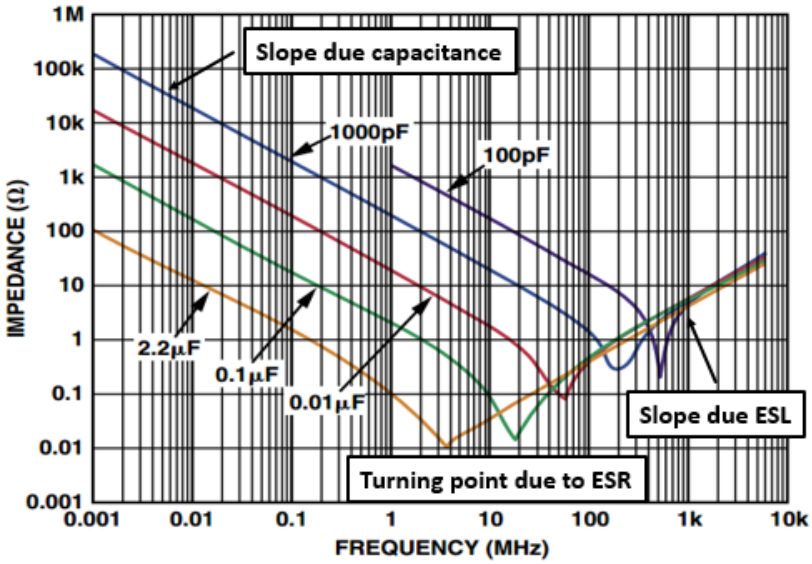

Figure 3.5: Impedance response of a capacitor vs. frequency

The decoupling technique was involved in each electronic design of the thesis, and the detailed capacitor selections will be further discussed in different chapters. For example, a standard 100nF ceramic capacitor was generally applied to every power pin of an op-amp, while a 100nF ceramic capacitor and a 10µF tantalum capacitor are usually added in parallel to each power pin of a digital IC. Mathematically, the capacitance of these two capacitors is same as that of a 10.1µF capacitor. However, the performance of two-capacitor decoupling structure works much better than applying only one 10.1µF capacitor. The figure is reproduced based on [63].

Another important situation of applying decoupling capacitors is when working between analog high-precision circuits with high-speed digital circuits. As the supply voltage for an IC is fixed, the changing power demand of the IC is only represented as the changing current demand. A voltage regulator is capable of accommodating these power demands by drawing different amount of current, while maintaining as little voltage change as possible. However, the power regulator cannot alter supplying current at the exact time when the power demand changes, and consequently the output voltage at the regulator will be changed for a short period before the power regulator responds and provides relevant changing current. A common regulator is able to response up to kHz, but most digital circuitry works at MHz or even hundreds of MHz. The responding time delay causes a voltage fluctuation on the regulator, and thus introduces unwanted noise to the relevant circuits that share the same power. To eliminate this effect, decoupling capacitors are applied to work as the circuit's local energy storage. They store a small amount of energy from DC power supply, and are able to respond to fast changing current demand, which helps the regulator maintain constant supply voltages. Based on the capacitance, a decoupling capacitor can effectively maintain constant voltage supplies from hundreds of kHz to hundreds of MHz. A decoupling capacitor is not efficient for events beyond this frequency range.

3.2 General experimental set-up considerations

Unlike simulations that work in relatively ideal situations, practical problems need to be considered and handled when conducting real-world experiments. The measured signal inevitably contains some noise and unwanted pick-up signals from the ambient environment, connectors, and motion artefacts. The interference becomes more deteriorated when measuring low-level analog signals. For example, data recording PC generally has digital input/output signals on its IO connectors. Any activity on these digital signals can be picked up via parasitic capacitors, and behave as a source of noise.

In a standard experimental environment, four types of noise pick-up are involved: conductive, capacitive, inductive, and radiative [64]. The conductive coupling is due to sharing currents from different circuits in a common path. Capacitive coupling is due to time-varying electric fields around the signal path. Comparatively, inductive coupling results from time-varying magnetic fields in the area of the circuit. If the electromagnetic field is insignificant around the signal circuit, the electric and magnetic field coupling are regarded as radiative coupling in general.

3.2.1 Conductive noise (ground loop)

Conductive noise occurs, because all the wiring conductors have small but non-zero impedance. The effect of these wire impedances must be considered when setting up an experiment. For example, Figure 3.6a demonstrates a simple connection between an analog temperature sensor and another load, powered from a +5V power supply. The output voltage of the sensor is proportional to the ambient temperature. However, in this setting, the output voltage from the sensor becomes $V_O + V_{ab}$ when the load switch is closed, because they share part of the current return path in the common ground line. If the load generates 1A on its line, which is combined with the sensor ground line at point a, the voltage between point a and point b will be added to the output of the sensor. Suppose the resistance between two points is 0.1Ω, the voltage V_{ab} is then 100mV, which generates 10˚C difference in the sensor.

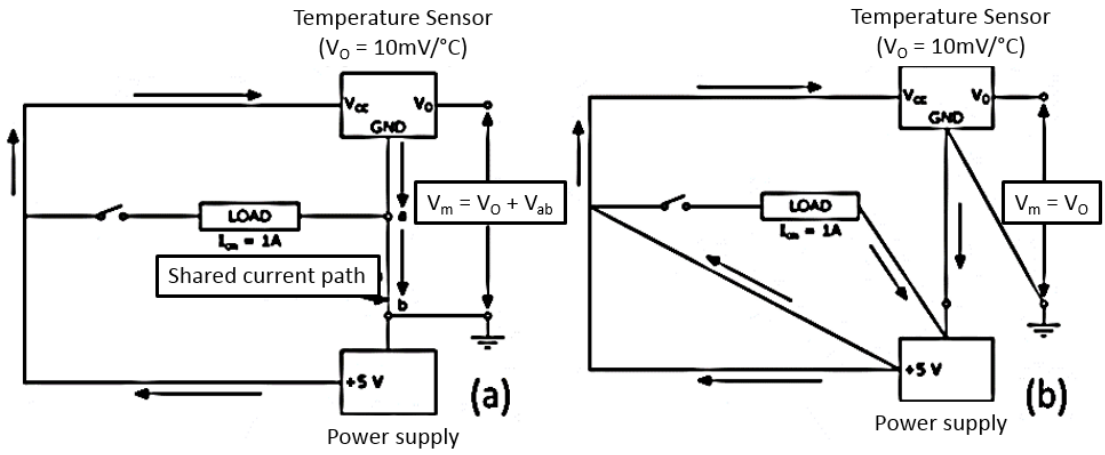

Figure 3.6: Serial grounding connections cause conductive coupling

The figure is adapted from [64]. It shows a measurement error from the temperature sensor, due to the ground loop in the experiment.

To avoid conductive coupling, each measurement unit should have separate ground return path and join at only one ground point (star joint point). The correct set-up for this measurement is shown in Figure 3.6b, and no unwanted conductive coupling is involved.

Ground loop analysis in a clinical environment

In a clinical monitoring environment, the issue from a ground loop occurs more frequently and the damage can be even fatal if reasonable care is not taken. It is very common to see a patient in an ICU being connected with multiple monitoring instruments. Each instrument has its own grounding system providing a ground electrode connected to the patient. If these two or multiple ground connections are not jointed together at a single star point, the ground loop issue is very likely to happen. If one ground is at a slightly higher potential than the other ground(s), a current from one ground will flow through the patient along the lead wire to the other ground(s). Electronically, this current produces common-mode voltages on the monitoring system. Therefore, the noise interference therefore increases significantly if the instrument has a poor CMRR.

More importantly, this ground loop current rises the clinical safety risk. Figure 3.7 shows a clinical set-up with two different monitors, an ECG monitor and an arterial pressure monitor, connected to the patient. The ECG monitor has a ground lead, connected to the patient's right leg. The blood pressure sensor has its own ground electrode, connected to the tissue closed to the heart. Under normal conditions, the leakage current within the ground loop is

insignificant, which will not harm the patient. However, if an external duty-heavy electrical device, such as a dusty damp electric floor polisher, is faulty, it can introduce maximum 5A current (maximum current tolerance in the fuse) to the grounding wire. The current flows along the ground wire (0.1Ω) to the hospital ground, which generates 500mV to the grounding system. Eventually, this 500mV will be added between the ground electrodes of the ECG monitor and the arterial pressure monitor. The equivalent resistance of the connected part of the body is about 300Ω (~200Ω for one limb and ~100Ω for the trunk), and hence more than 1mA current will flow through the patient's heart, which exceeds the patient safety limit (50μA) [65].

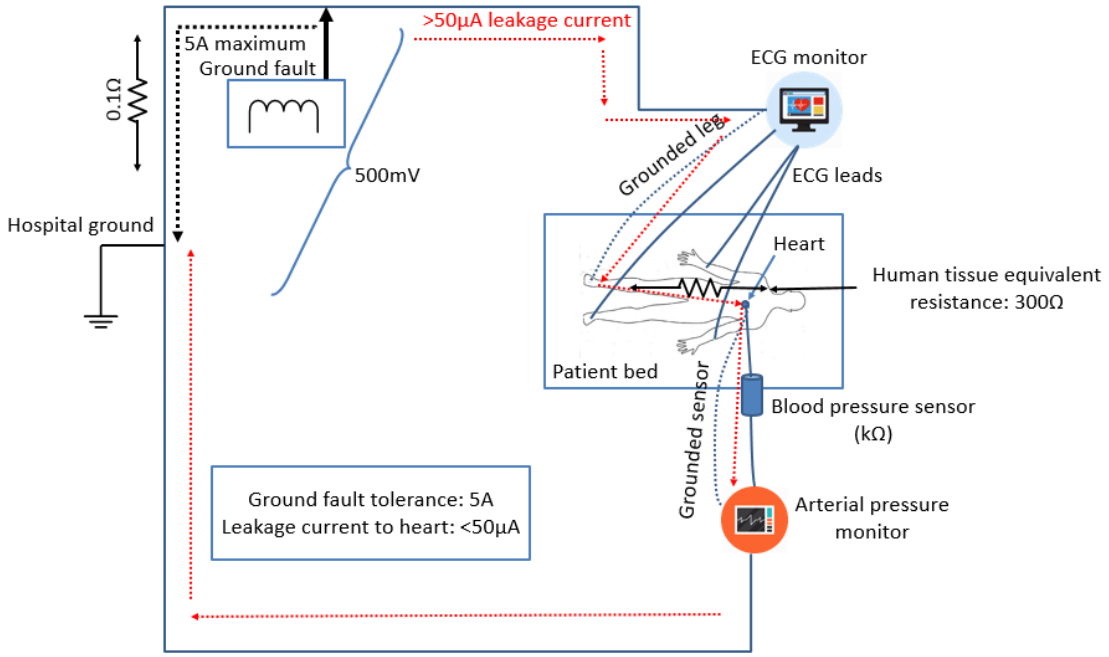

Figure 3.7: Clinical safety regarding ground loop and fault

A current in excess of the 50μA safe limit can flow through the ECG-patient-arterial pressure monitor ground loop, when a faulty device introduces large current into the ground. This effect can be avoided by connecting the grounds of all the devices used in the vicinity of each patient to a single patient-grounding point (star point). In addition, it also helps prevent faults at one patient's bed from affecting the safety of other patients [66].

3.2.2 Capacitive noise

Capacitive and inductive couplings are picked up via capacitors and inductors, respectively. It occurs when the circuit under test is working with other sources, like other PCBs, power sources, and signal generators. The equivalent capacitance C_{ef} is directly proportional to the area of overlap and inversely proportional to the distance between the two units (Figure 3.8).

In addition, the pick-up noise varies as the noise source voltages and frequencies. To minimise this coupling, either the capacitance C_{ef} or the noise source can be optimised. To reduce the noise source interference, one can place the experimental set-up away from the noise source, or completely shut down any unnecessary equipment around the set-up. To reduce the capacitance, one can apply a capacitive shield to the set-up, as it provides another path for the current to flow. In general, conductive metal or other materials in the vicinity of the signal path should not be left electrically floating, as this may introduce capacitive coupling.

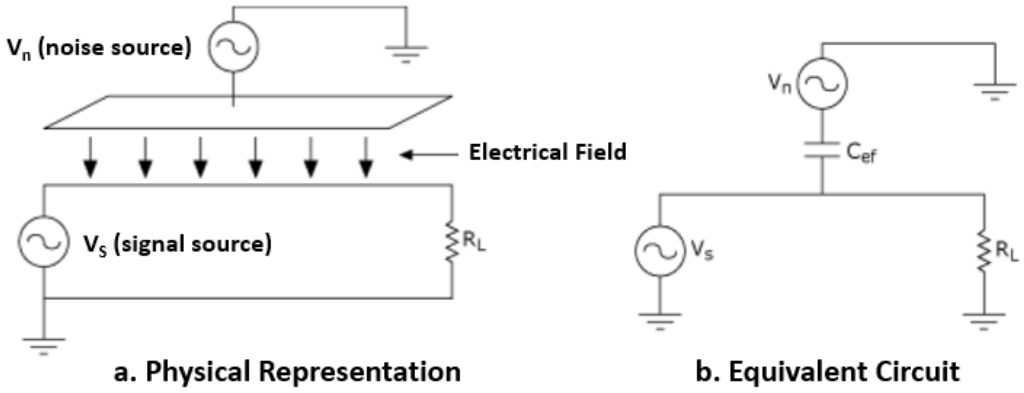

Figure 3.8: The capacitive coupling model

The figure on the left is the physical representation of the capacitive coupling model and the one on the right is the equivalent circuit. The figures are adapted from [64].

An ECG test is a good example, and Figure 3.9 shows a simplified ECG recording system. The main unwanted noise sources are the 50Hz interference from the mains and the resulting capacitive coupling current. When the 50Hz AC magnetic field goes through the shaded loop, the interfering voltages will be in series with the real ECG signal, V_{ECG}, which affects the system SNR. In addition, the capacitively-coupled current flows through each electrode and the body to the ground. The current does not flow into the differential amplifier, due to its high-input impedance, but rather through the skin-electrode interface and consequentially introduces two interfering voltages across the electrode impedances, Z_1 and Z_2.

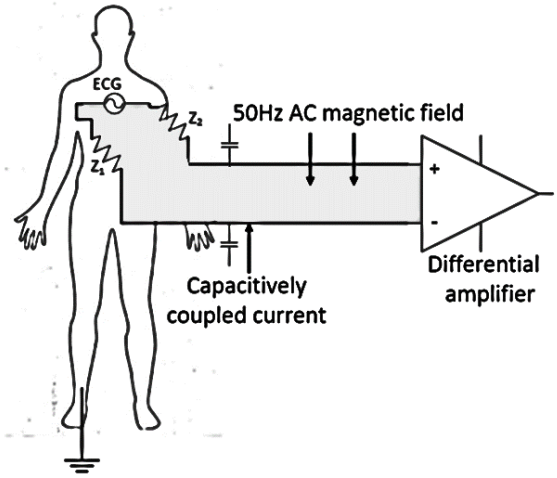

Figure 3.9: Simplified ECG recording system

Two possible noise interferences are stray magnetic fields and capacitive coupling current noise. The orientation of patient cables and the skin-electrode impedance are two main adjustments to improve the measurement output SNR.

As discussed, the coupling effect is proportional to the overlap area with the magnetic field. Therefore, if the plane of the cables is parallel to the AC magnetic field, the magnetically interference is eliminated. In practice, as the magnetic field is uncertain, the conducting cable should be twisted up to minimise the shaded area and hence the magnetic interference (Figure 3.10). If the cable can be shielded and the shield can be grounded, then the monitoring outcome can be even less noisy. In addition, reducing the electrode-skin impedance (Z_1 and Z_2), such as applying efficient high-quality conductive gel, is also effective to reduce the noise.

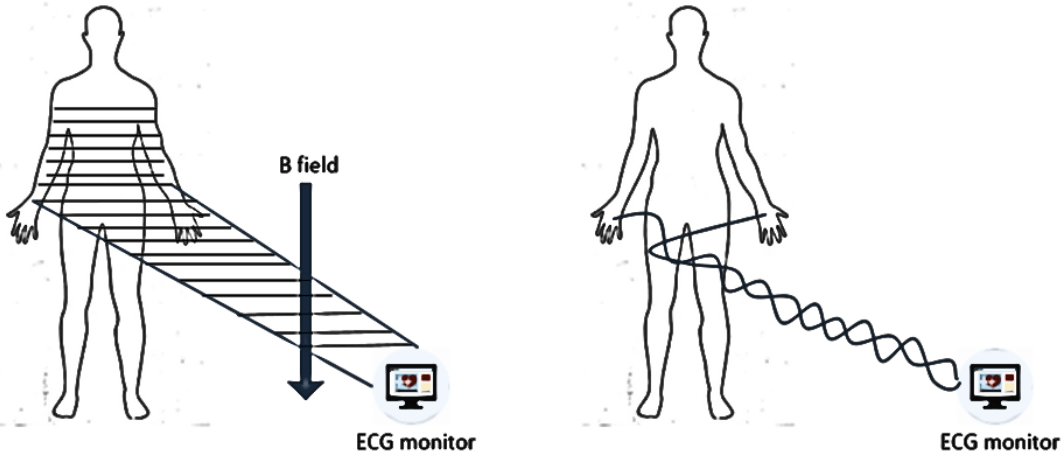

Figure 3.10: Electrode signal wires can be twisted to minimise magnetic interference

3.2.3 Inductive noise

Similar to the capacitive coupling, inductive coupling results from time-varying magnetic field, which is due to the nearby looping current (Figure 3.11). The mutual inductance M is directly proportional to the area of the receiver and inversely proportional to the distance between the noise source circuit and the test circuit. To minimise inductive coupling between two circuits, the distance should be increased and the loop area should be minimised.

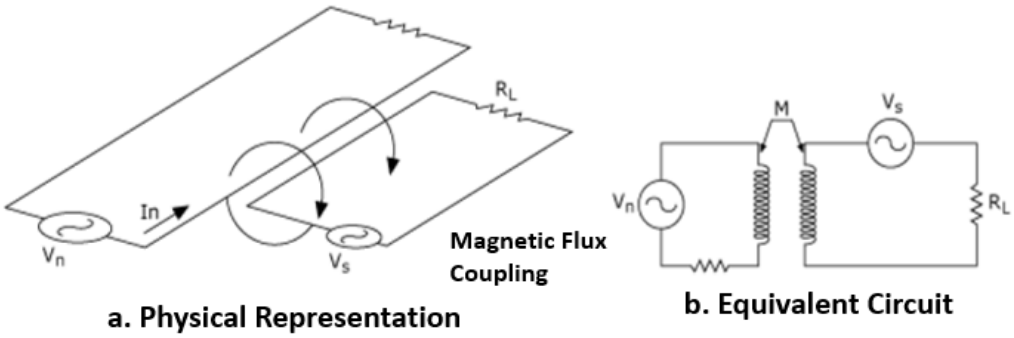

Figure 3.11: Inductive coupling and equivalent circuit

Figure a on the left shows the physical representation and Figure b on the right shows the equivalent electronic circuit. The figures are adapted from[64].

In summary, in order to optimise the performance, cares must be taken in both PCB layout routing process and the test phases. When observing unexpected noise during the measurement, a series of checking need to be conducted to investigate the noise source. In addition, when working in a clinical environment, the noise interference can even come from other surgical processes, such as an x-ray machine, a diathermy equipment, or other heavy-duty electric devices. Normally, the electronic device needs to be evaluated first and maintained to its lowest noise level. In industry, one commercial device needs to pass relevant electrical magnetic compatibility (EMC) tests before it can be released to market.

After the examination of electronics, all the unnecessary electrical devices need to be removed from the experimental area. Experimentally, the recording computer and monitor should be located as far as possible from the signal cabling. The interface between sensors and electronics need to be examined thoughtfully, as some sensor cables are unshielded and vulnerable to surrounding noise. If necessary, a proper Faraday cage (discussed in Section 3.4) can be involved to minimise the electromagnetic interference (EMI).

3.3 Connectors and Cables

Unlike simulations, another issue of a practical measurement is the cable/connector management. For analog signal transmissions, coaxial or triaxial cables are preferable as they can reduce the signal loss during transmission. A coaxial cable has an inner copper core surrounded by a tubular inner dielectric insulator, and surrounded by a woven copper shield and then protected by an outer insulating sheath. The simple schematic of a coaxial cable is shown in Figure 3.12a. The inner core carries the signal and the outer electrical layer is normally kept as ground. It is able to confine the electric and magnetic fields with little leakage, and prevent the core signal from electromagnetic interference (EMI), which makes it suitable for carrying subtle signals without significant signal loss. Various coaxial cables with different dimensions and configurations are available in the market [67]. Coaxial cables and connectors, such as SMA, SMB, BNC, and U.FL, have been used in the thesis.

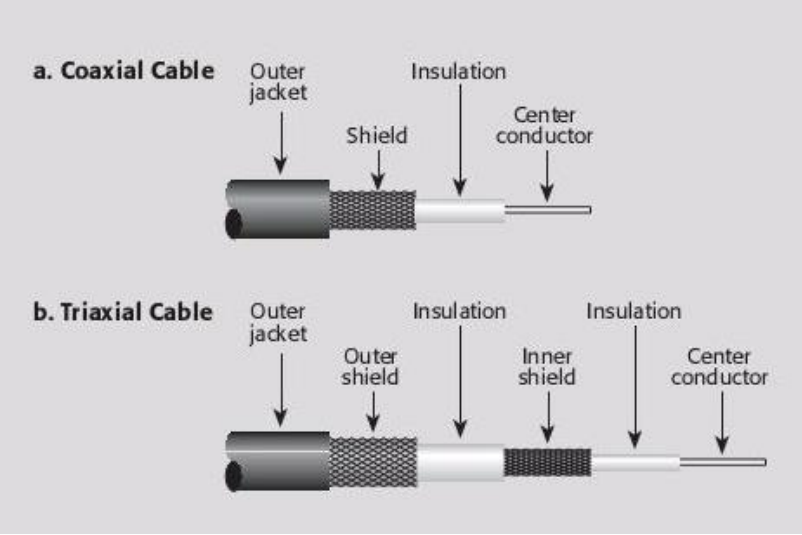

Figure 3.12: Configuration of a coaxial/triaxial cable

On the basis of a coaxial cable, a triaxial cable features an extra conducting sheath and an additional insulation layer. As discussed, a coaxial cable is efficient in blocking EMI, however it inevitably introduces a small leakage between two electrical layers since they are at different voltage levels. As for a triaxial cable, which is shown in Figure 3.12b, the outer shield is virtually grounded, and the inner shield is driven by the same potential as the core signal. In such configuration, the EMI can be eliminated from the outer shield as a coaxial cable does, and the leakage only exists between the outer and inner shields, where the voltage difference is. As for the core signal, it can be well protected from leakage, since there is no voltage

difference between the core and the inner shield. However, the practical disadvantages of applying triaxial cables and relevant connectors for every application are the size and cost. The six-layer configuration makes a triaxial connector inherently larger than a coaxial connector. In addition, a triaxial connector is about £50 in the market, and a triaxial-to-triaxial cable assembly is about £200, which is not suitable for low-cost applications. In the thesis, triaxial cables has only been used for extra-low current measurement and relevant performance test from a current source (in Chapter 4).

3.4 Faraday cage

To eliminate surrounding noise interference, a Faraday cage can be utilised, especially for measuring chemical sensors (with high-impedance electrodes). A Faraday cage is a solid/meshed enclosure, made of conductive metal, which blocks the electrical field interchanging between the interior and exterior of the cage. Therefore, an experiment should be set up inside the faraday cage to provide an electrical shield blocking external EMI.

Effectively, the application of a Faraday cage and coaxial cables is able to make the transmission becomes a triaxial configuration. The Faraday cage works as the outer shield of the triaxial cable. The shielding layer of the coaxial cable can be therefore driven by the same potential as the inner core signal, to prevent any leakage between these two layers. Figure 3.13 shows the difference when utilising a Faraday cage in an ion selective electrode (ISE) experiment. The sodium ISE is in the aCSF solution (0mM NaCl), and clinically this votlage is regarded as the background voltage. The standard deviation of the output signal is about 4mV (200 samples) when conducting the experiment without the Faraday cage. After shielded by the Faraday cage, the standard deviation decreases to about 0.24mV (200 samples).

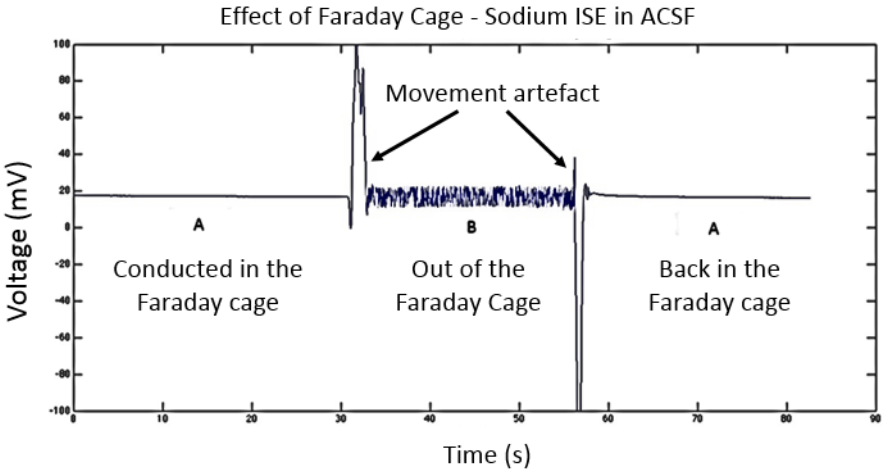

Figure 3.13: Noise reduction when shielding the experiment with a Faraday cage

This figure shows a comparison data of the output from a sodium ion-selective electrode in an ACSF solution. Part A is the noise level inside a Faraday cage, and part B is the noise level outside the cage. The intermediate large spikes are due to motion artefact when placing/removing the Faraday cage.

3.5 Summary

Most of the key PCB routing considerations and experience have been illustrated in this chapter. They have been applied to all the electronic designs and development discussed in this thesis. The experimental optimisation approaches discussed in this chapter have been utilised on both lab-based and clinical monitoring, to achieve high-quality signals and good overall performance.

Chapter 4: Amperometric Sensor Measurements in TBI Patients

4.1 Overview

As discussed in Chapter 1, relevant neurochemical changes of the local injured brain tissue in TBI patients are being monitored, to investigate secondary brain injuries. The concentration changes of glucose and lactate are currently the main parameters, as they indicate the depletion of local energy substrates and are associated with the ischemia. Both glucose and lactate sensors operate on the basis of three-electrode system. In the thesis, I have designed and developed two different electronic systems to support the electrochemical reactions. The relevant wireless implementations will be further discussed in Chapter 7.

Traditionally, to detect electrons generated from an electrochemical cell, a potentiostat is utilised. It is able to provide the required operating voltage to the electrochemical reaction and detect the current generated from the working electrode. To design such a potentiostat for TBI monitoring that the output current can be as small as pA, either a high-performance resistive transimpedance circuit or a capacitive switched-capacitor circuit can be applied. Each design has its own advantages and drawbacks. The relevant designs, implementations, and performance comparisons will be discussed in this Chapter.

4.2 Resistive amperometric circuit design

4.2.1 Why use transimpedance circuit?

As discussed above, the fundamental ability of the circuit is to detect the output electrons from the working electrode. Ideally, the whole electrochemical reaction can be regarded as a current source, as it generates a current signal to the processing electronics. As most electronic instrumentation accommodates voltage rather than current signals, the signal coming out of the working electrode requires a current-to-voltage conversion.

Following the Ohm law, current can be converted into voltage, by passing through a resistor. Figure 4.1 shows a straightforward circuit design. Signal current i_P from the working electrode (WE) flows in the load resistor R_L, producing a signal voltage, e_o. The op-amp voltage follower isolates R_L from any impedance loading error at the circuit output.

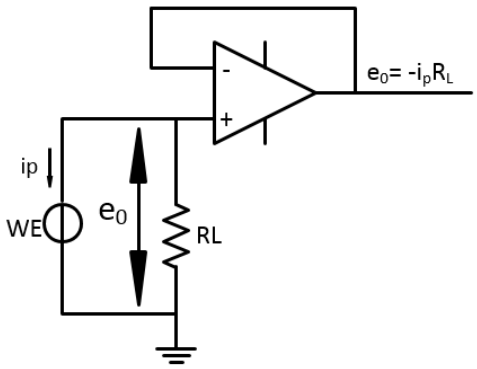

Figure 4.1: A straightforward circuit design for a current-to-voltage conversion

However, this simple circuit also creates the whole signal voltage e_0 across the working electrode and its capacitance. At high frequency, the resulting signal current in this capacitance shunts the current from the working electrode, producing a bandwidth limit. A more practical analysis is shown in Figure 4.2. The working electrode acts as a current source i_P with shunting elements R_D and C_D. C_D is the capacitance from the sensor electrode side, while R_D represents the high resistance of the working electrode, whose practical level is larger than the load resistor R_L. The voltage follower op-amp also presents additional shunting elements, the input resistance R_{icm} and the input capacitance C_{icm}. Since R_D and R_{icm} are much larger than the load R_L, they can be ignored when analysing the shunting elements. However, the capacitive elements from the electrode and the op-amp cannot be overlooked, as they can significantly shunt R_L and produce a bandwidth limit.

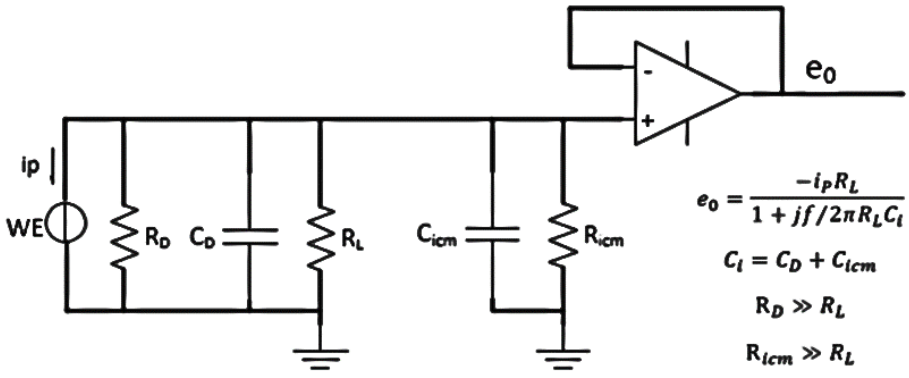

Figure 4.2: The sophisticated analysis of the simple current-to-voltage conversion.

This model considers all the relevant parasitic components in the circuit. The basic elements of the working electrode and the input impedance elements from the op-amp, for bandwidth analysis, are shown in the figure, which is adapted from [68].

Based on the analysis, the circuit is able to produce the ideal response $e_0 = -i_P R_L$, only until capacitive shunting diverts i_P at higher frequency. The combined capacitance of the input circuit C_i (= $C_D + C_{icm}$), produces a response roll off with a pole frequency of $f_p = 1/2\pi R_L C_i$. Then, as Figure 4.2 shows,

$$\frac{e_0}{i_p} = \frac{-R_L}{1 + {jf}/{f_p}} \tag{4.1}$$

In terms of this single-pole response, the circuit's -3dB bandwidth equals the pole frequency f_P, and the relevant time constant $\tau = R_L C_i$. The above equation reflects a classic gain-versus-bandwidth compromise. Increasing R_L produces higher gain for the current-to-voltage conversion, but reduces the bandwidth set by f_P in direct proportion. From the circuit perspective, this compromise results from corresponding signal voltage across the circuit capacitances. When increasing R_L to increase the conversion gain, it also increases the signal voltage across the capacitances, which results in increasing the portion of i_P that the capacitances shunt away from the load. Consequentially, the -3dB response point of the circuit decreases to a lower frequency.

In addition to the bandwidth problem, more importantly, the voltage between the working and reference electrode can hardly be constant. As the current output from the working electrode passes through the load resistor R_L, generating the voltage e_0, this voltage is also added back to the working electrode itself. The voltage eventually affects the voltage across the electrochemical reaction, and significantly increase the difficulty to maintain a desired constant voltage for the reaction.

To avoid the compromise, the signal voltage should ideally develop on the load resistor itself, but not on the working electrode or the parasitic capacitors. To achieve this, the conversion circuit can be slightly altered, which is shown in Figure 4.3. By convention, the circuit with the impedance (load resistor) placed across the op-amp, converting signal current to voltage, is called as a transimpedance circuit. Assuming the op-amp is ideal, the new circuit reduces the signal voltage across the working electrode and relevant capacitances to zero, since the feedback action of the op-amp forces two amplifier inputs to maintain the same voltage, offering a virtual ground to the electrode output current. The voltage across the load R_f is therefore transferred to the output of the op-amp, isolated from the electrode side.

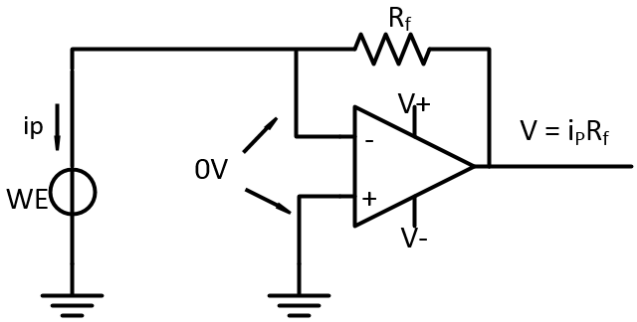

Figure 4.3: The transimpedance current-to-voltage (I-to-V) converter

The design isolates the load voltage, for improved bandwidth and stabilising the potential on the working electrode. The polarity of the voltage V follows the direction of the current i_P.

Practically speaking, the open-loop gain (A_{OL}) of an op-amp is high, but finite, which means it can only approximate the zero voltage condition discussed above. The finite gain results in a part of the signal voltage (V/A_{OL}) appearing between two inputs of the op-amp, and therefore the electrode and its capacitance. This residual signal introduce a new bandwidth limit and the potential of the circuit oscillation, which will be further discussed in Section 4.2.4.

4.2.2 Practical transimpedance circuit design

In general, the schematic of a simplified transimpedance circuit is shown in Figure 4.4. I is the current input following into the circuit, which comes from the working electrode of the sensor. R is the transimpedance, which is chosen by different current input levels. In DC and low-frequency range, the gain of the circuit can be presented as

$$G = \frac{V}{I} = -R \tag{4.2}$$

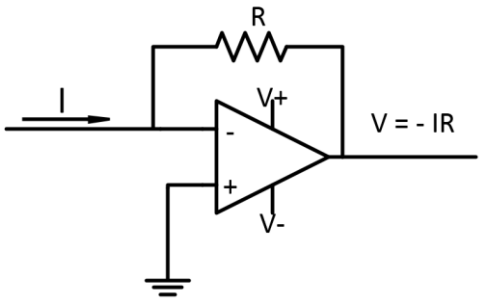

Figure 4.4: The schematic of a basic transimpedance circuit.

As discussed, the signal current from the working electrode is normally in pA or nA level for TBI applications, so it requires very large resistance to convert the current to a voltage that is large enough for display or further data analysis. For example, a 1GΩ resistor can be utilised

to convert 1nA current to 1 volt, and a 10GΩ resistor needs to be used to convert 100pA current to 1 volt. Since the output current from the sensor can vary significantly due to its sensitivity and application, multiple resistors (gains) have been used in the design, which is controlled by a high insulation-resistance switch (Figure 4.5).

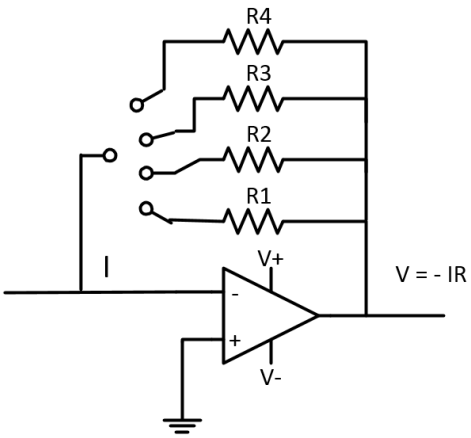

Figure 4.5: The schematic of a transimpedance circuit with multiple gains

The above circuit looks very straightforward and easy to design. However, it requires much more attentions when dealing with extra low current. Since the gains are large, there are several practical considerations when designing the circuit:

a) Gain resistors need to be chosen thoughtfully, since the tolerance and temperature coefficient can be huge factors at the output, introducing noise to the system.

b) Precision gain resistors with less than 1% tolerance and 100ppm/°C temperature coefficient are preferable.

c) The switch used in the design needs to maintain a high insulation resistance. If a standard slide switch is used, which has about 500MΩ insulation resistance, the difference between the on-off states, when connected to the 10GΩ resistor, is negligible (10.5GΩ when the switch is off, and 10GΩ when the switch is on). The switch selected in this design has an insulation resistance of 100GΩ, which is suitable to distinguish the on-off states for all the gain resistors.

d) The offset voltage and the input bias current from the non-inverting terminal of the op-amp, potentially result in a significant offset at the output voltage. Therefore, the main op-amp used in the circuit is LMP7721 from TI, which features maximum ±20fA input bias current at 25°C, and ±26μV offset voltage; an alternative op-amp is OPA129 from TI, and it can be used for applications that require large operating voltages, as it can handle ±18V power supply, while maintaining ±30fA input bias current.

e) In addition, the parasitic capacitor exists across the feedback resistor, and this effect generally sets the bandwidth for higher-gain cases. Low-gain applications reduce the significance of the parasitic capacitance, whereas the response limit is imposed when the transimpedance gain is large. The details will be further discussed in Section 4.2.3 and 4.2.4.

4.2.3 Bandwidth and stability

As the transimpedance circuit is connected with the three-electrode system, the circuit actually produces a two-pole, rather than a single-pole, response, which means that the circuit behaves like a parallel L-C circuit. As for a L-C circuit, the capacitor ("C") stores energy in the electric field between the plates, which is determined by the voltage across it, while the inductor ("L") stores energy in the magnetic field, which is determined by the current passing through it. When applying a large transimpedance gain, this feedback resistor can often make this equivalent L-C circuit resonate or even oscillate [68].

Compared with the initial set-up, the transimpedance circuit removes the signal voltage from the working electrode, however the op amp gain error signal e_0/A_{OL} remains across it (Figure 4.6). A_{OL} can maintain adequately ideal at low frequencies, and it starts to roll off at high frequencies, due to limited op amp bandwidth, and it produces the second response limit.

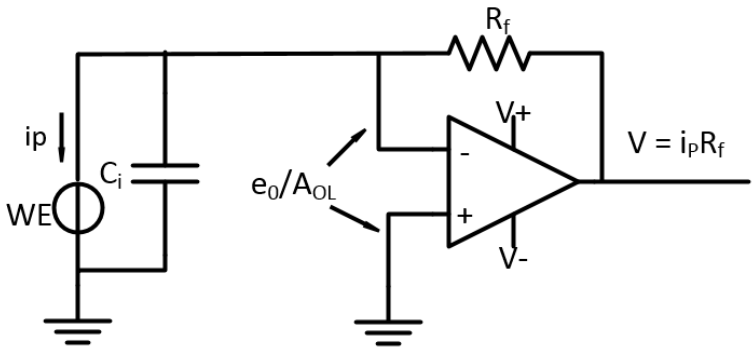

Figure 4.6: Practical op-amp limitation

The residual gain error e_0/A_{OL} is due to the op amp, and it introduces a new response limit.

As Figure 4.6 shows, C_i is the summing capacitance at the input, which constructs a low-pass filter with the feedback resistor. This low-pass response can be characterised as the feedback factor β, which is calculated as the following formula:

$$\beta = \frac{X_{ci}}{X_{ci} + R_f} = \frac{1}{1 + R_f C_i s} \tag{4.3}$$

where X_{ci} is the reactance of the capacitance C_i

When taking into account of this low-pass effect, the circuit response equation becomes:

$$V_{out} = i_P R_f + (-\frac{V_{out}}{A_{OL}} \times \frac{1}{\beta}) \tag{4.4}$$

$$V_{out} = \frac{i_P R_f}{1 + 1/A_{OL}\beta} \tag{4.5}$$

When operating at low frequencies, the feedback factor β has little effect on the gain, and thus the conversion response tends to be ideal. V_{out} is equal to i_pR_f, as long as $A_{OL}\beta$ is much greater than unity. As the frequency rises, the open loop gain A_{OL} rolls off while 1/β goes up. Figure 4.7 shows the slopes of the 1/β and A_{OL} curves, predicting stability. As shown in the figure, the conversion gain is constant at low frequency, and the circuit will start to oscillate at frequency f_i, where A_{OL} intersects with 1/β [68].

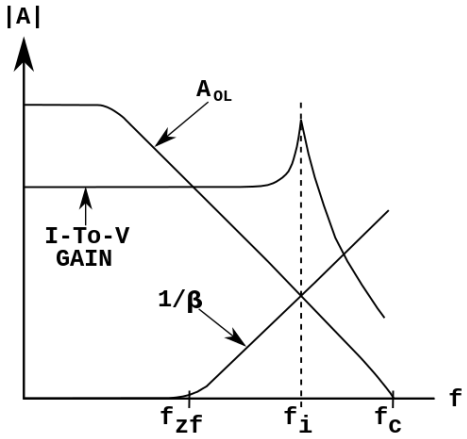

Figure 4.7: Bode plot with uncompensated transimpedance amplifier

The frequency response has a gain peaking at the intersection point between A_{OL} and 1/β. The cause will be discussed in Section 4.2.4. The figure is extracted from [68].

4.2.4 Compensation capacitor

As discussed above, the dual declines of the frequency response (on A_{OL} and β) create the two-pole gain peaking. The slopes of the 1/β and A_{OL} curves indicate the frequency stability conditions through the rate of closure of the two curves. Since both the 1/β rise and the op-amp roll off are due to a single pole or zero response, both curves features the 20dB/decade slopes and therefore the slop difference at the intersection point, fi, equals 40dB/decade.

Each 20dB/decade of slop is corresponding to 90-degree phase shift, and thus 40dB corresponds to 180-degree phase shift. Furthermore, the inherent structure of the negative-feedback current-to-voltage conversion amplifier produces another 180-degree phase shift, which results in a net 360-degree phase shift. At the point that 1/β and A_{OL} intercept, the loop gain is $A_{OL}\beta = 1$. A feedback loop with unity gain and 360-degree phase shift becomes self-sustaining, which is oscillation.

To avoid the significant gain peaking and relevant instability, a compensation capacitor is added to the feedback loop (Figure 4.8). This capacitor introduces a "zero" to the circuit's feedback factor β, which is presented as

$$\beta = \frac{1 + R_f C_f s}{1 + R_f (C_i + C_f) s} \tag{4.6}$$

where $C_i = (C_D + C_{id} + C_{icm})$.

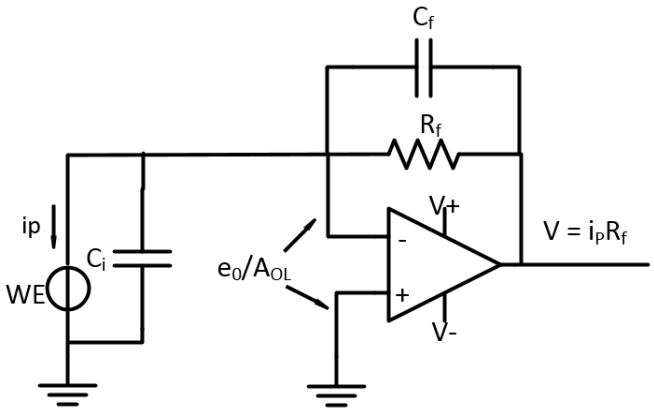

Figure 4.8: Transimpedance circuit with a compensation capacitor

C_f produces a zero at frequency $f_{Cf} = 1/2\pi R_f C_f$ that counteracts the pole produced by C_i at frequency $f_{zf} = 1/2\pi R_f(C_i + C_f)$. Figure 4.9 shows the C_f compensation of the op-amp roll-off and 1/β curves, reducing the rate of closure and preserving stability. When applying the same method to determine oscillation, the loop gain at the intercept remains unity, but the total phase shift is no longer a full 360°. Therefore, one of the two requirements for oscillation is eliminated with the present of C_f, making the circuit stable. This also reduces the gain peaking effect, which provides a flat overall response.

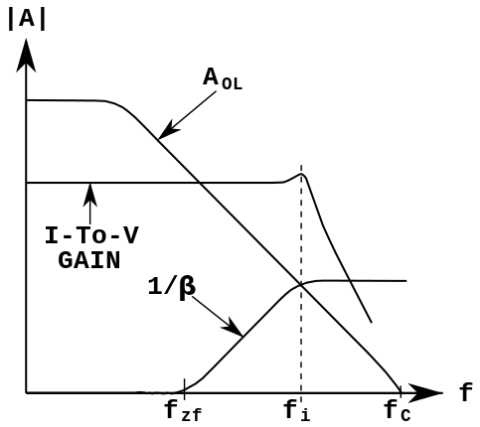

Figure 4.9: Frequency response with a compensation capacitor

The compensation capacitor in parallel with the gain resistor helps to reduce the gain peaking effect. The figure is extracted from [68].

The compensation capacitor is able to re-establish the stability, however it also shunts the output signal and therefore limits the bandwidth. This should be considered in high-frequency applications. Whereas in low-frequency applications, such as bio-signal measurement, whose effective frequencies are generally less than 10Hz, a large feedback capacitor is useful, since it offers large tolerance of PCB stray capacitance, additional phase shifts in the loop and excessive capacitive load. In addition, it can also reduce the response bandwidth to eliminate unnecessary high-frequency noise [62]. As discussed in Figure 3.4 and Table 3.1, high-quality capacitors with large parallel leakage resistance (≥ 100GΩ) are often desired for high-gain transimpedance circuits, otherwise the gain will be affected by this leakage resistor sitting in parallel with the gain resistor.

4.2.5 Noise analysis

Since the I-to-V conversion circuit normally requires a large gain to transfer the small signal current from the working electrode, the high-resistance feedback resistor increases the circuit's noise, both directly and indirectly. To investigate the noise effect, the spectral noise densities have been analysed, reflecting the noise in a 1Hz bandwidth at a given frequency range.

As for the noise analysis of the transimpedance circuit, three different noise sources need to be considered: the output noise from the feedback resistor e_{noR}, the amplifier's input current noise e_{noi}, and the amplifier's input voltage noise e_{noe}, and these noise sources are combined to produce the net output noise density e_{no}. The direct noise is from the feedback resistor itself, which follows Johnson-Nyquist noise (thermal noise) equation [69],

$$e_{nR} = \sqrt{4KTR_f} \tag{4.7}$$

K is Boltzman's constant, 1.38 × 10^{-23}J/°K, and T is the temperature in Kelvin, which is °C + 273.

This noise is transferred to the output end without any amplification, which indicates that $e_{noR} = e_R$. When sourcing high-quality high-resistance (≥ 10GΩ) gain resistors in the market, most of the high-precision resistors can maintain at best 1% tolerance, and some of them can only maintain 10% tolerance or worse.

i_{ni} represents the noise of the input bias current on the negative input end, I_{B-}, which has a noise density of

$$i_{ni} = \sqrt{2qI_{B-}} \tag{4.8}$$

where q is the charge on an electron, 1.6 × 10^{-19} C.

As this noise flows directly through the feedback resistor R_f, the output noise voltage

$$e_{nRi} = i_{ni}R_f = R_f\sqrt{2qI_{B-}} \tag{4.9}$$

It shows that a good op-amp with lower input bias current can produce less noise voltage e_{nRi}.

When analysing the amplifier's input noise voltage, e_{noe}, the input offset voltage e_{ni} is converted to the output via a non-inverting amplifier. At high frequency, the equation is

$$e_{noe} = \frac{1 + R_f(C_i + C_s)s}{(1 + R_fC_ss)}e_{ni} \tag{4.10}$$

R_D is bypassed by C_D in high frequency, which is not shown in this equation. At DC level, the circuit can be simplified as

$$e_{noe} = \frac{1 + R_f}{1 + R_D}e_{ni} \tag{4.11}$$

Due to the uncorrelated nature of these noises, the overall root mean square (rms) value is required to calculate these three different individual noises, rather than summing these values linearly. Therefore, the summing can be presented as

$$e_{no} = \sqrt{e_{noR}^2 + e_{noi}^2 + e_{noe}^2} \tag{4.12}$$

In summary, to achieve a better signal-to-noise ratio (SNR), all the noise sources need to be considered and minimised. High-precision feedback resistors, high-performance op-amps with low input-bias current and offset, are required.

4.2.6 Shield driver for the working electrode

Besides considering all the factors discussed above, a guard driver is also involved in the design to prevent any leakage current from the input connector and cable. Ideally, a tri-axial connector should be used in the design, to maximise the shielding performance, however, a tri-axial connector is generally very large and not cost-effective. Therefore, a co-axial (SMB) connector is applied in this design, whose outer shield is driven by an op-amp (LMP7715 from Texas Instruments) and a 100Ω isolation resistor. The overall transimpedance circuit is shown in Figure 4.10. By driving the shield to maintain the same potential as the core, the leakage current between these two layers can be therefore minimised. A Faraday cage is required if one needs to block high-frequency EMI and improve the SNR, which has been discussed in Chapter 3.

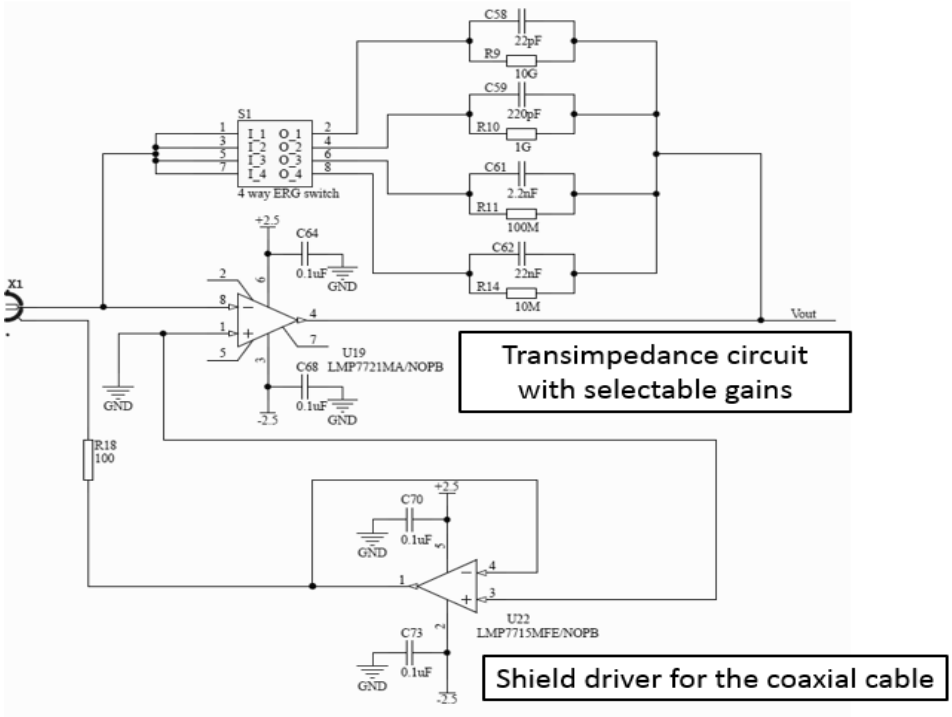

Figure 4.10: The schematic of overall transimpedance circuit

Two main chips, LMP7721 and OPA129, have been used for implementing different transimpedance circuits, as they are working in different voltages. LMP7721 is used for low-power application, and OPA129 is used for general lab-based transimpedance circuit. As they have similar schematic, only LMP7721 is shown in this figure. As for the shield, LMP7721 is associated with LMP7715, and OPA129 is associated with OPA140, based on their relevant operating voltages.

4.2.7 Electronic design for the reference and counter electrode

After discussing the requirement and relevant design of the working electrode, the considerations for the reference and counter electrode in the three-electrode system will be discussed in this section. This part of design contains two amplifiers, one is used for driving the reference electrode, and the other one is for providing selectable reference voltages and sufficient current to the electrochemical reaction. As shown above, the potential of the working electrode, $V_{working}$, is virtually tied to ground to simplify the output voltage calculation, otherwise the output voltage is

$$V_{OUT} = V_{working} + (-I \times R) \tag{4.13}$$

Therefore, the operating voltage of the electrochemical reaction is controlled by the reference electrode. For example, when the reaction requires +0.7V from the working to reference electrode, it is accomplished by setting the reference electrode to -0.7V. As the stability of this voltage can significantly affect the quality of the sensor's output current, the reference electrode is also shielded (Figure 4.11). In addition, a switch is added to allow users to select the reference voltage between the local ground and an external source. By providing this option, users can use an external signal generator to run a cycle voltammetry (CV) test for electrodes. The voltage can also be set at a constant potential, like -0.7V, for a specific electrochemical application.

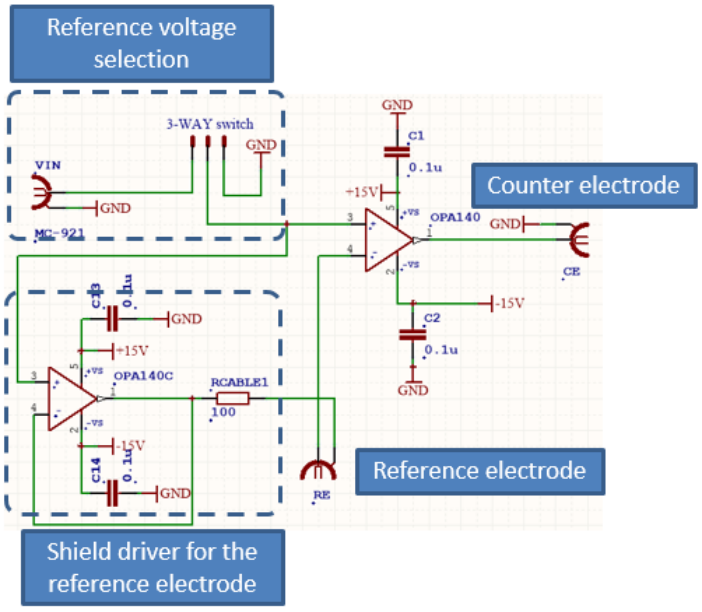

Figure 4.11: Schematic of RE and CE design

RE presents the reference electrode, and CE is the connection for the counter electrode. V_{IN} is the external bias voltage applied to the reference electrode.

4.2.8 PCB layout

The overall PCB layout and relevant labelling are shown in Figure 4.12. The overall dimension of the board is 47mm × 40mm. The upper part is the potentiostat, used for maintaining a desired voltage between the working and reference electrode (RE), and providing sufficient current to the counter electrode (CE). The lower part is the transimpedance circuit, converting the current to voltage, with selectable gains.

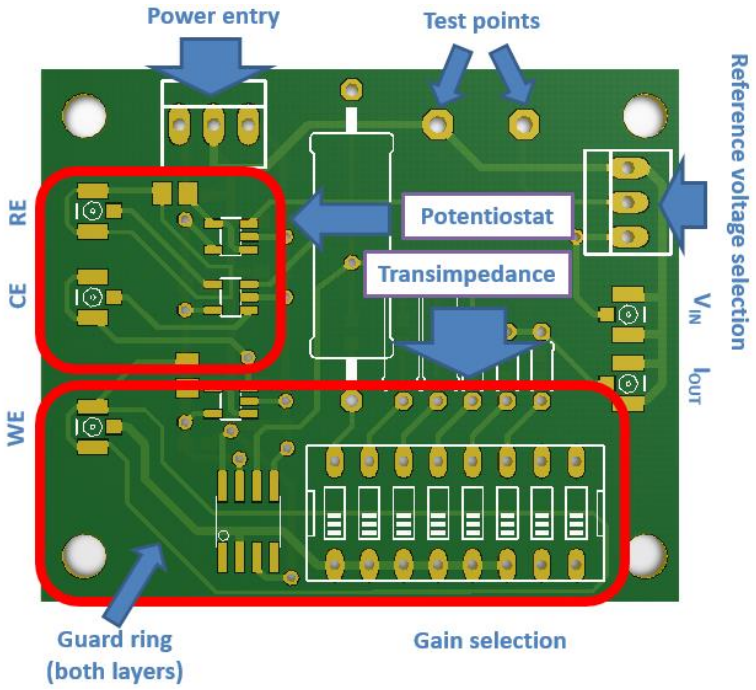

Figure 4.12: Resistive potentiostat layout

The power entry is placed perpendicularly to the signal travelling path, in order to minimise EMI. The guard ring is also used on both sides of the board to eliminate surface leakage current. As the board is shielded in an enclosure, a LED indicator is not added, but 2 test points are placed for fast debugging.

4.2.9 Experimental set-up and performance test

Current source

The first experiment was conducted with a current source, to validate the resistive I-to-V system. The data is shown in Figure 4.13. The graph on the left shows the current response at gain of 1nA/V. Following the equation V = - I × R, the output voltage will follow the step changes from the input source. Similarly, the data on the right was acquired from another gain channel of the board. By apply a higher gain (0.1nA/V), the circuit is capable of measuring hundreds of fA current. However, it is significantly noisier than the other gain channel. More specifically, the standard deviation when working at 1nA/V gain is 28mV (2s integration) and

that of 0.1nA/V is 166mV (2s integration). Clinically, a 10Hz digital low-pass filter is normally used to achieve better SNR.

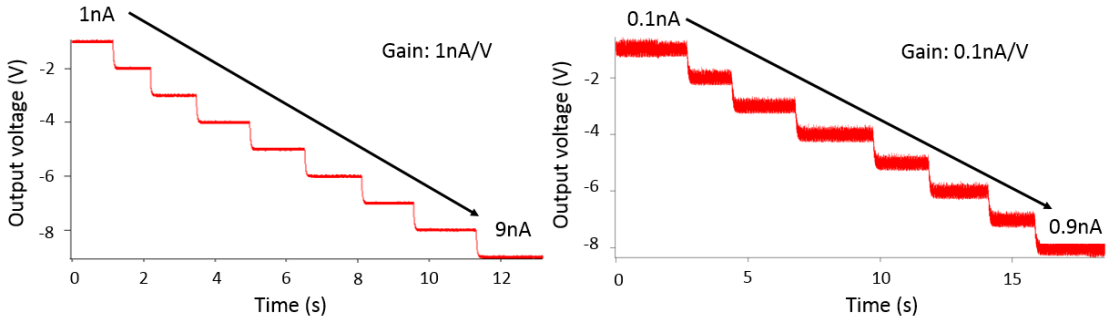

Figure 4.13: Resistive I-to-V conversion test with current source

The data from the two graphs were obtained from the same circuit and experimental environment. The difference is the gain. The first graph chose the transimpedance as 1GΩ, which indicates that the gain is 1nA/V. The second graph selected the 10GΩ as the transimpedance, and therefore the gain is 0.1nA/V. There is no filtering on either of the graph.

Electrode

To show the functionality of the design and interaction with real-world electrodes, a cyclic voltammetry (CV) test is presented in this section. CV is a commonly used technique in electrochemistry, in which the voltage between the working and the reference electrode is ramped linearly versus time, at a given scan rate. When the voltage reaches a certain pre-set value, the ramp is inverted and the voltage starts to scan in the reverse direction. The test is very useful, as it shows the properties of the electrode under test or the solution under test. For example, the plateau current of the CV is called as the steady-state limiting current I_{lim}, which follows the equation for a microdisk electrode:

$$I_{lim} = 4nFDrC \tag{4.14}$$

Where n is the number of electrons in the electrochemical reaction, F is the faraday constant, D is the diffusion coefficient, r is the radius of the disc electrode, and C is the solution concentration.

Figure 4.14 shows an example of applying the resistive I-to-V circuit board to run a CV test on an electrode. As the potential on the working electrode is virtually grounded, the bias voltage of the system was applied from the reference electrode, which was connected to the external signal source, PowerLab. In this example, the CV graph (Figure 4.14) was obtained using a platinum 50µm disc electrode in 1.5mM ferrocene monocarboxylic acid solution. The applied voltage was with respect to an Ag/AgCl electrode. During measurement, a 10Hz digital filter was added to eliminate any interference. Following Equation (4.14), the theoretical limiting current should be 8.29 nA (D = 5.73 x 10^{-6}cm^{2}s^{-1} [70]).

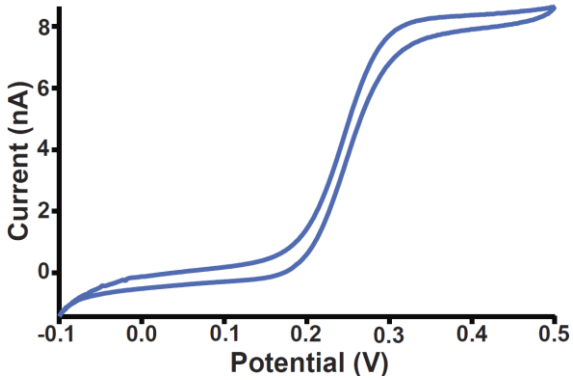

Figure 4.14: Cyclic voltammetry example

The voltage was scanned from -0.1V to +0.5V, at 10mV/s scan rate. The plateau current, measured at 0.5V, is 8.5 (±0.2) nA, which is close to the theoretical limiting current 8.29nA. The error may be due to the flatness and clarity of the electrode surface.

4.2.10 Summary of resistive amperometric circuit

In this section, a resistive amperometric circuit design has been presented, following by the tests from both standard lab instruments and real-world electrodes. The circuit only contains analog design, without any digital programming or processing. The operating principle is also easy to understand, as it only involves one transimpedance circuit, which yields $V = - I \times R$. To optimise the performance, one needs to be cautious of relevant current flow, component selections, and guarding techniques.

The board has become a common analytical tool for the electrochemists in the group, and been regularly used in the lab for daily electrochemical experiments. It has been also applied in clinical environment for measuring glucose and lactate concentrations in TBI patients, and the relevant data will be further discussed in Chapter 6. The board has also been implemented for wireless applications, which will be discussed in Chapter 7 and 9.

However, a resistive amperometric circuit also has its own disadvantages. The high-precision high-value resistors used in the circuits are physically very large. This inevitably increases the size of the circuit board and makes it vulnerable to noise. The 50Hz noise from mains and the harmonic noise (due to the switched-mode DC/DC converter) can be detected at the output. The noise can be attenuated by applying a digital low-pass filter (10Hz) via LabChart in practice, however this may become an issue if extra data converters and digital ICs are added for further implementation, like a wireless potentiostat.

4.3 Capacitive amperometric circuit

Unlike resistive amperometric circuit, a capacitive amperometric circuit employs capacitors rather than resistors to collect electrons from the working electrode, conducting the current to voltage conversion. Generally, a capacitor with two switches can be integrated as a simple capacitive I-to-V conversion unit, which is shown in Figure 4.16.

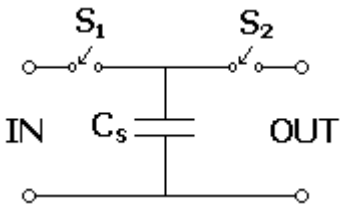

Figure 4.15: The schematic of a simple capacitive I-to-V conversion unit

The capacitor C_S can store the incoming current from the IN side and generate a voltage across it, which can be then detected from the OUT side.

When switch S_1 is closed and S_2 is open, the input current is integrated into capacitor C_S, and the charge, Q, after a period Δt is calculated as

$$\Delta Q = I_{IN} \times \Delta t \tag{4.15}$$

When S_1 is open and S_2 is closed, the collected charge will be discharged to the output side,

$$\Delta Q = C_S \times \Delta V_{OUT} \tag{4.16}$$

As the charge is the same on both equations, we can have

$$I_{IN} \times \Delta t = C_S \times \Delta V_{OUT} \tag{4.17}$$

Therefore, the conversion rate (or equivalent resistance) R, can be presented as

$$R = \frac{\Delta V_{OUT}}{I_{IN}} = \frac{\Delta t}{C_S} \tag{4.18}$$

The conversion rate is determined by the integration time Δt and the intermediate capacitance C_S. By controlling the on/off state of the switches, the circuit can be equivalent as a resistor. Some ICs employ switched-capacitor techniques to implement “R-C” filter, which is called as “switched-capacitor filters” [71]. The properties of such filters only depend on the ratio of capacitors, which makes it more suitable for ICs. Based on the same principle, a resistive I-to-V circuit can be converted into capacitive, which eliminates all the disadvantages of utilising high-resistance resistors.

In a recent decade, Texas Instruments has released a series of capacitive I-to-V ICs, which belong to the DDC family. The ICs in the family has identical operating principles, and the main difference is the number of channels on each IC. In the thesis, DDC 112 (2 channels) was used for prototyping, and DDC114 (4 channels) has been finally selected as it has more channels and features internal high-precision capacitors.

4.3.1 DDC114

In general, DDC114 is a 4-channel 20-bit current-input ADC. For each input, DDC114 provides a dual-switched integrator front-end, which allows for continuous current integrations and measurement. It features 8 different internal capacitors, ranging from 3pF to 87.5pF. The integration time, Δt, can be adjusted from 50μs to 1s, which indicates that it can theoretically measure current from fA to μA.

As for the power supply, DDC114 requires single 5V analog supply, and 2.7V to 5.25V digital supply. This indicates DDC114 is capable of communicating at both standard 3.3V and 5V logic level. In addition, DDC114 is SPI compatible and it also features complementary digital SPI clock and digital data out signal connections to eliminate crosstalk.

4.3.2 Operating principle

The simplified schematic of the DDC114 is shown in Figure 4.16. The major capacitive current-to-voltage conversion circuitry in each channel is shown in the zoom-in area. As discussed, two identical integrators are involved in each channel with 8 different built-in capacitors in each integrator.

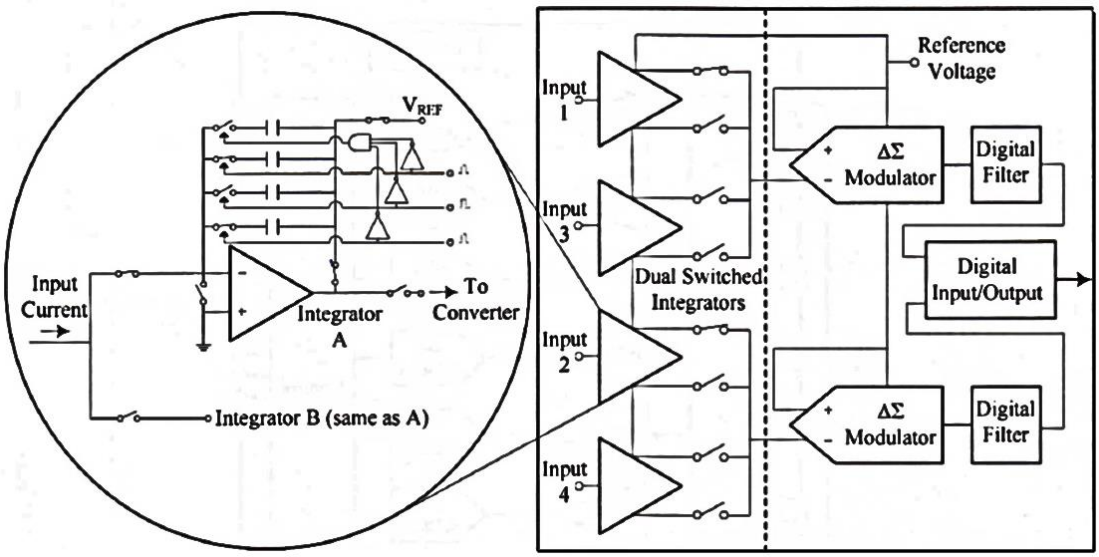

Figure 4.16: Simplified schematic of the DDC114

4 channels are involved in DDC114, and the zoomed-in part shows the internal structure of an individual channel. The figure is adapted from [72].

More specifically, the average measured current during one integration is determined by the integration time and the charge changes, following by equation:

$$i_{average}(t) = \frac{1}{T_{Int}} \int_0^{T_{Int}/_2} \partial q(t) = \frac{q\left(T_{Int}/_2\right) - q(0)}{T_{Int}} \quad (4.19)$$

Where T_{Int} is the total integration period for each dual-switched integrator of the chip. q(t) is the charge at time t, and the charge difference can be then represented as voltage changes (4.15).

Therefore, these two factors can be used to configure DDC114's operating ranges. More specifically, DDC114 provides three external digital IO pins, RANGE0 - RANGE2, to allow the user to select a specific integration capacitor, C_F (Table 4.1).

RANGE2	RANGE1	RANGE0	C_F (pF)	INPUT RANGE (pC)
0	0	0	3	-0.048 to 12
0	0	1	12.5	-02 to 50
0	1	0	25	-0.4 to 100
0	1	1	37.5	-0.6 to 150
1	0	0	50	-0.8 to 200
1	0	1	62.5	-0.1 to 250
1	1	0	75	-1.2 to 300
1	1	1	87.5	-1.4 to 350

Table 4.1: Range selection of the DDC114

The table is reproduced from [72]. As the table shows, different selection has overlap in input range. As the capacitance becomes smaller (from 87.5pF to 3pF), the stability of the measurement becomes lower. Therefore, when given a certain current input range, one should choose as large capacitance as possible and achieve different detections (in pC) by controlling the integration time, to achieve optimum performance.

By selecting a certain range (integration capacitor), the current-to-voltage conversion rate is then only determined by the integration time, which is controlled by the CONV pin. The specific operation model is shown in Figure 4.17. As discussed, two integrators are involved in one channel, and this figure only shows the configuration of one integrator, half of the channel. When completing an analog-to-digital conversion, the switches are configured as Figure 4.17a shows. In this manner, the integration capacitor is charged to the reference voltage, V_{REF}. Once completely charged, the switches are turned to the wait configuration (Figure 4.17b), such that V_{REF} is not connected and the circuit is waiting for the next integration. When detecting the rising edge of CONV, S_{INT} closes, which starts to accumulate charges in C_F and integration process in integrator A (Figure 4.17c). At this stage, charge from the input signal is collected from the integration capacitor, which causes the output voltage to decrease. The falling edge of CONV terminates the integration, by switching the input from integrator A to B. Then, as shown in Figure 4.17d, the output voltage of integrator A is presented to the analog-to-digital converter.

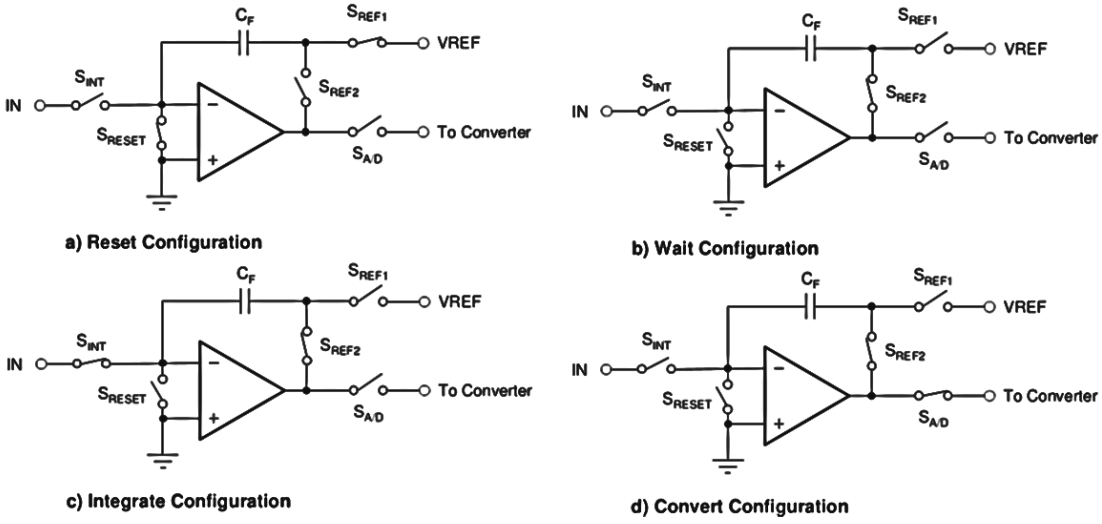

Figure 4.17: The four configurations of the integrator in DDC114

Four different operating stages and relevant configurations are shown from (a) to (d). The figure is extracted from [72].

As for the integrator B, the configurations are the same as integrator A, but the timing is exactly opposite. When CONV stays high (rising edge to falling edge), integrator A integrates

the charges from the input node while integrator B converts the previous output voltage and resets. When CONV stays low (falling edge to rising edge), integrator A converts the output voltage and resets, while integrator B integrates the input charges. By such a double-integrator configuration, one channel is capable of continuously monitoring the input signal.

4.3.3 Schematics and PCB appearance

To support multiple amperometric sensors working in parallel, 4 DDC114s have been involved in the design, which are controlled by a FPGA (Spartan 3E series) to concurrently output the information of all the channels. The recommended PCB layout can be found in the datasheet [72]. Each power pin is decoupled by a 0.1µF and a 10µF capacitor in parallel. Voltage reference chip REF5040 and a high-precision op-amp OPA365 have been chosen to provide accurate and stable reference voltage to DDC114s.

As discussed, an amperometric sensor requires an external bias voltage to operate. In the resistive potentiostat section, the bias voltage can be selected from an external signal source or the internal local ground. By only providing a connector on the board, the resistive potentiostat is miniaturised. However, in this capacitive design, a FPGA has been involved, therefore an 8-channel bipolar digital-to-analog converter (DAC) (Maxim5735) was added, to locally provide any desired bias voltage to different amperometric sensor systems.

Based on these considerations, a neurochemical biosensor interfacing circuit board has been designed and developed (Figure 4.18). The overall schematic and PCB layout are attached in appendix 4.1[1]. The PCB has an 8 electrical layer, following general routing rules described in Chapter 3. It contains 7 major functional parts: bioelectrical potential acquisition, biosensor interface, DAC-controlled sensor excitation circuitry, central data processor (FPGA), medical-grade DC/DC converter, isolated USB interface, and isolated analog outputs.

[1] The actual PCB described in this section was designed and the manufacture fabrication files were generated by Dr. Kostas Papadimitriou in the group. My role in this design contains: generating initial design ideas, selecting relevant components, debugging the PCB design, embedded programming on the FPGA, problem shooting, and conducting experiment discussed in the following sections.

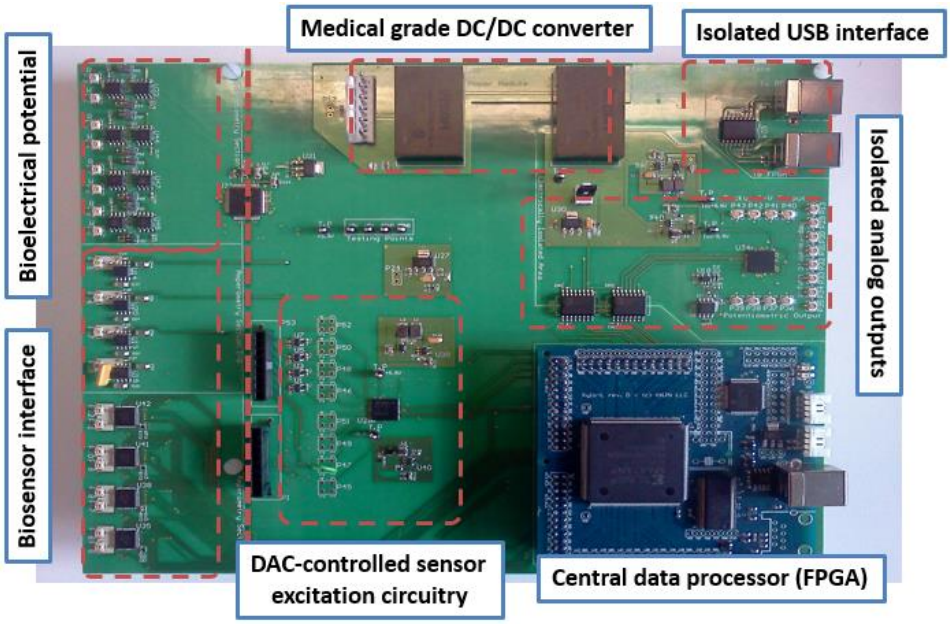

Figure 4.18: Neurochemical biosensor interfacing circuit board

The DDC114 chips are located in the biosensor interface section. For comparisons, 4 standard resistive transimpedance-based current-to-voltage conversion units are also involved. The bioelectrical potential measurement section is involved in this board as the design also aims to monitor bioelectrical signal. The main IC used in this section is ADS1298, and this part of design will be discussed in Chapter 5.

The main part relevant to this chapter is the biosensor interface. In this part, both resistive and capacitive current-to-voltage conversion circuits have been implemented. The upper region of the biosensor interface block in the figure is a 4-channel transimpedance circuit, and the lower region is 8-channel capacitive I-to-V circuit, which contains 4 DDC114 (only 2 channels are activated in each DDC114 to eliminate cross talk between channels).

As the circuit board aims at incorporating with amperometric sensors and monitoring traumatic brain injury patients in clinical environment, the DC/DC converter (RECOM6-0505) certifies IEC60601:3rd edition safety requirement. It is able to convert +5V DC to isolated ±5V DC. Both USB connections and the analog output channels are optically isolated (ADuM4160, ADuM4400, and ADuM4401) from the analog sensor interface.

The overall electrical characteristics of this neurochemical TBI board has been summarised in Table 4.2. The Potentiometry design will be discussed in Chapter 5.

	Sections		
Characteristics	**Switched-capacitance amperometry**	**Transimpedance amperometry**	**Potentiometry**
Number of Input channels	8	4	8
Resolution (bits)	16/20	-	24
Data rate (kSPS)	3.125	-	0.5-32
Total analog current supply (mA)	56	5.2	15.1
Total digital current supply (mA)	2	-	0.5
Board dimensions (cm)	23*19		
Medically graded	Yes		
IC controller	Spartan3e – 64MHz - FPGA		
Power supply	220V AC, 50Hz		

Table 4.2 Electrical characteristics of the neurochemical board

4.3.4 Experimental set-up and performance

To validate the performance of the capacitive current-to-voltage conversion system, different experiments have been conducted. The basic experimental set-up is shown in Figure 4.19. The relevant performance comparisons to a resistive transimpedance circuit, will be discussed in this section.

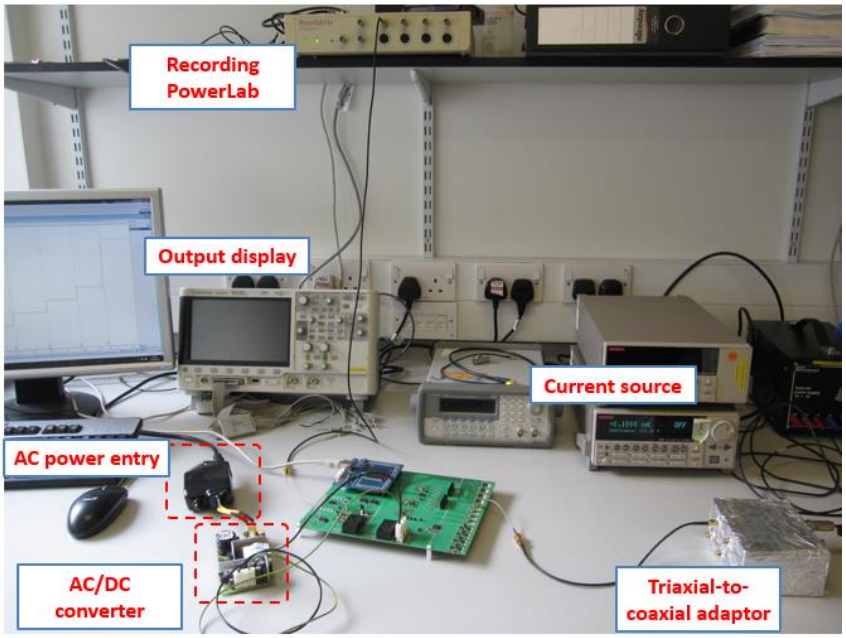

Figure 4.19: Experimental set-up to test the capacitive I-to-V conversion system

The PCB is powered by the mains through a medical-grade AC/DC converter, however it can be powered by batteries to reduce the noise.

Current source test

To evaluate the performance of the DDC114, the circuit has been first tested with a high-precision current source. Different operation ranges can be achieved by different internal capacitors or adjusting the integration CONV time. The performance among different capacitor and CONV time selections have been summarised in Table 4.3 and 4.4.

Capacitance: 25pF			
CONV time (ms)	**Approximate detection range (pA)**	**Mean conversion rate (V/pA)**	**Standard deviation (mV)**
600	160	3.2	20.22
300	320	1.6	11.37
150	650	0.8	10.79
75	1400	0.4	9.22

Table 4.3: Performance comparison among different CONV time selections

The conversion rate is proportional to the CONV (integration) time. When the CONV time decreases, the detection range also becomes larger, and the standard deviation is slightly reduced.

CONV time: 300ms			
Capacitance (pF)	**Approximate detection range (pA)**	**Mean conversion rate (V/pA)**	**Standard deviation (mV)**
87.5	1200	0.46	7.86
75	900	0.53	8.97
50	650	0.80	15.04
25	320	1.6	11.4
12.5	160	3.2	32.14
3	40	13.6	94.98

Table 4.4: Performance comparison among different capacitances

The conversion rate is reversely proportional to the capacitance. As the capacitance becomes smaller, the conversion rate increases, which means the IC is more sensitive to the input current and the same amount of current can now be converted to larger voltage. However, when working in lower capacitance, the noise level (standard deviation) of the output signal becomes larger. In addition, the detection range of the IC becomes smaller as well.

To compare the performance between the capacitive approach (DDC-based) and the classic resistive current-to-voltage (I-to-V) conversion method, these two systems have been tested under the same experimental condition. The testing current source, connection cables, and working environment remain the same for both experiments. The current source injects current from 0pA to 100pA, with 10pA steps, and the comparison result is shown in Figure 4.20 without applying any filter. The one on the left is from DDC114. The equivalent gain on this DDC114 setting is 62.5pA/V, which means every 10pA change corresponds to 0.16V. This can be verified by the mean values (labelled in dots) at different steps. The standard deviation of each step is about 2.6mV (200 samples) in voltage and therefore 162.5fA in current. The

graph on the right is the classic resistive I-to-V test. The transimpedance is 10GΩ, which means the equivalent gain is 100pA/V. The mean value (labelled in dots) at each step also validate that every 10pA change corresponds to 0.1V. As for the standard deviation of the resistive I-to-V measurement, it is about 100mV (200 samples) in voltage and therefore 10pA in current, which is much larger than that of the DDC measurement.

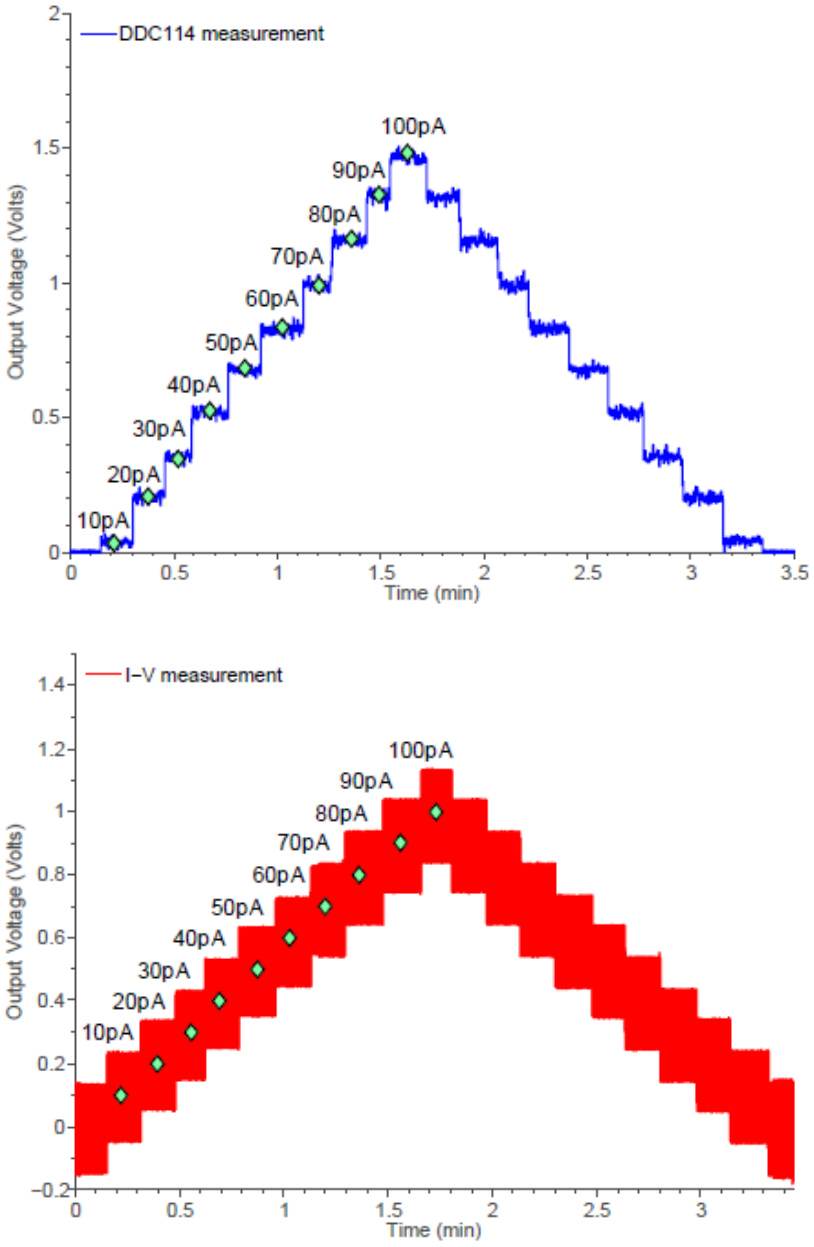

Figure 4.20: Comparison between capacitive and resistive I-to-V design

The graph on the left shows the step changes of the capacitive I-to-V circuit from 0 to 100pA with 10pA steps. The relevant standard deviation is only 162.5fA in current. The graph on the right shows the experiment with a resistive I-to-V circuit at 0.1nA/V gain (10G transimpedance). The relevant standard deviation is 10pA in current.

Through this experiment, the capacitive method shows the capability of measuring current in different levels, and more importantly, it provides much clearer and less noisy response in low-level (pA) current measurement. Fundamentally, this is due to the advantages of applying capacitors over resistors. Large-value resistors (tens of GΩ) generally have poor tolerance and temperature coefficient. In addition, high-impedance sources are generally more vulnerable to EMI, which also affects the noise level of the system. The DDC architecture does not employ any large-value resistor, and the whole system can be powered by a battery without introducing any interference from the switched-mode AC-DC converter. Therefore, it contains much less noise. Furthermore, compared with the resistive I-to-V design, whose gain has to be changed manually, the gain of the capacitive I-to-V design is controlled by the internal capacitor and integration time, which can be both controlled digitally by the central controller.

Electrode

As the system has been validated by the current source test, the capability of interacting with three-electrode system will be illustrated in this section. Figure 4.21 shows a calibration process, conducted in a RuHex, $Ru(NH_3)_6Cl_3$, solution to check the electrode sensitivity. The bias voltage was set as -0.7V, and the electrode would be tested in different pre-set concentrations. This figure shows one complete calibration event, from 0mM to 1mM with 2 intermediate steps (0.25 and 0.5mM). The data has not applied any filter, and the processed calibration curve is also shown in this figure. This experiment shows that the capacitive I-to-V circuit is able to support a three-electrode system and detect the current from a practical electrochemical reaction.

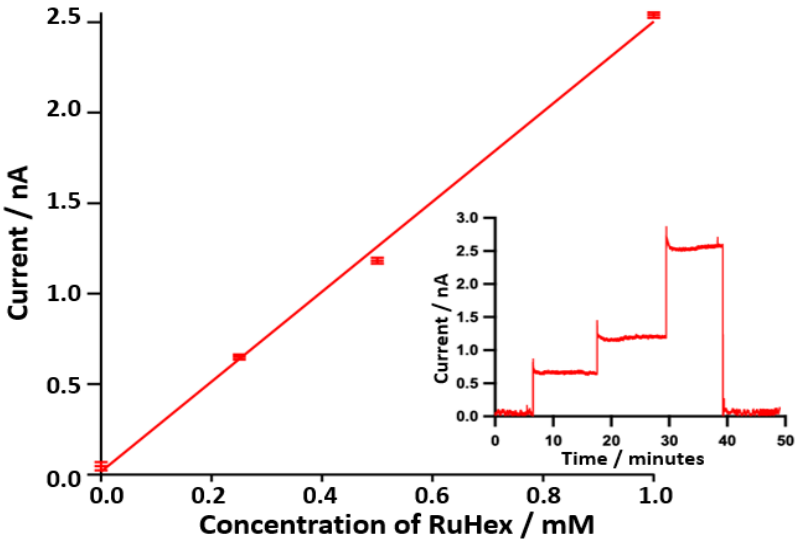

Figure 4.21: Electrode calibration with RuHeX solution

Four different concentrations (0mM, 0.25mM, 0.5mM, and 1mM) were applied during each calibration. The processed calibration curve of the electrode sensitivity is shown as the main graph and the raw data is attached on the right.

Biosensor

After testing with the current source and the electrode, the system was tested with a glucose biosensor, to further analyse its detection limit. In order to detect the glucose concentration changes with respect to the reduction current (positive current to the electronic circuits), a series of chemical reactions were involved in this test (Figure 4.22). Initially glucose is oxidised by glucose oxidase producing hydrogen peroxide, which is then reduced by horseradish peroxide (HRP). To regenerate HRP, 2 ferrocene molecules are oxidised to ferrocinium ions. These can be then detected at the working electrode by reduction (Fc^+ to Fc) at 0V. These electrons flow from electronics to the working electrode, and therefore it represent as a positive current to the processing electronics. By convention, electrochemists regard this reduction current as a negative current.

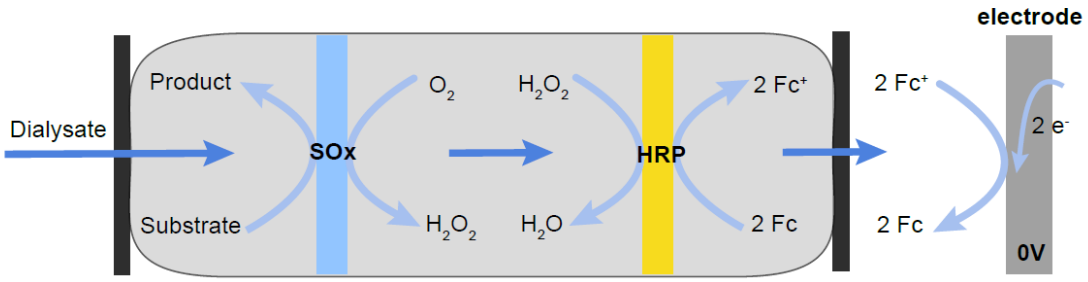

Figure 4.22: Reaction mechanism of reduction-based glucose detection

By pumping different reactors at different speeds, the mixture maintains different desired concentrations. The glucose concentrations sent to the microfluidic chip were respectively 100µM, 75µM, 50µM, 25µM, and 0µM, which are the standard values to calibrate a glucose sensor in TBI applications. The raw data and relevant processed calibration curve of the glucose sensor is shown in Figure 4.23. In the raw recording data (the mini graph in the figure), clear 200pA steps with 1nA baseline can be detected.

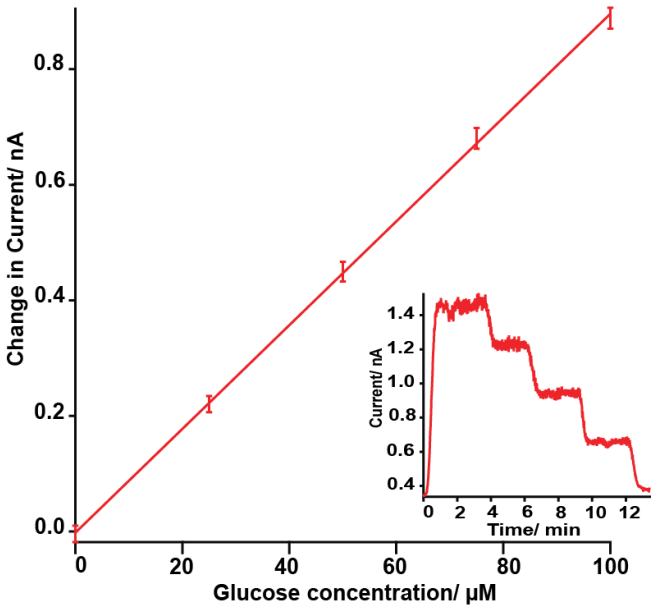

Figure 4.23: A biosensor calibration event conducted by the capacitive I-to-V system

The noise here is dominated by the flow variation caused by the microfluidic pumps.

4.3.5 Discussion

The DDC-based capacitive I-to-V conversion system has shown the capability to interact with current source, practical electrodes, and biosensors. Compared with a traditional resistive I-to-V conversion, the new approach shows much less noise and better SNR. In addition, the internal operation range selections make it more convenient and automated.

However, the DDC family also has its own disadvantages. The main shortcoming is that it can only detect positive current. One can achieve detecting negative current by shifting up the baseline of the measurement, however the ICs can only work in a certain offset, which may not be suitable for some applications. Therefore, the chip is only able to support any system based on reduction reactions, such as oxygen sensors and HRP-based glucose sensors.

4.4 Conclusion

This chapter has introduced two different approaches of measuring amperometric sensors for TBI applications. The first approach is the traditional resistive current-to-voltage conversion, based on the transimpedance circuit and potentiostat. The system is relatively easy to design. In addition, the system is capable of measuring bipolar current, which makes it possible to be applied in any amperometric measurement. The disadvantages are the noise and the cost, due to large-value resistors. A high-quality switch is also required if one wants to use multiple transimpedance gains.

Based on the issues in the resistive design, a capacitive current-to-voltage conversion system has also been designed and developed. The system utilises capacitors, instead of resistors, to accomplish the conversion, which significantly reduces the noise level and improves the overall system SNR. After a series of experiments, the system has been proved to be a reliable design for amperometric sensor measurement. However, it also has its own disadvantages, and the main issue is that it can only detect positive current, which means it can only work with reduction-based amperometric sensor system, such as oxygen sensors.

Chapter 5: Bio-potential Monitoring System Development for TBI Patients

This chapter describes the development of a low-noise high-precision electronic monitoring system, specially aiming at the detection of spreading depolarisation (SD) and seizure events with intracranial electrodes (strip and depth electrodes) and EEG.

5.1 Introduction

As discussed in Chapter 1, there are many classes of dynamic secondary insults to the injured human brain, and two important insults are SD and seizures [73]. To gain a better understanding of secondary brain injuries, several key parameters are being measured in the Intensive Care Unit (ICU). Many centers look at global parameters, such as intracranial pressure and blood pressure. In addition to these global parameters, King College Hospital also focus on local measurements, such as Electrocorticography (ECoG), tissue oxygen, and tissue temperature, as SD and seizure events (detected by ECoG signals) have been reported to correlate with poor patient outcome [17].

From the measurement with the existing system, we have characterised SD waves and seizure events by their electrical properties (Table 5.1) [18].

Electrical properties	ECoG strip electrode	ECoG depth electrode	EEG
frequency	Near DC – 100Hz	Near DC – 100Hz	3Hz – 100Hz
DC baseline	2 – 20mV	1 – 20mV	100µV – 10mV
AC signal	500µV	200µV – 2mV	50µV

Table 5.1: Electrical properties of SD

As the signals are very small and have a relatively wide frequency range, the challenge of this work is to develop a highly sensitive and low-noise electronic system for EEG recording, and maintain sufficient bandwidth and stability to allow near-DC or ideally DC recording of SD events. As the measurement baseline and signal strength vary among patients, the internal gain of the monitoring system should be programmable, to allow the system to be applied in different cases.

5.2 Existing monitoring system

The current monitoring instrument for ECoG signal acquisition, used in Kings College Hospital, is the Octal Bio amp from ADINSTRUMENTS. Octal Bio amp is an 8-channel pre-amplification system with built-in configurable filters. The device can be connected with PowerLab via an I^2C port, and configured from the LabChart. The key specifications are summarised in Table 5.2 [74]. In addition, the instrument has been approved to IEC60601 BF rated (body protection), which allows it to be connected to patients.

Octal Bio Amp Parameters	
Recording channels	8
Dimension	60mm × 300mm × 300mm
Power requirement	240AC
Weight	4kg
Power consumption	10W
Digital communication	I^2C port
Internal high-pass filter	first-order (±0.25% accuracy)
Internal low-pass filter	fourth-order Bessel (±3% accuracy)
Cut-off frequency	Software configurable
Detection range	±5V to ± 100mV (± 1.5% accuracy)
Isolation	4000 V_{rms}

Table 5.2: Key parameters of an Octal Bio Amp

The instrument provides a straightforward solution for bio-signal acquisitions, however, there are a few practical drawbacks when applying the instrument to do the clinical ECoG monitoring:

1. The instrument has an effective high-order low-pass filter, to eliminate high-frequency noise interference, whereas only a first-order high-pass filter to remove the DC offset. This high-pass filter can remove the offset and maintain the low-frequency components, such as the low-frequency component in EEG signals (~3Hz). However, when monitoring an ECoG signal (near DC), the high-pass filter will attenuate the signal when trying to remove the offset.

2. As the Bio amp is physically large and requires power from mains, it cannot be placed too close to the patient. As a result, the instrument is normally located about 2 meters away from the patient's bed, connected by long cables, carrying the detected brain potential (Figure 5.1).

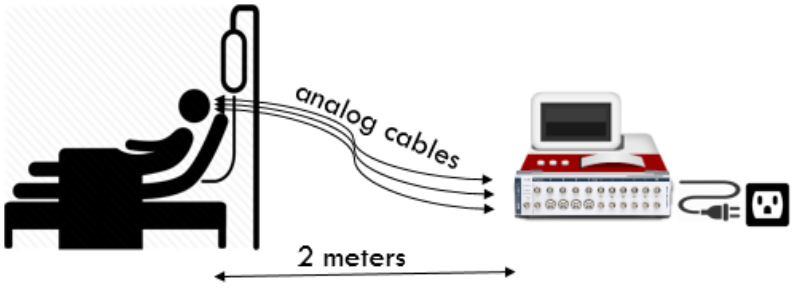

Figure 5.1: Previous clinical monitoring set-up

The Analog cables here refer to the cables that carry subtle analog signals from the brain.

3. The sterile electrodes used for measuring ECoG signals are manufactured to be mechanically safe and clinically clean, but they are not electronically shielded, which makes them very vulnerable to surrounding electrical noises. This is critical as these unshielded cables carry the most subtle signals from the patient's brain. If these signals travel too long in the unshielded cables before they go into processing electronics, the output signal will be largely affected by all the noise sources, especially in an electronically noisy environment, such as an Intensive Care Unit (ICU) and an operating theatre. In addition, the Bio amp is powered from mains, which inevitably introduce 50Hz noise interference, degrading the signal quality.

4. Another issue is that clinicians and researchers start to show interests in the DC characteristics and relevant physiological effects on TBI patients. Due to the built-in high-pass filter, this instrument is unable to obtain pure DC information.

Based on these practical issues, a new bio-potential acquisition system with more suitable experimental set-up, flexible detection range and DC coupled, has been designed and developed in the thesis[2]. The new system has been tested on standard lab instruments and human. In addition, the performance comparison test with the commercial monitoring device, Bio Amp, has also been conducted. The relevant data will be further discussed in later sections of this chapter.

[2] The actual PCB described in this section was designed by Dr. Kostas Papadimitrious in the group. My role in this design contains: generating initial design ideas, selecting relevant components, checking the PCB design, embedded programming on the FPGA, problem shooting, and conducting experiment discussed in the following sections.

5.3 Designing consideration for the new system

As discussed, I have developed the new system in two different functional parts: a head-stage analog board and a monitor-side digital board. The head-stage board works as an interface to ECoG electrodes, pre-amplifying the input signal, converting into digital form, and transmitting the digital data to the digital board via a 2-meter long cable. This analog board has been miniaturised to place close to the patient. The digital board stays at the monitor side, processing the incoming digital data from the analog board and updating the patient data on the monitoring laptop (Figure 5.2).

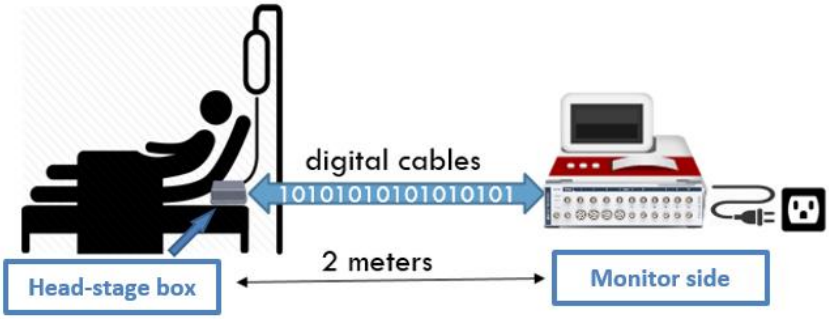

Figure 5.2: New clinical monitoring set-up

Since a PowerLab remains the main data recorder used in the hospital, which is also used for monitoring other parameters, this 2-meter keep-out distance cannot be shorten. However, if the data in the transmission cables are in digital form, which generates only “1”s or “0”s by thresholds, the transmission data will not be so vulnerable to the surrounding electrical noise. In addition, the analog board can be battery powered, which eliminates 50Hz noise interface from mains and protects patients from being electrocuted by any unexpected electrical failure through mains.

To optimise the signal quality, a low-noise high-precision and high-resolution analog-to-digital converter (ADC) is required. In addition, careful PCB layout and relevant shielding techniques are also essential to maintain a good SNR. Further design details will be discussed in the following sections.

5.4 Head-stage analog circuit board design

In this section, the PCB design and relevant essential application notes of the head-stage analog board will be illustrated.

5.4.1 Main chip selection for the analog board

ADC selection

The ADC used in the design is ADS1298 from Texas Instruments. ADS129x is a family of 24-bit, low-noise, low-power, multichannel, simultaneous sampling analog-to-digital converters (ADCs) with built-in programmable gain amplifiers (PGA). "x" indicates the number of monitoring channels in one chip. ADS1298 is highly integrated to offer 8 different monitoring channels with PGA (ranging from 1 to 12), and configurable sampling rates from 250 to 32K sample per second (SPS) [75]. Each channel can be enabled or disabled with individual gain selections. In addition, multiple ADS129x chips can be cascaded together to achieve more than 8-channel data processing. This cascaded configuration and application details will be further discussed in Chapter 8.

Furthermore, another key feature of the chip is that it can be powered up/down by either physically connecting/disconnecting the power pin or receiving a "start"/"end" operation code from the controller. This feature allows the user to control the head-stage box by sending "start" or "end" operation code from the main controller in the instrument box, eliminating the necessity of installing a power switch on the head-stage box.

ADS1298 can operate with either unipolar or bipolar power supplies, as long as rail-to-rail power supply, V_S, does not exceed 5.5V and digital power supply, V_{DD}, is less than 3.8V. It also features internal voltage reference and a built-in oscillator, to save external components and PCB space. The common-mode rejection ratio (CMRR) is -115dB, which means the common-mode noise can be significantly attenuated in the measurement, and therefore maintain a better SNR. In addition, the input-referred noise in 0-150Hz bandwidth is 4 μV_{P-P}. Based on the digital conversion (Table 5.3) in the datasheet [75], the detection limit with respect to the ADC resolution is $V_{REF} / (2^{23} - 1) = 0.5\mu V$ (as V_{REF} is 4V). Compared with Table 5.1, it shows the device is more than sufficient for detecting different essential bioelectrical potentials.

Input signal, VIN (AINP - AINN)	Ideal output code
≥ VREF	7FFFFFh
+ VREF / (2^{23} - 1)	000001h
0	000000h
- VREF / (2^{23} - 1)	FFFFFFh
≤ - VREF (2^{23} / 2^{23} - 1)	800000h

Table 5.3: Input signal versus ideal output code when the gain is 1.

As for digital communications, ADS1298 supports SPI configuration and provides an additional DVAILD (interrupt) pin to inform the controller, when there is a new set of data available. The SPI timing and data input/output sequence can be found in the datasheet, which will be further discussed in the coding section.

Front buffer selection

The front units before ADS1298 are the input buffers and pre-amplification stages. Low-noise, low-offset, and low-power op-amps are desired in this phase, to buffer in the raw ECoG signals from the electrodes and amplify them to achieve better detection resolution in the following digitalisation phase. Normally, a standard ADC only has input impedance of 30kΩ - 500kΩ. Without applying a buffer, the impedance of the ADC is not large enough to load the input voltage.

The chip used in this design is a chopper amplifier, AD8629, from Analog Devices. It applies a combination of auto-zeroing and chopping techniques, which utilises an internal oscillator to switch between two different op amps to continuously balance out the offset [51, 52]. As discussed in Chapter 2, this method allows the chip to maintain very low offset voltage over a wide temperature range and throughout their operating lifetime. In addition, 1/f (flicker or pink) noise, the major noise source in low-frequency measurement, has been significantly reduced by applying the auto-zero op amps. 1/f noise appears as a slowly changing offset to the inputs of AD8629, and the auto-zero feature corrects any dc or low frequency offset. The schematic of the buffer and pre-amplification stage is shown in Figure 5.3. As all the channels have the same schematic, only one channel is shown below. A 100k isolation resistor is placed between the electrode and the positive input terminal of the op amp, to ensure the patient safety, which will be further discussed in Chapter 6.

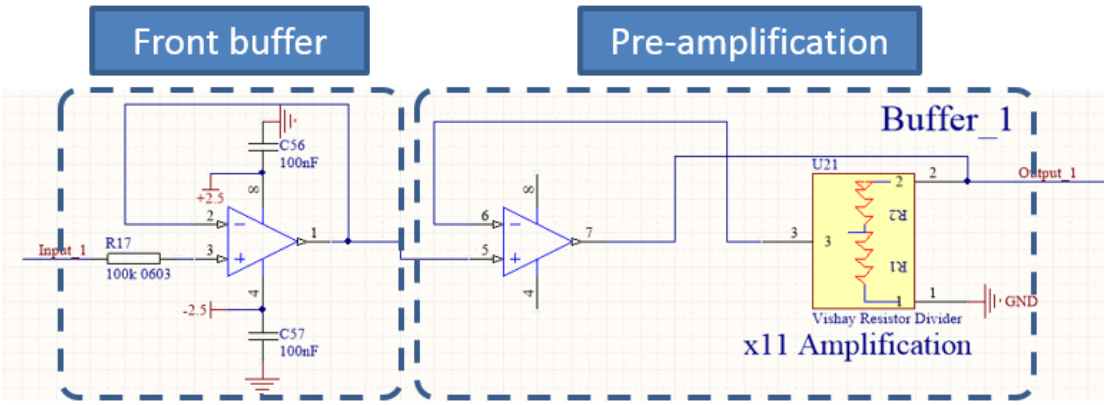

Figure 5.3: Schematic of the front buffer and pre-amplification stage

Digital isolator selection

Another key component used in this design is a digital isolator, which is used for preventing any unexpected large voltage/current from the digital transmission lines. The one used in this design is Si8652, from Silicon Labs. Si8652 is a low-power 5-channel digital isolator, supporting high-speed operation up to 150M bit per second (bps) with typical 10ns propagation delay. Each channel employs an RF transmitter and receiver, which is separated by a semiconductor-based isolation barrier [76]. This modulation scheme provides up to 5K V_{RMS} isolation (with IEC60601-1 safety regulatory approval), which is enough to block any unexpected large incoming voltages, as well as maintain normal digital communication.

5.4.2 Head-stage analog board circuitry design and PCB layout

In this section, the circuit design and relevant PCB layout of the analog board will be discussed.

ADS1298 circuitry implementation

ADS1298 offers the option of selecting different reference voltages for different input channels, however in the TBI application, all the input signals refer to the same point. Therefore, all the negative input ends are tied together, connecting to the common reference point.

To eliminate high-frequency noise interference and compensate fast-changing current in the IC, each power pin is connected in parallel with a 0.1µF and a 10µF de-coupling capacitors to the ground. Even though 10uF and 0.1uF in parallel is equal to a 10.1uF capacitor, according

to the frequency response of a capacitor, discussed in Chapter 3, the parallel design works better than a single summed decoupling capacitor.

As mentioned above, ADS1298 can be activated by either physical power connection or operation code. This feature is controlled by an external pin, START. If the START pin is tied HIGH, the chip will automatically run in the default mode once it is powered up. However, if the START pin is LOW when it is initially powered, the chip will stay in the sleep mode, until a certain operation code is detected. To investigate the feature, the START pin has been connected to a three-way header, which allows users to select between these two modes. The details about how to initialise ADS1298 communication will be further discussed in the ADS1298 coding section.

Power Management

Three different Power regulators have been applied in this design, and they all get power from the same power supply, +4.8V (4-AA battery pack). They generate respectively +2.5V, -2.5V, and +3.3V. Among them, ±2.5V are used for the analog circuitry, while +3.3V is the power for the digital supply to the ADS1298 as well as the digital isolator. Since the digital power supply is inherently noisy due to the high-frequency data transmission, these power circuits have been placed separately and restricted to different grounding systems.

TPS7A7001 has been used to obtain +2.5V from the standard +4.8V power supply. It is a high-performance positive low-dropout (LDO) voltage regulator, with configurable output voltages. In addition, the chip has a physical “enable” pin, which allows users to control the regulator and its powered circuit, if power sequencing is required. Furthermore, an internal temperature sensor is integrated to provide the thermal shutdown function, avoiding any extra damage due to unexpected electrical failure or high temperature. The input voltage ranges from 1.425 voltage to 7V, and the equation of the output voltage and relevant schematics are shown in Figure 5.4. This equation for the output voltage is described as,

$$V_{OUT} = 0.5 \times (1 + \frac{R_1}{R_2}) \tag{5.1}$$

High-quality resistors with low temperature coefficients have been used to generate an accurate ratio of R1/R2 as 4, and therefore yields the output voltage as 2.5V.

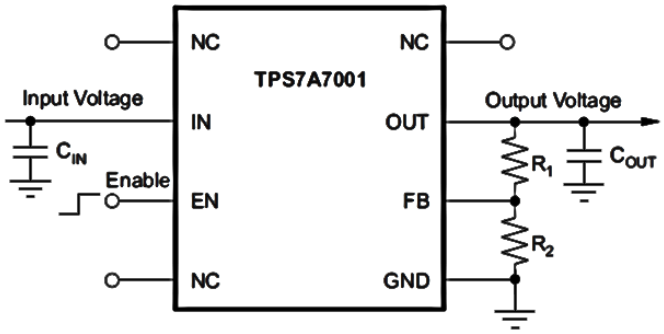

Figure 5.4: Schematic of TPS7A7001

The figure is extracted from [77].

The same chip and schematic have been also applied to obtain the digital 3.3V power supply, and the only difference is the R1/R2 ratio. To get 3.3V output, the ratio needs to be 5.6. By searching for the available precision resistors in the market, 30.1K and 161K resistors have been used in this design.

A normal linear regulator is not viable to obtain -2.5V from a +4.8V. An inverting voltage regulator with programmable outputs, LT1611 from Linear Technology, has been applied in this case. The chip has very low noise (1mV$_{P-P}$ output ripple) and low output impedance (0.14Ω). The chip also features a shut-down function, which is activated if the input voltage is higher than 10V. The schematic for implementing LT1611 is shown in Figure 5.5. By tuning the value of R1 and R2, different output voltage can be obtained, based on the equation:

$$\mathrm{R1} = \frac{|V_{OUT}| - 1.23}{\frac{1.23}{R2} + (4.5 \times 10^{-6})} \tag{5.2}$$

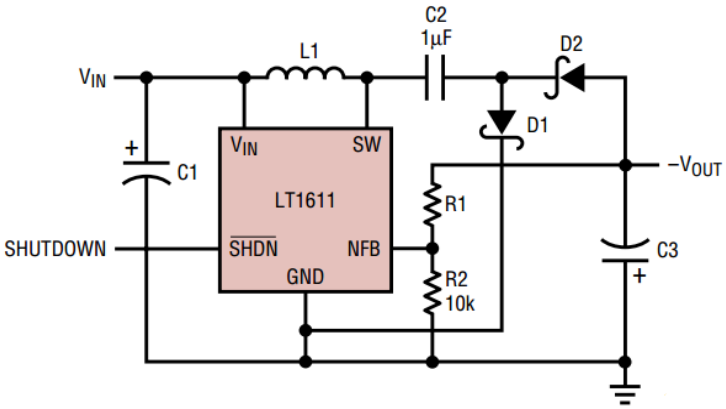

Figure 5.5: Schematic and output voltage equation for LT1611

The figure is extracted from [78].

To get -2.5V output, the R1 and R2 have been chosen as both 10K (with 0.1% tolerance). As the inverting regulator utilises an internal oscillator running at 1.4MHz, the output voltage can contain serious oscillation (output ripple). As the datasheet indicates, increasing the inductance of L1 lowers the ripple current, which effectively smoothens the output voltage ripple. In addition, decreasing the equivalent series resistance (ESR) of the output capacitor, C3, can also degrade the output voltage ripple.

PCB Layout

As demonstrated in Chapter 3, the analog and digital circuits have been placed separately. Significant overlap between analog and digital circuits, including both components and their relevant traces, have been eliminated. To avoid the signal cross talk, two different ground planes have been created, and these two planes only joint at one single star point. Each ground plane creates a small-impedance area for its own current flow. The single joint point effectively minimises the interference between the digital and analog circuitry. Furthermore, different power planes have also been introduced, such that digital switching leakage current would not affect the analog circuitry.

As the input signals are small and sensitive, a small portion of power leakage will be likely to affect the signal. For example, if -2.5V supply trace is placed close or underneath the input signal traces, the AC component (in mV level) of the -2.5V power supply is likely to couple into the input signal (hundreds μV) via parasitic capacitors between traces and layers. The subtle input signal will be heavily distorted by this interference and cannot be restored in the following process. Therefore, the input traces should run orthogonally to the power traces with ground plane in between. The orthogonal routing is able to minimise capacitive coupling, and the internal ground plane also becomes an electrical shield.

In addition, the stray capacitance introduced by the ground plane at the input increases the op amp's input capacitance, which decreases the phase margin and therefore may cause instability. Therefore, no nets on the ground or power plane should be placed under or close to the input area, to maintain a good SNR and stability. Figure 5.6 shows the PCB layout in the software, and indicates different functional parts and the considerations of the relevant trace placement.

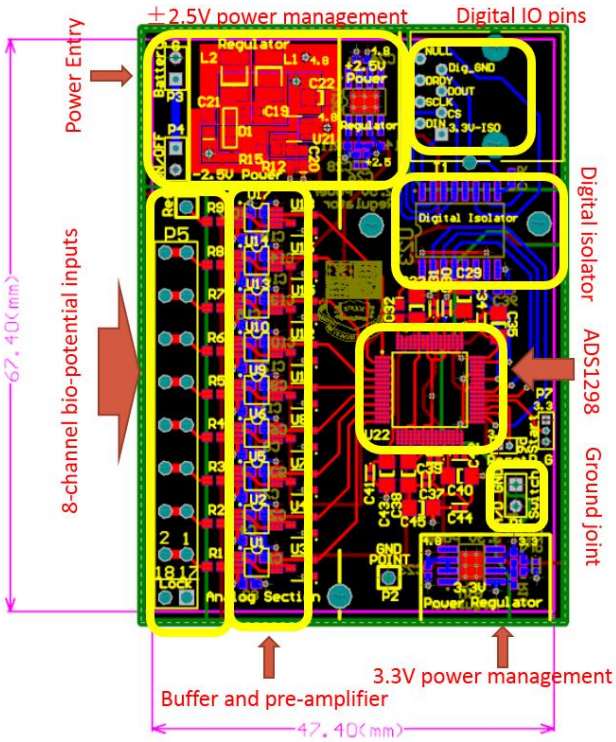

Figure 5.6: PCB layout of the analog board

Main functional parts have been labelled in the figure. The overall dimension of the board is 67.4mm × 47.4mm.

Overall signal flow chart

In summary, Figure 5.7 shows the signal flow from the electrode interface, to pre-amplifiers, high-precision ADC, and eventually through the digital isolator to the digital board.

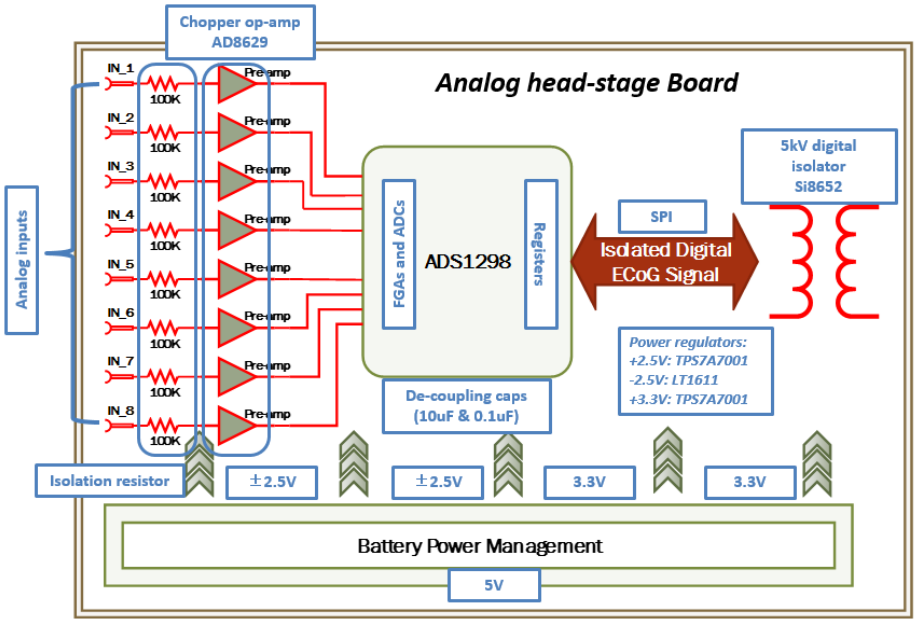

Figure 5.7: Signal flow on the analog circuit board

5.4.3 ADS1298 coding

After designing the analog board, the remaining task is to configure ADS1298's registers to make it function as desired. As the datasheet indicates, the chip will go into configuration mode when it is initially powered up or receives a "RESET" command. The flow chart in the configuration mode is shown in Figure 5.8.

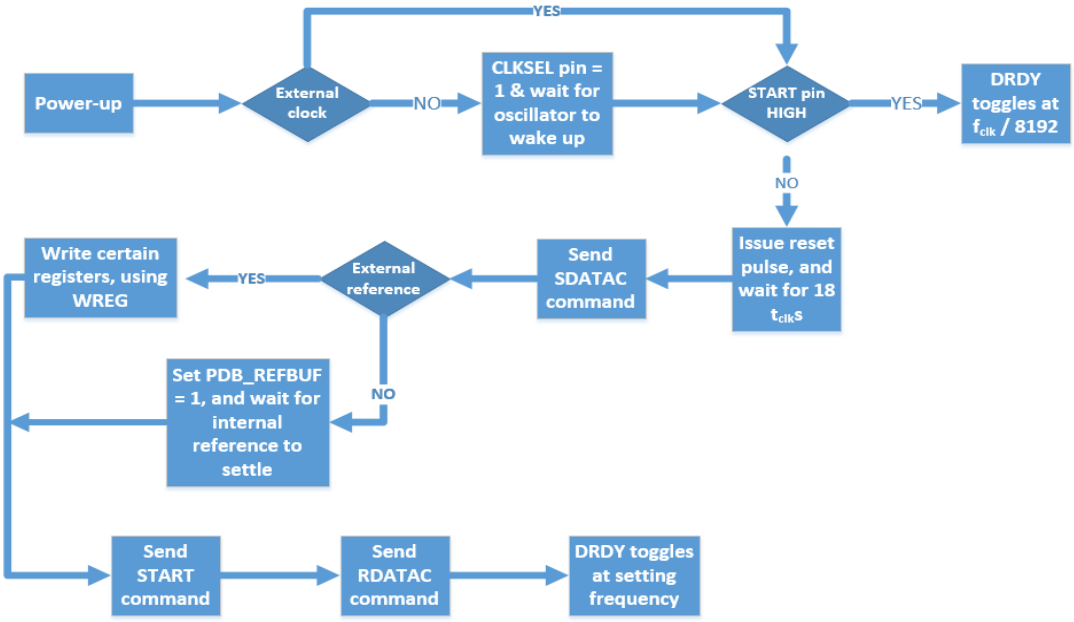

Figure 5.8: ADS1298 power-up sequence

The code needs to be loaded in such an order to successfully communicate with the registers. Three different types of operational commands are available in ADS1298, which are summarised in Table 5.4.

Type of commands	Length (byte)	commands
System	1	WAKEUP, STANDBY, RESET, START, STOP
Data read	1	RDATAC, SDATAC, RDATA
Register read	2	RREG, WREG

Table 5.4: Operational commands in ADS1298.

If ADS1298 receive 2-byte commands as "01000011 00000001", the chip will address at 03h (CONFIG3), as the last 4 bit of the first byte (0011) indicates. The first 3 bits of the first byte indicate whether it is a reading or writing command. If it is "010" is writing command, while "001" is the reading command. In this case, it is a writing command. In addition, the last byte is "00000001", which is corresponding to 1 in decimal, meaning that the number of registers is 1 + 1 = 2. Therefore, after receiving the 2-byte data, ADS1298 will locate at register CONFIG3 (03h), and start to write to the following 2 registers, including CONFIG3 itself. The details of all the commands and their relevant operational code can be found in the datasheet page 38 [5].

ADS1298 register configuration

As the flow chart shown previously, the actual program loading sequence is:

RESET (00000110) → SDATAC (00010001) → WREG_3 (01000011) → one_register (00000000) → CONFIG3 (11100001) → WREG_1 (01000001) → two_register (00000001) → CONFIG1 (11000000) → CONFIG2 (00000000) → WREG_5 (01000101) → eight_register (00000111) → channel_gain_1 (00010000) → channel_gain_1 (00010000) → channel_gain_1 (00010000) → channel_gain_1 (00010000) → channel_gain_1 (00010000) → channel_gain_1 (00010000) → channel_gain_1 (00010000) → channel_gain_1 (00010000) → START (00001000) → RDATAC (00010000)

By loading these settings, ADS1298 works in the high-resolution mode, 500 samples per second (SPS), daisy-chain and clock output disabled, with enabled internal 4V reference voltage. All the 8-channel internal amplifier gains have been set as 1, which was 6 by default. The setting can be altered for different applications, and the details can be found in the datasheet [75].

ADS1298 SPI communication and data format

ADS1298 communicates via SPI, and it works in different SPI modes between reading and writing data. When writing data to the ADS1298 registers, the chip latches data on DIN pin at the falling edge of the SPI clock (SCLK). When reading data from ADS1298, data on DOUT are shifted out on the rising edge of the SCLK.

When ADS1298 has a set of new available data, it turns DRDY pin low, and wait for the communication to be initialised. Once the communication has been set up by the controller, DRDY pin will become high at the first falling edge of the SLCK. By this configuration, DRDY signal should be regarded as the main interrupt signal, informing a set of new data. Once the controller detects this falling edge of DRDY, it should turn the CS pin low and initialise the data transmission.

A full set of data contains 216 bits, 24-bit commands and 8-channel 24-bit data. During one data transmission, the chip always transmits most significant bit (MSB) first. The data format is 2's complement, which indicates that the positive maximum voltage is presented as 7FFFFFh and the negative maximum voltage is presented as 800000h (Table 5.3).

Key notes of debugging ADS1298

Followed by the loading sequence, one should be able to communicate with ADS1298 registers. The quickest way to figure out whether the communication is successful is to alter

the device sampling rate. As shown, the time for DRDY pin to issue a falling-edge interrupt signal is totally determined by the device sampling rate. By changing the sampling rate, ranging from 250SPS to 32kSPS, one should be able to check the timing from a digital oscilloscope. According to the datasheet, once the ADS1298 issues a DRDY falling edge to indicate that there is a new available data, DRDY pin will stay low until the first rising edge of SCLK. However in practice, if the SPI communication has not been set successfully, the DRDY pin will stay low until the next available data. Since the device requires to send a falling edge of DRDY at this point and the current DRDY is still tied low, due to the absence of SPI communication, ADS1298 will quickly issue a pulse (rising edge + falling edge) (Figure 5.9).

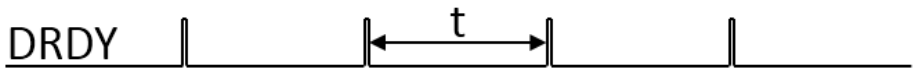

Figure 5.9: DRDY response when no SPI communication

When the digital communication has not been set up, DRDY still issues falling edges, following the pre-set timing. However, it only issues a pulse rather than a falling edge, as there is not a SCLK action to turn DRDY high.

If the SPI has not set up as desired, a few steps can be considered for fast debugging:

a. If one cannot see the DRDY pulse shown in Figure 5.9, this means the device has not been activated. The problem can be the malfunction of power supplies, RESET pin tied low, or START pin tied low;
b. If the pulses in Figure 5.9 can be seen but the period (t) cannot be changed, then it indicates the SPI communication has not been successfully set up. The SPI timing and register loading sequence may be the main problems. As the datasheet shows, command data needs to be sent at the falling edge of the SCLK, and the CS pin needs to be tied low during a complete SPI transmission;
c. If DRDY pulses can be seen and altered, this means the SPI communication link has been activated when sending data to ADS1298 registers, however it breaks when retrieving data from ADS1298. In this case, the problem is likely to be the DRDY interrupt and the data retrieval timing. The microprocessor needs to initial the transmission, once it detects the DRDY drop. The communication cannot be set if the microprocessor fails to do so.

In addition to this, every bit of data needs to be retrieved at the rising edge of the SCLK, and totally 216 SPI clock cycles require to be issued for one complete transmission.

If the microprocessor is required to program the register setting to ADS1298 once it is powered up, the targeted ADS1298 needs to be powered first, as the internal oscillator needs 1-2 seconds to wake up. After obtaining digital data as the datasheet indicates (Figure 5.10), a successful SPI communication has be built.

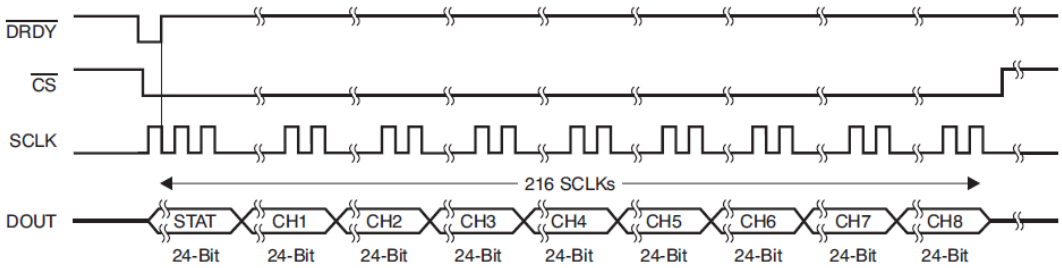

Figure 5.10: Successful SPI digital data output

The figure is extracted from [75].

5.5 Monitor-side digital circuit board design

The analog circuit board has been previously demonstrated, and the relevant digital data should be retrieved on the digital board. In this section, the monitor-side digital circuit board design will be discussed. As for the main data processor, it is the same FPGA demonstrated in Chapter 4. The main difference is the output digital-to-analog converter (DAC) and relevant pin mapping.

5.5.1 DAC selection

This design requires a digital-to-analog conversion stage, as the main data recording device (PowerLab) only receives analog signal. The one used in this design is AD5362, from Analog Devices, which features 8-channel 16-bit resolution, with SPI compatible interface and built-in thermal shutdown function. The output voltage ranges from -10V to +10V, which is the same as PowerLab. As for digital communication, AD5362 works with 2.5V to 5.5V digital interface, which makes it possible to communicate by either 3.3V or 5V logic level. In addition, AD5362 allows users to set different offsets and gains, by configuring its register. Each power pin has been decoupled by two capacitors (10uF and 0.1uF) in parallel, similar to the ADS1298 set-up.

5.5.2 PCB layout and layer explanation

The PCB used for the digital board design also contains 4 layers: top signal layer, ground plane, power plane, and bottom signal layer. The board receives in the transmitting digital data from

the analog board, passes them to the FPGA, processes the data, and eventually sends them to the output DACs. There are two identical DACs on the digital board, so it can support up to 16-channel outputs. As the feature of FPGA, both DACs are running in parallel, and there is no delay on updating incoming data between two chips. The overall dimension of the digital board is 107.4mm × 137.4mm (Figure 5.11).

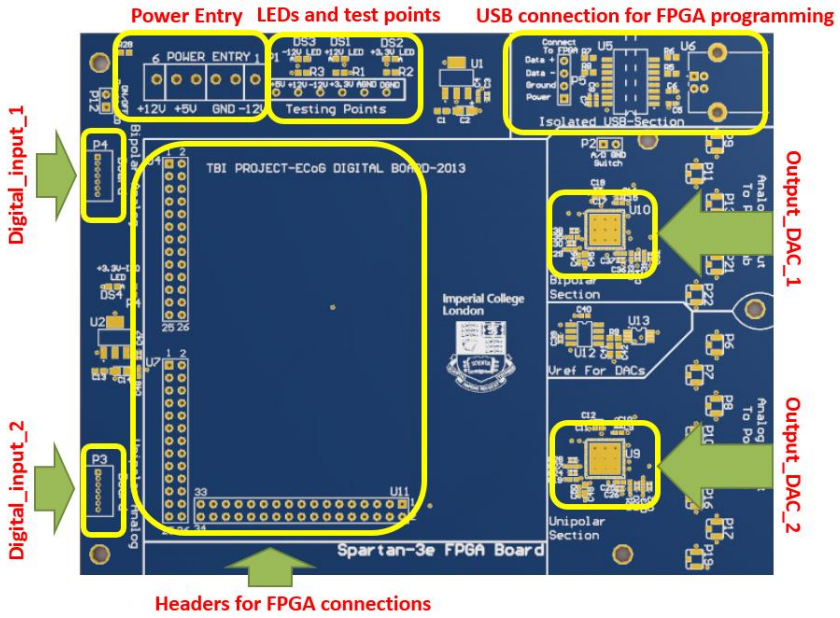

Figure 5.11: PCB layout of the monitor-side digital board

The dimension of the digital board is 107 × 137 mm^2. It can support two sets of seperate digital transmissions, from "digital_input_1 and "digital_input_2". The analog output can be delivered from either "output_DAC_1" or "output_DAC_2".

5.5.3 AD5362 coding notes

AD5362 also employs the SPI protocol for digital communication. In addition to general application notes for SPI, like timing and CS control, several extra features have been added to AD5362. The DAC supports both offset binary and 2's complement coding, which can be selected from an external pin, BIN/2COMP. Since the incoming digital data from ADS1298 are based on 2's complement, AD5362 has been configured to work in 2's complement data mode as well. As the offset and gain can be programmed, the SPI communication for AD5362 offers the option to write/read to its input data registers or its function registers. The same input digital data can be updated to all the output channels, one bank of the outputs (4 channel), or an individual channel. The chip also features a BUSY pin, to indicate that the chip is currently working on internal data processing, and unable to accept any new incoming data.

The input data for AD5362 contain 24 bits, 2-bit command (M1 & M0), 6-bit address (A5-A0), and 16-bit data (D15-D0). The functions of the control bits are shown in Table 5.5.

M1	M0	Action
1	1	Write to DAC data register
1	0	Write to DAC offset register
0	1	Write to DAC gain register
0	0	Special function, used with other bits

Table 5.5: AD5362 command bits

The address map can be found in the datasheet [79], the detailed channel mapping is attached in the appendix 5.1. As the input data from ADS1298 has 24-bit and AD5362 has only 16-bit resolution, the last 8 bits are discarded. However, the full 24-bit data are still retrieved and restored in FPGA for future applications.

5.5.4 Power selection

As the digital board is at the monitor side, the overall size and power consumption are not as important as in the analog board. However, the safety of using the instrument becomes the major consideration. Since other equipment used at the monitor side are powered from mains, the digital board has been also designed to obtain power from mains. To ensure safe operation, a medical-grade AC/DC converter has been applied. The one used in this design is LPT50-M, from Artesyn Embedded Technology, which is a triple-output (±12V and 5V), 55-watts medical-grade AC/DC converter.

The converter has very wide input range (90-264 VAC), and high converting efficiency (80% at full load). With built-in electromagnetic interference (EMI) filter, it provides electronically quiet power supplies. As for safety, the converter features with overpower (30-50% above nominal output voltage) and short-circuit protections on all the outputs [80].

5.6 Initial bench test

In this section, I will mainly discuss the initial experimental tests, results, and relevant issues.

5.6.1 Experimental set-up

After designing all the parts, the initial validation experiment has been conducted in the lab. The analog board and the digital board have been intentionally separated and connected via

a 2-meter RJ45 digital cable, in order to simulate the practical clinical environment (Figure 5.12). The input signal is simulated by a signal generator, and the end data recorder is PowerLab, which is the same model as the one being used in the hospital. A signal generator has been used to simulate a standard sine wave with different frequencies and amplitude. The analog board is powered by a bench DC power source, and the digital board is power by the AC/DC converter discussed above.

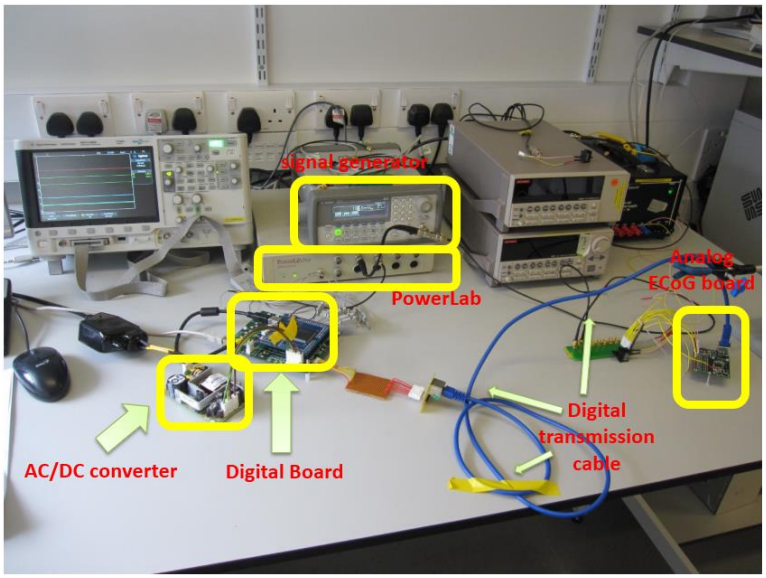

Figure 5.12: Initial experimental set-up

5.6.2 Digital code debugging with Xilinx simulator

To ensure all the FPGA I/O pins to perform as desired, a simulator is used to mimic its digital communication. When receiving a periodic input trigger “DRDY”, all the sub-sequential processing should be activated. The simulator window shows the behaviours of all the relevant pins, as well as the pre-set incoming 216-bit ADS1298 data (Figure 5.13).

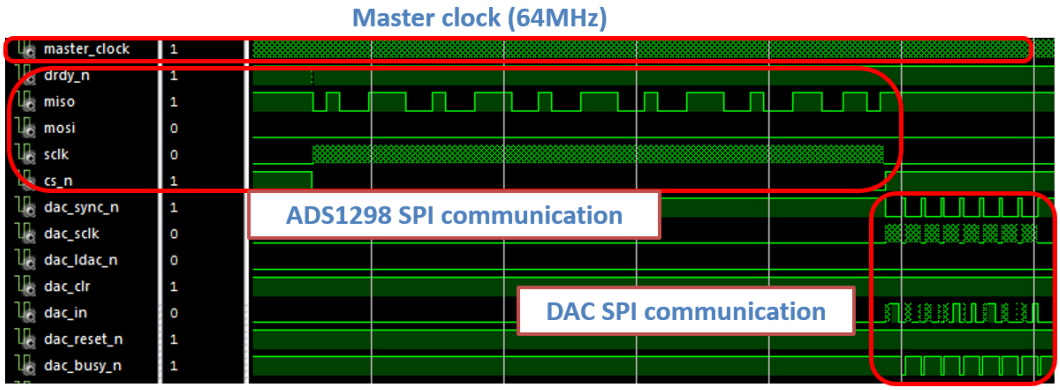

Figure 5.13: Simulated results for the system

The first line is the main clock signal, which operates at 84MHz. The lines from 2nd line (drdy_n) to 6th line (cs_n) are digital data for ADS1298 SPI transmission. The lines from 7th onwards are the SPI communications for the DAC.

The overall simulation speed follows the master clock ("master_clock"). The result indicates the FPGA will response by the time it detects a DRDY ("drdy_n") falling edge, issues the ADS1298 CS pin ("cs_n") low, and then initialises the SPI communication ("miso" and "sclk"). After retrieving a complete set of data, FPGA processes this 216-bit data, and allocates them to individual channels. After the data assignment, every last 8 bits of each 24-bit data are discarded and re-assign a new 8-bit data, which are the command and address bits. Initialising the DAC SPI transmission by turning the DAC CS pin ("dac_sync_n") low, the new set of processed data ("dac_in") will be transmitted to the output DAC. After loading one-channel data to the DAC, it is required to toggle the BUSY pin (dac_busy_n) as a loading delay. After the DAC SPI transmissions for all the channels, the FPGA circles back to the waiting loop and stays idle, until the next DRDY falling edge comes.

5.6.3 Initial tests, relevant results, and issues

After setting up the experiment and testing with the simulator, the code should work for at least basic SPI communication. To simplify the debugging process, all the input channels have been tied together and connected to the signal generator. During the test, the generator outputs a pre-defined sine wave. As Figure 5.14 shows, the output signal has a readable sine wave shape, but with full of spikes.

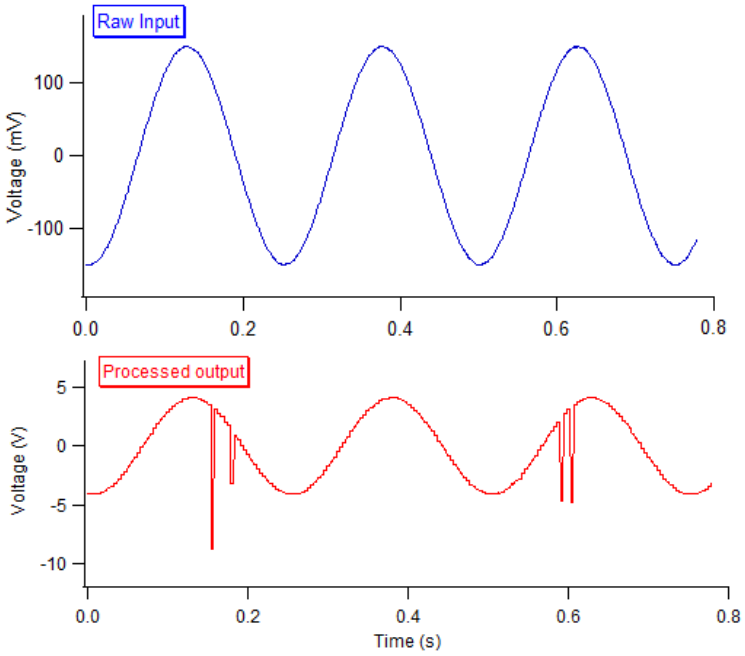

Figure 5.14: Initial data with spikes

The upper graph is the raw input with 300mV$_{p-p}$ and 0V base line. The lower graph shows the output from the system. This is the initial data, which contains spikes. The issues will be investigated in the following sections.

Judging from the data, the device has the ability to digitalise the data and restore them back to analog and show on the display, via PowerLab. This means the SPI communication has been built for both the ADC and the DAC sides. In addition, the frequency of DRDY can be altered by loading different codes to ADS1298's registers. This fact also indicates that the SPI communication has been set up. As if the spikes are due to analog communication, they should appear at any voltage level. To investigate where these spikes come from, three different sources are taken into considerations:

a. It comes from the ADS1298 itself, due to the faulty digitisation at some points.
b. It results from the malfunctioned output DAC when it tries to convert good digital data back to analog.
c. It comes from the intermediate communication, which involves physical connections, software coding, and timing.

5.6.4 ADS1298 debugging with Arduino DUE

As the system has two different function parts, this makes the debugging process easier, as each part can be examined separately. To investigate the first possibility, the analog board has been connected to an Arduino DUE development board. The main microprocessor of the

Arduino DUE is SAM3X, which is an ARM-based processor, and the details will be further discussed in Chapter 8.

The fundamental reasons of using this board to debug the analog board are that the SAM3X on Arduino DUE board is the high-performance processor and it supports 3.3V SPI. If a 5V processor had been used, an extra logic level shifter would be applied to convert the signals between 3.3V and 5V. Another key factor of using the Arduino product, is that the Arduino integrated development environment (IDE) is relatively easy to use and it has built-in serial monitor, which allows users to see the digital data on the screen. In addition, the programming language has been developed in JAVA, but it allows users to use C or C++ to program.

Based on the same ADS1298 programming flow chart, a new C language code has been generated on the Arduino IDE to debug the analog board (Appendix 5.2). By applying this code, ADS1298 is capable of digitalising all the 8 channels and transmitting the relevant digital data to the Arduino DUE. Once it retrieves a full set of data, it will update them in the serial monitor on the PC. By checking the digital data and manually converting them back to analog based on the given table, every channel follows its own analog inputs without any data distortion or spike.

5.6.5 Output DAC debugging with Arduino DUE

Followed by the ADS1298 debugging, the digital board without the FPGA has been also connected to an Arduino DUE board, in order to check if the spikes come from the DAC side. By sending the code with pre-set value (Appendix 5.2), the DAC on the digital board can response to its loading digital data, without distortion or spikes. Furthermore, the analog board and the digital board are connected together, controlled by the Arduino DUE, instead of the FPGA. The data of this set-up is shown in Figure 5.15, and the signal is clean without any spikes. In addition, by manipulating the ADS1298's register setting, the sampling rate and internal gain of each channel can be altered. As the debugging process goes, possibility (a) and (b) have been eliminated.

More importantly, the main ICs and the extra debugging development board (Aruidno DUE) have been validated. The figure is the raw data captured from LabChart 7, used for demonstration only.

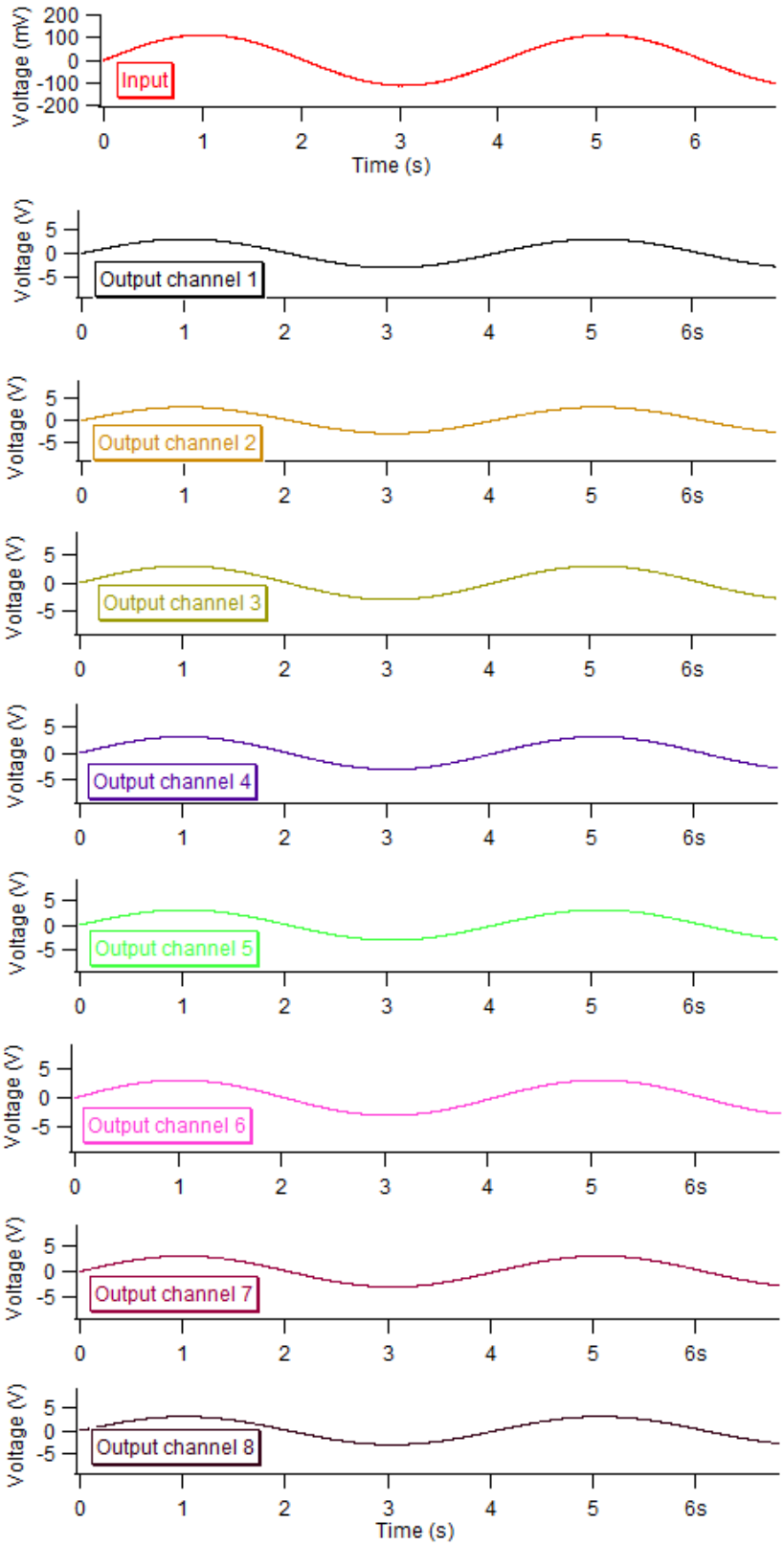

Figure 5.15: Test result with Arduino DUE

Clean sine waves from the Arduino DUE-based testing set-up, with the same ADC (ADS1298) and DAC (AD5362). Channel 0 (Input) is the raw input signal, ±110mV and 0.25Hz, and signals from channel 1 to 8 are the corresponding output signal after processing in the system. The output has the same pattern and frequency response as the input. The amplitude of the output is ±3.025V.

5.6.6 Physical wiring checking

As discussed above, both the analog board and the output DACs have been approved to work properly. Therefore, the remaining potential problem are electrical wiring and VHDL code. When checking the electrical wiring, a standard multimeter with the connectivity testing function is preferable. Whenever doing an electrical test, an engineer has to potentially trust his/her tools. If the tools malfunction without being noticed, the testing result will be wrong. Furthermore, early wrong results will lead the engineer down wrong arm of a decision tree, which makes the debugging process even more misleading and time-consuming. A good habit is to always test it before trusting it, and use the things one has tested to do further testing. Take the connectivity test as an example: always test the multimeter by touching the 2 pins, and see if it functions before starting to test other connections. When checking the connectivity, several additional points need to be considered:

a. The two probes should cover as much distance as possible. For example, when testing a connection between two integrated circuits (ICs), the probe should softly touch the leg of the IC, instead of the pad, as this helps to check the soldering quality as well.
b. Do not push the probes down when doing the test, as it can force a faulty connection between the leg and the pad even if they are not well soldered.
c. Check the connectivity of the device when it is not powered up. The operating principle of the connectivity test is by poking a little voltage into the circuit and seeing how much current flows through two probes. If there is already voltage in the circuit, the test may not be correct.
d. A standard multimeter is not able to distinguish small resistors (less than 100Ω) or inductors, as these components behave as short circuits, like wires, to a multimeter. When hearing a “beep” sound, it does not necessarily indicates the two points are connected.
e. If the beep sound is not continuous, it means the two points are connected, but the connection is bad. This normally introduces unwanted noise and measurement error, which should be avoided when soldering the components.

5.6.7 VHDL code debugging

After thoughtful electrical connection testing, the spikes still exist in the output signal. The main potential problem remained the VHDL coding. Since Texas Instruments haven’t published any document or solution related to the spike issue, the detailed debugging process is discussed in the thesis for further reference.

By checking the digital data from the digital oscilloscope, and working on different code combinations, the problem has been finally located at the ADS1298's CS control. In the previous code, the CS command is right after the FPGA detects a DRDY falling edge. However, as VHDL code is running in parallel in a very high speed (64MHz) and this pin activation command is too close to the DRDY interrupt, this line of command can be overlooked by program frequently. This means the FPGA SPI communication is still active without turning CS pin low. Therefore, it cannot retrieve any useful data from the ADS1298, as the DOUT pin on the ADS1298 has not been enabled due to CS tied high. In this case, the incoming data will be either all "1"s or "0"s, depending on the last bit of DOUT of the last successful transmission. This explains why the spikes only go to ground or the power rails in the analog domain.

By introducing an additional internal variable, a flag, which executes faster than a physical pin command, the code is capable of capturing every DRDY falling edge, and therefore the spikes have been removed. This timing problem seems to be insignificant, but it can be fatal to the output results. In addition, as simulator is only capable of mimicking ideal situations, one can hardly spot this problem from the simulation. Many trials and tools have been applied to spot this "tiny" bug in the system. The clean data and relevant analysis will be discussed in the following sections.

5.7 Performance test in lab

After a series of debugging processing, the system starts to run properly, and various tests have been conducted to evaluate the performance.

5.7.1 Gain response of the system

As demonstrated, each channel of the system has 4-stage gains, 2 of which are programmable. The first gain is from the front buffer amplifier, which introduces a fixed gain as 11. The second-stage gain is controlled by the internal programmable amplifiers in the ADS1298, which can be set from 1 to 12. The third stage gain is fixed, due to the reference voltage ratio between the input ADC and the output DAC. By providing different reference voltages, the same digital code can represent different analog values. The reference voltage of ADS1298 is 4V, and that of AD5362 is 10V.

Therefore, a gain of 10/4, 2.5 is inevitably added into the system. The last gain stage is from the output DAC, which is also programmable. Based on these factors, the overall gain can be calculated as:

$$G_{overall} = 11 \times G_{ADS1298} \times 2.5 \times G_{AD5362} = 27.5 G_{ADS1298} G_{AD5362} \quad (5.3)$$

When setting the gains for both ADS1298 and AD5362 as 1, the overall minimum gain of the system is therefore 27.5. Figure 5.16 shows the amplitude response, which follows the theoretical system gain. The input from the signal generator is a 0.8Hz and 120mV$_{P-P}$ sine wave, the processed output follows the same sine pattern with 3.3V$_{P-P}$, which yields the amplification as 27.5.

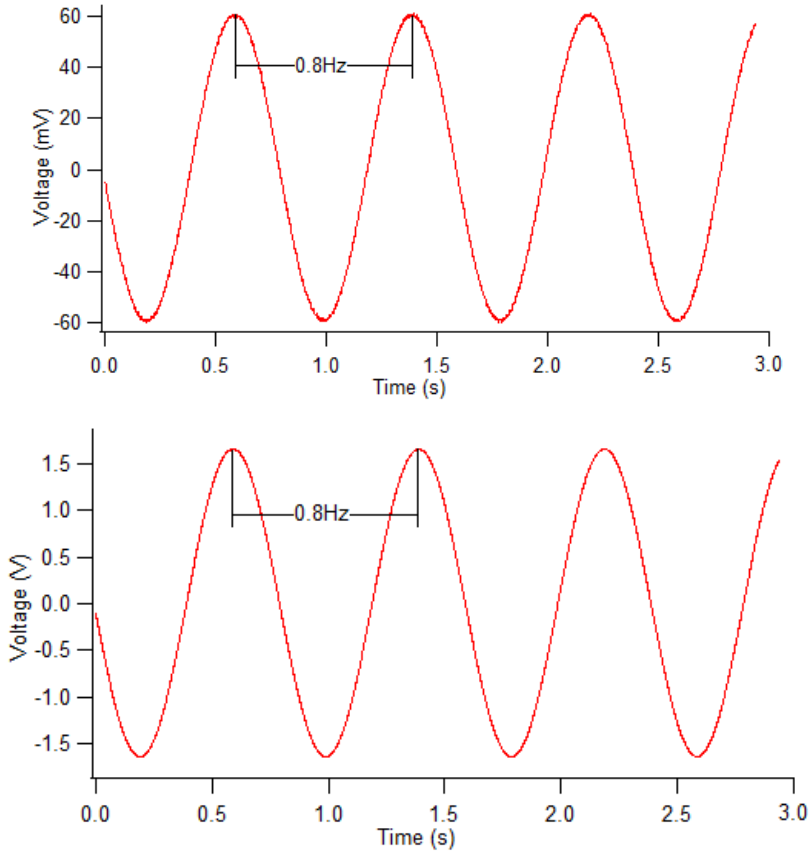

Figure 5.16: System amplitude response

The upper graph is the raw data, which is a 0.8Hz, 120mV$_{p-p}$, and 0V baseline sine wave. The lower graph is the processed data from the system with 27.5 gain.

5.7.2 Detection range

As each signal processing unit has its own operating range, the final output will be saturated as long as one goes beyond its power supply range. The system has three main stages: pre-

amplification, ADC, and DAC. The front buffer op-amp works within ±2.5V. Taking the amplification into account, the viable input signal should be:

$$Maximum\ input\ signal = \frac{\pm 2.5V}{11} = \pm 227mV \tag{5.4}$$

ADS1298 can digitalise any signal, after the internal amplification ($G_{ADS1298}$), between ±4V. If the internal gain is 1, ADS1298 will never be saturated, because the input signal can only be within ±2.5V from the buffer op-amp. However, if the internal gain is higher, then the operating range decreases to ±4/(11$G_{ADS1298}$) V. As for the last stage, the output DAC, AD5362, works within ±10V, and it follows the digital code of ADS1298. If ADS1298 is saturated, it will generate all "1"s to the DAC, which saturates the DAC as well. In addition, if the internal gain of the DAC has been set to a different value other than 1, it is possible to saturate the DAC without sending a series of "1"s. The input range of the whole system is therefore within ±10V/(27.5 × $G_{ADS1298}$ × G_{AD5362}).

$$Maximum\ input\ signal = \frac{\pm 10V}{27.5 \times G_{ADS1298} \times G_{AD5362}} \tag{5.5}$$

To verify the equation, the DAC gain has been set as 1, and hence the detection range lays between the ±227mV and ±4/(11$G_{ADS1298}$) V. For example, if the $G_{ADS1298}$ is 12 (used for EEG detection), then the detection limit of the system is 30.3mV. Figure 5.17 shows the detection range measurement when setting both $G_{ADS1298}$ and G_{AD5362} as 1.

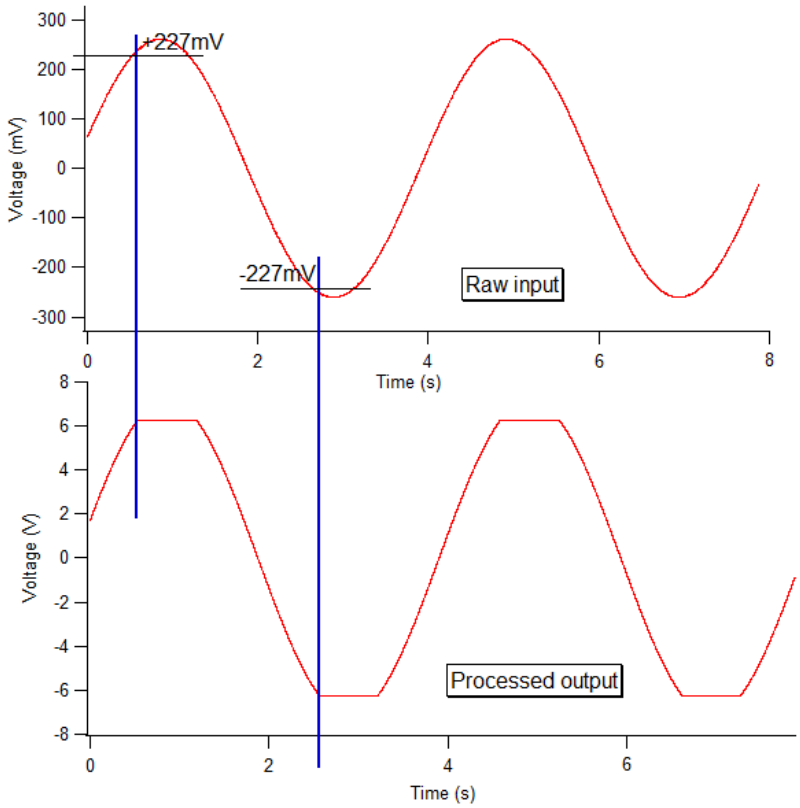

Figure 5.17: Detection range when programmable gains are 1

The output signal starts to be saturated when the input is larger than +227mV or smaller than -227mV. This confirms the theoretical detection range of the system

5.7.3 System noise

The noise of the system has been analysed by sending a stable DC signal, comparing the results between the raw data input and the processed output data. As for the input signal, the mean voltage is 0.484mV, with 0.34mV standard deviation (200 points). In terms of the output noise of the system after the amplification (27.5), the average voltage is 14.951mV, with 0.308mV standard deviation (200 points). Therefore, the standard deviation from the input, is 0.308/27.5, about 11µV. In analytical chemistry, the detection limit of the instrument can be characterised as three time of the standard deviation, which is 33µV.

5.7.4 Simulated EcoG test

After all the characteristic performance tests, a simulated EcoG signal has been sent to the system. Figure 5.18 shows 8-channel concurrent output of the system. The first channel is the raw EcoG input, and the following 8 channels are the output signals from the system. The simulated EcoG signal has been configured as 20mV peak-to-peak amplitude with -160mV baseline and the frequency is set as 1mHz (once every 1000s). These parameters are set to

evaluate the system performance in a reasonable physiological range. As mentioned, the gain has been set as 27.5, and the output processed data are shown in output channel 1-8. The process signals maintain 550mV peak-to-peak aptitude, with -4.4V baseline. In addition, every output channel follows the same signal pattern and frequency response of the raw input, without any distortion.

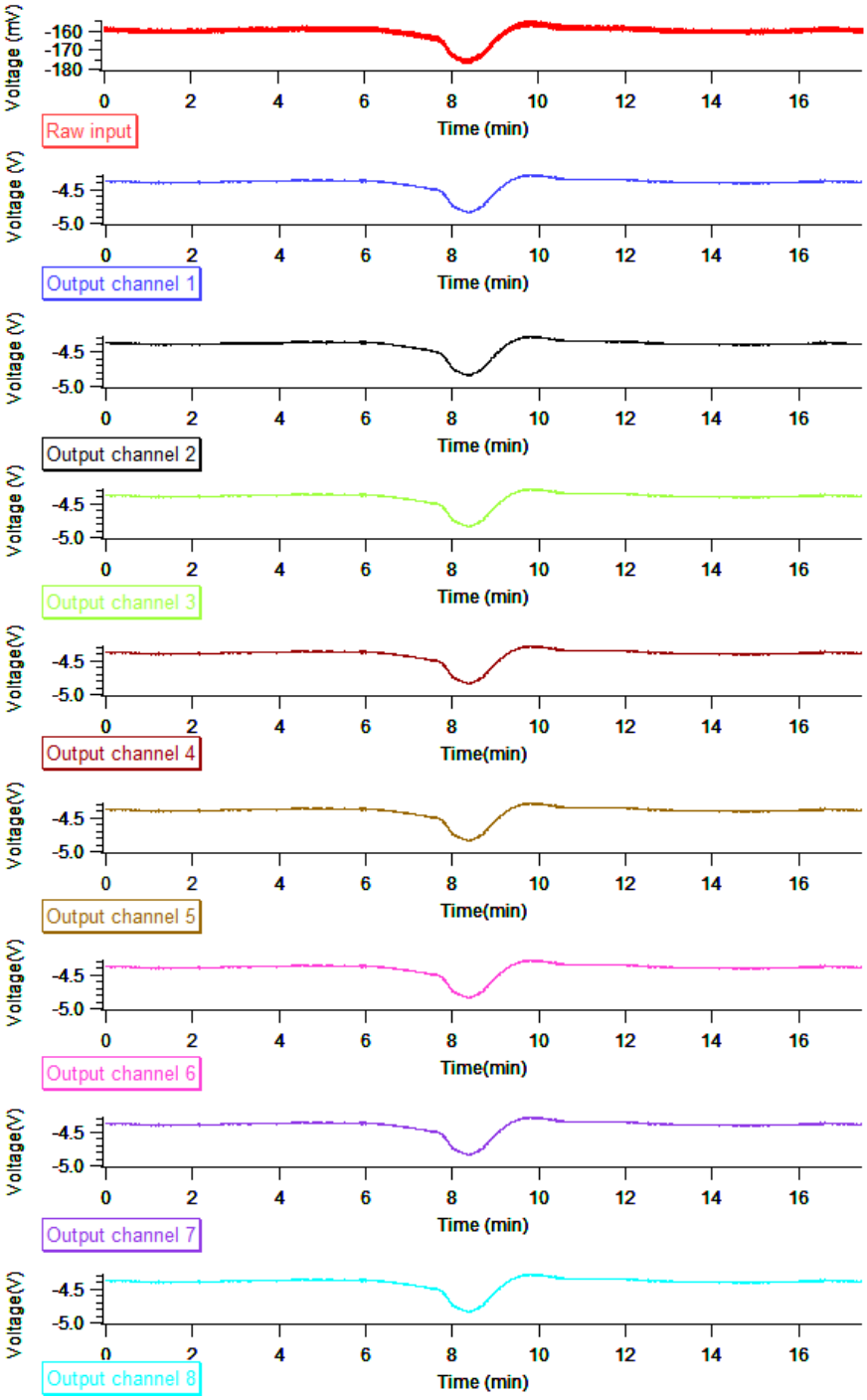

Figure 5.18: Simulated EcoG test

The peak-to-peak amplitude of the simulated EcoG signal is 20mV, the frequency is set as 1mHz, and the offset is -160mV. These parameters were set to mimic the ECoG signal in a physiological range.

5.7.5 Power consumption

As the analog head-stage board is battery powered, the power consumption needs to be roughly calculated, to estimate its operating hours. The power consumption of the analog head-stage board is determined by the power consumption of each component and relevant regulators' efficiencies. As data sheets indicate [75, 76, 81-83], the power consumption of each op-amp is roughly 1mA, that of each ADS1298 channel is around 0.75mW, and the current required for the digital isolator is 1.5mA per channel.

In addition, the efficiency of different regulators are different. TPS7A7001, which regulates +2.5V and +3.3V, has an efficiency as

$$\text{Efficiency} = \frac{I_o V_o}{(I_o + I_q)V_i} \approx \frac{V_o}{V_i} \tag{5.6}$$

I_q is the quiescent current, which is much smaller than the output current, I_o. Therefore, the efficiency is roughly as the ratio between input and output voltage. When the regulator generates 2.5V, the efficiency is roughly 50%. When it generates 3.3V, the efficiency becomes 75%. In addition, the efficiency of LT1611, which regulates -2.5V, is given as 70%.

Taking both power consumptions and efficiencies into account, the overall power consumption, P_{all}, should be calculated as:

$$\begin{aligned} P_{all} &= \frac{\frac{P_{op-amp} + P_{ADS}}{2}}{E_{+2.5V}} + \frac{\frac{P_{op-amp} + P_{ADS}}{2}}{E_{-2.5V}} + \frac{P_{Si}}{E_{+3.3V}} \\ &= \frac{\frac{5\text{V} \times 1\text{mA} \times 2 \times 9 + 0.75mW \times 8}{2}}{50\%} + \frac{\frac{5\text{V} \times 1\text{mA} \times 2 \times 9 + 0.75mW \times 8}{2}}{70\%} + \frac{1.5\text{mA} \times 3.3\text{V} \times 5 \text{ channels}}{75\%} \\ &\approx 100 + 70 + 40 = 210\text{mW} \end{aligned} \tag{5.7}$$

$P_{op\text{-}amp}$ is the power consumption of all the op-amps. Each channel applies two op-amps, one for the front buffer and the other for the first-stage amplification. 9 channels are involved in the design, as it has one reference channel and 8 working channels. Therefore, in Equation (5.7), $P_{op\text{-}amp}$ is multiplied by 2 and then by 9. P_{ADS} is the power consumption of the ADS1298, which has 8 channels, and therefore it is multiplied by 8. Similarly, the digital isolator is multiplied by 5, as it features 5 isolation channels.

The analog board is powered by 4 AA batteries (4 × 1.2V), with a 2850mAh capacity. Therefore, the operating hours are:

$$t = \frac{4 \times 1.2 \times 2850}{P_{all}} \approx 65 \text{ hours} \quad (5.8)$$

Following a series of calculations, the theoretical operating period is 65 hours, which is long enough for clinical monitoring. Experimentally, the system has been left running for 48 hours with a fully-charged battery pack. This is shorter than the theoretical value, due to the battery efficiency and experimental set-up. Therefore, if a certain clinical process lasts more than 48 hours, the batteries can be replaced every 1 or 2 days. As the batteries are rechargeable, two battery packs can meet the requirement of long-term clinical monitoring.

5.7.6 Lab-test system performance summary

After a series of debugging and tests in the lab, the performance of the system has been evaluated. The performance is summarised in the following table.

Electrical characteristics	
Operating voltage	4 – 7V
Overall gain	27.5 – 330[1]
Digitalisation channels	8
Data acquisition resolution	24bit (2's complement)
Detection limit	33μV[2]
Input offset	~60μV
CMRR	-115dB
PSRR	130dB
Sampling rate	250 – 32k sample per second
Power consumption	~210mW[3]
Digital isolation	5kV
Maximum Patient leakage current	50μA (BF standard)
Mechanical characteristics	
Dimension	68mm × 48mm

Table 5.6: Characteristics summary of the system

1: The gain is calculated based on setting output DAC internal gain as 1. This gain can be changed by configuring its registers, however, throughout the thesis, it has not been changed. Therefore, the overall gain has not taken DAC internal gain into account.
2: 24bit ADC works on 2's complement format, therefore the detection limit for the ADS1298 is only $\pm V_{ref}/2^{23}$, ±0.5μV. This detection limit is calculated from the standard deviation of the system (Section 5.7.3).
3: This is the theoretical power consumption of the analog head-stage board, which is calculated by each component's power consumption and relevant regulator's efficiency on the analog board.

Compared with the commercial device, Bio-Amp (summarised in Table 5.1), the new device has a better resolution and detection limit. In addition, the new device features two functional parts, which significantly reduces the noise interference during the signal transmission. Mechanically, the new device is also much lighter and smaller than the Bio-amp. The comparison result between these two devices will be discussed in Section 5.9.

5.8 Head-stage casing design

The simulated ECoG test also indicates the device has the ability of minoring human ECoG. To implement the electronics as a clinical device, especially the head-stage analog board, a proper casing is required.

The case requires to be physically shielded, with water-proof connectors. The one used in this design is the 1.5mm touch-protected panel-mounted socket (DIN 42802) (Figure 5.19), which is compatible with clinical electrodes. The case should be made of plastics, instead of metal, as plastics offer a barrier (reinforced insulation, class II equipment) between the electronics and the outside world, preventing any effect from the leakage current or expected electronic short circuit. To prevent any electrical static discharge (ESD) damage, the connectors should be touch-protected. In addition, the case should not have easy access to the PCB, however it should allow users to change batteries easily.

Figure 5.19: 1.5mm touch-protected connectors

The receptacle is on the left, and the electrode connector is on the right.

Based on these considerations, the first version of the case has been designed based on a commercial Acrylonitrile Butadiene Styrene (ABS) box (100mm × 65mm × 36mm). The 4 AA batteries have been placed in series in a battery holder, which is securely screwed and stabilised on the side wall of the box, hanging on top of the circuit board. With relevant engineering work, the first-version head-stage box is shown in Figure 5.20 in comparison with a standard ID card. The box provides a physical shielding for the internal PCB. The electrode

connectors have been panel-mounted, eliminating the force added to the PCB when plugging/unplugging the electrode cables. The box is enclosed and secured by screws, which offers no easy access in a clinical measurement.

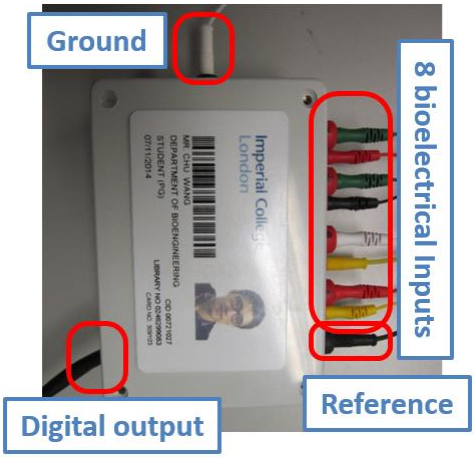

Figure 5.20: ECoG head-stage box

The head-stage box works fine in clinical measurements, and the data will be discussed in the following section. However, two practical issues still remain:

a. As one clinical monitoring can last for 5 to 7 days, the batteries need to be replaced during the surgical process. This involves extra efforts and tooling to change the batteries, which may not be available in operating theatres or intensive care units (ICU).
b. In addition, the box is a cube and hard to be stabilised on the patient bed, especially in operating theatre. When the box is moved, the cables attached are likely to be stretched and the electrodes in the brain may fall off accidentally.

Based on these practical issues, the second version of the casing has been designed. By drawing the design in SolidWorks and printing it by a 3-D printer, the new customised enclosure can fix the practical problems and maintain its original functionalities (Figure 5.21). The 3-D model is attached in Appendix 5.3, and the main improvements lay on the following aspects:

a. The case introduces a wing-shape base, in order to stabilise the box on the bed with either screws or clips.
b. The battery pack has been designed to stay next to the circuit board, instead of stacking on top of it. This helps to reduce the overall height, so that the board can be more stable. In addition, it keeps the PCB and the battery separately. The circuit board

can be installed from the slot underneath, which is secured by screws. The battery stays in the other slot, which features a sliding access. It allows users to change batteries easily, without touching the PCB or internal wiring.

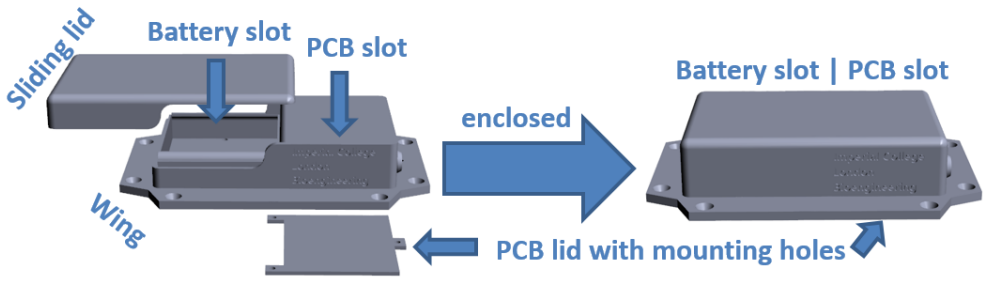

Figure 5.21: Second-version head-stage box (open vs. close)

The figure on the left shows its design considerations: the circuit board is capsulated in the PCB slot, and isolated by the lid and skewers. The batteries are placed in the battery slot, which has a sliding lid. This allows the users to easily replace the battery without getting in touch with the main PCB and set-up. The wing is used for stabilising the head-stage box on the patient bed or under the pillow.

5.9 Clinical data acquisition

By implementing a proper casing, the head-stage analog board is able to monitor clinical human data. As mentioned, the system is designed for ECoG recording, but it can be also used for other bio-signal acquisitions.

5.9.1 ECG measurement

The fundamental ECG components and relevant electrical characteristics have been demonstrated in Section 1.3.4, and the experiment aims at validating the instrument capable of detecting all the essential components in an ECG signal. The internal gain in ADS1298 is set as 12, and the output DAC remains gain of 1, which yields the total gain as

$$Total\ gain = 11 \times 12 \times 2.5 \times 1 = 330 \tag{5.9}$$

The sampling rate of ADS1298 has been set as 500 samples per second (SPS). 5 healthy volunteers have been involved in the test, and the ECG signal has been acquired from both the new device and the commercial bio-amplifier, Bio Amp. A conductive gel has been applied on the electrode contacts to reduce the contact impedance and improve the signal quality. PowerLab has been set as “AC coupled and 50Hz low-pass filter” on both channels, to remove DC offset interference as well as eliminate high-frequency noise. In order to mimic the clinical

set-up, volunteers stayed 2 meters away from the main detection equipment, while the analog head-stage box was placed close to the volunteers.

Figure 5.22 shows the acquired ECG signal of a complete cycle, and different characterised waves are labelled. Compared with the ideal ECG response (Figure 1.6), the detected signal explicitly contains all the featured waves, naming P wave, PR segment, QRS complex, ST segment, and T wave.

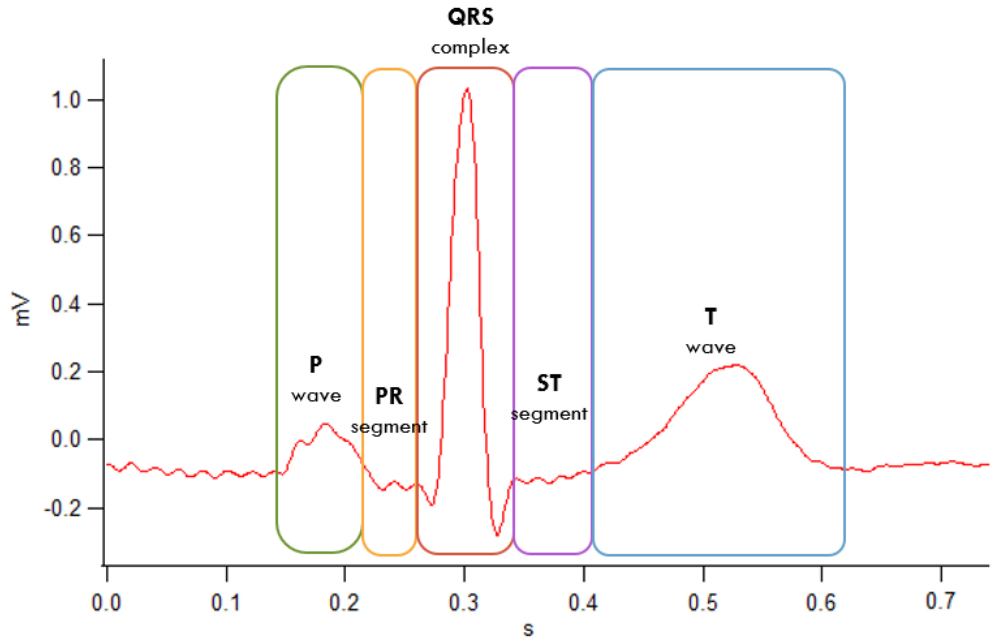

Figure 5.22: Wave analysis of the acquired ECG signal

The comparison result with the Bio Amp is presented in Figure 5.23. The experiment has been conducted on the same volunteer and under the same environment. As it shows, the output signal of the new device has the same amplitude ($1.3V_{P-P}$) and frequency response (0.75s) as the Bio Amp, which confirms the reliability of the detection from the new device.

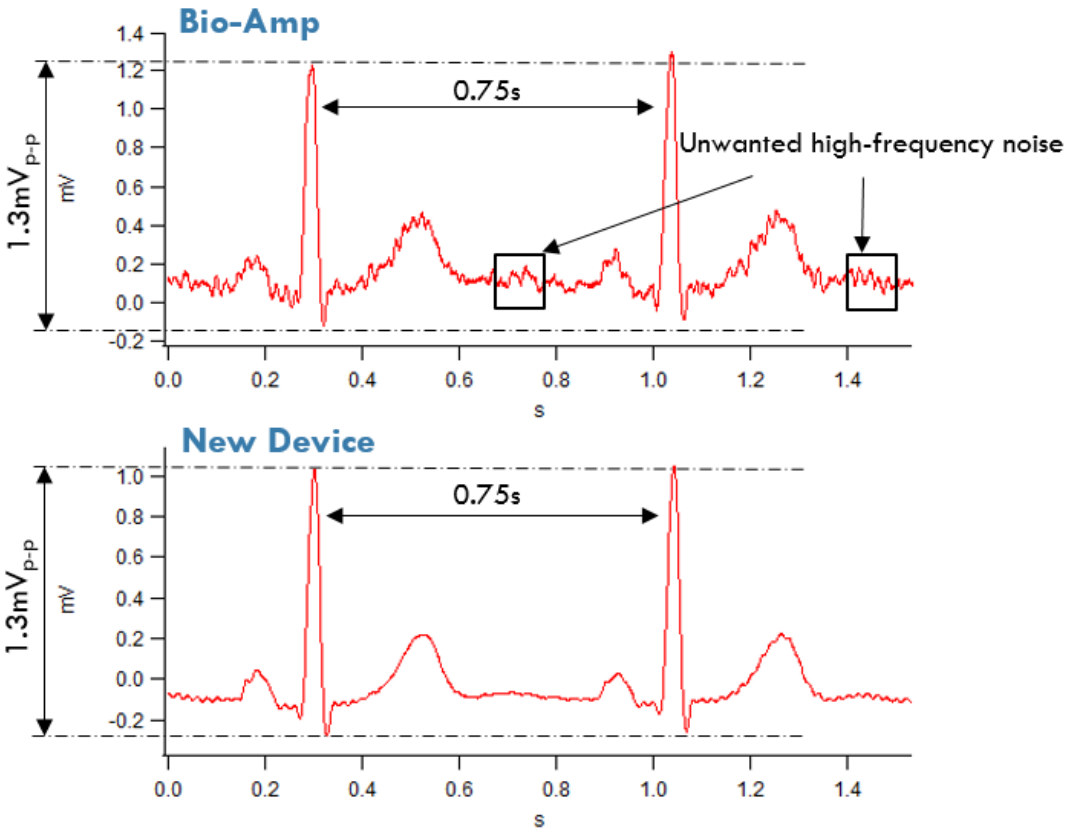

Figure 5.23: Comparison ECG result between the Bio-Amp and the new device

They have the same signal pattern and frequency response. Moreover, the new device shows better SNR than the commercial Bio-amp. The main interference of the bio-amp measurement is from the 2-meter keep-out distance for analog signal transmission.

Furthermore, the new device shows better performance than the commercial Bio amp, as large unwanted high-frequency noise appears on the output of the Bio amp, due to its internal design and more significantly the 2-meter keep-out distance. Quantitatively, if capturing a very short period of both signals (0.05s), assuming the signals remain unchanged during this period, the standard deviations for both signals can be calculated. In this experiment, the standard deviations (200 samples) for the Bio amp is 13.4µV, and that for the new device is only 1.5µV (after removing the amplification). The value indicates the detection limit of a monitoring device. For the Bio-Amp test, the ECG signal is still readable, as the SNR is relatively large, however, EEG test pushes the Bio amp to the limit as it requires to detect even smaller changes (10-50 µV). EEG test, comparison result, and relevant analysis will be discussed in the next section.

5.9.2 Adult EEG measurement

The fundamental EEG components and relevant electrical characteristics have been discussed in Section 1.3.4. When measuring an EEG signal, the amplification of the system remains the same, 330. Four healthy volunteers have been involved in the experiment, and a professional EEG technician helped to set up EEG electrodes and distinguish featured EEG waves. Similar to the ECG test, the same conductive gel has been applied to optimise the detection. In terms of the overall experimental set-up, the volunteers stayed 2 meters away from the main recording devices, same as ECG test, to mimic the real clinical environment (Figure 5.24).

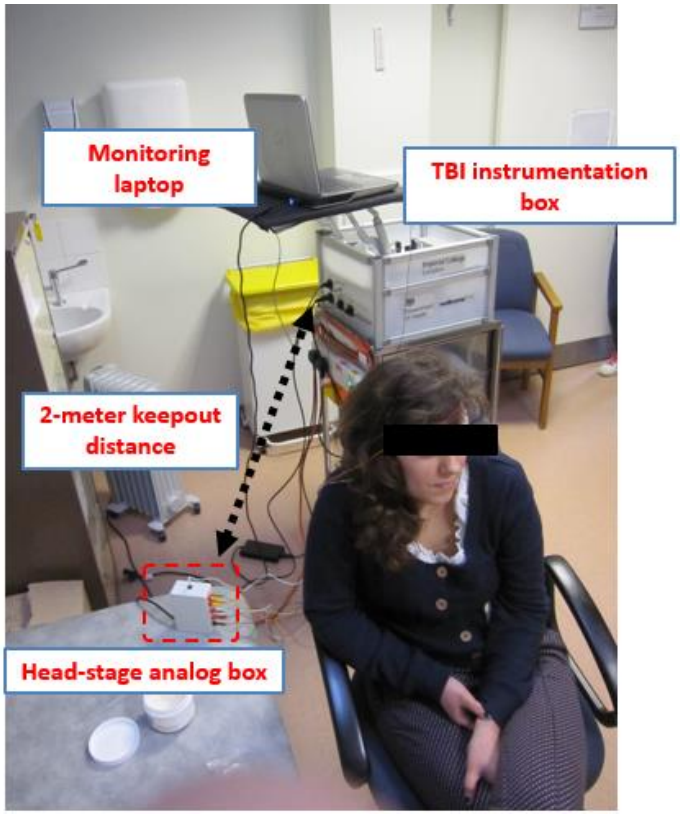

Figure 5.24: Experiment set-up for the EEG measurement.

The experiment was guided by the technician, commanding the volunteer to open/close/blink their eyes, and each experiment run for 10 minutes. A featured data block is shown in Figure 5.25, which involves all the three eye status and relevant electromyography (EMG) and EEG response.

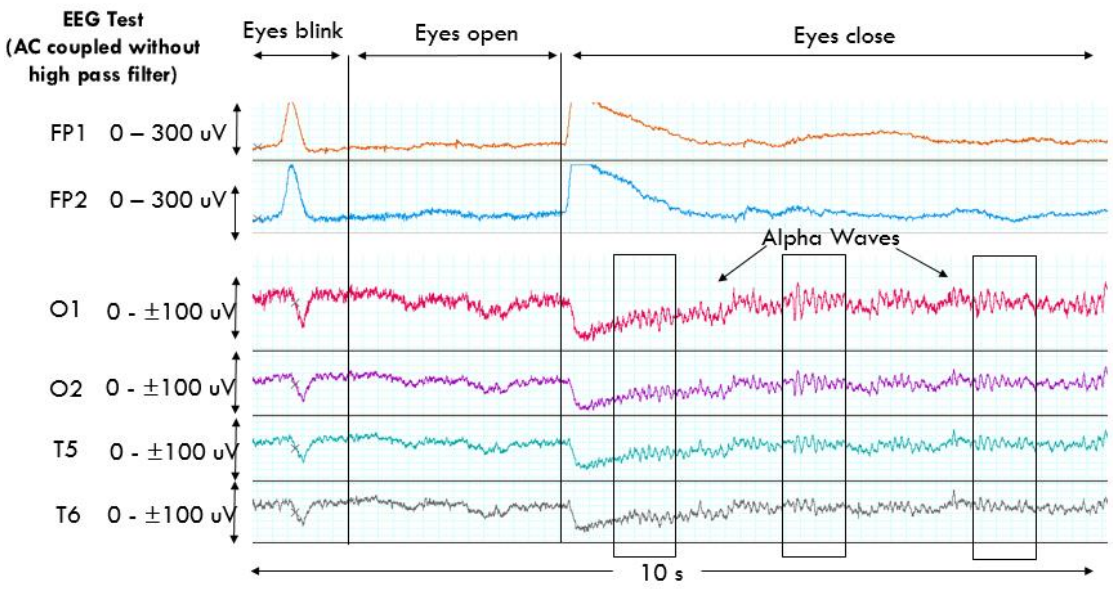

Figure 5.25: Selected waves of the detected EEG signal using the new device

When eyes blink, the relevant eye muscle changes (EMG signals) can be observed in the first interval. During the phase of eyes open, no significant change should be detected. When the volunteer was asked to close eyes, EMG signals can still be explicitly detected from position FP1 and FP2. More importantly, at position O1, O2, T5, and T6, clear alpha waves can be detected, which is regarded as the main featured wave in the EEG signal.

The comparison data with the Bio amp is shown below (Figure 5.26). The data in the lower figure is the measurement result from the Bio amp (in EEG mode, 0.1Hz high-pass and 60Hz low-pass filter). The upper figure shows the result from the new system, with only a 0.1Hz high-pass filter and no low-pass filters. During one event of eyes close, alpha waves can be detected from both devices, and they have the same signal amplitude, which further confirms the viability of applying the new device for bioelectrical potential measurement.

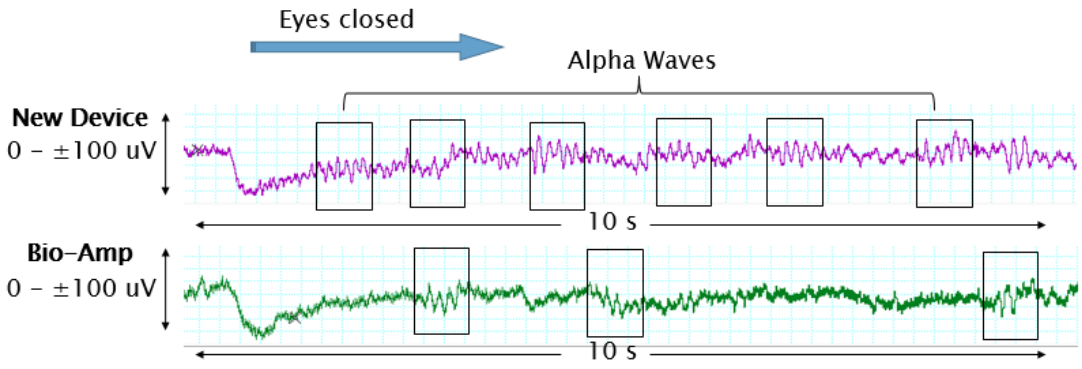

Figure 5.26: EEG performance comparison between the new device and the Bio-Amp

Furthermore, same as the ECG test, the new device shows better performance than the Bio amp. In the Bio amp, the unwanted high-frequency components appear on top of the real EEG signal, which contaminate the over output signal and therefore significantly affect the SNR. Visually, multiple alpha wave events can be detected from the new device, while only few can be observed from the Bio amp. Quantitatively, similar to the ECG analysis, capturing a short and flat period, the standard deviation for the new device is therefore calculated as 1µV, and the value for the Bio-Amp is 6µV. Compared with the ECG test, the new device roughly maintained the same electrical performance. The Bio-Amp performed better than the ECG test, as it maintains a special EEG mode, with different filtering options. In addition, the experimental set-up was different from the ECG tests, which is another factor of the signal quality.

5.10 Conclusion and further development

In this chapter, a low-noise high-resolution bio-potential acquisition system have been introduced. By applying high-performance front-end ADC, ADS1298, the instrument is capable of monitoring small signal changes in µV level. In order to optimise the quality of clinical monitoring, the whole instrument has been designed in 2 different functional parts: a head-stage analog board and a monitor-side digital board. A 3-D printing head-stage box has been designed to further facilitate clinical measurements. The digital board has been properly shielded and placed together with other essential electronics in an instrumentation box, which will be discussed in the next chapter.

When analysing the performance of the instrument, a variety of signal sources, such as standard high-performance signal generator, human ECG and EEG, have been utilised. In

addition, the existing commercial analog data processing instrument, Bio amp, have been used as a performance comparison.

More importantly, the design has validated that these main ICs and relevant circuit designs are suitable for bio-potential acquisition applications. The next main task for the future design is to use similar ICs and implement wireless bio-potential acquisition system. A wireless system can help to remove the digital transmission cable, and further facilitate the clinical team.

Chapter 6: TBI Instrumentation Box Development

To gain a comprehensive understanding of secondary brain injuries, several key parameters are being measured in the intensive care unit (ICU). To summarise the discussion of previous chapters, the phenomenon of cortex bio-potential changes due to the cortical spreading depolarization (SD) has been reported as an effective method to investigate the secondary brain injury, which can be characterised on electrocorticography (ECoG). Since the brain tissue needs massive extra energy to recover from the injury, the neurochemical concentration changes of glucose and lactate are also regarded as important signs for investigating traumatic brain injury (TBI) events; In addition, the brain cell membrane potential is maintained by the concentration difference of various ions across it. During a SD event, the concentrations of different ions across the membrane are significantly changed, which can be regarded as another method of investigating TBI. Globally, blood pressure, intracranial pressure, tissue oxygen concentration, and body temperature are the standard parameters that need to be measured from TBI patients. Practically, a 3-D accelerometer is also required to detect the real-time patient movement, in order to avoid any signal artefact. In this chapter, a multimodal TBI instrumentation box will be introduced, which is capable of measuring and recording all these essential parameters simultaneously.

6.1 The previous monitoring system

The previous TBI monitoring set-up is shown in Figure 6.1. From bottom to top, the instruments are consisted of a certified isolation transformer, which protects the monitored patient safety, a PowerLab, which is the main data recorder, an uninterruptable power supply (UPS), which allows the instrument to work while being unplugged, for example moving it between the lab and the ICU, a Bio-amp, which is used for ECoG signal detection, and a microdialysis pump system, which perfuse the required solutions and conveys patient samples to the monitoring trolley. The finial component is the chemical analysis system (with electrochemical biosensors in a Faraday cage), which has been mounted on a cantilever arm to allow it to be placed close to the patient head. This analysis system measures the concentration of glucose, lactate, and potassium, and the overall system is controlled using a monitor laptop. The clinical trolley is located about 1-2 meters away from the monitored patient's bed.

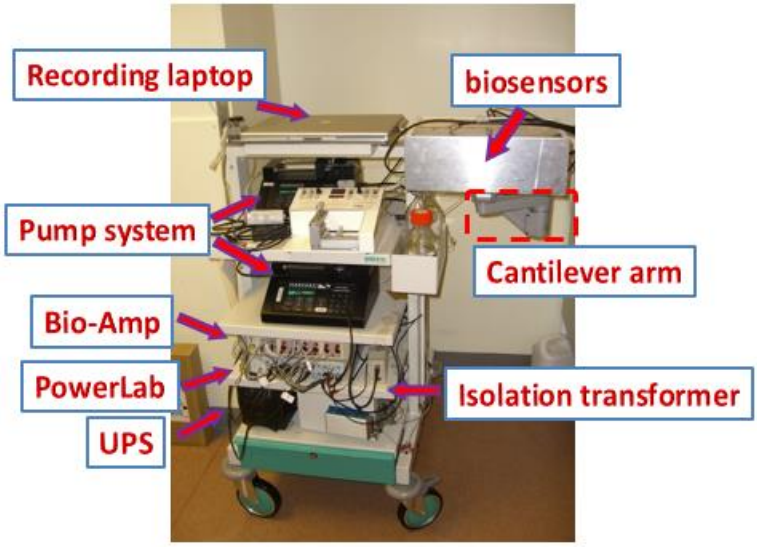

Figure 6.1: Previous TBI monitoring set-up

Practical issues of the previous TBI set-up

The system is able to do clinical TBI monitoring and helps researchers to study TBI related events and relevant chemical changes [18, 84]. However, the system has several practical issues and they can be mainly concluded in the following 4 folds:

a. The trolley, purchased from *CTL Medical*, is very large (1.5m tall × 0.57m wide × 0.67m deep) and heavy, due to the complexity and large power requirement of the rapid sampling microdialysis system. Consequently, the system requires at least 2 persons to move around.

b. The space in an ICU is normally limited, which makes the trolley hard to be placed close to the patient. ECoG signals are carried via a 2-4 meter long unshielded ribbon cable, the standard component from *AD-TECH*, used to connect between ECoG electrodes and monitoring electronics. As the system is used in an electrically noisy environment, such as operating theatres and ICUs, the subtle ECoG signals (μV) in the long cable are inevitably interfered, which affects the output signal quality of the monitoring system.

c. The rapid sampling system and the ECoG recording system used in the trolley consume very large power. Specifically, the ECoG recording system is powered from the mains, and it has relatively large power consumption, due to the internal medical-grade AC/DC converter. The rapid sampling system requires large power to switch the internal valves fast enough and align them very precisely to relevant inlet/outlet.

d. To allow the analysis system to be close to the patient, the electrochemical sensors are at the end of a cantilever arm with long unshielded cables from the arm to the main trolley. Same as the ECoG signal acquisition, this transmission configuration also introduces noise interference to the system.

6.2 New TBI instrumentation box

To improve the performance of the signal recording and cause less interference to the clinical process, a new TBI instrumentation box has been designed and developed. The new box optimises all the electronic components presented in the previous monitoring trolley, as well as applies state-of-the-art sensor techniques. In general, the appearance of the new TBI instrumentation box is shown in Figure 6.2. By connecting to the relevant external devices, the box is able to measure 16-channel essential information of a TBI patient (Table 6.1).

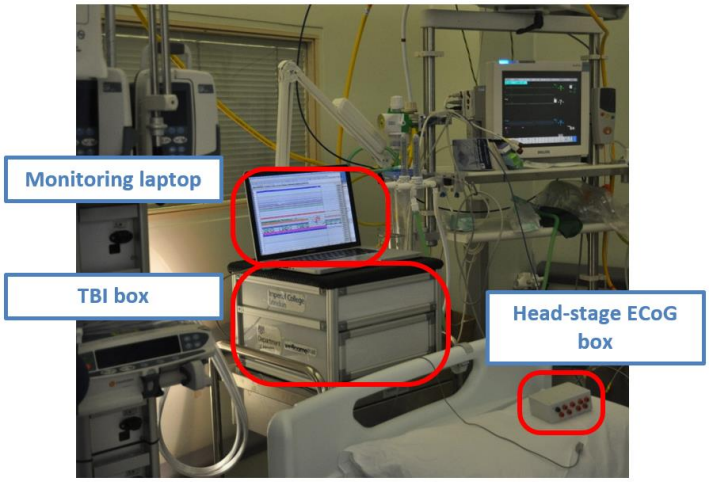

Figure 6.2: New TBI instrumentation box

Channel	Monitoring information	Source
1	Patient movement	3-axis accelerometer
2	Body temperature	Commercial LICOX monitor
3	Intracranial pressure	Commercial Philips pressure monitor
4	Blood pressure	Commercial Philips pressure monitor
5	Blood oxygen	Commercial LICOX monitor
6	Glucose	Biosensor and potentiostat (discussed in Chapter 4)
7	Lactate	Biosensor and potentiostat (discussed in Chapter 4)
8	Potassium	Ion selective electrode and high-impedance buffer amplifier (discussed in Chapter 2 and 6)
9-16	8-channel ECoG	Head-stage analog board (discussed in Chapter 5)

Table 6.1: Monitoring information in the TBI instrumentation box

In addition, this new TBI box also features a microfluidic-based auto-calibration system for ion selective electrodes and biosensors. As the sensitivity of a sensor can vary significantly over time, it needs to be calibrated regularly to ensure the sensing accuracy and reliability. The details about developing and operating this auto-calibration system will be discussed in Chapter 9.

The data recorder used in the new TBI box is the latest PowerLab 16/35 series. Compared with the old version, the new PowerLab provides better SNR, faster processing speed, and it is also much smaller (70mm × 240mm × 260mm) than old ones. The new PowerLab equips 16-channel standard BNC connectors, and it also features 8-pin DIN connectors (Figure 6.3) for the first four channels [85]. As shown in the figure, each DIN connector is able to provide ±5V, with maximum 50mA supplying current. The 3-axis accelerometer in channel 1 is connected to the DIN connector, utilising the ±5V power supplies and sending the real-time patient motion information to the PowerLab.

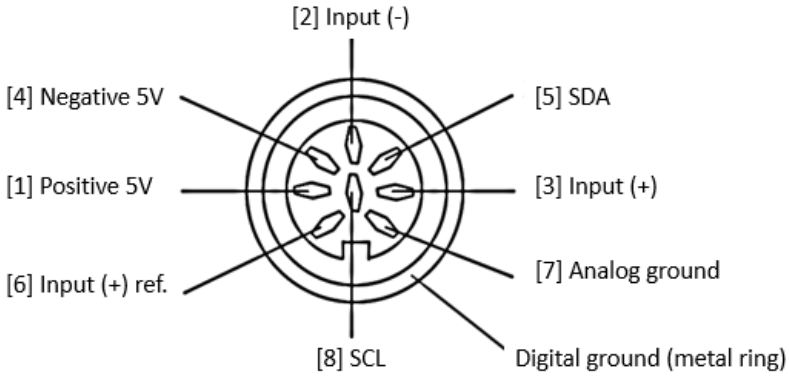

Figure 6.3: Pinout of the DIN 8-pin connector on PowerLab

The DIN connector was used to power and control the accelerometer mentioned in this chapter, as well as the receiver of the Xbee-based wireless potentiostat, which will be discussed in Chapter 7. The figure is reproduced from [85].

6.3 TBI box design

As for the internal design of the box, both operational safety and efficiency have been taken into considerations. As all the sensor-related operations are conducted inside the box, the potential fluidic leakage to the electronics needs to be prevented. In addition, users need to have easy access to the sensor platform, as the position of the sensor and relevant microfluidic tubing need to be checked regularly. However, the box should not provide any access to the electronic components, once they have been properly set up.

Based on these requirements, the instrument has been designed as three separate layers. Figure 6.4 shows the simplified schematic, compared with the real TBI box. All the sensors, together with their auto-calibration platform and connection tubing, have been placed on the upper layer (sensor layer), all the processing electronics sit on the lower layer (electronic layer), and the certified isolation transformer stays underneath the TBI box (isolation layer). In addition, all the essential external connectors and power entry have been mounted on the lower region of the back panel.

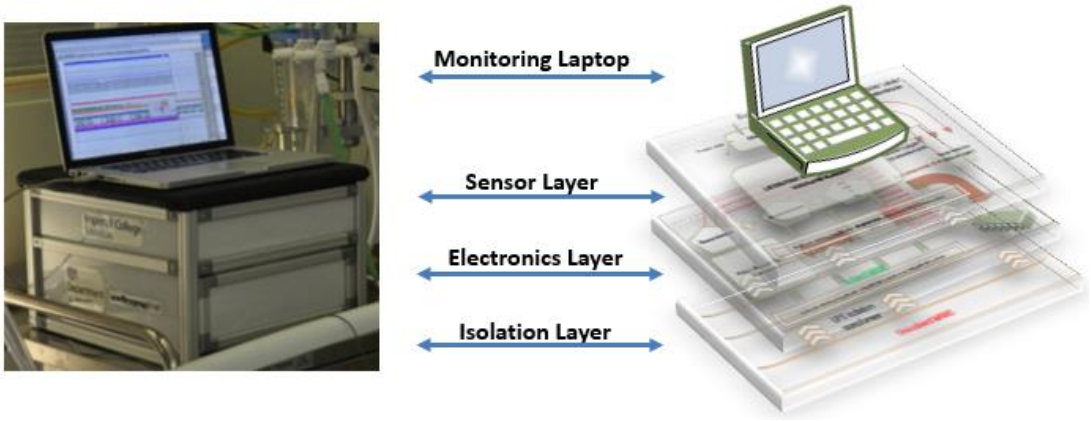

Figure 6.4: Simplified schematic of the TBI box, compared with its real appearance

6.3.1 Sensor layer (upper layer)

The flow chart of the sensor layer is shown in Figure 6.5. All the neurochemical sensor operations are performed on this layer. As the sensors measure local neurochemical concentration changes ex vivo, using microdialysis techniques [86, 87], a microfluidic tubing is required to connect to the box to convey the patient's sample into the sensors. A high-precision magnetic coupler is applied on the chassis, as it provides good tubing alignment, strong adhesive force, and neat finishing. Once the sample is conveyed into the box, it goes through the microfluidic chip, and then the needle sensors in the microfluidic chip start to detect the concentrations of relevant chemicals. All the supporting electronics, such as AC/DC converter and potentiostats, have been placed on the low layer, which will be discussed in next section.

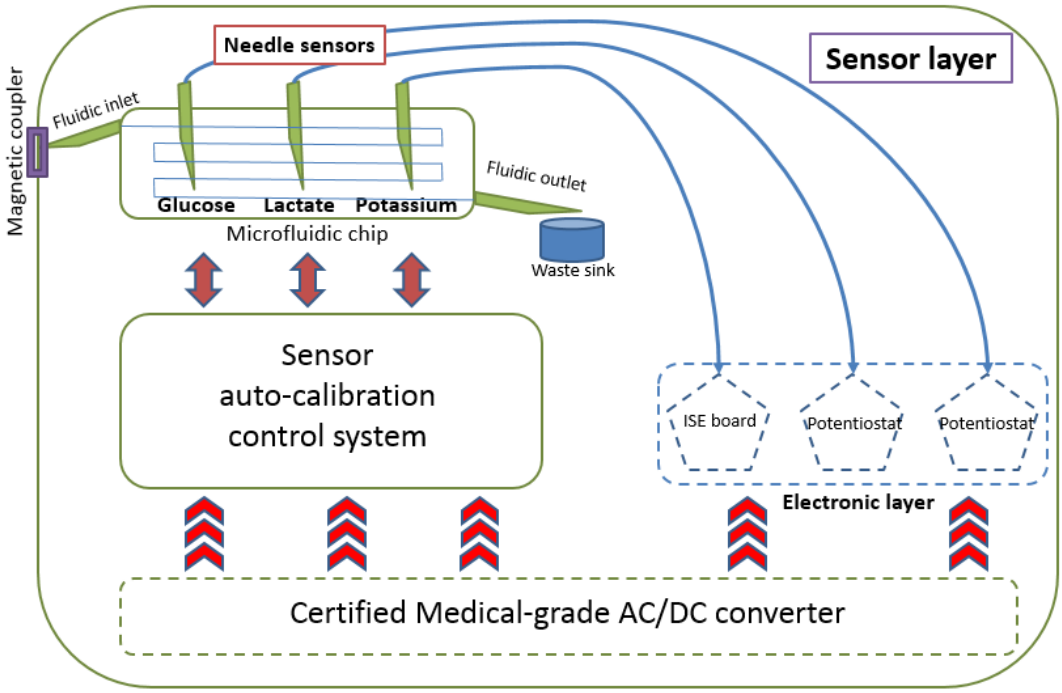

Figure 6.5: Flow chart of the sensor layer

The ISE board mainly contains an instrumentation amplifier (INA116 from Texas Instruments), and it is used for measuring the potassium concentration in the analyte, via the potassium ion selective electrode. The fundamental design of the ISE board has been written in Dr. Delphine Feuerstein's thesis [88]. The potentiostat used in this design is the traditional resistive one, as it is able to measure bipolar signals and can be miniaturised to fit in the box.

6.3.2 Electronic layer (lower layer)

All the essential electronic components have been placed in this layer to process, record, and display relevant patient information (Figure 6.6). The resistive potentiostats, illustrated in Chapter 4, have been applied for measuring neurochemical (glucose and lactate) changes. The ECoG digital board, discussed in Chapter 5, has been also placed on this layer. By providing connections to external devices that monitor blood pressure, intracranial pressure, body temperature, oxygen, and patient movement, the internal PowerLab is therefore capable of recording 16-channel essential information simultaneously.

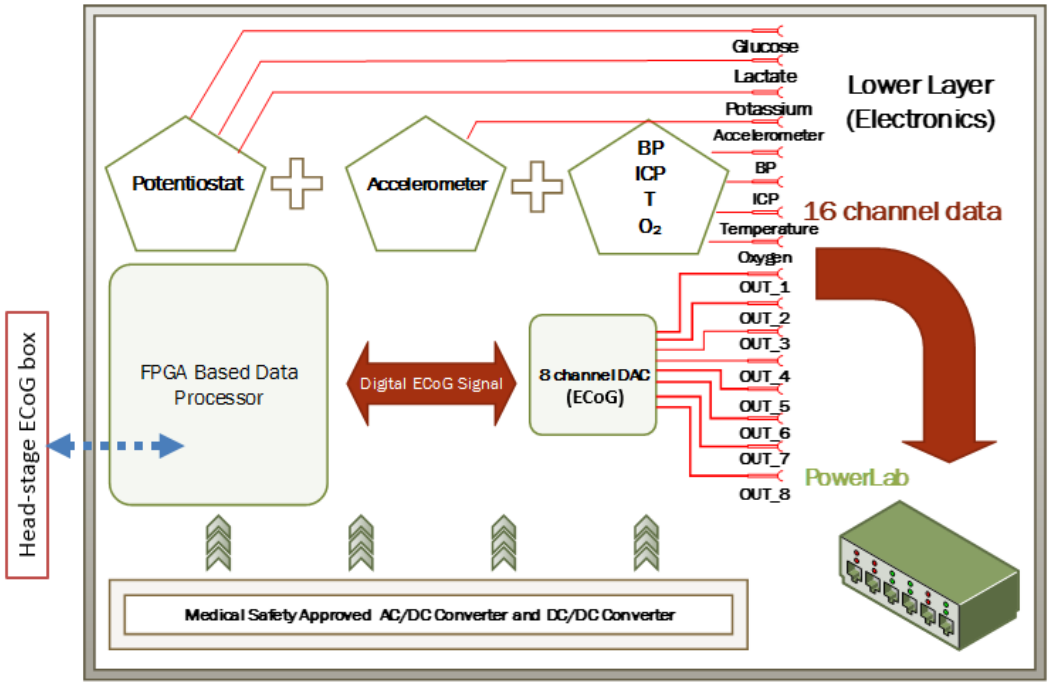

Figure 6.6: Float chart of the electronic layer

In addition, a medical-grade AC/DC converter is used to provide all the necessary DC power to the monitoring electronics on this layer (Table 6.2). A PCB used for the power distribution has also been applied (Figure 6.7) to minimise the internal wiring requirement.

Devices	Operating voltages
Analysis potentiostats (for biosensors)	±12V
Analysis buffer amplifiers (for ISE)	±12V
ECoG digital board	±12V and +5V
Sensor auto-calibration system	±12V

Table 6.2: Operating voltages of different electronics in the TBI box

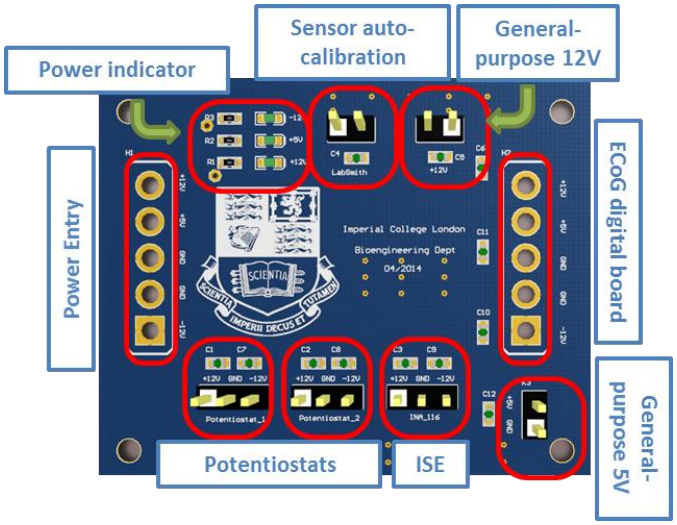

Figure 6.7: Power distribution board

Different connections are respectively labelled. The board provides a general-purpose 12V and 5V connections for further development. Different power indicators are applied to provide visual signs for the power conditions. The vias in the middle of the board are used for the heat dissipation. ISE here stands for ion selective electrode.

6.3.3 Isolation layer

For clarity, even though it is called as a "layer", the components in this layer are not inside the TBI box. However, they are indispensable for the TBI box to be safely operated in clinical monitoring. Two main components on this layer are: an uninterruptable power supply (UPS) and a medical certificated isolation transformer. The UPS allows the TBI box to operate continuously, even when it is unplugged for a short time (1 – 2 hours). This normally happens when moving the box from the lab to the ICU/operating theatre, or experiencing an electrical examination in the hospital. The isolation transformer is certified for medical use, and able to provide enough protection to the patient, operators and electronics. The details of medical safety considerations will be discussed in Section 6.6.

6.3.4 Back panel

As the instrumentation box is intended to provide no access to the electronic layer, some internal connectors for the PowerLab have been extended to the back panel, so that external devices can be connected to the internal data recorder. In addition, two USB sockets have been mounted on the back, such that the PowerLab and the LabSmith platform (the auto-calibration system) can communicate with the monitor laptop. In addition, a RJ45 socket has been used to allow the head-stage analog ECoG board (discussed in Chapter 5) to communicate with the digital board in the TBI box. Furthermore, only one power socket has been used, and it has been placed at the left lower corner (Figure 6.8). The power has been

split into 2 branches inside the box. One is used to power the PowerLab, and the other is connected to the AC/DC converter, providing DC power for all other electronics.

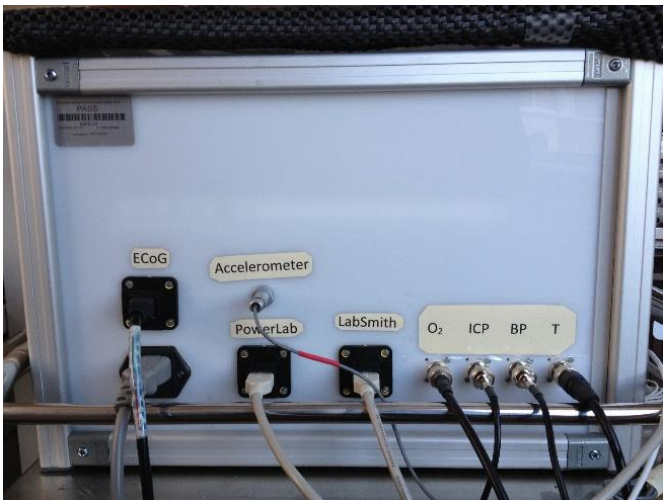

Figure 6.8: Layout of the back panel

6.4 TBI box construction

After the demonstration of individual layers, the overall construction and engineering considerations will be discussed in this section. In order to fill in all the components in a minimal size, the overall dimension of the TBI instrumentation box has been finalised as 340mm (width) × 370mm (length) × 260mm (height), which is roughly the same size of a miniaturised printer. The surface area of the box is large enough to support a monitor laptop, such as 13-inch Macbook Pro, 227mm (width) × 325 mm (length).

The side wall of the box is made of 3mm white opal acrylic sheet, and the base is made of 5mm white opal acrylic sheet. The frame is made of aluminium beams with built-in slots (Figure 6.9). The sheet can be slide in and stabilised in the slot by polyvinyl chloride (PVC) strips. 2-T slot beams have been used to build the outer frame, while 3-T and 4-T slot beams have been used for internal connections. Two or more beams are jointed by the connector kits. After building the frame and relevant walls, a front door (with smooth curving and finishing) for the electronic layer has also been designed. The door is specially used for engineers to regularly check and test the internal electronics, however it is not intended to open during standard clinical monitoring process.

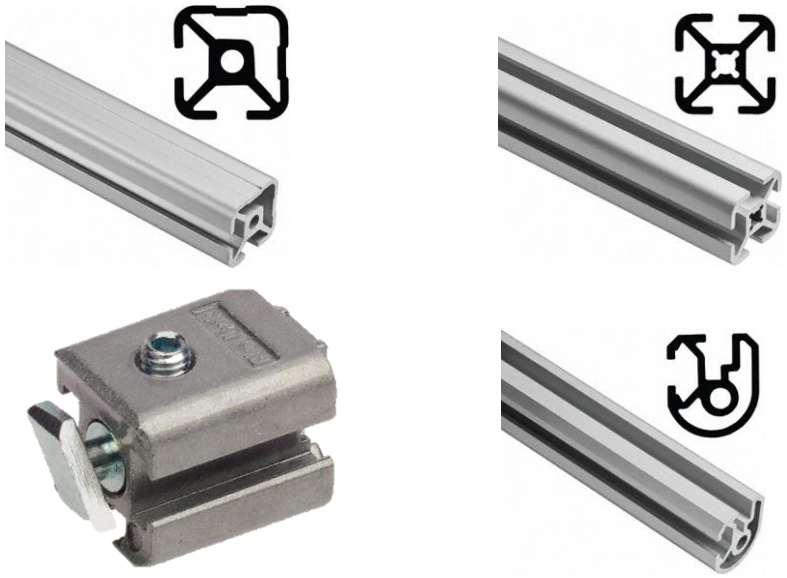

Figure 6.9: Standard construction components of the TBI box

The standard components contain: 2-T slot beams (upper left), 4-T slot beams (upper right), connector kits (lower left), and round door beams (lower right)

By confining the size of the door and applying PVC strips, the door can be shut down properly when being slightly pushed. To avoid the door accidentally open during monitoring, no external handle is added to the door.

The top lid of the box features a sliding lift-up design, which has been built on two lift-up fitting bodies (Figure 6.10) with internal gas springs. Springs of different forces can be selected for specific applications. The flap is initially designed for lift-up kitchen cupboard doors. As the monitor laptop needs to stay on top of the box during the whole monitoring process, the top lid is required to remain level, especially when the user needs to open the lid and check the sensors. An alternative lid design is to move the lid sideway, however this requires more space to slide, which may not be applicable in some space-limited conditions, such as ICUs or operating theatres. In addition, the side sliding design also requires a strong mechanical connection, as it works as a lever against the weight of the laptop and the lid.

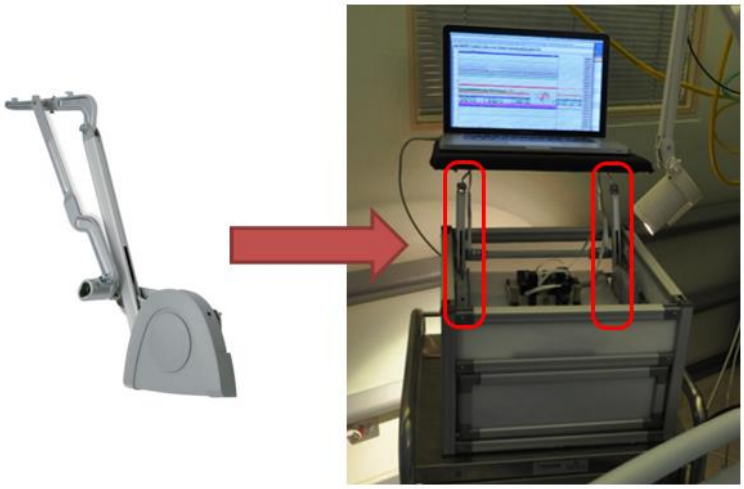

Figure 6.10: Lift-up fitting flap and the top lid design

Force of the flap needs to consider carefully, as different forces can only fit in specific applications. If the force is too small, it cannot facilitate the operator when opening it. If the force is too large, the item on top of the lid, laptop in this case, may be bounced away.

6.5 Safety consideration

The current legal framework for evaluating the device safety is to estimate the potential of the device being a hazard, which causes safety issue and harm [89]. The risk is a measure of the combination of the hazard, the likelihood of occurrence of the hazard, and the relevant impact of the hazard. In general, both users and monitored patients must be adequately protected against danger of physical injury or other damages, which might be caused by direct or indirect electrical contact. In addition, radiation, arc, or temperatures must be regulated within safety regions [89]. A medical device needs to meet IEC60601-1: 3rd edition medical device safety standards and conducts risk analysis defined in ISO14971.

6.5.1 IEC standards

Unlike information technology equipment, medical equipment is designed to diagnose, treat, or monitor a patient, which requires intentional contact with the patient. Patients can be unconscious and connected with multiple monitoring devices, which significantly increases the risk of electric shock. Therefore, the isolation of medical devices plays a critical role in the industry [90]. Two worldwide recognised standards for medical devices, Underwriters Laboratories (UL) and International Electro Technical Commission (IEC), have been applied to ensure that all the medical devices are able to provide a high safety level for both patients and operators.

IEC60601 is a series of standards, which contain the core safety requirement for all medical electronics in "*Medical Electrical Equipment – part I General Requirement for Safety*"[20]. IEC60601-1 defines the operation safety conditions of medical devices to protect operators, patients, and the surroundings. In addition, collateral standards are also generated, based on specific technology-related safety requirement, and by convention they are named as IEC60601-1-xx. Different regions in the world may have slightly different medical safety regulations. Particularly in Europe, IEC60601 is associated with regional deviations, as a harmonised standard, which is named as EN60601. In 2005, the latest (3rd) edition of 60601-1 was first published, and in Europe, the standard has been adapted as EN60601-1:2005 [65].

6.5.2 End device types

Medical end devices have been mainly categorised in 3different types (Figure 6.11) [65]:

a. Type B – the device has no electrical contacts with the patient and can be earthed.
b. Type BF – the device has floating or isolated applied part(s)[3] to the patient but not directly to the heart.
c. Type CF – the device has floating or isolated applied part(s) to the patient and directly to the heart.

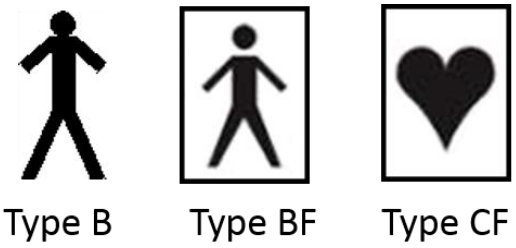

Figure 6.11: Common medical end device symbols

Each type has its own safety requirement. Unlike other standards, electrical safety is not analysed and evaluated on the basis of voltage, but on the (leakage) current. If a device has direct contact to patients, based on the skin resistance (Table 6.3), a very low voltage can cause large leakage current when it directly applies to internal tissues or organs, which can be fatal to the patient. The detailed terms and relevant current leakage limit will be discussed in the following section.

[3] An applied part is defined as any piece of the device that is able to be intentionally or unintentionally in contact with the patient.

Position	Resistance
External: skin (horny layer)	tens kΩ to several MΩ
Internal: limb	~200Ω
Internal: trunk	~100Ω

Table 6.3: Skin resistance in the human body

Therefore, the resistance between any two limbs is about 500Ω, and the resistance between one limb and the heart is 300Ω [66]. That is the reason, in Figure 3.7, the resistance between the patient's right leg and the heart is labelled as 300Ω.

6.5.3 Leakage currents

Several terms are involved in evaluating leakage currents of a device. They are defined as:

a. Earth leakage – the amount of current following in the earth conductor
b. Enclosure leakage – the amount of current following from the enclosure to earth via the patient
c. Patient leakage – the amount of current flowing from an applied part to earth via the patient
d. Patient auxiliary – the amount of current flowing from one applied part to another applied part via the patient.

Apart from different leakage currents, medical devices should also follow the principle of the single fault condition (SFC) evaluation. It indicates that the medical device should be designed to operate safely in not only normal conditions (NC), but abnormal, single fault conditions. Therefore, the standard for different device types and relevant leakage current needs to be regulated in both conditions, and the respective maximum leakage currents have been summarised in Table 6.3.

Leakage current	Type B		Type BF		Type CF	
	NC	SFC	NC	SFC	NC	SFC
Earth leakage	500µA	1mA	500µA	1mA	500µA	1mA
Enclosure leakage	100µA	500µA	100µA	500µA	100µA	500µA
Patient	100µA	500µA	100µA	500µA	10µA	50µA

Table 6.4: Leakage currents for different end device types

The table is re-produced from [65].

6.5.4 Safety evaluation of the TBI box

To safely apply the TBI instrumentation box to patients, all the safety requirements need to be satisfied. The whole instrumentation involves 5 stages to isolate electrical hazard, minimise leakage currents, and meet the EN60601-1:2005 safety standard (type BF). For TBI monitoring,

it requires the device to meet type BF (500µA patient leakage current), but the system has been designed to meet type CF (50µA patient leakage current), which makes it possible to directly monitor the activities of the heart.

The whole system contains 5-stage protections, which have been summarised in Figure 6.12. Starting from the most critical section, mains power supply, a certified medical-grade isolation transformer has been applied. This is the most important power isolation, as It provides safe and isolated power to the system, instead of the un-isolated power from mains. In this set-up, any unexpected external failure from mains will not affect the system, the operators, or the patient.

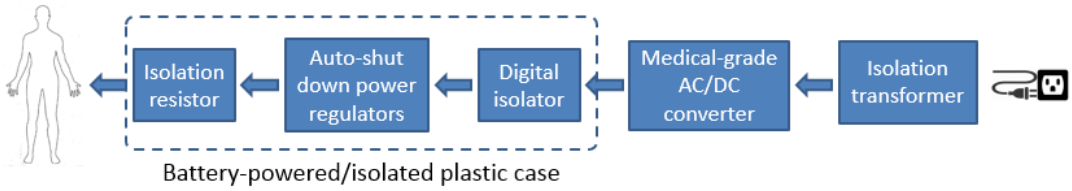

Figure 6.12: Schematic of the safety protection chain

As discussed, a medical device should take both the normal operation and single fault condition into consideration. The TBI box is powered by 240V AC, and this voltage can be fatal to human if the isolation transformer does not function. To avoid this risk, a medical-grade AC/DC converter has applied. The converter is able to govern the leakage current within the safety level, as well as protect the system when an electrical failure occurs, preventing the 240V AC power from going into the analog ECoG board or the patient.

As mentioned in Chapter 5, a digital isolator (opto-isolator) has been placed on the ECoG analog board, to prevent any unexpected large power spikes from the digital board and the TBI instrumentation box. The isolator can protect as much as 5kV voltage shock, without damaging its protected circuitry, which effectively isolates the monitored patient. In a single fault condition, even if the digital transmission line somehow becomes live (240V AC), the analog board and the monitored patient are still well protected.

In terms of the head-stage board itself, it needs to be placed on the patient bed, which makes it vulnerable to mechanical load, which can cause electrical failures. As the power regulators supply current to other components, these regulators are likely to be first overheated if there is any electrical failure on the board. In such cases, the connection pins on the overheated

regulator suffer the risk of being de-soldered. If the local temperature reaches the melting point of the solder paste, the components will disconnect and fall off. Since the heat goes off once the components are disconnected, the solder paste turns in the solid form again. Therefore the disconnected components can re-join the circuit board at any random place, which potentially causes unexpected circuit failure and harms the patient. To avoid any overheated situation, the power regulators used in this design, have internal temperature sensors and auto-shut down functions. As the ambient temperature exceeds a certain threshold (70˚C), the regulators will automatically shut down, stop providing any current to the board, and therefore protect the board and the monitored patient.

In addition, since ECoG analog board has direct connections to the electrodes that are connected to the patient's brain, it requires extremely careful safety consideration. Apart from all the effective protections, to prevent any significant leakage current from the circuit board flowing back to the patient, a 100K isolation resistor has been added to each monitoring channel, limiting the theoretical largest leakage current to 50μA. More specifically, in the worst-case scenario, both power supplies (± 2.5V) are shorted under an electrical failure, the largest patient leakage current is:

$$\mathrm{I} = \frac{2.5V - (-2.5V)}{100k\Omega} = 50\mu A \tag{6.1}$$

As mentioned in Chapter 5, to avoid any clinical contamination or electrical fault due to operation, the analog board is physically shielded in a plastic box with touch-protected connectors (Figure 5.23). It helps to minimise the risk of electrical faults, electrical static discharge (ESD), and unnecessary external force to the PCB during clinical operations, which effectively lowers the electrical risk of the system and significantly extends the life time.

6.5.5 Classification of electrical medical device

To provide a reasonable assurance and effectiveness to a certain medical device, it should be categorised as one of the following three types (Figure 6.13):

a. Class I device: a device that provides a reliable protective earth, so that all accessible metal components are not able to become live, in the event of a basic insulation failure.
b. Class II device: a device that does not have a protective earth, but maintains double or reinforced insulation (typically a plastic enclosure).

c. Class III device: a device with internal power source, normally a battery, that no voltage in operation is higher than the safety extra low voltage (SELV), 25VAC or 60VDC.

In addition, if a battery-operated device has external connection, directly or indirectly connected to the mains, it must be safely tested as either class I or II device.

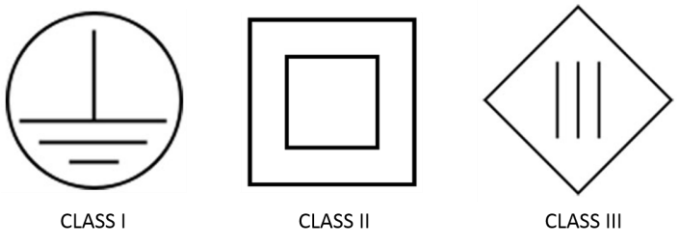

Figure 6.13: Medical device class symbols

As for the TBI box, even though all the frames are made of aluminium, they are not electrically connected to any internal device, power supplies, or earth. Each internal element has its own enclosure with protective earth, and they are placed away from the frame. When an insulation failure occurs, the metal frame of the TBI box cannot become live. Therefore, it belongs to class II. In addition, the analog head-stage box should be classified as well. It is a battery-operated (+4.8VDC) device, which should belong to class III. However, it has external connections, via the digital cable. In practice, the PCB is properly shielded by a plastic enclosure, which reinforces the insulation. Hence, the analog head-stage box should be regarded as a class II device. The battery-powered wireless potentiostat, described in Chapter 7, would be class III device, as it has no external electrical connections.

6.6 Clinical set-up and data

Initially, each individual monitoring electronics in the TBI instrumentation box has been tested in the lab. By pumping in prepared sample solutions and measuring different parameters by relevant sensors, the user is able to mimic the clinical monitoring environment. After testing individual parts, the box is sent to the physics department of King's College hospital to conduct the safety test. A medical instrument needs to pass all the essential regulations and safety tests, before it can be applied on patients. After it has successfully passed the safety test (receipt is attached in appendix 6.1), the box is ready to be used for clinical TBI monitoring in King's College Hospital (KCH).

After several validation tests, the TBI instrumentation box has been moved to the ICU in KCH, to monitor and collect clinical information from TBI patients. The clinical set-up, schematic, and relevant clinical data are shown in Figure 6.14. The data in the figure shows a spreading depolarisation event (indicated by the potassium concentration changes) and corresponding neurochemical changes (glucose and lactate)[4].

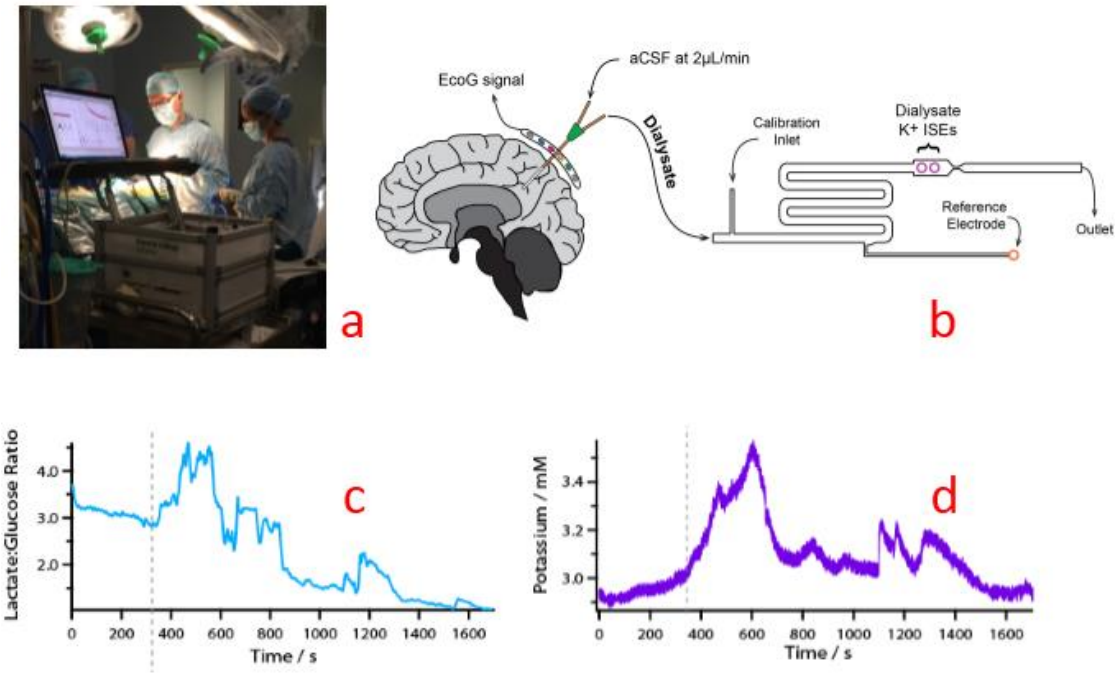

Figure 6.14: Clinical set-up, schematic, and example data for monitoring a TBI patient

(a) is the clinical environment when using the TBI box to monitor a patient. (b) is the schematic of the experiment. Stripe electrodes were used to detect the electrical activity of the brain, and the dialysate was extracted via a microdialysis tubing every 2µL/min. The dialysate was then conveyed to the microfluidic chip, different biomolecules were detected from the ISEs and biosensors. (c) is the lactate/glucose ratio during a spreading depolarisation (SD) event, which started from t = 310s (labelled as a dot line). The ratio increased, which indicates a depletion of local energy and blood supply in the brain tissue. (d) is the relevant potassium changes during this SD event. The concentration increased (depolarised) at the about same point, reached the peak at t = 600s, and decreased back to normal at t = 1600 (repolarised). The trend of the potassium changes also verifies the occurrence of the SD event.

6.7 Conclusion and further development

The chapter mainly discusses the requirement, components, safety regulation, realisation, and clinical tests of the TBI instrumentation box. The box integrates different TBI-related electronic designs discussed in Chapter 4 and 5, and it is able to simultaneously monitor chemical, physical, or electrical parameters from a TBI patient. The box has been carefully

[4] This work has been submitted to the Journal of the Royal Society Interface for publication in 2015. The paper is named as "High-Performance Bioinstrumentation for Real-Time Neuroelectrochemical Traumatic Brain Injury Monitoring".

designed to meet the medical safety regulation (IEC60601:2005), and it limits the leakage current to 50μA under single faulty condition.

In addition, this multimodal box design also improves the screen integration in the clinical environment. To some extent, it helps to improve the clinical care standard, as multiple screens around a patient bed often introduce confusion to the clinical team and it may even result in a wrong treatment to the patient. The multimodal monitoring design only utilises one screen and one recording software. It is able to display up to 16-channel information. Another practical issue in ICU is the cable congestion as multiple monitoring equipment are connected to patients. This increases the requirement of wireless solutions on the existing TBI-related electronics, which will be discussed in Chapter 7 and 8.

The system developed so far is only capable of showing electrical outputs in real time. These data can be processed afterwards, however they cannot be interpreted to real-time neurochemical concentration changes that actually help the clinical team in the ICU or the operating theatre. The main barrier from converting the raw electrical output to the concentration is the sensitivity of a biosensor. The sensitivity can vary significantly during a long-term monitoring process, which means the same electrical output can correspond to totally different neurochemical concentrations. To allow the system to provide real-time concentration outputs, a wireless-controlled microfluidic-based sensor auto-calibration system has been developed, which will be discussed in Chapter 9.

Chapter 7: Wireless Electronic Implementations for TBI Monitoring

7.1 Overview of wireless technology

Driven by the revolution in portable computers, tablets, and smartphones, wireless technology has been transferred into low-cost, high-performance, low-noise miniaturised devices. The advantages of using this technology in a clinical environment is clear: patient access, mobility, cost, and ability to monitor at home or on-the-move.

- As more and more electronics are involved in the clinical environment, the congestion caused by electronic signal and power cables becomes a major issue in daily medical practice.
- The cost of high-quality electronic transmission cables and connectors are generally much more than electronics themselves.
- With all the monitoring cables plugged in, the patient's mobility is also extremely confined. On the one hand, the patient is not able to move freely even when he/she is conscious; On the other hand, doctors are unable to acquire the valuable data from free walking or standing patients [91, 92].

For example in the ICU of King's College Hospital, nurses have to record patients' health conditions bed to bed every half an hour, because most of the monitoring devices have wired connections and each bed has its own set of monitoring devices. Due to the current monitoring set-up, nurses are unlikely to report any emergency immediately if a suspicious event happens to the patient.

Recent decades have seen rapid development and great achievement in continuous cable-free monitoring for medical purposes, such as monitoring vital signs in ICUs [93], remote monitoring chronically ill patients [94, 95], monitoring people in their daily life and providing early detections for various diseases [96], and assisting living of the elderly at home [97]. Therefore, the mobilisation of monitoring electronics becomes the main trend of improving monitoring quality in health care. Equipping wireless clinical monitoring electronics provides better access to clinical information, creates neater surgical environment, reduces the cost, offers immediate medical action to patients in ICUs, and eventually improves the quality of the whole healthcare system.

7.2 Comparison of different wireless techniques in ISM band

There are a variety of Radio Frequency (RF) protocols that can be used to create wireless networks. Some protocols are proprietary to individual vendors, and others belong to the common industry standard. The worldwide available band is the 2.4GHz Industrial, Scientific and Medical (ISM) radio bands, which can be used to develop wireless medical devices with few restrictions. The brief comparison of features and applications with several popular wireless techniques in the ISM band are shown in the Table below [98].

	Zigbee and IEEE 802.15.4	**Wi-Fi and IEEE 802.11**	**Bluetooth and IEEE 802.15.1**
Major Application	Monitoring and Control	High-speed Internet	Device Connectivity
Battery life	Years	1 week	1 week
Number of channels	16	14	79
Channel bandwidth	2MHz	22MHz	1MHz
Separation bandwidth	5MHz	5MHz	1MHz
Transmission rate	250 Kbps*	Up to54 Mbps**	2Mbps**
Transmission range	100+ meters	50-100 Meters	10-100 Meters
Advantages	Low power, Cost	Speed, Ubiquity	Convenience

*Kbps: Kilobits per second ** Mbps: Megabits per second

Table 7.1: Comparison of properties of different networks

The data in the table are reproduced from [99].

Wi-Fi is a local area wireless technology, based on the IEEE 802.11b/g/n standards [100]. The data rate is generally as high as 54 Mbps (IEEE 802.11g), which is much more than required for bio-signal transmissions. The potential issues of applying Wi-Fi technology are the power consumption, connection accesses, and data security. As TBI devices are most likely to be used in hospitals, where Wi-Fi access is limited, an external Wi-Fi router is required to allow the monitoring devices to communicate in Wi-Fi environment. In addition, Wi-Fi protocol potentially has the security issue. As all the end devices on the same Wi-Fi network can share information, the patient data can be divulged.

The other two protocols, Bluetooth (based on the IEEE 802.15.1 standard [101]) and Zigbee (based on the IEEE 802.15.4 standard [102]) have similar features. Both protocols support point-to-point communications, with security authentications and paired device address acknowledgement. The fundamental differences between these two protocols are data rate and transmission range. A standard Zigbee device is theoretically able to transmit data at up to 250 bits per second (bps), with a distance of more than 100 meters outdoor. A Bluetooth

device is able to transmit at about 2Mbps, with only 10-meter range. Some Bluetooth devices are able to reach as much as 100 meters, but they compromise with the data rate, which makes it work as a different version of Zigbee devices.

As discussed, both protocols have the potential to be implemented on TBI monitoring devices. In this chapter, the properties of the Zigbee protocol, Zigbee-based wireless modules, and relevant implementations will be discussed. In addition, the advantages and potential drawbacks of applying Zigbee modules to TBI electronics will be also demonstrated. The implementations of Bluetooth modules will be discussed in Chapter 8 and 9.

7.3 Zigbee module implementation

The IEEE 802.15.4 standard, developed by the institute of Electrical and Electronics Engineers (IEEE), is a low-rate wireless personal area network (LR-WPAN), which defines the physical layer (PHY) as well as media access control (MAC) to provide network functionality with low data rate, simple connectivity, low cost, and long battery life communication [102]. More importantly, the transmit scheme used in 802.15.4 has been designed to promote co-existence, which makes devices work in this standard more reliably. The study from *Petrova M. et al.* (Figure 7.1) [103] shows the relationship between bit error rate (BER) and signal-to-noise ratio (SNR) among different standard in the ISM band. Compared with other standards, IEEE 802.15.4 shows an exponential increase in reliability (BER value) at any given SNR. The transmission performance is 7-18dB better than 802.11b (Wi-Fi) and Bluetooth.

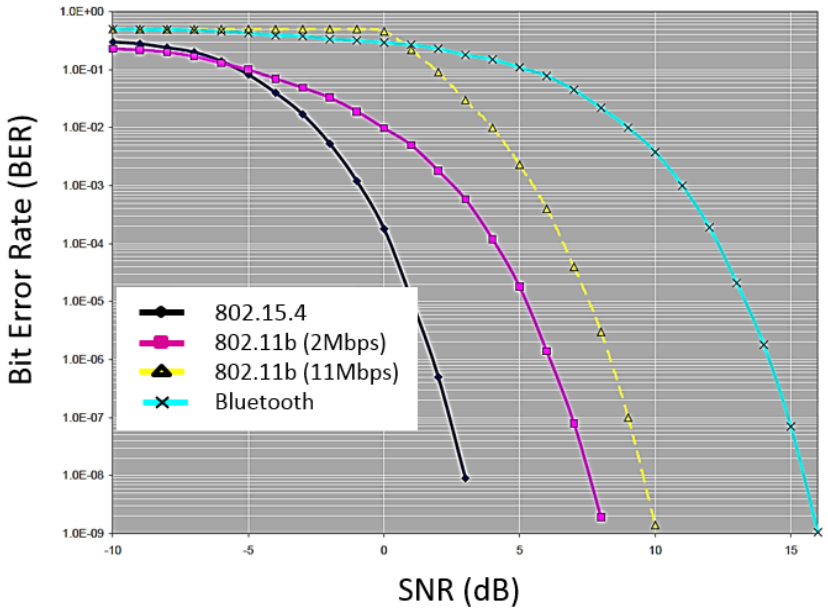

Figure 7.1: The BER to SNR relations among different protocols in the ISM band

The figure is adapted from [103]. Zigbee belongs to the protocol 802.15.4, and Wi-Fi belongs to 802.11b.

Based on this standard, Zigbee protocol has been developed by the Zigbee Alliance, which is a group of companies that cooperate to work on this network protocol [104]. Zigbee is commonly used in low-speed applications that require long battery life and secure wireless communication. It provides wireless solutions to smart homes, buildings, and personalised healthcare systems. In addition, Zigbee devices are generally simpler and cheaper than other local wireless network in the ISM band, like Wi-Fi and Bluetooth.

7.3.1 Xbee module introduction

IEEE802.15.4 and Zigbee products have been regularly demonstrated around the world, and the Zigbee module used in the project is Xbee, from Digi International. The wireless Xbee module is mainly a system on chip (SoC), utilising the Zigbee wireless protocol and providing a low-cost, low-power, point-to-point wireless network solution. Many Xbee modules have been released for different applications, and the one used in this project is Xbee series 2. Xbee modules have their own configuration software, X-CTU, which allows users to either remotely or locally program it. The dimension of the Xbee S2 module is 27.6mm × 24.3mm with 2 10-pin connectors, whose pitch is 2mm (Figure 7.2).

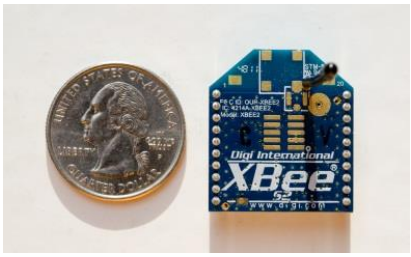

Figure 7.2: An Xbee S2 module

The size comparison between an Xbee S2 module and a US quarter coin is show in the figure, which is extracted from [105].

7.3.2 The Xbee S2 module

As Figure 7.3 indicates, an Xbee module has 20 pins, and pin 1 and pin 10 are respectively power and ground. Pin 2 and 3 are the built-in Universal Asynchronous Receiver Transmitter (UART), which can be used to communicate with PC or a microcontroller. The module has 7 10-bit built-in ADCs, which are located from pin 15 to 20 and pin 11. The reference voltage for the ADCs is controlled by pin 14, which is equal or less than the power supply, 3.3V. In addition, the module also features a sleep mode that allows the module to enter the sleep mode to save power when it is idle. The sleep mode is controlled by pin 9, active low. As no DAC is integrated in the module, it utilises pin 6 and 7 to generate Pulse-width Modulation (PWM) signals to mimic analog outputs. In practice, most of the IO pins have several functionalities, which can be configured in the X-CTU software. In addition to the configuration in the software, an Xbee can also be remotely configured by sending an Application Programming Interface (API) packet from another Xbee module.

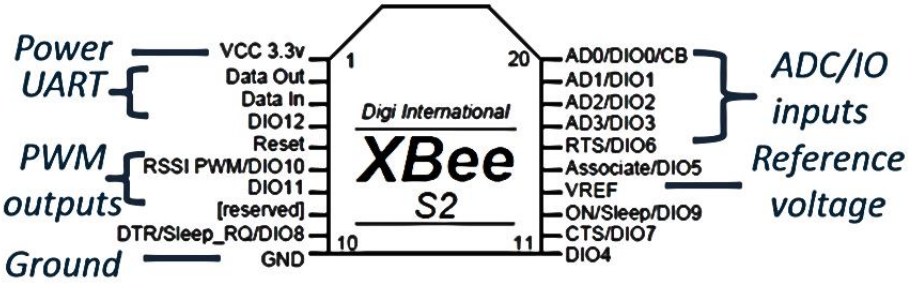

Figure 7.3: The pin out for Xbee S2 module

7.3.3 Electrical characteristics of the Xbee module

An Xbee Module works in 3.3V CMOS logic voltage level, and the operating voltage is 2.1 – 3.6V. As mentioned above, Xbee module has sleep modes to save power. Two different sleep

modes can be configured: Hibernate mode and Doze mode, and the relevant characteristics are summarised in Table 7.2.

	Active	Doze mode	Hibernate mode
Power Consumption	40mA	50µA	10µA
Wake-up time	NA	2ms	13ms

Table 7.2: Comparison between different sleep modes in Xbee

Table 7.1 shows that Zigbee devices are capable of transmitting data with maximum 250k bits per second (bps), over 100 meters. However, due to the overhead of the protocol and duplex [98], the actual theoretical maximum data rate is about half of that. In practice, Xbee only works in a good condition when the data rate is below 80k bps. If transmitting data in a very high data rate, the signal may get corrupted and deteriorate the bit error rate (BER) [98].

Xbee modules have two different operating modes: AT (transparent) mode and API (command) mode. In AT mode, Xbee simply works as a cable replacement. It receives the data from its RX pin, and transmits them wirelessly to its paired Xbee module, without any data processing. The data can be also generated from the Xbee itself (ADCs and I/O pins) using a standard data format. When working in API mode, Xbee is able to send or receive data blocks (frame-based data) to and from a radio's serial UART port. The API mode allows users to change Xbee setting, view and analyse the sending/receiving data. When connecting the Xbee in the API mode, a MCU or a computer can remotely control the setting of its paired Xbee module.

7.3.4 Communication security and pin ID setting

When paring Xbee modules before a transmission, they can be recognised and distinguished by two addresses: extended address and network address. Inherently, each Xbee module has its own unique serial number, which comes from the factory setting. It contains 64 bits, and it is called as the extended address. In addition, when configuring Xbee in the software, each Xbee needs to be given a 16-bit Pin ID, which is the network address. To pair with another Xbee module, the destination address needs to be matched with its paired module's address (Figure 7.4). For example, the transmitter module is set as:

DL – Destination Address Low = 1234
MY – 16-bit Source address = 5678

In order to activate the transmission, the relevant receiver needs to be set as:

DL – Destination Address Low = 5678
MY – 16-bit Source Address = 1234

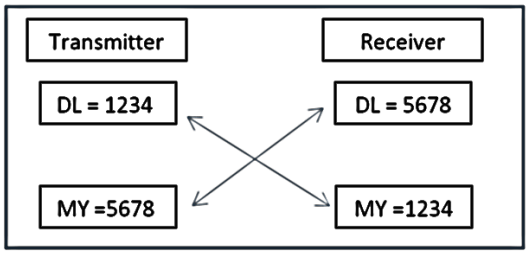

Figure 7.4: Xbee module address matching

Only when Xbee transmitters and receivers have the paired pin ID (network address) can they communicate with each other. Note that network address can be changed, whereas the extended address is pre-programmed and cannot be changed. This feature allows a module to fill in any Xbee network, while maintaining its unique identification.

7.3.5 Data format

Xbee modules follow the general IEEE 802.15.4 Medium Access Control (MAC) and Physical layer (PHY) formats, which is demonstrated in Figure 7.5.

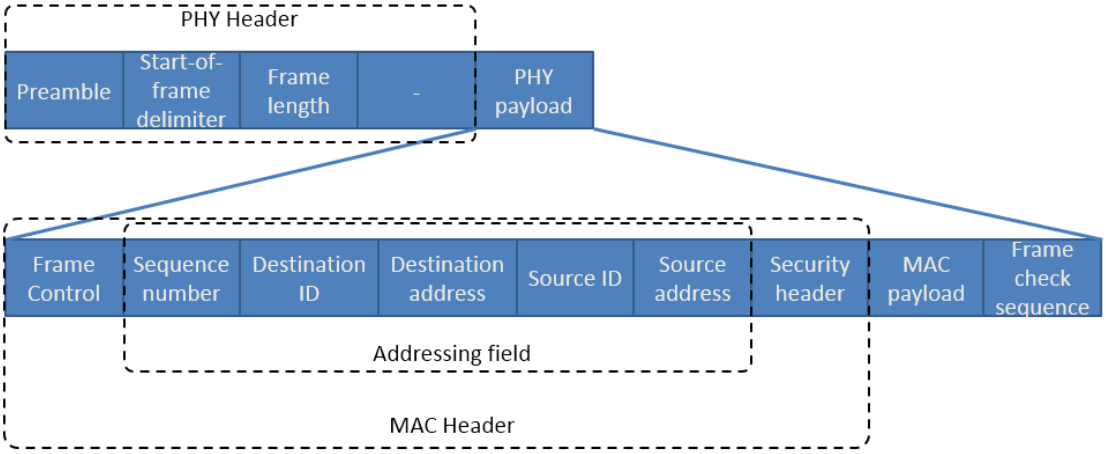

Figure 7.5: General MAC and PHY formats for the IEEE 802.15.4 standard

The figure is adapted from [106]. The data format for an Xbee module is constructed on the basis of the general IEEE 802.15.4 standard

For example, the transmitting Xbee module is configured as shown in Table 7.3.

Pin	Function
17	Digital input
19	Analog input
20	Analog input

Table 7.3: Pin configuration of the Xbee transmitter

After re-programming the transmitting the Xbee module, another Xbee module is connected to the host computer and configured as its paired receiver, working in the API mode. By the time the transmitting Xbee is properly wired and powered up, a string of hex values should appear on the serial monitor, which displays in hexadecimal format and shows all the information from this transmission. Figure 7.6 shows one complete set of the data block, and the explanation of each byte is also demonstrated.

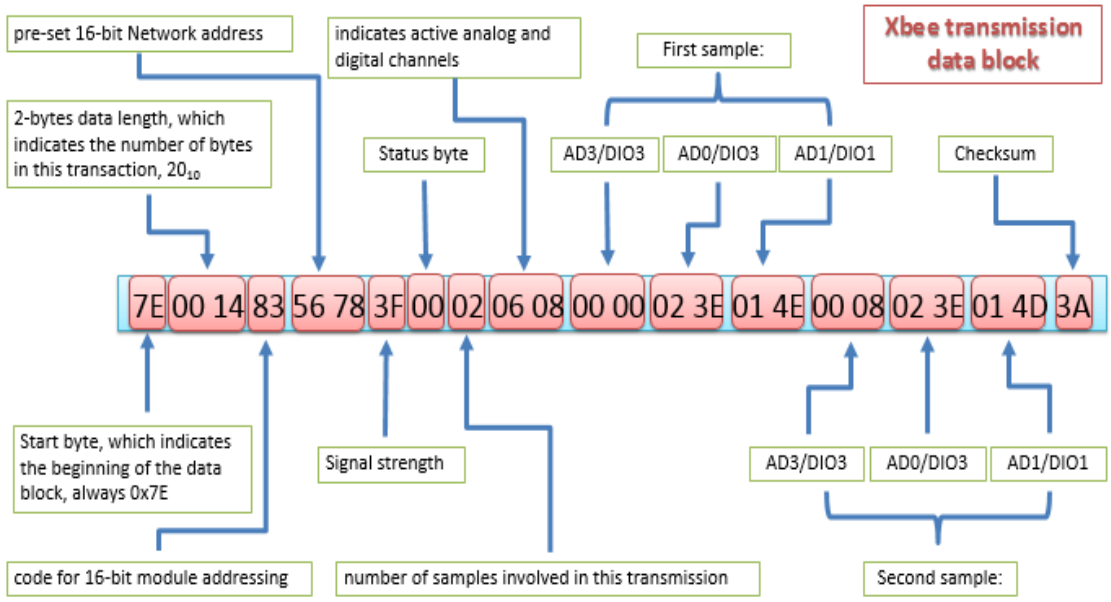

Figure 7.6: An example data stream from an Xbee receiver

As Figure 7.6 describes, the pin ID for the transmitter is set as 0x5678, and two samples are collected before sending the string. The two bytes data (0x0608) is to indicate the active channels, on the basis of the protocol described in Table 7.4. In the table, A5-A0 are corresponding to analog channel 5 to 0, while D8-D0 are corresponding to digital channel 8 to 0. These bits are active high, which means “1” on a certain bit indicates the channel is activated. As the 2-byte data for channel activations are 0x0608, which is 0000 0110 0000 1000 in binary, this indicates analog channel 0, 1, and digital channel 3 are activated.

	First Active-Signal Byte								Second Active-Signal Byte							
	First Hex Character				Second Hex Character				First Hex Character				Second Hex Character			
Bits	B7	B6	B5	B4	B3	B2	B1	B0	B7	B6	B5	B4	B3	B2	B1	B0
function	X	A5	A4	A3	A2	A1	A0	D8	D7	D6	D5	D4	D3	D2	D1	D0
Data	0	0	0	0	0	1	1	0	0	0	0	0	1	0	0	0

Table 7.4: Bit allocations in the active-channel byte

Table 7.4 shows which analog or digital channels are activated. Table 7.5 illustrates the bit arrangement for all the information in the activated digital channels. I/O pin 3 is low during the first sample (0h0000), and it turns high during the second sample (0h0008).

	First Digital-Data Byte								Second Digital-Data Byte							
	First Hex Character				Second Hex Character				First Hex Character				Second Hex Character			
Bits	B7	B6	B5	B4	B3	B2	B1	B0	B7	B6	B5	B4	B3	B2	B1	B0
function	X	X	X	X	X	X	X	D8	D7	D6	D5	D4	D3	D2	D1	D0
Data	0	0	0	0	0	0	0	0	0	0	0	0	1	0	0	0

Table 7.5: Digital-data bytes in the block

After 2-byte digital status, 2-byte readings from each analog channel are transmitted. Since the built-in ADCs have 10-bit resolutions, the 2-byte data ranges from 0x0000 to 0x03FF. If multiple channels are sampled and transmitted at the same time, the data sequence is from the first analog channel (AD0) to the last one (AD6), if applicable. The digital data received for AD0 is 0x023E, with the reference voltage as 1.2V. Therefore, the analog voltage is

$$\frac{0x23E}{0x3FF} \times 1.2\,V = \frac{574}{1013} \times 1.2\,V = 0.673\,V \tag{7.1}$$

The last byte is the checksum byte. The transmitter calculates the value based on the previous data in the stream. The receiver also calculates a checksum on the basis of the received data. These two checksum will be compared to check the accuracy of the transmission. If the checksum values do not match, a transmission error will occur and the receiver will discard the received information without generating any notice. This checksum mechanism ensures the accuracy of each successful data transmission, however this mode cannot be used to evaluate the bit error rate (BER) of the wireless transmission, as it automatically discards unsuccessful data block.

When calculating the checksum, only the data after the “channel length” byte and before the “checksum” byte itself are taken into account. As the checksum contains only one byte, the data may have overflow during calculation, and only the two least significant (right-most) hexadecimal digits are left. After the summation, subtract the summed value from 0xFF, and then the answer is the checksum.

For example, in this data stream, the theoretical checksum should be calculated as:

$$\begin{aligned} Checksum = 0xFF \\ - (0x83 + 0x56 + 0x78 + 0x3F + 0x00 + 0x02 + 0x06 \\ + 0x08 + 0x00 + 0x00 + 0x02 + 0x3E + 0x01 + 0x4E \\ + 0x00 + 0x08 + 0x02 + 0x3E + 0x01 + 0x4D) = 0x3A \end{aligned} \quad (7.2)$$

This is the same as the received checksum value.

7.3.6 PWM output

Since the Xbee module does not feature any DAC, the best way for the Xbee module to emulate an analogue signal is using PWM. The PWM outputs are consisted of square-waves with 3.3V peak amplitude and variable duty cycles. The PWM signal can be decomposed into a pure DC component (“analog part”) and a new square-wave with the identical duty-cycle, but with zero time-average amplitude (Figure 7.7) [107].

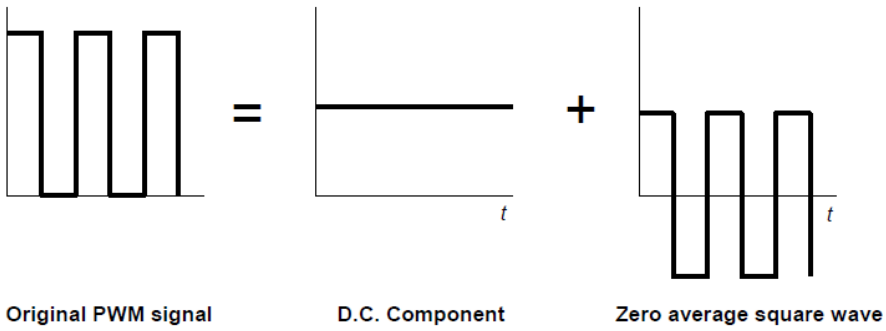

Figure 7.7: Decomposition of a PWM signal

The original PWM signal can be decomposed as a DC component (bias) and a non-bias same-frequency square wave. The figure is extracted from the TI application note [107].

The high-frequency square wave has average amplitude as 0, which means the amplitude of the signal is only based on the DC components. In order to preserve the DC component and remove the high frequency pulses, a low-pass filter needs to apply (Figure 7.8). The quality of

the output analogue signal highly relies on the ability of the low-pass filter to eliminate the high-frequency components of the PWM signal. If applying a filter with very low cut-off frequency, the bandwidth of the acquiring signal will be limited and the response speed is slower due to the integration time in the low-pass filter; If applying a filter with very high cut-off frequency, the high-frequency components will not be completely eliminated, which remains to be a major noise source of the output signal.

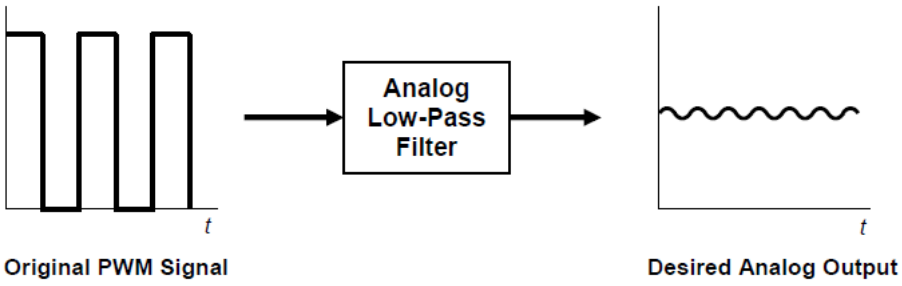

Figure 7.8: Effect of adding a low-pass filter on PWM

An analog low-pass filter can smooth a PWM signal and convert it into an analog output with fluctuations. The figure is extracted from the TI application note [107].

The aim of the design is to measure neurochemical changes in the human tissue, which has very slow variation. Therefore a RC filter with low cut-off frequency has been applied after the PWM signal, to smoothen the PWM signal and recover the optimum analog components from the mixed signal.

Even though each Xbee S2 module has 4 ADCs, only two PWM outputs (PWM0 and PWM1) are available. Based on the datasheet, PWM0 at the receiver end only updates the input analog signal from ADC0 at the corresponding transmitter, and PWM1 only updates ADC1. It indicates that each pair of Xbee modules can only transmit up to 2 different analog signals.

By utilising the built-in ADCs, the module is able to be easily integrated with other TBI devices, such as the potentiostat and ECoG analog board. This allows the devices to detect and transmit the patient's information wirelessly and securely. The details of the integrations will be discussed in the following sections.

7.4 Wireless Xbee-based potentiostat

As discussed in Chapter 4, a potentiostat is the electronic circuit used for controlling the three-electrode system in most electrochemical reactions. On the basis of the potentiostat, the bi-

potentiostat and poly-potentiostat have been also designed, which are capable of controlling two and more than two working electrodes, respectively [108].

To measure the electron exchanges from the electrochemical reaction, either resistive or capacitive method can be used, and both methods have been demonstrated in Chapter 4. The capacitive method (DDC114-based) requires a microcontroller to operate. To maintain a miniaturised design, the built-in ADC in the Xbee module has been utilised, and therefore the traditional resistor-based transimpedance circuit has been applied.

7.4.1 Xbee-based wireless potentiostat transmitter

The core potentiostat design is similar to the one described in Chapter 4, and the only difference is the power management units. The power used in this design is +4.8V, which is consisted of 4 AA batteries. To generate the necessary negative power supply to the op-amps, a voltage inverter, ICL7660 from Intersil, has been applied. In addition, a 3.3V Low Dropout (LDO) regulator, TPS73633 from TI, has been used to regulate the power to the Xbee module. The connectors have been mounted on the bottom layer away from the sensitive input ends. The appearance of the transmitter is shown in Figure 7.9.

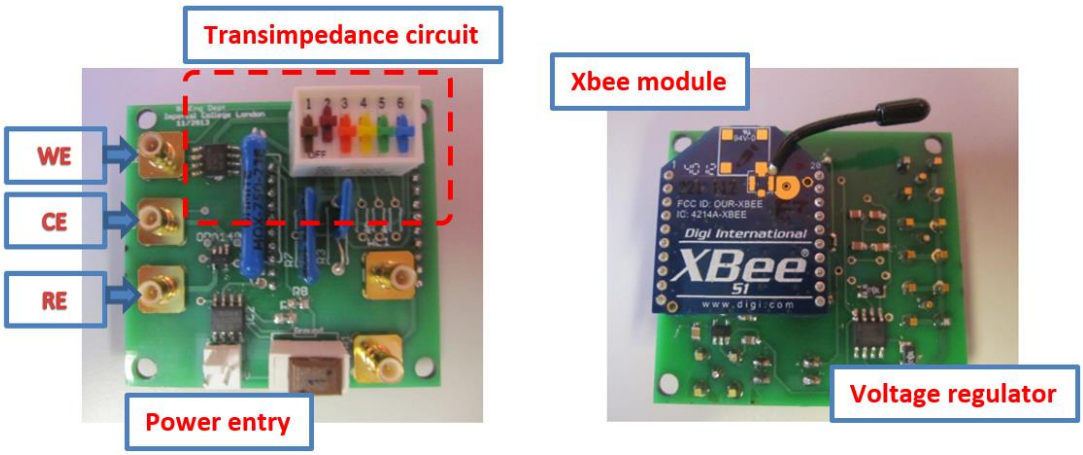

Figure 7.9: Appearance of the wireless potentiostat transmitter

The figure on the left shows the top view of the wireless potentiostat transmitter, which is similar to the one described in Chapter 4. The figure on the right shows the bottom view of the board with an Xbee module mounted.

7.4.2 Wireless potentiostat transmitter setting

In this experiment, the Xbee module needs to activate one ADC channel, set the pin ID, and destination address. In order to make the ADC work properly, pin V_{REF} should be connected to 3.3V to provide correct reference voltage for ADCs. Since the device is used for monitoring

slow neurochemical changes, the sampling rate has been set as 10 Hz (once every 100ms) to reduce the power consumption and high-frequency noise. The detailed setting from the X-CTU software is shown blow:

DL – Destination Address Low *= 1234*
MY – 16-bit Source Address *= 5678*
D0 – DIO0 configuration *= 2 – ADC*
IT – Samples before TX *= 01 (TX sends data every time it samples)*
IR – Sampling Rate *= 64 (0x64 = 100_{10} ms)*

In summary, by setting the Xbee transmitter as shown, D0 (pin 20) has been activated as an ADC while other I/O pins are disabled to save power. The module sends one sample each time, and the sampling period is 100ms. Most importantly, it only sends data to its receiver, of which "MY address" is 1234.

7.4.3 Xbee-based wireless potentiostat receiver design

After configuring the wireless potentiostat transmitter, the Xbee receiver design will be discussed in this section. Two different methods are viable to implement the receiver:

a. The module can be connected with a microcontroller, which works as a decoder, and send the useful digital information to an output DAC. However, this method requires extra components and programming.
b. The second method is to utilise the built-in PWM signal to mimic analog outputs. As two PWM output channels have been implemented in the module, a receiver is able to output "analog signals" from two different channels (ADC0 and ADC1).

In the thesis, option b (PWM output) has been selected, as it does not require extra ICs, which helps to minimize the size, cost, and power consumption. The overall size of the receiver is 26mm × 30mm excluding the antenna (Figure 7.10). The circuit board has been designed to maintain the same shape and pin out of the Xbee module, which allows the Xbee module to be mounted on top of the receiver PCB.

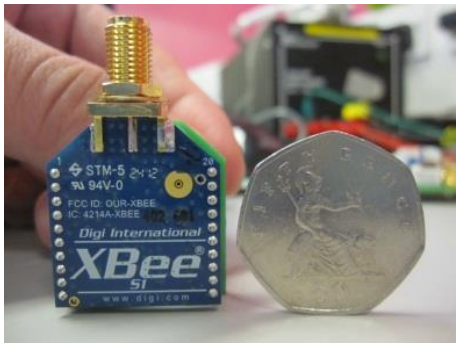

Figure 7.10: The appearance of the Xbee receiver

The receiver is 26mm × 30mm, roughly the same size of a British fifty pence coin. An external antenna can be connected to the SMA connector for better connectivity, which is not included in the figure.

In addition, the receiver has been design to get power from the PowerLab, via a DIN connector (Figure 5.4), so that the receiver PCB does not require any external power source and it helps to minimise the overall size.

7.4.4 Xbee potentiostat receiver setting

In the receiver setting, most of the I/O pins are irrelevant, but the function of accepting API packet needs to be activated, which allows the receiver to understand the arriving data frame. All the unused pins should be disabled to save power. The detailed configuration is shown below:

DL – Destination Address Low	*= 5678;*
MY – 16-Bit Source Address	*=1234;*
AP – API Enable	*= 1 – API ENABLED;*
IA – I/O Input Address	*= FFFF (lets the receiver accept all I/O data packet);*
P0 – PWM0 Configuration	*= 2 – PWM OUTPUT;*
PT – PWM Output Timeout	*= 00 (disable the timeout period for the PWM output).*

7.4.5 Xbee wireless potentiostat test

In this section, three different types of experiments have been conducted to test the performance of the Xbee-based wireless potentiostat.

Current source test

As for the first bench test, a current source has been selected to evaluate and calibrate the wireless potentiostat system. The transmitter is powered by a battery pack, while the receiver is connected and powered from the PowerLab. By passing through the 10GΩ transimpedance resistor and relevant analog signal processing units, the over gain of the system is 1.14nA/V. In figure 7.11, the starting current is 1nA, following by 5 0.1nA steps. The graph shows the raw

data from the experiment without applying any filter. Normally, the 50Hz interference to the experiment is significant. Without apply a digital low-pass filter, the output signal is not able to be observed clearly. However, in this set-up, the power supply is a battery pack, which eliminates the 50Hz components from the mains. In addition, the output PWM has been attenuated by a first-order analog low-pass RC filter, and therefore the output signal becomes clear. It does have poor time response (τ) as a trade-off, due to the large R and C in the filter (τ = RC). The standard deviation of the signal is about 5mV in voltage (200 samples), and therefore 5.7pA in current.

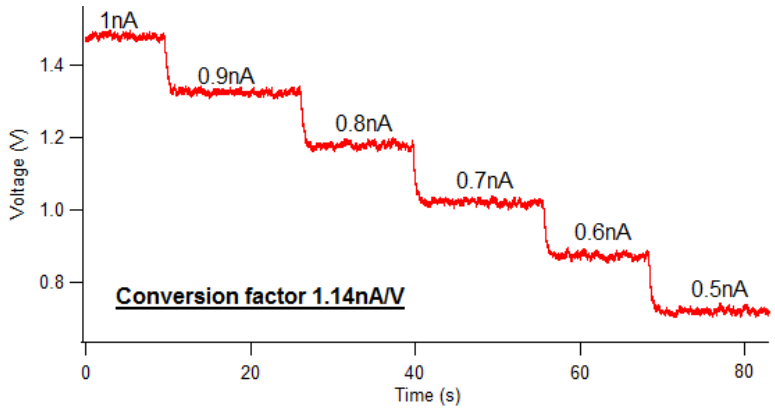

Figure 7.11: Wireless signal response with current source

0.1nA steps generated from KETHLEY 6221 DC/AC current source, recorded from LabChart via Xbee-based wireless potentiostat. The data is presented with applying any digital filter. Experimentally, it has 0.6V offset, due to the 10GΩ transimpedance resistor. Therefore the output voltage is equal to the offset + current × conversion ratio.

Three-electrode system test

After the validation test from a current source, a redox couple has been used to test the sensor-electronics interface and relevant performance. Combined needle electrodes have been prepared as discussed in Chapter 2, and 1mM Ruthenium Hexamine solution has been used in the test. The main reasons of choosing Ruthenium Hexamine are its chemical activity and the reduction current generated from the electrochemical reaction. When applying a negative voltage between the working and reference electrode, it activates the reduction reaction of Ruthenium Hexamine, which requires extra electrons to go into the reaction. Therefore, the electron flows from the signal processing electronics to the working electrode. As the electrons flow out of the circuit, the input current to the transimpedance op-amp is therefore positive. After passing through the transimpedance circuitry, the output voltage becomes negative, as V = - IR. As discussed above, the built-in ADC on Xbee is only able to detect positive input. Another inverter has been added on the board, such that it can detect

the changes from a reduction reaction. During the experiment, different voltages (step changes) have been applied to both wired and wireless potentiostats, and the comparison results are shown in Figure 7.12.

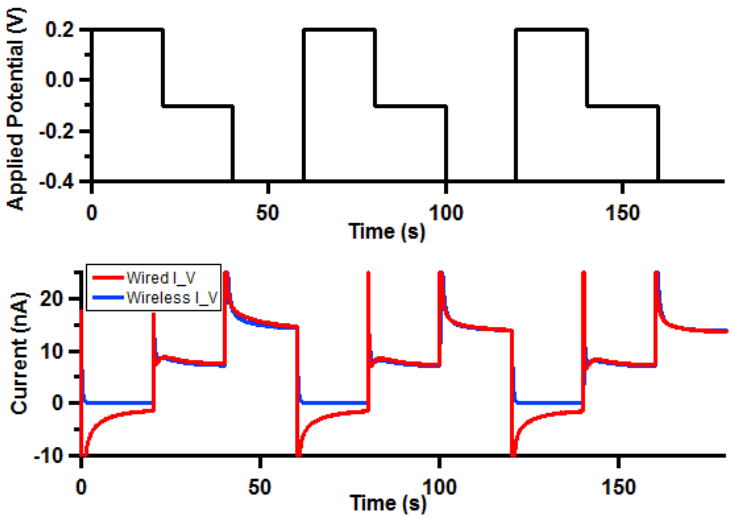

Figure 7.12: Data comparison between wired and wireless potentiostat

The experiment was conducted in Ruthenium solution. The upper figure is the applied potential overall time, while the lower graph shows the corresponding detected current from both wired and wireless potentiostat. The output current in the lower graph was inversed by the electrochemical conversion.

As seen in this figure, the upper graph is the applied potential, which changes between -0.4V, -0.1V, and 0.2V. The relevant response from both circuits is shown in the lower graph. The blue line is the output from the wireless potentiostat, and the red line is the comparison data from a wired potentiostat. When applying negative voltages (-0.4V or -0.1V) to activate the reductive reaction, the response from both potentiostats are very similar (superimposed in the graph), which validates the functionalities of the wireless potentiostat.

However, the wireless potentiostat does not follow the trace of the wired potentiostat when the applied voltage becomes positive. As the applied voltage turns positive, the ruthenium solution undergoes the oxidation, which generates a negative current to the potentiostat. Due to the limitation of the built-in ADC, this wireless potentiostat is not able to detect any negative current. Compared with the current source test, the main difference of the electrode test is that the result shows an immediate spike whenever altering the applied voltage. The spikes are due to the charging current of the double-layer capacitor on the electrode surface, and they can also be recorded from both potentiostats.

Glucose sensor test with HRP

In order to detect the glucose concentration changes with respect to a reduction reaction (negative current to electronic circuits), as discussed in Chapter 4, horseradish peroxide (HRP) has been selected as an extra intermediate reactant. To regenerate HRP, 2 ferrocene molecules are oxidised to ferrocinium ions. These can be then detected at the electrode by reduction (Fc^+ to Fc) at 0V, requiring 2 electrons. These electrons flow from the processing electronics to the working electrode, and therefore it represents as a positive current to the following signal processing units (Figure 4.23).

By pumping different reactors at different speeds, the mixture maintains different concentrations. The glucose concentrations used in the experiment are respectively 0µM, 25µM, 50µM, 75µM, and 100µM, which are the standard values to calibrate a glucose sensor in TBI applications. Figure 7.13 shows a 5-point glucose sensor calibration curve with raw step changes in the mini graph. As the output PWM is able to smoothen the signal, no extra digital filter is added to the data. In the figure, 3 times standard deviations (3 × 14pA) have been labelled as relevant error bars. By plotting a best fit line, the sensitivity of the glucose sensor, b, can be therefore calculated as 15.817 ± 0.228 nA/mM.

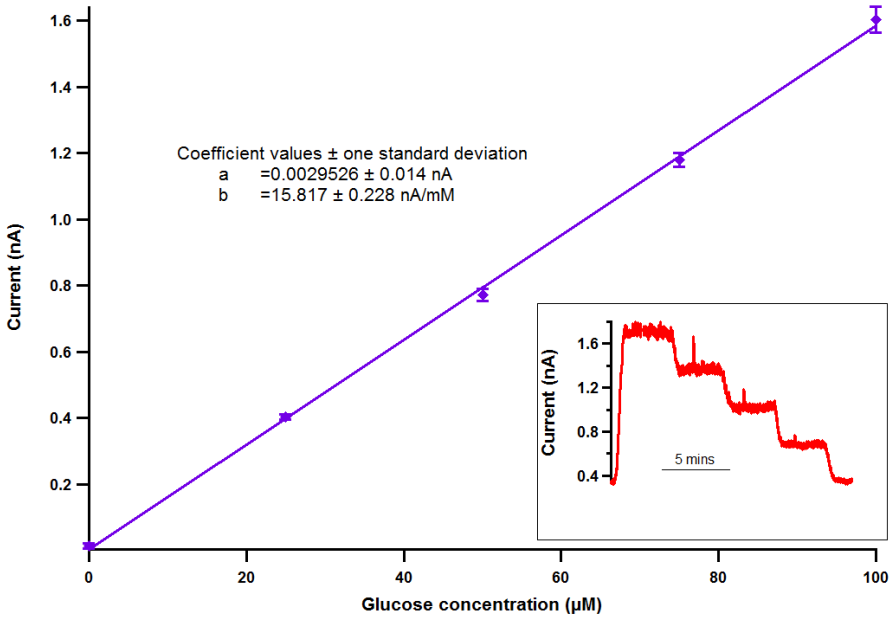

Figure 7.13: Biosensor interface test

The figure shows a calibration curve of a glucose biosensor generated from the wireless potentiostat. The coefficient a is the background current in the experiment, which is about 3pA. The coefficient b indicates the sensitivity of the glucose sensor, which is 15.82nA/mM. The spikes in the raw data are the artefact in the measurement.

7.4.6 Xbee-based potentiostat discussion and further development

In the previous several sections, an Xbee-based wireless potentiostat and the relevant performance tests have been demonstrated. It shows that this wireless potentiostat is a viable design with many potential applications. Both transmitter and receiver have been miniaturised and easy to implement and configure. Especially for the receiver, no external power supplies or microcontrollers are required. The design and relevant tests provide the possibility of implementing a miniaturised wireless potentiostat for monitoring in clinical operations, such as a free-flap surgery[5].

However, the design also has its own disadvantages. As the built-in 10-bit ADC is utilised for the data conversion, the digitalisation error is relatively high. In addition, the detection range of module is too small (0 - 1.2V) and it can only detect unipolar voltages. By adding/removing the inverter, the wireless potentiostat is able to detect any reduction/oxidation reaction. As for the receiver, the PWM output has to go through a low-pass filter to mimic the analog signal, which also limits the sampling rate of the input signal. Furthermore, only two PWM channels are in the Xbee module, which also limits the number of transmitting channels.

In summary, the design has its own advantages and drawbacks, which makes it possible to apply in some situations. The miniaturised design works well with low-sampling-rate bio-sensing applications, where the size of the monitoring device is extremely limited.

7.5 Xbee-based wireless bio-potential acquisition system

An Xbee module can be configured to digitalise input signals from its own ADCs. The relevant setting, circuit design and tests have been demonstrated in the previous sections. However, the 10-bit resolution makes the module unable to detect small signal changes. In addition, some bio-signals, like ECoG and EEG, feature with a negative DC offset. As the built-in ADC can only detect positive inputs, it cannot be implemented as a wireless bio-potential acquisition system.

Based on these limitations, Xbee modules should be configured to the AT mode, working as only a cable replacement. In AT mode, Xbee module transmits all the incoming data to its paired receiver, which in turn sends the data to the host computer via its TX pin. An Xbee

[5] Further tests have been conducted during writing the thesis, and the paper “wireless potentiostat design for monitoring glucose and lactate in a free-flap surgery” is in preparation.

module applies Zigbee-based Digimesh transmission protocol when working in API mode, which is designed for low-speed network. However, when working in AT mode, Xbee can run without any protocol, transmitting data blindly to its paired receiver, which is also called as transparent mode. The advantage of running in the transparent mode is that it does not require a data relay, which effectively reduces the transmission time. However, it requires acknowledgement bytes to indicate the starting bit of the transmission. As running in this mode, extra microcontrollers, ADC, and DAC are required. Consequently, the quality of the transmission is no longer determined by the Xbee built-in ADCs.

As discussed in Chapter 5, a wired-version high-precision low-noise bio-potential acquisition system has been introduced. In this section, the integration of AT-mode Xbee modules with that system will be demonstrated. The head-stage analog board was connected with the monitor-side digital board via a digital cable, and now the cable can be replaced by the wireless modules.

ADS1298 employs the SPI protocol to communicate, whereas the Xbee module only supports UART. An additional signal processor is required to work as a data coordinator. During the ADS1298 spike-debugging process discussed in Chapter 5, Arduino DUE has been used to test the performance of ADS1298 and relevant DAC. Therefore, to reduce the development time, the same development board and similar code have been applied to this application. The only difference in the code is that after completing a full transmission from ADS1298, the processor sends the data to the Xbee module, instead of initialising another SPI transmission with the output DAC. Two acknowledgement bytes, 0xFF and 0xFE, have been added in front of the transmitting data stream, so that the receiver can distinguish the starting point of the data, and therefore correctly split all the data into different channels. As for the receiver part, another Arduino DUE has been used together with the receiver Xbee and the output DAC. The signal flow chart of the overall transmission line is shown in Figure 7.14.

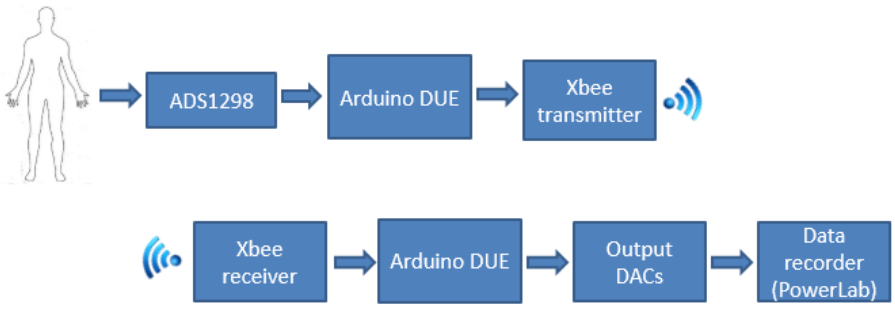

Figure 7.14: Flow chart of the wireless transmission line

By implementing the device in this configuration, the device has been with the signal generator. The testing results are shown in Figure 7.15.

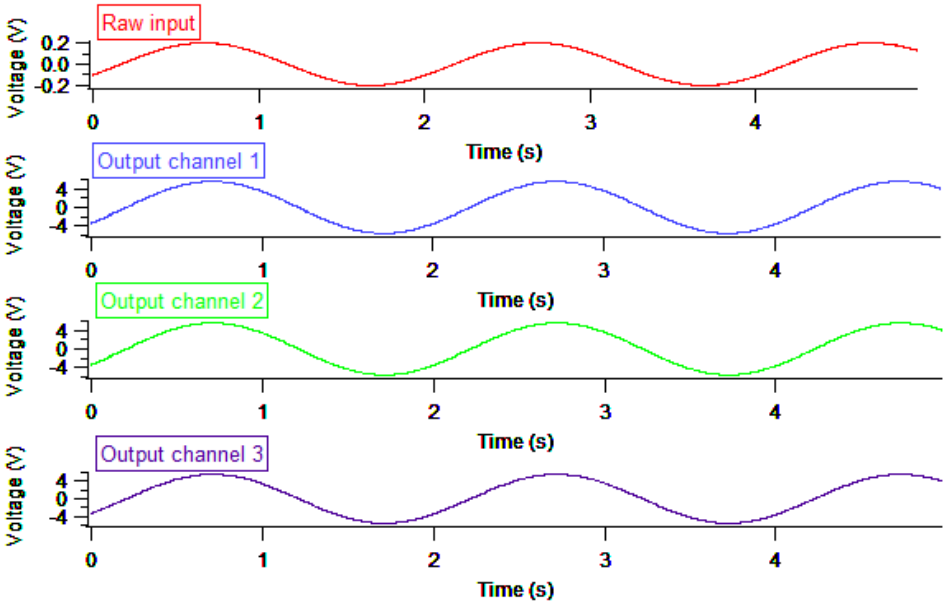

Figure 7.15: 3-channel Xbee-based wireless transmission

As the figure indicates, up to 3-channel wireless data can be obtained without any signal distortion. During the measurement, 0.5Hz 0.4V_{P-P} sine wave has been generated and sent to the system. The overall gain of the system has been set as 27.5. The output signals from the receiver maintain the same sine wave pattern with an aptitude of 11V_{P-P}. The ADS1298 has set to sample at 500Hz (1 sample every 2ms). However, when analysing the data, the frequency of updating sample is 100Hz (1 sample every 10ms), which indicates the system is down sampled. This is due to the speed and accuracy of the wireless transmission. Even though the system is slightly down sampled, it is still capable of monitoring most bio-signals as they change slowly, normally from near DC to 30Hz.

Compared with applying the built-in ADC on Xbee modules, the resolution of the ADC in this design is now 24bit. It allows the system to detect smaller and finer changes of the signal. In addition, the new wireless system is able to detect bipolar changes. 3-channel data can be monitored simultaneously.

As discussed, the data quality is better than utilising the built-in ADC, however, the design still has its own drawbacks. The main issue is the data transmission speed of the Xbee module itself. If one system requires to detect or analyse more than 3-channel information, Xbee transmission may not be sufficient for it. Figure 7.16 shows the data outcome when trying to transmit 4-channel data from the ADS1298.

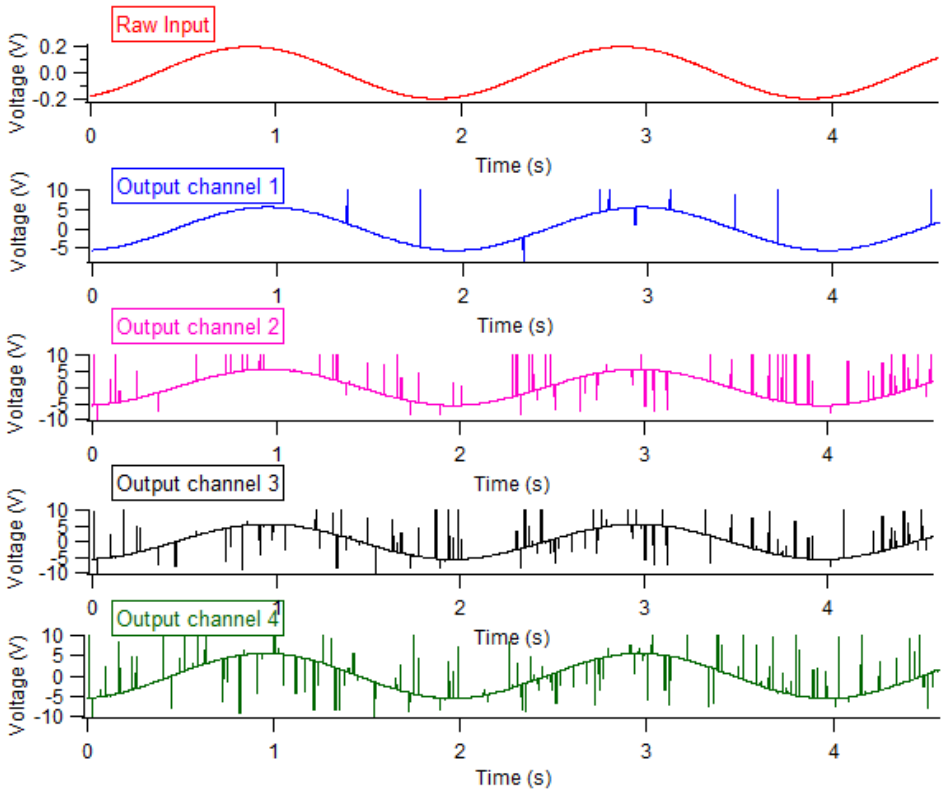

Figure 7.16: 4-channel Xbee-based wireless transmission

When increasing the number of transmission channels to 4, the data got corrupted, which is due to the insufficient transmit speed of the Xbee wireless module.

When transmitting 4 channels, the output signal starts to corrupt. In addition, the distortion gets severer from the first to the fourth channel. When activating three channels, the system has already been down sampled. As for running 4 channels, the timing becomes the main issue of this distortion. More specifically, four major events occur every transmission period (2ms). $T_{ADS1298}$ is the time spent in ADS1298 SPI communication (216 bit), T_{TX} is the wireless

transmission time, T_{RX} is the wireless receiving time, T_{DAC} is the DAC SPI communication time (192 bit), and $T_{PROCESS}$ is the time the processor takes to execute intermediate code.

$T_{ADS1298}$ and T_{DAC} are highly determined by the SPI transmission speed (SCLK rate). By setting both at 0.5MHz, the total SPI time, t_{SPI}, is:

$$t_{SPI} = t_{ADS1298} + t_{DAC} = (216 + 192) \times \frac{1}{0.5MHz} = 816\mu s \quad (7.3)$$

The time spent on transmitter and receiver, t_{UART}, should be the same, as they follow the same baud rate to communicate. The baud rate is set as 59600 bit/s, and there are 64 bits (3 channel + 2-byte acknowledgement) to be sent/received during one transmission. Therefore the time spent on writing/reading from/to wireless modules is:

$$t_{UART} = t_{TX} + t_{RX} = 2 \times \frac{64\ bit}{59600\ bit/s} = 2.22ms \quad (7.4)$$

Taking into account of the SPI communication and processing time (at 84MHz), the total time spent should be around 4ms. In addition to the electronic processing time, another main delay is the propagation time during the wireless transmission. The propagation delay depends on distance, accuracy, and propagation speed. Practically the updating rate of the system is 100Hz, 1 sample every 10ms, and therefore the propagation time should be around 5ms. As DRDY issues falling edges at 500Hz, ADS1298 transmits a new set of data every 2ms, however the transmitter only transmits one set of data every 10ms, ignoring the upcoming 4 sets of data.

When attempting to transmit 4-channel data, the time spent on electronic transmission increases. As DRDY is not synchronised with the whole transmission, DRDY issues external interrupts at random timing which is likely to mess up the signal. To fix the data corruption, the module transmission needs to be faster, which requires the module to run in a larger baud rate. In practical, Xbee module can only work in a good condition under 80 kbit/s. The next standard baud rate for module communications is 115200 bit/s, but Xbee modules are not suitable of operating in this baud rate, and the bit error rate significantly increases, which results in even more issues.

To transmit 4 or more channels, the wireless transmission speed needs to be increased. When setting the baud rate to higher speed, like 230400 bit/s, the transmitting data corrupts severer, even with only 1-channel analog information. Therefore, a different module with higher throughout rate is required to implement the task.

7.6 Conclusion and further development

In this chapter, different wireless implementations have been introduced. Different wireless techniques and their relevant applications have also been discussed. Xbee-based wireless data acquisition systems have been designed and illustrated in this chapter. Xbee modules have built-in ADCs and different functional IO pins, which can be a straightforward wireless solution. Both AT and API modes are useful for specific applications, and the relevant advantages and disadvantages have been discussed as well.

In addition, the bit error rate (BER) of the IEEE 802.15.4 network can be affected by co-existence of other networks. A study from NXP [99] has shown that a physical separation from the wireless local area network (WLAN) access point of 8 meters is recommended, to achieve 1% packet error rate (PER). 9-10 meters is required if the IEEE 802.15.4 network operates in a particularly saturated WLAN link. The interference from Bluetooth is more common, but less significant. The study shows a 2-meter keep-out distance is recommended.

The result and relevant timing calculation from the previous section yield the requirement of the high-speed wireless module, if all 8-channel information from the ADS1298 are required. Wireless modules working in Bluetooth standard have therefore been taken into considerations, as they provide higher data rate. The details will be discussed in the next chapter, together with a stacking modular electronics design.

Chapter 8: Stackable Modular Design for Prototyping Medical Devices

As discussed in Chapter 1, the prototype phase is indispensable to the process of designing a medical instrument. It helps designers to clarify the viability of the selected components, relevant PCB designs, microprocessor programming, and sensor interfaces. In general, a final design should be close to the prototype, however, some design compromises need to be explored. In this chapter, practical prototypes for a wireless TBI instrument will be illustrated, and both lab-based and clinical data will be discussed.

8.1 Stackable system and shields

To maximise the functionality and flexibility, I implemented a stackable modular design with different functional shields. Shields are referred to individual circuit boards, which are able to be plugged on top of the base PCB, extending its capabilities, like the Xbee and motor shield for Arduino UNO (Figure 8.1). Shields are easy to mount, and the fabrication risk is also very low, as they can be designed and tested separately.

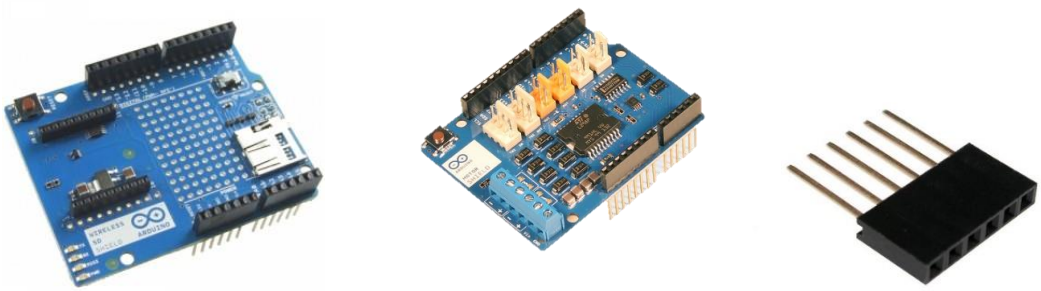

Figure 8.1: Shields examples and relevant stackable header

The ones on the left and middle are the commercially available shield for Arduino UNO, and the long-leg header on the right is used for stacking different shields together

The stacking design has different layers (or shields) with different functionalities, and all the layers maintain the same connection pinout. By employing the stackable headers with long-leg pins (Figure 8.1), all the functional layers can be integrated together.

8.2 Why use a stackable design?

As mentioned, the standard electronic flow chart of designing a medical instrument has been shown in Figure 1.12, and a simplified diagram is shown in Figure 8.2. As it shows, each stage

has various different options. Based on different sensing interfaces and signal fidelity, the relevant processing electronic selections can be altered significantly.

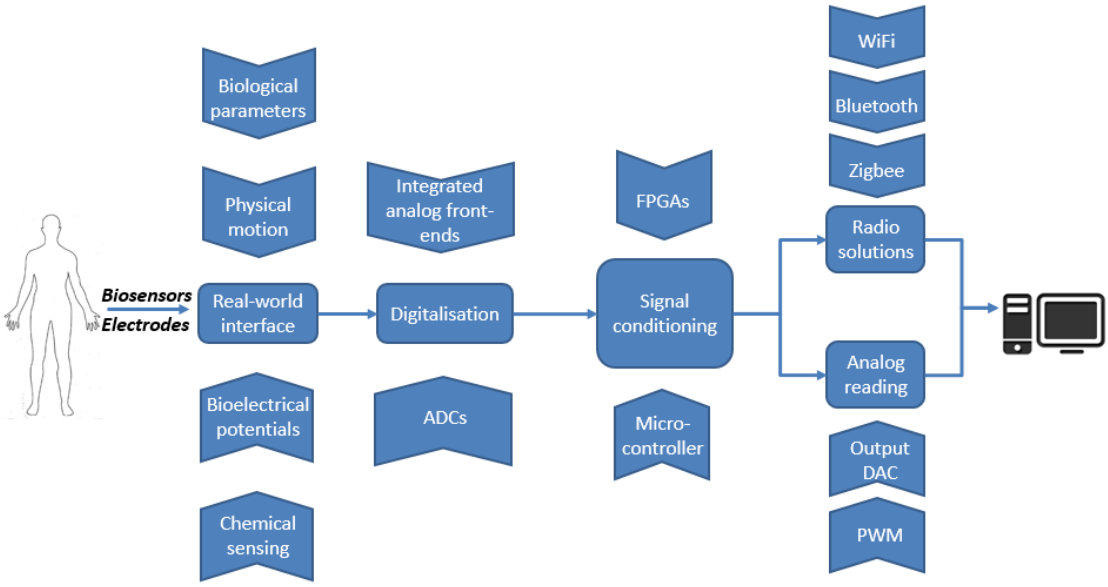

Figure 8.2: A simplified signal flow chart of a medical device

As mentioned in Chapter 4, a wide-spreading multimodal instrument is capable of monitoring most of the parameters required for a certain application. However, such a design is relatively large and costly, which makes it not suitable to work in limited spaces, such as ICUs and operating theatres. In addition, when applying a multimodal instrument in a specific monitoring task, not all the functions in the instrument will be used. Some features may even never be used during their entire life span. In addition, a wide-spreading multimodal design also increases the design risk and potential cost, as all the electronic components are mounted on the same PCB and share the same power supplies. One mistake in the PCB design or a single faulty operation may cause the whole system malfunction.

Compared with a large multimodal monitoring circuit board, a stackable system splits the board into different functional parts, which can be stacked up for different applications. In such way, the overall board size for a certain application is much smaller, as the stacking system only has necessary functional layers, and the board is stacked up in 3D, instead of spreading components in 2D. Refer to Figure 8.2, each stage can be designed as a separate layer, and the variations in a certain stage can also be implemented as different layers. Therefore, when measuring in a specific application, only necessary layers need to be integrated. In addition, this is also of great importance in debugging and prototyping phase,

testing new ideas, ICs, and modules. If one layer does not function as desired, one can simply change this layer, instead of re-designing the whole system. Apart from the flexibility, more importantly, a stackable system provides the possibility of implementing the state-of-art electronic technologies. For example, during writing the thesis, two potential technologies, a double-core microcomputer from Intel and the Bluetooth v4.2 protocol, have been released. They can be both applied to the stacking system, to test their functionalities and viability, during the prototyping phase of a latest medical instrument development.

The potential drawbacks of the stacking system is its noise, due to these physical stackable header connections, and the actual performance comparison with the spreading design will be discussed at latter sections of the chapter.

8.3 Introduction and construction of different functional layers

In this design, 4 different layers have been initially introduced for standard signal processing, and they been named as:

- ADS layer, which contains two ADS1298s, working as a 16-channel ADC (“real-world interface” and “digitalisation” phases in Figure 8.2).
- DUE layer, which is Arduino DUE development board (“signal conditioning” phase in Figure 8.2).
- DAC layer, which contains two DAC7634s, working as an 8-channel DAC (“analog” reading phase in Figure 8.2).
- BT layer, which contains a wireless module connector, a temperature sensor, and a 3-D accelerometer (“wireless solution” phase in Figure 8.2).

8.3.1 ADS layer

In previous chapters, ADS1298 has been proved to be a reliable and high-quality IC for building bio-potential acquisition systems. The programmable gains, sampling rates, and high resolution offer the flexibility of monitoring various signals in different applications. Therefore, it has been selected as the main IC at the digitalisation phase. This layer contains two ADS1298s, working in a cascaded mode, which creates a 16-channel front-end analog-to-digital converter.

Due to the dimension and pinout limitation, one ADS1298 has been mounted on top side of the board and the other one on the bottom side (Figure 8.3). The SPI serial pins have been located in the middle, which follows the pinout in Arduino DUE. The power management circuitry has been placed on the upper section of the top side. To optimise the performance, the PCB has been designed to contain 6 electrical layers, four of which are signal layers and the other two are internal planes, a power plane and a ground plane. Following the general PCB routing rules discussed in Chapter 3, the ground plane has been split into an analog ground plane and a digital ground plane, which are joined at a star point. In addition, the power plane has also been split, to avoid unnecessary cross-talk between digital and analog circuitry. The detailed layer/plane management and relevant design files has been attached in appendix 8.1.

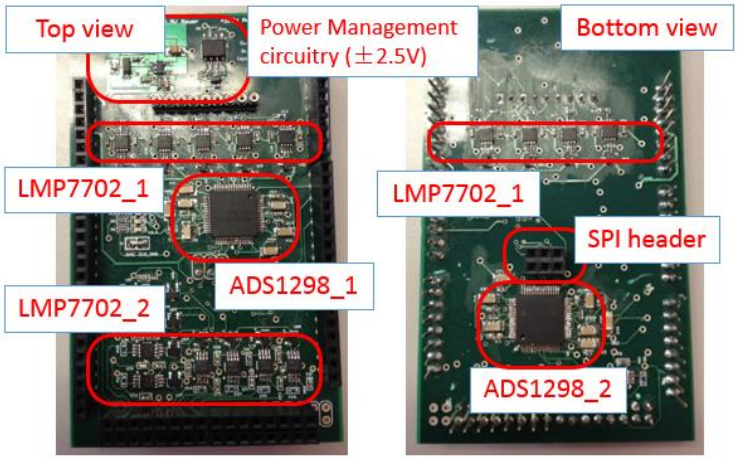

Figure 8.3: ADS board and relevant component arrangement

Left: top view, right: bottom view. Two ADS1298 are involved in the design, and the PCB has totally 6 electrical layers: top layer, internal signal layer 1, ground plane, power plane, internal signal layer 2, and bottom layer. In terms of component selections and placement, it is very similar to the board discussed in Chapter 5. The only difference is that the front buffer has been changed to a high-impedance op-amp, LMP7702, to interface with high-impedance sources, like ion selective electrodes.

As for the schematic and pin out, the ADS layer is similar to the head-stage analog board, discussed in Chapter 5. The main difference is that in each channel high-impedance op-amps, LMP7702, have been used for the front buffers to work with high-impedance sensors, like PH sensors and potassium ion selective electrodes. All the 16 channels have the same front signal processing set-up, so only one-channel schematics is shown in Figure 8.4.

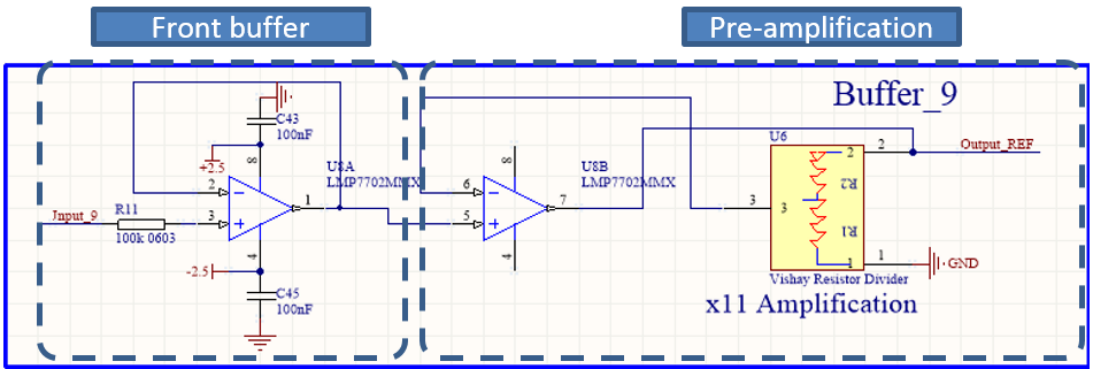

Figure 8.4: Schematics of the front data processing unit on ADS layer

As the implementation of ADS1298 has been demonstrated in Chapter 5, only new features will be discussed in this section. In this layer, two ADS1298s work in a cascaded mode, which requires some extra settings for both ADS1298s. As the datasheet [75] indicates, multiple ADS series devices can work together in one system, in either cascaded mode or daisy-chain mode. The serial interface typically requires four signals: DIN, SCLK, DOUT, and CS. With one additional chip select (CS) per device, multiple devices can be connected together, and the number of pins required for N devices is 3 + N.

The key factor needs to be noticed is the clock setting when connecting multiple devices. One ADS129x must be set as the master, and this master device needs to enable the internal oscillator (CLKSEL pin = 1). In order to bring out this internal clock source, the CLK_EN bit in the register one needs to be tied high (“1”). By applying such configurations, the master ADS129x starts to output the clock source to other connected devices. On the contrary to the master ADS129x, all the slave ADS129xs need to disable the internal oscillator (CLKSEL pin = 0) and use the external clock source from the master. When synchronising multiple devices, the START and CLK pins also require to be connected as Figure 8.5 shows. Moreover, only the master DRDY pin is connected to the processor, working as the external interrupt input, while other DRDY pins from the slaves remain floating.

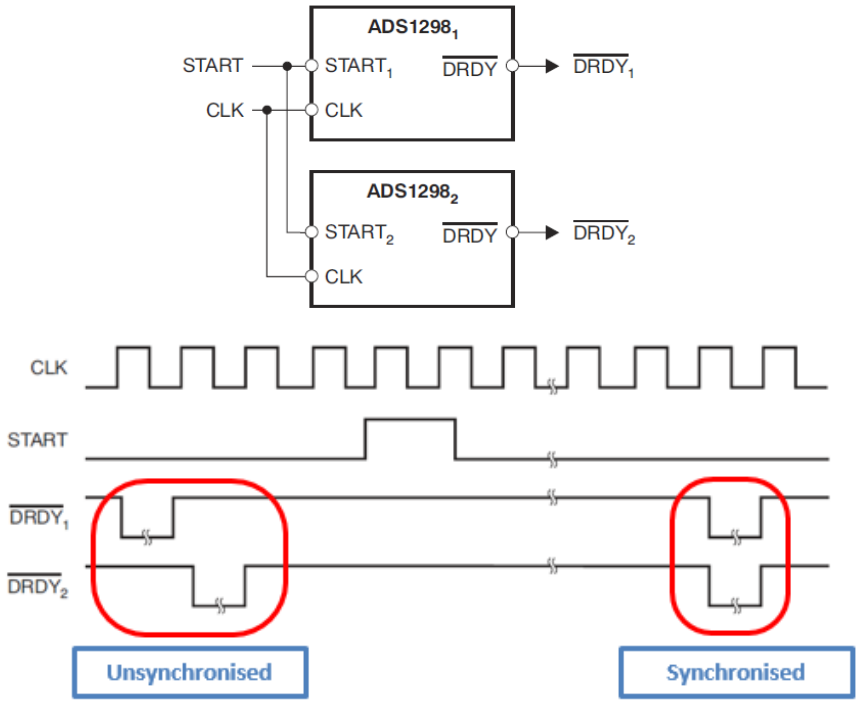

Figure 8.5: Multiple cascaded ADS129x connection and relevant waveform.

The upper figure is the connection for START and CLK pins, and the lower waveform is the synchronisation of 2 ADS129x, controlled by a START command. The figure is adapted from [75].

The synchronisation problem, due to clock confliction, can be observed if the devices are not well connected as either method demonstrates (Figure 8.6). During this test, two ADS1298s were working in the cascaded mode. As ADS1298 allows clock synchronisation error in a certain range, the output contains both “synchronised” and “unsynchronised” signals, which occurs periodically.

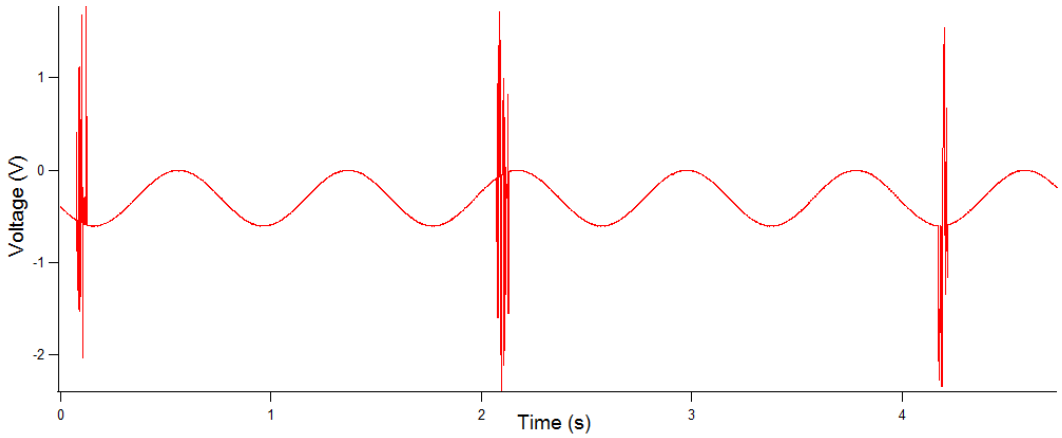

Figure 8.6: Unsynchronised output signals

The output signal is corrupted by periodic spikes, due to the unsynchronised clock source.

The major difference between the cascaded mode and the daisy-chain mode is the connection of CS and DIN. In the cascaded mode, all the devices share the same DIN, DOUT and SCLK, but utilise different CS pins. By toggling different CS pins, the main processor is able to communicate with different devices. In Figure 8.7 (left), ADS1298 and ADS1294 share the same serial interface pins, but have different CS pins (ADS1298_CS – GPIO0, ADS1294_CS – GPIO1).

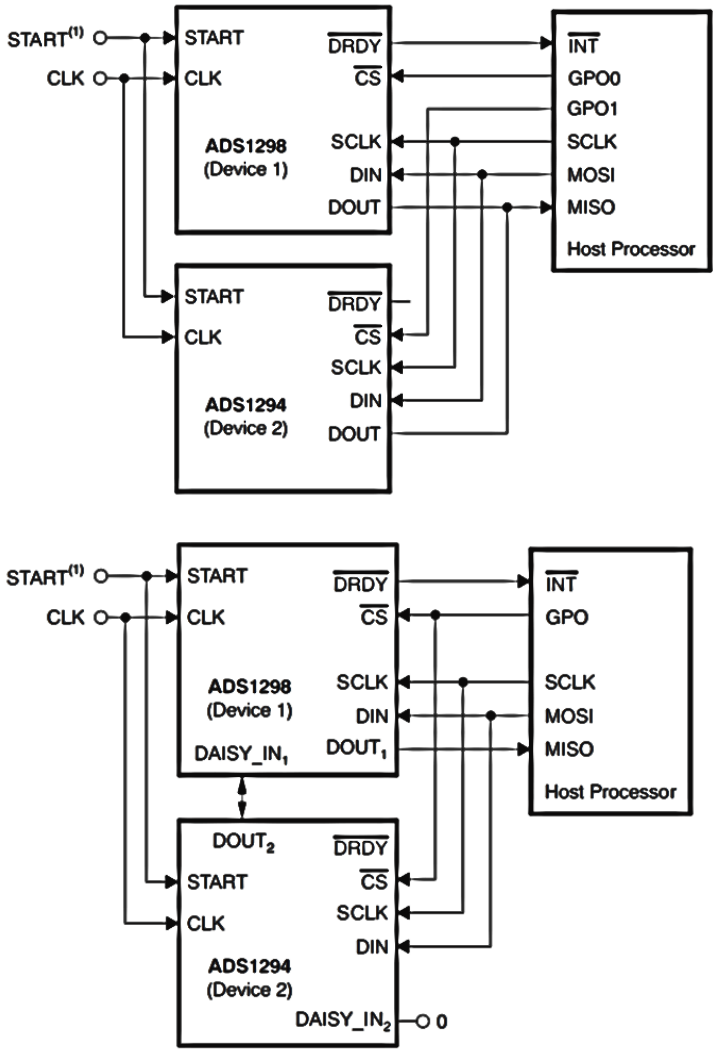

Figure 8.7: Multiple ADS129x operation modes

The one on the left is set up in the cascaded mode and the right one is in the daisy-chain mode. the figure is extracted from [75].

Whereas working in daisy-chain mode, all the devices share the same CS, SCLK, and DIN, but use different connections for DOUT. DOUT for the master ADS129x is connected to the MISO pin of the microprocessor, while the slave DOUT is connected to the DAISY_IN pin of the previous chained ADS129x. The configuration is shown in Figure 8.7 (right), and more devices

can be added in this mode as long as the DAISY_IN pin of the previous device is connected to the DOUT of next one.

8.3.2 DUE layer

As for the signal conditioning phase, the microprocessor is required to run in a high speed, with quick internal data processing, fast mathematical operation, and sufficient I/O pins, in order to support multiple data converters, wireless modules, and sensors to operate in the system. In addition, such a processor needs to have an easy program environment and sufficient open sources. Since an individual microprocessor generally requires a few essential peripherals and pre-setting, such as boot-loading (discussed in Chapter 9) to function correctly, a miniaturised development board with such microprocessor is preferable. A stackable design requires all the layers to have the same connector layout, which also makes a development board better fit than a bare microprocessor. Followed by the same circuit-designing philosophy, always test new things with the tools that you trust. Arduino DUE has been selected to be the main base processor for the design, as it has been tested to be a high-performance development board, when debugging the spike issue in Chapter 5.

As mentioned, Arduino DUE (Figure 8.8) is designed and released by Arduino, which is an open-source electronics platform. The actual microprocessor on DUE is Atmel SAM3X8E, a 32-bit ARM Cortex-M3 core chip from Atmel, and the main characteristics are shown in Table 8.1. Compared with typical 8-bit microcontrollers, the 32-bit ARM core makes the chip capable of operating on 4-byte wide data within one single CPU clock. More importantly, the interrupt latency from ARM cortex M3 is much smaller than a standard AVR microcontroller, which significantly reduces the data processing time.

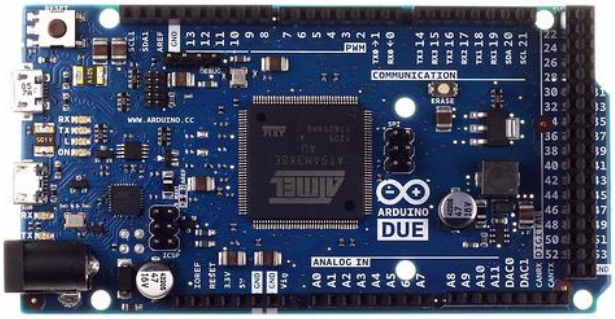

Figure 8.8: The appearance of an Arduino DUE

Arduino DUE	Features
Main clock	84MHz
External IO pins	54 (12 of which are PWMs)
Serial ports	4
Data converters	12 12-bit ADCs and 2 12-bit DACs
Digital communications	SPI, I2C (3.3V TTL)
Memory	512k bytes flash memory

Table 8.1: Main characteristics of Arduino DUE

As for the power regulation, DUE can be powered from USB ports directly (+5V) or a 7-12V input through a 2.1mm DC power jack connector. DUE has resettable polyfuse to prevent it accidentally draws unexpected high current from the host computer or its separate power supply. When more than 500mA is applied to the USB port, the fuse on DUE will automatically break the power connection, until the short or overload is eliminated. Due to the on-board power regulator and protection fuse, DUE can be safely powered from a wide range, however, the main microprocessor, SAM3X, only works at 3.3V. All the connected electronic components have to operate in the same voltage level, otherwise a standard 5V input to an I/O can possibly damage the chip. If a connected device operates at 5V, a 5V-to-3.3V level shifter, such as TXB0106 from Texas Instruments, has to be added to ensure the communication to run correctly and safely.

8.3.3 DAC layer

The DAC used in this design is DAC7634, from Texas Instruments, which has four 16-bit voltage output channels. The DAC can operate from a single 5V supply, or ±5V dual power supplies. In this layer, two DAC7634s have been placed in the daisy-chain mode, which allows the layer to function as an 8-channel 16-bit DAC (Figure 8.9). As indicated in the figure, power management circuitry has been located on the upper section of the board. Similar power management circuitry has been added on each ADS and DAC board, which allows the

individual board to work separately. More importantly, each set of power supplies on one board is able to regulate its own current flow.

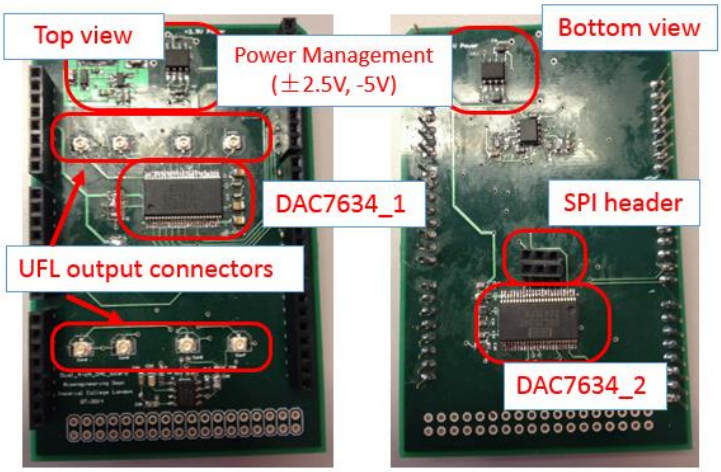

Figure 8.9: DAC board and relevant component arrangement

Instead of using the DACs discussed in the previous chapter, such as AD5362, the main reasons of applying 2 DAC7634s (from TI) in the daisy-chain mode are its output resolution and the power requirement. Most bipolar high-precision DACs require ±10V power supply, which are not available in this design. The main voltage input for the stacking system is 5V, and it has been regulated down to 3.3V, to supply the main microprocessor, different data converters, and other modules. +2.5V and -2.5V are also available on board, since ADS1298 and relevant front op-amps require dual power supplies. In theory, by applying a boost DC/DC converter [109], like TES2-0522M from Traco Power, one can still acquire ±10V from a single +5V power supply, but the size of such a converter is generally large. Moreover, this 20V difference (from -10V to +10V) is likely to introduce PCB surface current leakage, which also affects the signal quality.

Based on these factors, I used DAC7634 in this design, together with a voltage inverter (ICL7660A), generating -5V from the +5V power supply. DAC7634 supports SPI serial communication, and it acquires every bit of data at the falling edge of SCLK. When the SPI transmission ends (i.e. CS is turned high), SCLK stays high until the next SPI transmission (i.e. CS is turned low).

Daisy-chain mode

In general daisy-chain mode, digital data for different devices need to be sent in an order, from the last one to the first one. As Figure 8.10 indicates, all the SPI slaves share two SPI serial connection pins: SCLK and CS, whereas the previous DOUT is connected to the DIN on next daisy-chain device. The DIN pin on the first slave is connected to the MOSI pin on the microcontroller. A single active-low SS signal controls all the slaves in the chain, and all the slaves receive the same clock signal. As Figure 8.10 shows, only the first slave in the chain (slave 1) receives the digital data directly from the microcontroller, while other slaves in the network receive their DIN data from the DOUT output of the preceding slave in the chain.

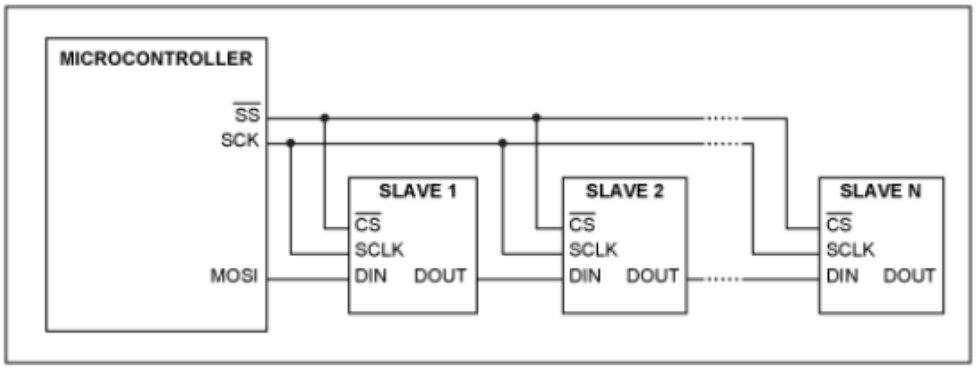

Figure 8.10 Basic schematic of SPI daisy-chain connection

Only the DIN of the first slave is connected to MOSI, and only the DOUT of the last device is connected to MISO. The figure is extracted from the Maxim application note [110].

In order to make daisy-chain work correctly, the slave must be able to input a command at DIN pin during a given command-cycle (i.e. the number of clock pulse required to clock in one command, defined by a certain device), and output the same command at DOUT during the subsequent command-cycle [110]. The device only executes the command that is just written to it on the rising edge of active-low CS or a certain control pin (e.g. LOAD on DAC7634). As long as the active-low CS stays low or the control pin has not been activated, the slave ignores the command and output it at the DOUT pin, on the following command-cycle. This process allows every slave in the chaining network to execute different commands, while only three necessary SPI I/O pins are required from the microcontroller.

More specifically in a daisy-chain network in Figure 8.10, Slave 1 receives data directly from microcontroller (MOSI). This data (data_1) is clocked into Slave 1's internal shift register. If the active-low CS remains low and no extra control pin is activated, this data propagates through to Slave 1's DOUT pin on the following command cycle. DOUT of Slave 1 goes into DIN of Slave

2. Therefore, on the next command cycle, new data (data_2) go into slave 1 while the previous data go into slave 2. If the CS or the control pin remains the same status, one more set of data (data_3) go into the network, which makes a data shift to the whole chain. Consequently, data_3 is stored in Slave 1, data_2 is in Slave_2, and data_1 is in Slave_3 (Figure 8.11).

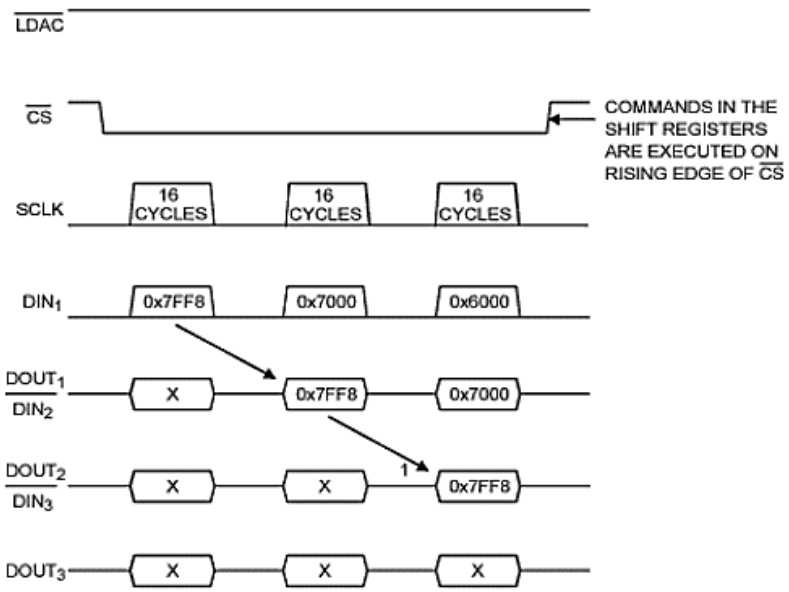

Figure 8.11: Command loading sequence in daisy-chain mode

The transmission data is shifted from the first to the last slave in the daisy-chain mode. The last set of the data sent from the master stays in the first slave, and the first set of the data sent from the master arrive to the last slave. The figure is extracted from the Maxim application note [110].

In daisy-chain mode, first set of data is sent to the last device in the network, while the last set of data is stored in the first device. As the DAC7634 datasheet demonstrates, multiple DAC7634 can be daisy-chained, by connecting the SDO pin of one device to the SDI pin of the following device in the chain, which is shown in Figure 8.12.

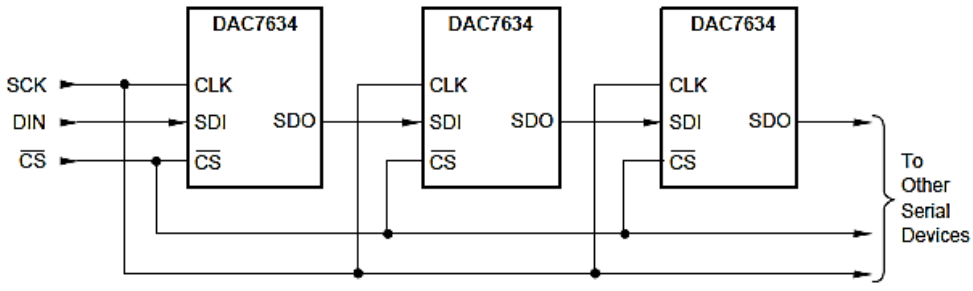

Figure 8.12: Daisy-chain of DAC7634

The figure is extracted from the DAC7634 datasheet [111].

8.3.4 BT layer

To provide the wireless communication capability to the stacking system, a BT layer has been added. On this layer, an Xbee footprint-compatible connector has been designed (Figure 8.13). The connector is able to communicate with either an Xbee module described in Chapter 7, or another module with the same pinout. As discussed in Chapter 7, Xbee is only able to transmit up to 3-channel ADS1298 data, a Bluetooth module is required if more than 3-channel data are desired. The Bluetooth module used in this project is RN42 from Microchip.

Figure 8.13: BT layer and relevant component arrangement

Key steps to set up the RN42 Bluetooth module

The Bluetooth modules in this design have been bonded, so that they are able to automatically search and set up the connection, once they are powered up. In order to make the module work correctly, one module needs to be set as the master, searching available Bluetooth modules and establishing the connection, while the other module is set as slave waiting for the connection inquiry signal. All the setting commands are transmitted by downloading the Arduino code (appendix 8.2), via serial port 3. In order to see response of the module, the serial monitor connected to serial port 0 is activated. With this configuration, commands can be typed in via the serial monitor (port 0), which will be transmitted to port 3 and sent out through the transmitter to its receiver. At the receiver end, it passes the incoming data to port 3 of the receiver processor, which then send the data to serial monitor via port 0 (Figure 8.14).

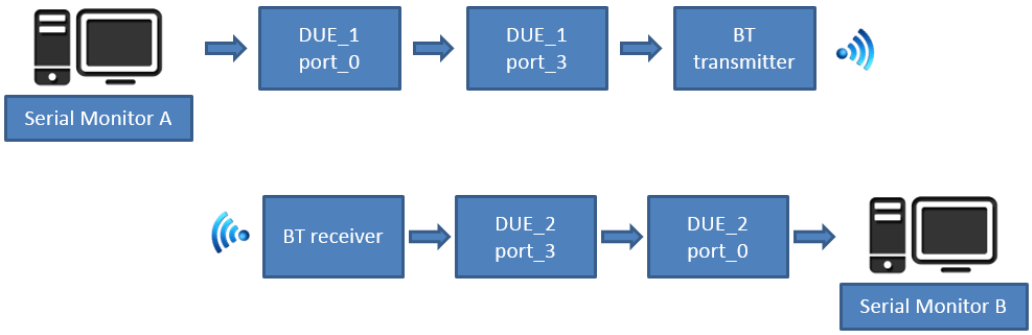

Figure 8.14: data transmission line between two BT modules and processors

The transmitter (Master) settings and relevant commands are shown below:

$$$
SU, 230 (change baud rate to 230400)
SN, master_"last 4-bit part number"
SM, 3 (auto mode)
SX,1 (bond)
SA,3 (Authentication)
SR, paired slave part number
R,1 (reboot)

In order to configure the module correctly, several key principles need to follow (the red parts are the non-officially-documented notes):

a. Send three dollar symbols, without "Enter", to activate the command mode of the module, which allows the module to accept any setting changes.
b. Apart from the initialisation symbols, all the other commands need an "Enter" to execute.
c. There is no "space" between the commands, comma, and the relevant parameter.
d. The default baud rate in this module is 115200, which has been changed to 230400 for higher data transmission speed (SU, 230).
e. The module name can be changed by "SN" command, however, the suffix has to be the last four digits of the module's part number, for example master_2EFA and slave_07A8.
f. There are 5 different modes the module can operate, and the one for the master module is mode 3, "auto" mode.
g. When working in this mode (SM, 3) as well as enabling bonding function (SX, 1) and authentication (SA, 3), the module automatically searches for paired slaves and connects, as long as it is powered. Even though the datasheet set the SA command as "1", the module actually works better when setting this value as "3".

h. The key command for pairing is SR. By adding the slave's part number after this command, the master will be paired with this slave and try to connect to it whenever it is powered.
i. After all these settings, "R, 1" will issue a software restart of the device. This restart process is essential as well, since all the setting changes will only be activated after restarting the module.

Sending a character "D" to the module allows the user to check all the current settings of the module, and the settings for this master transmitter are shown below:

BTA=00066662A1C6
BTName=master_A1C6
Baudrt=230K
Mode =Auto
Authen=3
PinCod=1234
Bonded=1
Rem=000666629E7C

Similar to the master's setting, the considerations of configuring the slave are:

a. The baud rate on the slave module has to be exactly the same as the master. As the master has been set as 230400, the same command will be sent to slave as well.
b. In term of naming the module, it works in the same way as described in the master mode.
c. Set SM command as 0, in order to let the module operate in the slave mode.
d. Activate the bonding function by sending "SX, 1". The authentication bit needs to set as 0, and pair the master module by sending the master part number to SR command.
e. "R, 1" is sent to the module, to issue a software restart.

Following by this configuration logic, the actual command code is list below:

SU, 230 (change baud rate to 230400)
SN, slave_"last 4-bit part number"
SM, 0 (slave mode)
SX,1 (bond)
SA, 0 (Authentication)
SR, paired master part number
R,1 (reboot)

By issuing a "D", the basic settings of the module are listed:

BTA=000666629E7C
BTName=slave_9E7C
Baudrt=230K
Mode =Slav
Authen=0
PinCod=1234
Bonded=1
Rem=00066662A1C6

In addition, there is a LED indicator on the module, which helps users to recognise the current status of the module (Table 8.2).

LED status	Indication
Off	The module is not properly powered
On and blinking slowly (1Hz)	The module is in idle
On and blinking rapidly (3-5Hz)	The module is in the command mode
Continuously on	The module has been connected with its paired one, and ready to communicate

Table 8.2: The LED indicator status on the Bluetooth module.

8.4 Functional tests with different stack combinations

As different functional layers have been introduced in the stacking system (Figure 8.15), different combinations are able to offer different functionalities. Based on the integrations, the system can work as a 16-channel bio-signal acquisition system, or an 8-channel wireless monitoring system. More importantly, it facilitates prototyping and offers the possibility of further development. The detailed tests and relevant results are shown in the following sections, and each section will begin with a “Lego” diagram.

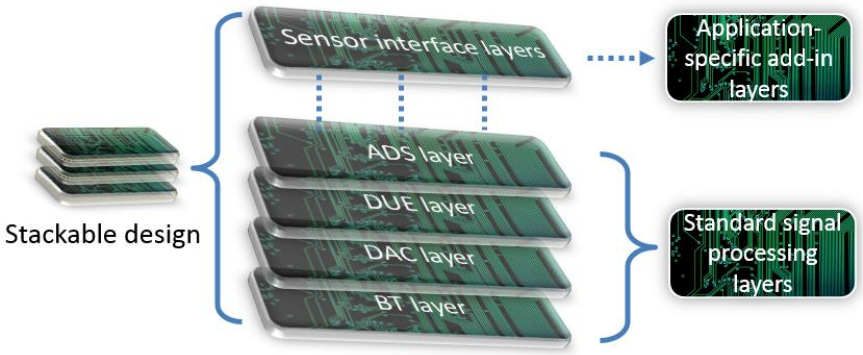

Figure 8.15: Different layers in the stacking design

8.4.1 16-channel front-end bio-potential acquisition system

As shown in Chapter 5, an 8-channel ADS1298-based bio-potential acquisition system has been designed and applied in clinical applications. However, in some particular uses, like scalp EEG and PH sensor array, more than 8-channel information are desired. Therefore, for these applications, the stackable design can meet the requirement, as one ADS board has 16 channel and it is viable to stack multiple ADS boards, to achieve a 16×N-channel system.

For demonstration, this section employs one ADS board (2×ADS1298), 2 DAC board (4×DAC7634), and a DUE board, in order to implement a basic 16-channel voltage recording system (Figure 8.15).

Figure 8.16: Stackable 16-channel voltage recording system

By simulating various voltage inputs to the system, relevant waveforms have been measured. As the ADS1298s have been set as 1000 samples per second, the stacked system is able to detect fast changing signals. In this experiment, the internal gains of both ADS1298s have been set as 1, therefore the gain is 11 from the front non-inverting amplifiers. The amplitude of the input sine wave is 150mV$_{p\text{-}p}$, with -35mV offset, and the frequency is configured as 1Hz. The 16-channel output data for this input is shown in Figure 8.17, and it follows the input signal in both frequency and amplitude.

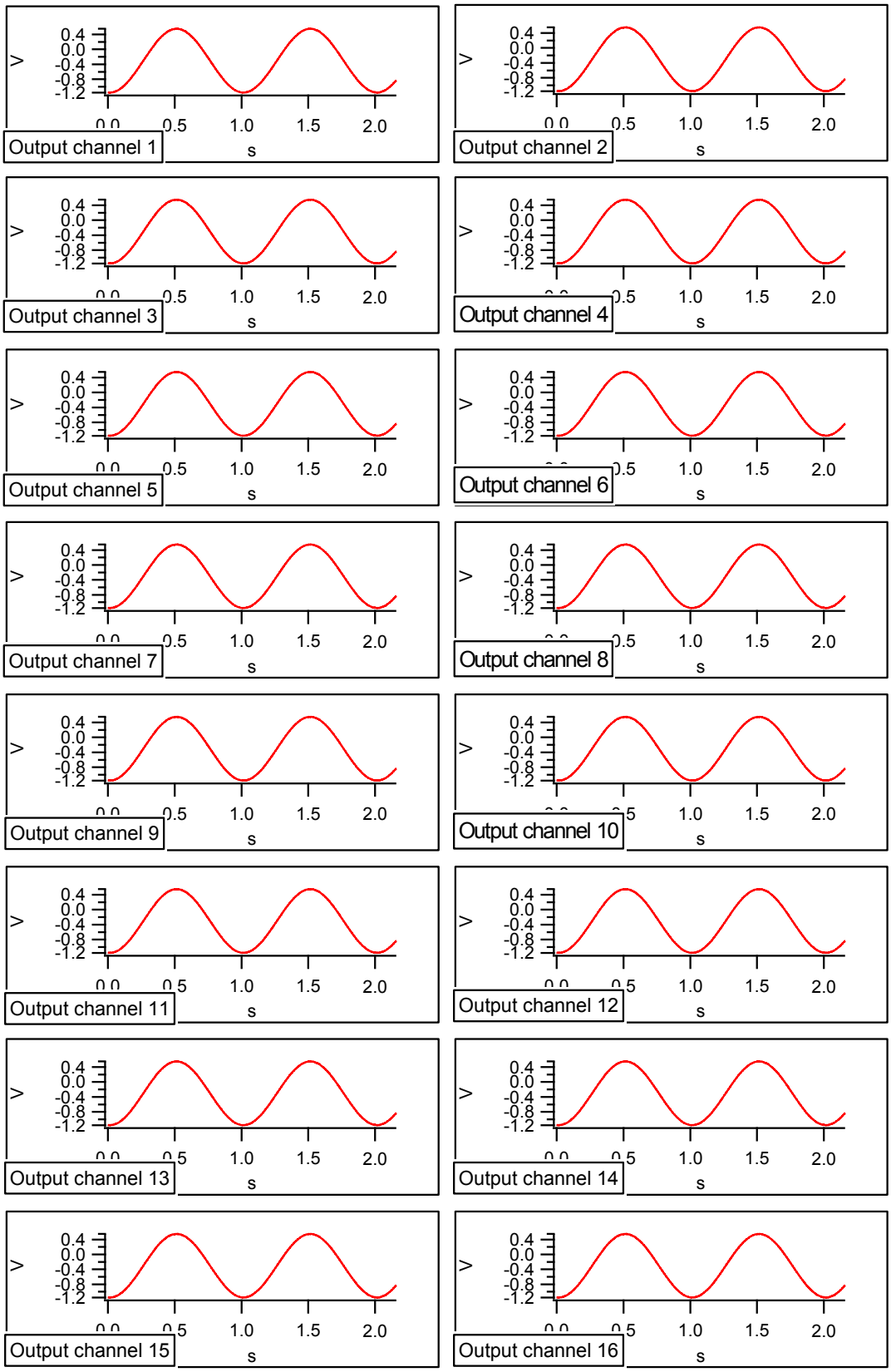

Figure 8.17: 16-channel stacked system test with fast sine waves

The figure shows simultaneous 16-channel outputs from the stacking system. Each channel has the correct amplitude and frequency response, without generating any distortion.

This experiment validates the design of a 16-channel signal acquisition system, and the viability of operating the data converters in cascaded/daisy-chain modes. In addition, this data prove the concept of building a 16-channel bioelectrical signal monitoring system. Based on this prototype, a 16×N channel bio-potential monitoring system can be then designed and developed for specific applications, such as scalp EEG.

As for the noise analysis, the standard deviation (200 samples) has been calculated. When setting the gain as 11 (minimum), the output standard deviation is 0.5mV. Therefore, the input detection limit of the system is 0.5mV/11, 45µV. Compared with spreading ADS1298-based design, whose value is 10 µV discussed in Chapter 5, the standard deviation of the stackable system is slightly higher. This is due to the leakage between the stackable connectors and inevitable digital/analog cross talk in the stackable architecture. However, 45µV still makes the stackable system capable of measuring most of bioelectrical signals, and it is a good approach to prove the concept and provide preliminary tests of a 16×N channel bio-potential acquisition system.

8.4.2 8-channel wireless front-end bio-potential acquisition system

In this section, the BT layer is involved, and the acquisition system is able to transmit data wirelessly. As for a standard wireless transmission set-up, at least one transmitter and one receiver are required. By loading different code and Bluetooth module settings (attached in appendix 8.3), a DUE board integrated with one BT layer can work as either a transmitter or a receiver.

In this experiment, the transmitter part also integrates with the ADS layer, which digitalises the input analog signals and wirelessly transmits to its paired receiver. The receiver system has been stacked with a DAC board, which is able to convert the digital data back to analog and send the analog data to the recorder, PowerLab. In general, a Bluetooth module is normally capable of directly communicating with a host laptop or smart phone, via its built-in Bluetooth. The method has its specific applications in portable monitoring, which will be further discussed in Chapter 9. However in this experiment, the aim of a separate receiver is to convert and store the signal via PowerLab, which allows users to do real-time data analysis.

Therefore, the whole system in this experiment requires one ADS board, one DAC board, two DUE boards, and two BT boards (Figure 8.18).

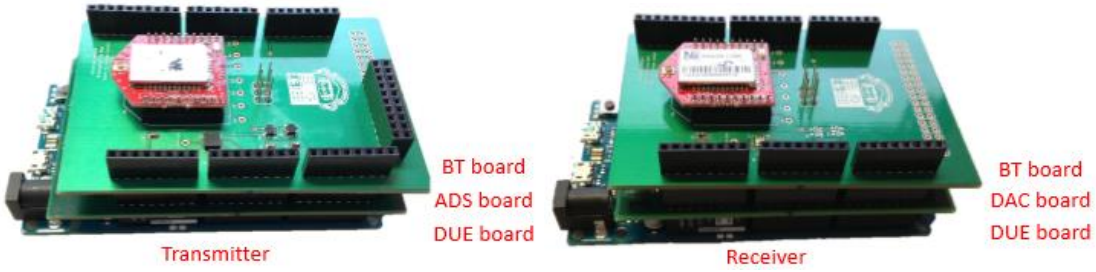

Figure 8.18: 8-channel wireless stacked system: transmitter (left) and receiver (right)

To verify whether the device is able to work as an 8-channel recording system, a simulated ECoG signal has been sent to the system from the signal generator, and the relevant data is shown in Figure 8.19. The amplitude of the simulated ECoG signal is $10mV_{P-P}$ and the period is 2min. The rest channels in the figure are the wireless outputs from the system. As the gain of the system remains to be 11, the output amplitude is $110mV_{P-P}$, and the signal follows the same signal pattern as the input, showing a clear classic negative potential drop during a spreading depolarisation event.

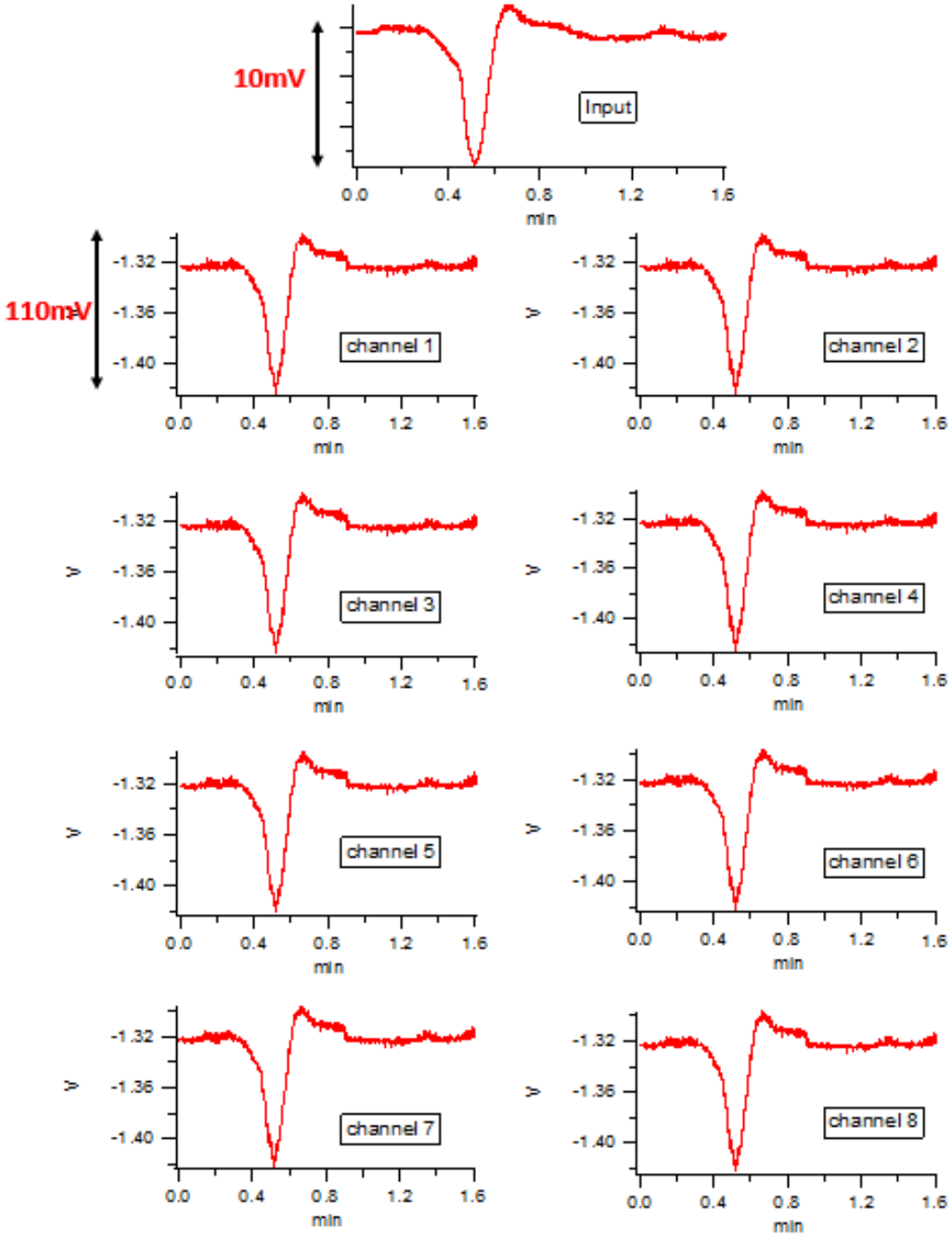

Figure 8.19: 8-channel wireless data from the stacking system

The figure shows 8-channel wireless output from a simulated ECoG signal, which has 10mV$_{P-P}$ and the period is 1.5min. With the 11 times amplification, the output maintain the same ECoG pattern with 110mV$_{P-P}$ and same period

8.4.3 8-channel wired and wireless transmission comparison

In order to only compare the difference between the wired and wireless transmission, all the interference from other sources, such as experimental noise, transmission cable length, and power supply, need to be in the same level for both systems. Therefore, only one ADS board is required in this experiment. After converting the input analog data to digital, the digital data will be sent to both the local DAC board (DAC board A) and the remote DAC board (DAC board B) on the wireless receiver. Figure 8.20 shows the integration of different shields for both the transmitter and the receiver.

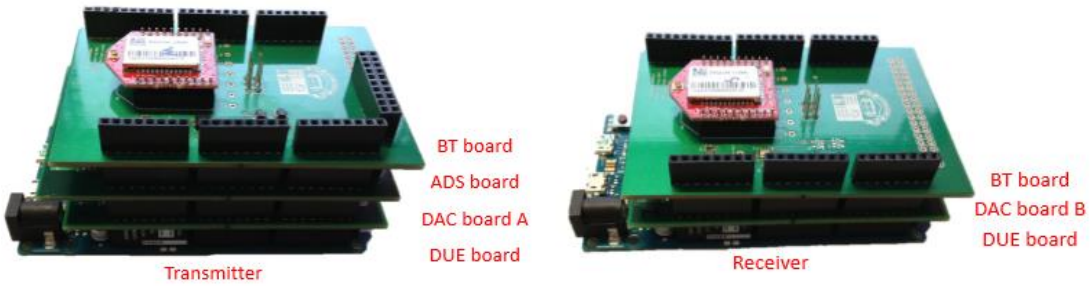

Figure 8.20: Stacking set-up when performing the comparison experiment

The left figure is the transmitter, which involves a DUE board, a DAC board (A), an ADS board, and a BT board (configured as a transmitter). The right figure is the receiver, which contains a DUE board, a DAC board (B), and a BT board (configured as a receiver).

Figure 8.21 shows the comparison data between the wired and wireless system. With the same input, both outputs have the same amplitude and frequency responses. Ideally, they should present exactly same quality data, however two major issues can be detected from the wireless output:

a. Compared with the wired output, the wireless output has a slight response delay, which is due to propagation time between the wireless modules. More specifically, the delay is about 50ms.

b. The wireless output has transmission errors, which can be visually observed as a flat line. This is due to the receiver setting of eliminating wireless transmission errors. During transmission, 2-byte acknowledge (0x7FFE) has been added in front of the transmitted data block. At the receiver side, it is configured to detect these acknowledge bytes to initialise the receiving process. Therefore, any transmission error will be automatically discarded. This setting makes the receiver only output valid

data, and hence the output is accurate and reliable. However, this also introduces an output delay if the incoming bytes are erroneous, as the output DAC remains the previous level if it cannot detect any new digital input.

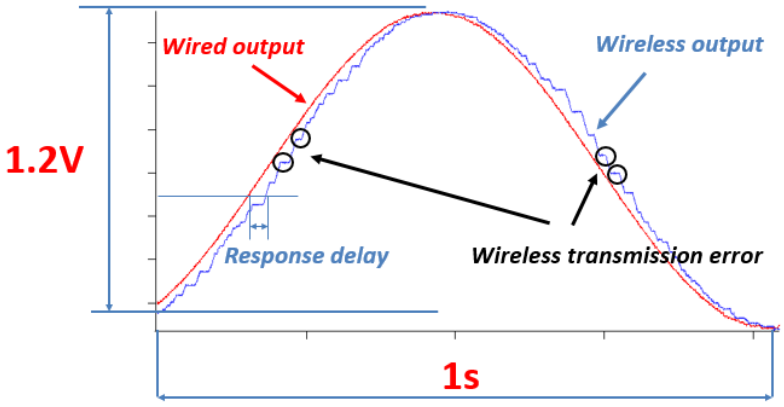

Figure 8.21: Performance comparison between wired and wireless system

The packet/bit error can be caused by the co-existence of other networks, such as IEEE 802.15.4 (Zigbee devices) and IEEE 802.11 (Wi-Fi). A study from Intel also shows that a Bluetooth transmission can be interfered by USB3.0 devices [112]. Effectively, this transmission error can be regarded as lowering the sampling rate of the system. Practically, the module is capable of wirelessly transmitting signal below 40Hz, which makes it possible to monitor bioelectrical signals from DC to 40Hz, such as ECoG and EEG. In addition, with another shield, it can seamlessly monitor chemical changes in TBI patients, as most chemical changes are below 10Hz. The relevant implementation will be discussed in the following section.

8.5 Practical implementations based on the stackable design

Several fundamental shields for the wireless stackable design has been discussed, and their performance has also been evaluated. By re-designing the potentiostat discussed in Chapter 4, and implement it as a separate layer (shield) for this stacking system, it therefore becomes a multi-channel wireless potentiostat.

Based on the confined size, two potentiostats (four gain selections on each one), are involved on this shield, which is called as “I_V layer”. The output from this layer can be sent to the input of the ADS layer, which is able to process and wirelessly transmit the data. Each I_V layer can transmit 2 channels, and 2×N channel monitoring can be achieved by integrating N I_V layers. In addition, both glucose and lactate sensors require a 0.7V bias voltage between the working

and reference electrode, and the working electrode was virtually grounded. A voltage reference IC (TPS76201) followed by an inverter were used to provide constant -0.7V to the reference electrode. The layer construction has been shown in Figure 8.22.

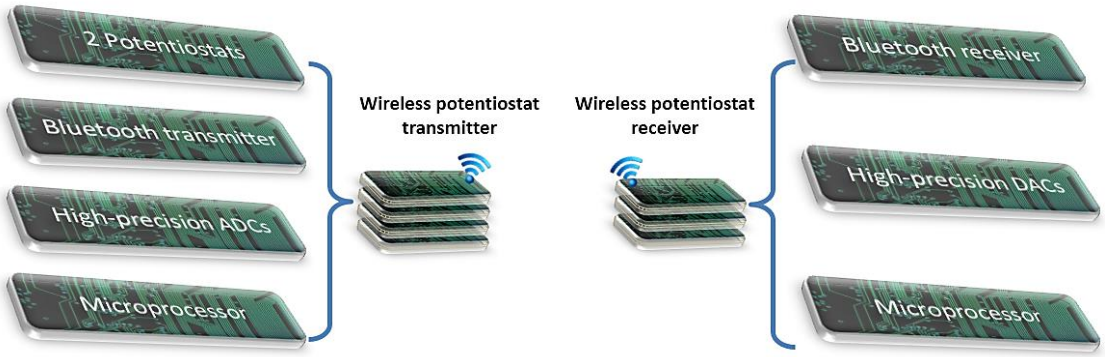

Figure 8.22: Stacking system configuration for the cycling experiment

The wireless potentiostats has been applied to a cycling experiment, which aims to study the real-time human tissue metabolite levels in cyclists undergoing a training regime[6]. In the experiment, glucose and lactate concentrations were monitored by the stacking system presented in this chapter, and the relevant experimental information is shown in Figure 8.23.

[6] This work has been published in paper "A 3D printed microfluidic device with integrated biosensors for online analysis of subcutaneous human microdialysate" in 2015.

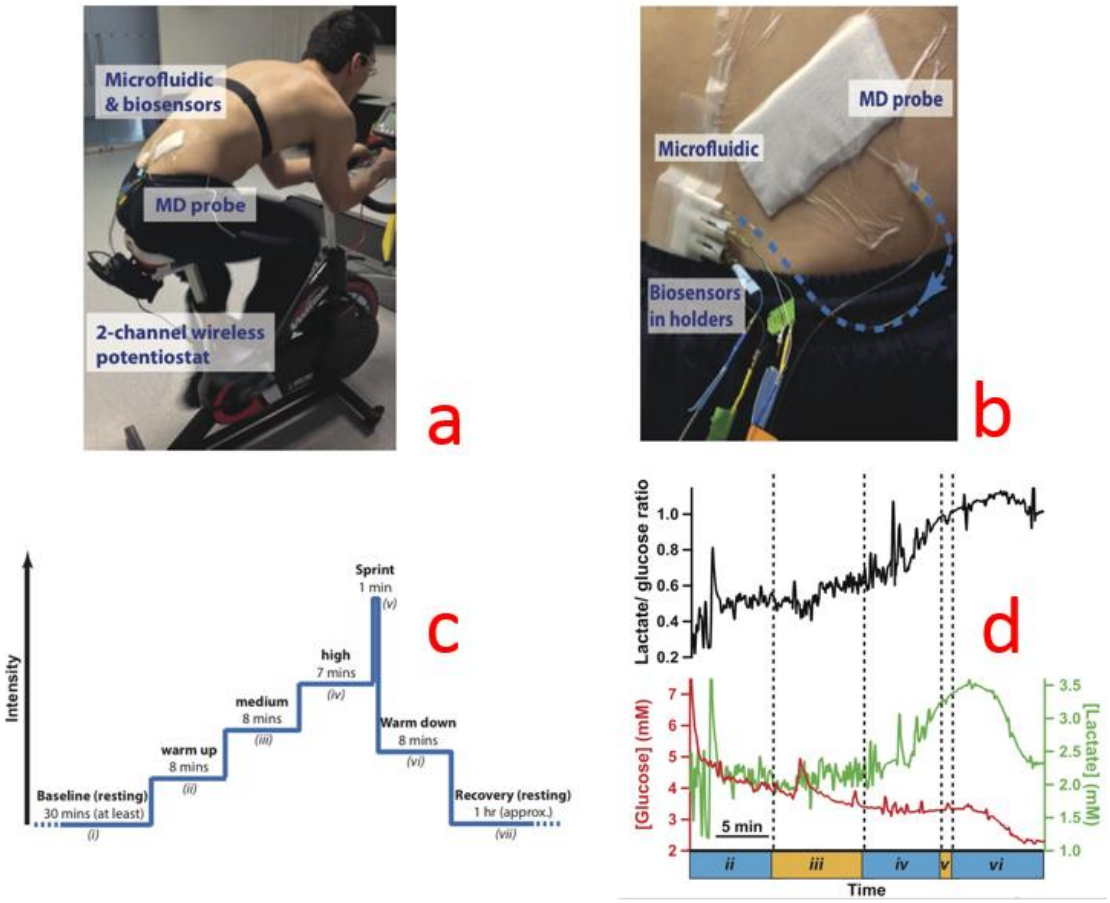

Figure 8.23: Practical cycling experimental set-up and results

(a) and (b) are the experimental set-up on the cyclist: microdialysis (MD) probe was applied to extract the sample from the cyclist. The dialysate will then flow into the microfluidic chip and biosensors, which are stabilised in a 3-D printed cage. The output signal from the sensors will then fit into the 2-channel wireless potentiostat. (c) is the experimental protocol. 7 stages are involved in the experiment: initial resting stage (i), low/warm-up (ii), medium speed (iii), high speed (iv), sprint/maximum speed (v), warming down (vi), and final resting/recovery (vii). (d) indicates the glucose and lactate changes during different stages in the experiment. The upper graph shows the ratio between lactate and glucose, while the lower graph shows individual changes over the experiment period (the red line is the glucose change and the green line is the lactate change).

8.6 Conclusion and further development

In this chapter, a stacking prototype system has been introduced. By designing and testing different layers separately, the overall risk and cost can be minimised. More specifically, 4 fundamental layers have been demonstrated: DUE layer, ADS layer, DAC layer, and BT layer. By utilising different layers, the system can work for different applications.

One ADS layer can detect up to 16-channel information. If more than 16-channel recording is required in a specific application, multiple ADS layers can be integrated together and work as a 16×N potential acquisition system. 2 extra DAC layers will be needed when adding 1 more

ADS layer. Other application shields, such as potentiostats, have also been designed and developed for specific applications. This wireless potentiostat has been used in different monitoring, and the one used for studying the real-time human tissue metabolite levels in cyclists undergoing a training regime has been published in 2015.

In addition, the system has the potential for further development, or works as a pure prototype base station. Combine different intelligent ICs, such as DDC series (discussed in chapter 4), the stackable system can be implemented to wirelessly sense extra-low current. For future development, state-of-art ICs can be also added into this system and test during the prototyping phase, to avoid any unnecessary cost and risk when attempting new ideas and designs.

Chapter 9: Microfluidic Biosensor Auto-calibration System Development

9.1 Overview

This chapter describes the construction of a microfluidic-based sensor auto-calibration system. As discussed in previous chapters, various biosensors and ion-selective-electrodes (ISEs), like glucose sensors and potassium ISEs, are commonly used in monitoring traumatic brain injury (TBI) patients. The monitoring period of each patient varies significantly, due to the severity of the illness and the complexity of relevant surgeries. This yields a challenge to the monitoring sensors. Their sensitivities change over time, which means the same output voltage from the monitoring electronics may correspond to different chemical concentrations. This uncertainty becomes the main barrier for the clinical team to use the sensor output as a real-time indicator of the patient condition. To deal with the sensitivity changes, a sensor calibration system is introduced, which calibrates the monitoring sensors in a certain period and generates the most up-to-date sensitivity. By applying this method, the output voltage has more physiological meaning, as it can be interoperated and present as real-time concentration changes.

The calibration system used in the thesis is µProcess from LabSmith, which is an electronic operation platform, including a range of hardware and software products. They aim to facilitate users to construct and control their microfluidic sensor systems. The main devices from LabSmith, known as µdevices, are SPS01 programmable syringe pumps, AV201 automated selector valves, 4VM valve manifolds, and µProcess software, which controls µdevices through an Electronic Interface Board (EIB) (Figure 9.1). In order to enable the communication with multiple devices, the EIB needs to be connected to the breadboard where all the devices sit on. If only one device needs to be controlled, the EIB can be directly connected to the device without using the breadboard.

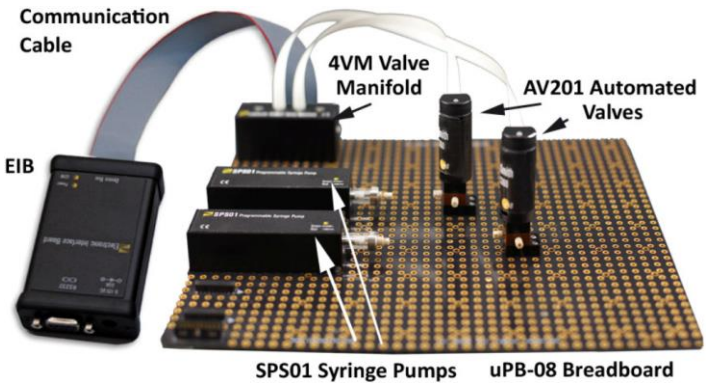

Figure 9.1: µProcess system components and standard set-up

The figure is extracted from LabSmith website [113].

Operation principle

The schematic of the operation principle is summarised in Figure 9.2. In a basic calibration system set-up, two pumps are pre-filled with solutions of known concentrations. The valves control the flow path of the fluidic samples. During standard monitoring, the valves are set in position A, such that the sample can flow into the microfluidic chip and then be detected by different sensors. During a calibration event, the valves are switched from position A to B. In this case, instead of taking sample from the external monitored target, the sample is from the mixture of the pre-filled pumps. One pump is filled with the maximum concentration required for the calibration (for example, 1mM glucose in TBI monitoring), and the other is filled with minimum concentration (for example, 0mM glucose, aCSF). By pumping these two solutions in different speed ratios, different levels of concentrations can be therefore obtained. For example, 0.5mM glucose can be acquired, by setting the two pumps to have the same speed.

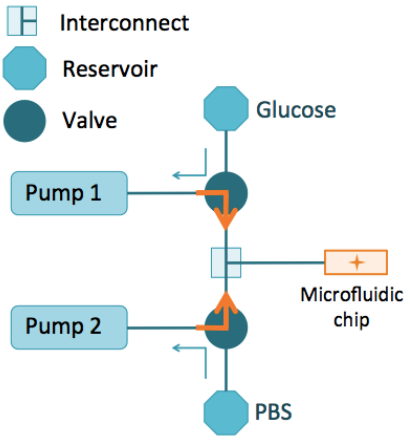

Figure 9.2: Operation principle of the calibration system

9.2 LabSmith µDevice electrical interface

All µdevices are connected on the breadboard via the same connector, whose part number is 151220-7422-TB. This is a double-row 20-pin connector with 2mm pitch, and the pinout of its electronic connections are shown in Figure 9.2. Two different power supplies, +12V and +5V are required to power the system. By using the EIB, the +12V pin can supply up to 2A while the +5V pin is able to supply up to 1A. However, a typical µDevice draws much less power than the rated power (Table 9.1).

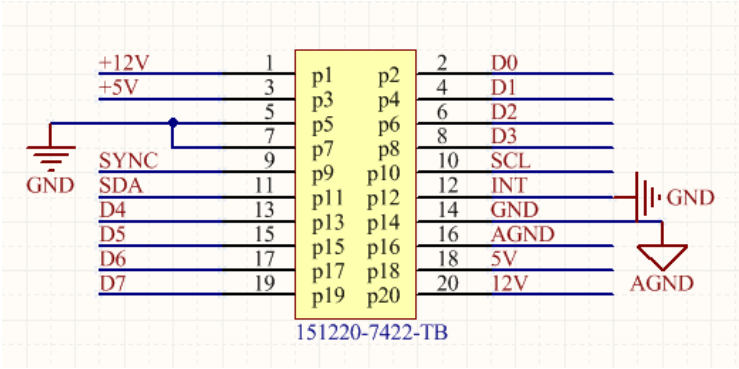

Figure 9.2: µDevice-side interface connector pinout

The common current return line or ground is labelled as "GND". To reduce analog sensing noise, a separate analog ground line (AGND) that draws little current was used. In the driving circuitry, this line should be connected to ground (0V) in a way that current drawn on the GND lines do not couple offset voltage to the AGND line. The digital lines (D0-D7) are designed to support enhanced time resolution sequencing, which may be used for handshaking, signalling, or timing. The INT pin is used for generating an interrupt for event-driven functions. The signal line "SYNC" is used to provide a high-accuracy time synchronization (better than 1%) of all µdevices. Four lines (D0-D3) can be configured in the firmware as analog sensing lines, ranging from 0V to 5V. These lines are intended to use in an application specific manner, such as to control the flow rate of a syringe pump via the analogue output of a µDevice pressure sensor or an external potentiometer.

Syringe pump status	+12V (10 – 13.6V)	+5V (4 – 5.5V)
Running	200mA	50mA
Idle	1mA	20mA

Table 9.1: Power supply ranges and relevant current drawn of a syringe pump

A syringe pump draws a maximum of 200 mA from the +12V supply and less than 50mA from the 5V supply when it is running, and it draws less than 20mA from +5V and less than 1mA from +12V when it is idle. In terms of the range of the supplying voltages, the 5V should not drop below 4V or rise above 5.5V, while the 12V supply should not drop below 10V or rise above 13.6V.

9.3 I²C packet for µdevices

The main digital controlling lines on the connector breakout are SDA and SCL, which is built on the 2-wire I²C communication interface. The standard I²C protocol has been discussed in

Chapter 2, and only specific requirements and features for µdevices will be demonstrated here.

Each µdevice employs an 18F series PIC microcontroller, to control the internal motor and valves. Each controller contains 512 byte of unused RAM, 4k of unused instructions, and 128 bytes of unused EEPROM space to support user coding for different specific applications.

A µdevice has a 7-bit address, between 0x01 and 0x6F. Each one has its own pre-set address from the manufacture, but can be changed by commands issued over the I^2C bus. When the master tries to write to a slave (µdevice), the slave loads an internal buffer with the response to this "write packet". The data in this buffer is sent back to the master during a "read packet". For this reason, in order to properly configure to a µdevice, a "write packet" command should be always followed by a "read packet" command, retrieving the feedback information from the slave. During transmission, all the multiple-byte integers in this I^2C protocol are transmitted with the least significant byte (LSB) first.

Write Packets

A few steps need to be performed, in order to write packets from a master to a slave:

1) Initial the packet with an I^2C "start" sequence (S).
2) The first transmitted byte is the I^2C address (addr), comprising the device (slave) address bit shafted to the left with a zero ("write") inserted in the least significant bit (LSB) position.
3) After initialising a write command to the slave, the master transmits the number of bytes (Cnt) that will follow in the packet.
4) The master then transmits a one-byte command (Cmd). If the command needs additional specification data, the master transmits the data after the command byte.
5) Finally, the master transmits a checksum (Chksum)
6) End the whole transmission by issue an I^2C "stop" sequence (P)

In summary, the whole data packet can be presented as the following figure:

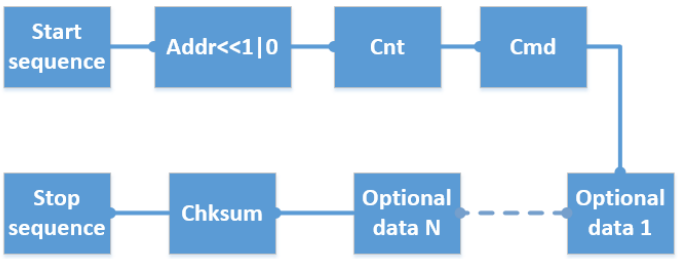

Figure 9.3: Writing data sequence

Note that Cnt counts all the byte after this Cnt byte. For example, if the master sends a command byte followed by 2 more data bytes and 1 checksum, then Cnt should be set as, 1+2+1, 4. The checksum is calculated by subtracting all the previous bytes in the packet from zero and truncating the result to 8 bits (1 byte Chksum). The equation of calculating Chksum is shown in the following formula:

$$\text{Chksum} = 0 - (\text{addr} \ll 1) - \text{Cnt} - \text{Cmd} - \text{data1} - \text{data2} \cdots - \text{dataN} \quad (9.1)$$

Read Packets

As discussed, µdevices response when a write packet has been received. After sending the address bits and "1", indicating reading data from the slave, the first data byte of the response from the slave (µdevice) is the status token (Tok), followed by the count (RCnt) of bytes including the checksum. The sequence looks like:

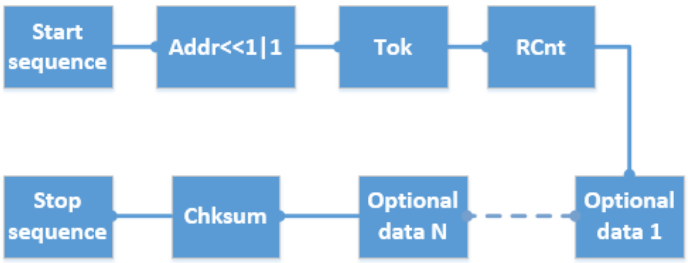

Figure 9.4: Reading data sequence

Compared with the sequence of writing packets, there are a few variants:

1) Tok is the status token, which normally has two different values: 0xAA (170 in decimal), and 0XEE (238 in decimal). 0XAA means command executed; 0XEE means command not executed. A non-executed command is normally due to a checksum or other command packet error.
2) RCnt is zero, if the packet contains no checksum or data

9.4 Issue of current LabSmith set-up

By employing these µdevices, it becomes possible to implement a miniaturised microfluidic-based sensor system with real-time neurochemical concentration display. However, when attempting to construct such a system, the electronic Interface board (EIB), cables, and the relevant power adaptor, become the main size determinants as they are relatively big and their sizes are fixed. Furthermore, the controlling software µProcess can only work in Windows, and it requires scripts for different tasks.

As all µdevices are independent and programmable, they are able to be directly controlled by an external microcontroller via the I^2C bus. In this case, my approach to this problem is to remove the EIB and create a customised command-controlling library on a relevant microcontroller's Integrated Development Environment (IDE). In this thesis, an 8-bit AVR-based microcontroller, ATMEGA328 from ATMEL, has been chosen and a custom C++ LabSmith library has been developed. The full code are attached in Appendix 9.1, and only essential coding logic process, typical example code, and relevant hardware implementation will be discussed in the following sections.

9.5 Hardware implementation

As I used the same microcontroller as the one on Arduino UNO development board, ATMega328 can be directly programmed through the Arduino IDE. To make the most of the miniaturised µdevices, I have wirelessly programmed the chip via a Bluetooth module. In this set-up, no extra cables are required when dynamically changing the configurations of the µdevices.

9.5.1 EZ-link Bluetooth module

The Bluetooth module used in the design is Bluefruit EZ-Link V1.0, from Adafruit. This module (Figure 9.5) works as a wireless serial-to-USB adaptor, and more importantly, it is able to change the baud rate on the fly. The DTR/RTS/DSR flow control pins are automatically synchronised to the computer serial port, which means that if the computer sets the hardware flow control DTR or RTS pins high or low, the pins on the Bluetooth module will follow. The module supports most common baud rates, 2400, 4800, 9600, 19200, 38400, 57600, 115200 and 230400. As Figure 9.5 shows, the module has an on-board voltage regulator, which requires nominal +5V input (V_{IN}). Once the module is paired with the host computer, it will be

automatically connected when it is powered, which is very suitable for a wireless embedded system without introducing extra accesses/headers for re-programming or debugging.

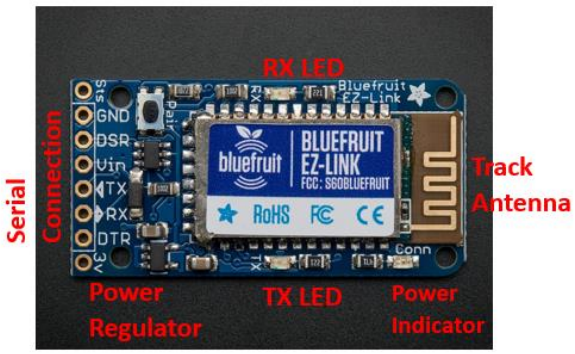

Figure 9.5: The appearance of the Bluetooth module

The power indicator LED lights up when the module is powered, and the RX/TX (blue) LED will blink when the module communicate with the host computer. The module will be connected to the main board through the serial connector, which is an 8-pin standard header with 2.54mm pitch. The Bluetooth module appears on the host computer as a virtual COM port, which means users can check the RX/TX data from a COM port monitor in the computer.

9.5.2 Power Bank

The power plug and the relevant cable have been replaced by a battery-based power bank. The power bank needs to provide required voltage with sufficient rating current. The capacity should be as big as possible given size constraints. The one used in the thesis, is Astro Pro2, from Anker. The power bank has a capacity of 20000mAh, with +5V and +12V output selections. The overall dimension is 185 x 125 x 15mm, roughly the same size as the LabSmith prototype board.

9.5.3 Layout of first-version wireless controller

Two versions of wireless controllers have been designed and developed in the thesis. In the first version, the design aims at wireless programming and µdevices controlling. The through-hole package of ATMega328 has been applied in this design, as it can be easily replaced or programmed from an Arduino UNO board in case the wireless module is faulty. The PCB employs a 4-layer design, and the size of the PCB is 45mm × 25 mm (Figure 9.6). As the board has the mating connector of the LabSmith platform, it can be directly plugged on a LabSmith breadboard.

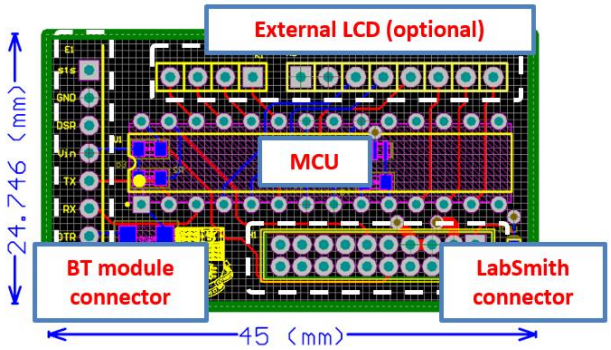

Figure 9.6: The PCB layout of the first-version wireless LabSmith controller

The left 8 vias are the wireless module connection, the right bottom 2-raw 20-pin header is for the LabSmith board connection, the right top header is used for an optional LCD display, and the central middle header is used for the main microcontroller.

9.5.4 Microcontroller bootloader

A bootloader is a piece of program pre-installed in the microcontroller, so that it can communicate with the host computer via certain software. The code is burned in the controller's flash, which is not erased during standard IC programming. Once the microcontroller is powered up or reset, the bootloader is called first, to detect whether there is a new program from the host computer. As the flowchart indicates in Figure 9.7, the status of the bootloader is checked first when a microcontroller is powered up. If no bootloader is detected, the programming process will be halted. If a valid bootloader is stored in the memory, the bootloader starts to direct the microcontroller based on the availability of new program. After the process, the microcontroller starts to run as the new/existing program shows, and the bootloader will not be called again, as long as the chip is continuously powered.

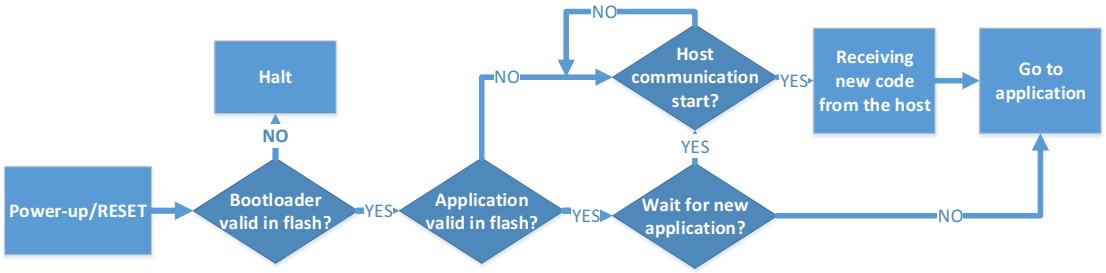

Figure 9.7: Bootloader start-up sequence

There are many methods to burn a bootloader into a microcontroller, and the way used in this design is to take advantages of an Arduino UNO development board and burn the bootloader,

via SPI ports. When wiring the devices, most pins follow the standard SPI connections, except the CS pin. As the bootloader access is only available when resetting the device, the CS pin on the Arduino UNO board needs to be connected to the RESET pin of the targeted microcontroller (ATMega328). In such set-up, the bootloader was burn to the target microcontroller when the Arduino UNO toggles its CS pin. The bootloader code was written in C language and executed in Arduino IDE.

9.6 Software implementation

After designing and developing the hardware, this new controller is able to communicate with µdevices. In addition, after successfully boot-loading the MCU, all the codes can be wirelessly downloaded via the Bluetooth module. Without the Bluetooth module, the microcontroller can still be programmed via a FTDI (UART-to-USB) chip/cable. A C++ based library has been developed to implement all the essential functions of the µdevices.

9.6.1 Major functions of µProcess

As discussed, µdevices can be mainly categorised as pumps (SPS01), valves (4VM01), and manifold. Some functions are universal, such as naming/re-naming a µdevice, changing the address, and pausing the current process. Some functions are device-specified. For example, moving a pump to the certain position/volume is only available to the pumps, and setting valves position can only be applied to valves. The main functions and relevant command codes have been summarised in Table 9.2.

Functions	Command code	Target	Arguments	Notes
GetBlockData	0x00	µDevice	None	Device dependent
Ping	0x01	µDevice	None	To check the existence of a µDevice without changing its state
SetDevAddr	0x02	µDevice	1-byte new address	
GetVersion	0x03	µDevice	None	2-byte firmware, 2-byte bootloader, and 2-byte hardware version
Reset	0x05	µDevice	None	
Stop	0x06	µDevice	None	Stop the current process
Setperiod	0x07	SPS01	3-byte period	Associated with flow rate setting
SetValve	0x07	4VM01	1-byte setting	2 bits for one valves, and 1 byte for 4 valve control
MoveToPos	0x08	SPS01	2-byte position	0xFF is the internal stop and 0x00 is the external stop
SetName	0x0A	µDevice	16 byte char	
GetName	0x0B	µDevice	None	16 byte “name”
SetCal	0x12	µDevice	2-byte calibration positions	
GetCal	0x14	µDevice	None	2-byte calibration positions
SetDiameter	0x15	SPS01	2-byte unsigned integer	Unit µm
GetDiameter	0x16	SPS01	None	2-byte unsigned integer
GetStatus	0x1A	µDevice	None	1-byte motion status flags, 2-byte position, 2-byte micro-pulse count

Table 9.2: The list of different functions and relevant command codes

9.6.2 C++ library to replace EIB software

The complete code (more than 1000 lines) for all µDevice controlling is attached in the appendix 9.1, and only 2 functions have been attached in this section for demonstration. The first function is to send a single command to a slave µDevice, which aims at introducing the coding logic and specific I^2C loading sequences. This is also a general-purpose function, which can execute all the one-byte commands listed in Table 9.2.

```
bool LabSmith::one_byte_read_write(int address, int cmd):
{
   int data[2];
   Wire.beginTransmission(address);
   Wire.write(0x02);  //Cnt = byte sum AFTER this one (counting checksum)
   Wire.write(cmd); //stop
   Wire.write(0x00-(address<<1)-0x02-cmd);
   Wire.endTransmission();
   Wire.requestFrom(address, 2);
   while (Wire.available()==0);
    for (int i=0; i<2; i++)
    {data[i] = Wire.read();}
  Wire.endTransmission();
     if (data[0] == 0xAA)
     return true;
     if (data[0] == 0xEE)
     return false;
}
```

As mentioned, this function is a universal format for all the commands that do not require any following data bytes. Therefore, only two parameters are needed for this type of command. The first one is the µDevice address that the master is going to communicate with; the other one is the actual command code, such as stop, ping, reset, which can be found in Table 9.2.

The whole code contains 3 different steps: sending command, receiving response, and processing received data. The code starts to initial the I^2C communication from the targeted address by sending "Wire.beginTransmission(address)", followed by the counting byte. This byte is always 0x02 in this function, since there are no additional data bytes after the command bytes. Hence, the total number of bytes after the counting byte is 2, one command byte and one checksum byte. After the count byte, the command byte needs to be sent, followed by a checksum. The checksum should be equal to 0x00 subtract shifted address, count byte, and command code.

After sending the command, the master expects to receive response from the slave, which is stored in a 2-byte array (*data[]*). As discussed, the first response byte is the token, and the second byte is the count of data after this byte, which will be zero if no data bytes follow. The last part of the code is to justify whether the I^2C transmission is correct. If the first byte in the array is equal to 0xAA, it means the transmission is correct and complete, which returns *true*; if the byte is 0xEE, indicating the transmission is wrong or incomplete, which returns *false*.

Only these individual functions are not enough to perform all the jobs that µProcess requires. Some processes require multiple communications between the master and the slave, which also involves certain amount of data processing. For example, the following code configures the pump to perform a self-calibration before it starts any job, and this involves multiple communications:

```
void LabSmith::auto_calibration(int address){
LabSmith::getcal (address);
unsigned int old_outstop = (calibrationdata[1]<<8) | calibrationdata[0];
unsigned int old_instop  = (calibrationdata[3]<<8) | calibrationdata[2];
LabSmith::setcal(address, 0x0000, 0xFFFF);
LabSmith::getcal (address);
LabSmith::setspeed (address, (LabSmith::GetMaxRate()/2
 if (LabSmith::movetopos(address, 0xFFFF))
        delay(1000);
        do {
          delay(60); //60ms delay for detecting the stop point
        } while (LabSmith::IsMoving(address) && !LabSmith::IsStalled(address));
      unsigned int new_instop  = ((devicestatus[2]<<8) | devicestatus[1]);
      LabSmith::movetopos(address, 0x0000);
      delay(1000);
        do while (LabSmith::IsMoving(address) && !LabSmith::IsStalled(address));
      unsigned int new_outstop  = ((devicestatus[2]<<8) | devicestatus[1]);
      new_instop  -= 64;
      new_outstop += 16;
      LabSmith::movetopos(address, (new_instop - new_outstop)/2 + new_outstop);
       do {
          delay(60); //60ms delay for detecting the stop point
        } while (LabSmith::IsMoving(address) && !LabSmith::IsStalled(address));
LabSmith::setcal (address, new_outstop, new_instop);
LabSmith::one_byte_read_write(address, dev_stop);  //clear the stall indication   }
```

The flow chart and relevant explanations of the code have been described in Figure 9.8.

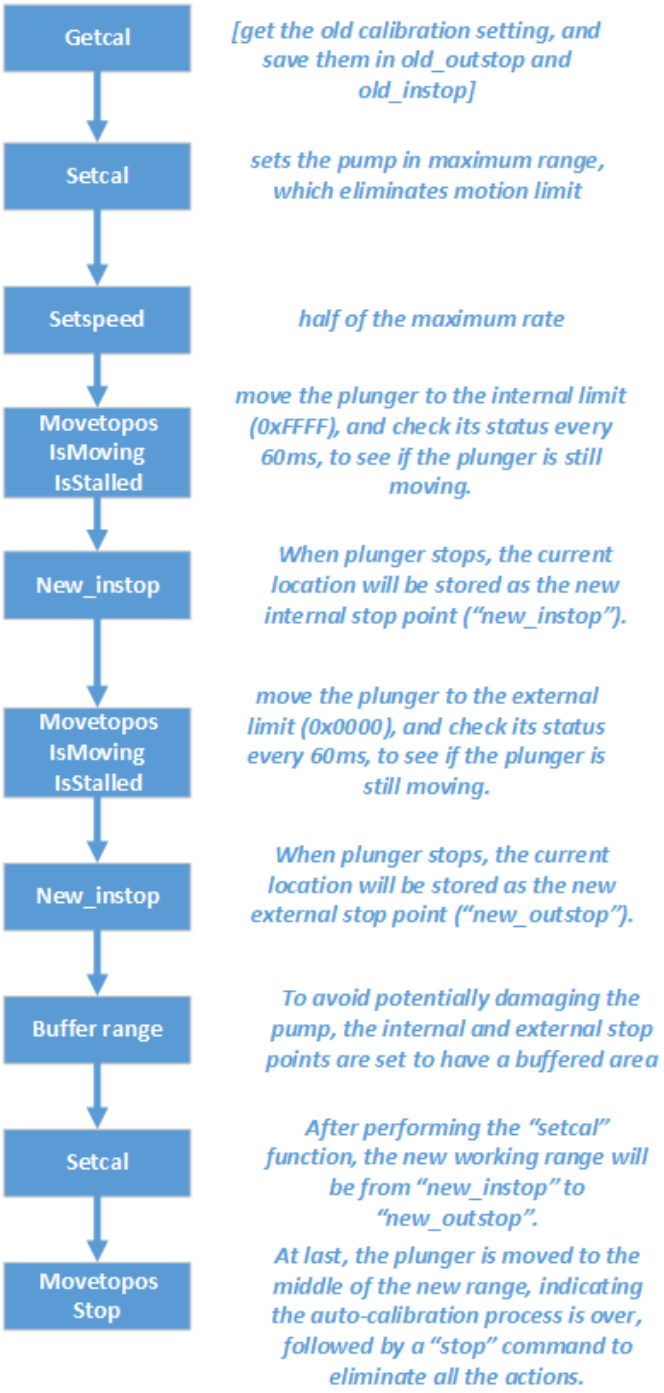

Figure 9.8: Flow chart of the pump's self-calibration function

Based on the diameters of the syringe pump and the calibration parameters, the current liquid volume can be deducted from the current position. The detailed deduction processes are in the function "GetVolumeFromPos(int pos)" and MoveToVolume(int address, double dVolume), which can be found in Appendix 9.1.

When setting the pump to reach a certain volume/position, the pump ramps up to full speed, cruises at the set speed, ramps down to a slower speed for the final motion (to avoid overshoot), then does a small back and forth motion to reach the target volume/position precisely. Based on this feature, the flow rate is not constant all the time, which results in artefacts from the output results. Since this feature of the pump is noticed, it does not significantly affect measurement or sensor calibration. The artefacts can be removed when post processing the data. In addition, the artefact can also be eliminated by different code-series settings. When setting the volume that the pump needs to move to, do not set the volume as the exact value, but a slight larger one. In the meantime, activate the timer in the microcontroller, and let the timer count for a defined time. When the time runs out, issue a "stop" command, which skips the ramp down and fine adjust steps.

9.6.3 Code validation

After implementing all the necessary functions in the library, I conducted several classic sensor-calibration experiment, to validate and debug the customised C++ library. With the same experimental set-up, the sensor has been first conducted a 5-point calibration, controlled by the traditional electrical interface board (EIB). Then, the same sensor repeats this calibration process, controlled by the new board. The comparison is shown in Figure 9.9, and the calibration curves are identical in both cases, which verifies this PCB design and the code. By integrating the controlling code with high-precision data converters and analog sensor interface, a new system will be able to control the calibration events, calculate the transient sensor sensitivity following Equation (9.2), and output real-time neurochemical concentrations.

$$\text{Sensitivity} = \frac{\Delta I_{OUT}}{\Delta[ion]} \tag{9.2}$$

Where ΔI_{OUT} is the difference of signal current output of the sensor, and ΔI_{OUT} is the concentration difference.

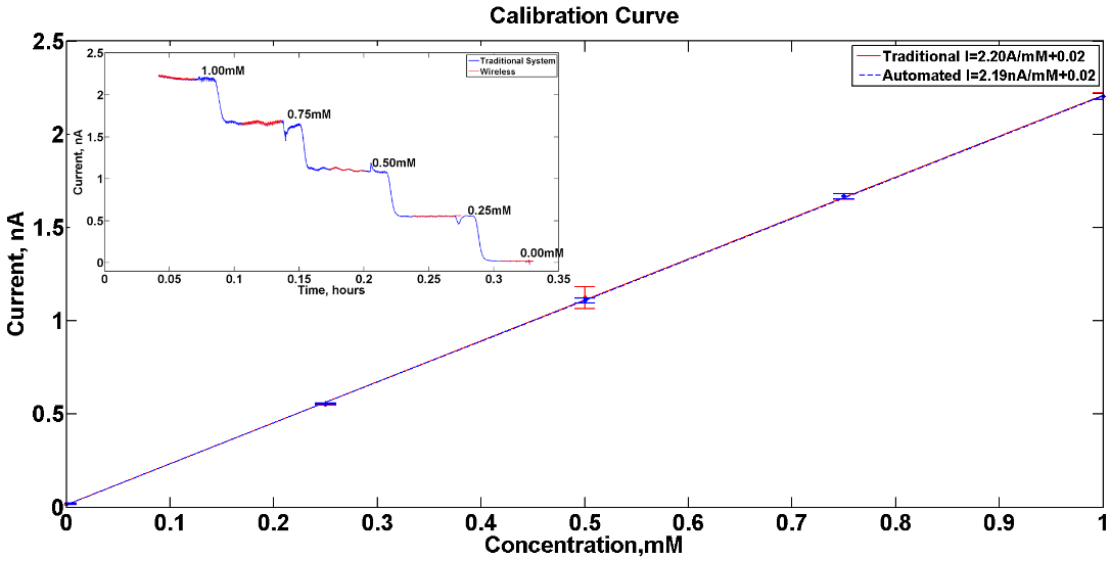

Figure 9.9: Customised code validation

Two calibration events of the same glucose sensor were conducted. Both raw data (mini figure) and processed calibration curve (main figure) are attached.

9.7 Real-time neurochemical concentration display

Traditionally, a monitoring system can only output the voltage/current changes. Since the sensitivity of a sensor varies, it is unreliable to convert the voltage/current to concentration changes, based on only one calibration parameters. Normally the sensor needs to be calibrated every few hours, the calibration data will be also recorded in the system. At the end of the whole monitoring process, calibration curves from different time are calculated, and then convert the voltage/current changes to concentration changes. Since all the concentration changes are calculated after the monitoring process, the whole system is not able to provide any valuable immediate feedback to clinical teams in the operating theatres, or to the nurses and doctors in intensive care units.

As discussed, the add-on wireless controlling module offers the potential of implementing a completely seamless ionic concentration monitoring system with auto-calibration. By filling in the up-to-date sensor calibration parameters, the system is able to report real-time concentration changes, rather than only a voltage/current output. The monitoring system can perform a calibration every few hours. After each calibration process, the MCU is able to calculate new calibration and sensitivity. By applying the new sensitivity, the system is capable of reporting ionic concentration changes from the sensors, which are more meaningful to the clinical team.

Furthermore, the calibration curves from different time can be analysed, and the calibration period can be adjusted accordingly. For example, if the sensitivity from time t does not change much compared with that from one hour later, t+1h, and two hour later, t+2h, the system can then start to regard the sensor as it is in a good condition, which means the sensor does not require calibration every hour. Since every calibration will run 5 to 10 minute, the system is able to get more useful patient data if the period between two calibrations gets longer. However, if the sensitivity from one calibration curve changes significantly, the system can generate a warning, reporting this situation. In addition, if the clinical team are focussing an absolute level of chemicals, like baseline K^+ levels, they may require auto-calibration to the sensor more frequently.

9.7.1 Component selection

In the previous sections, the first-version wireless controller and its relevant controlling code have been tested to work successfully with µdevices. In the second version, the same microcontroller and Bluetooth module have been still used. In addition, the amperometric circuit, discussed in Chapter 4, high-precision ADC, and DAC have also been added in the design, in order to output both raw voltages and the processed concentrations. A flow diagram of the general experimental set-up is shown in Figure 9.10. Both raw voltage output and processed concentration output are sent to the data recorder. For one input channel, two output channels are recorded simultenously.

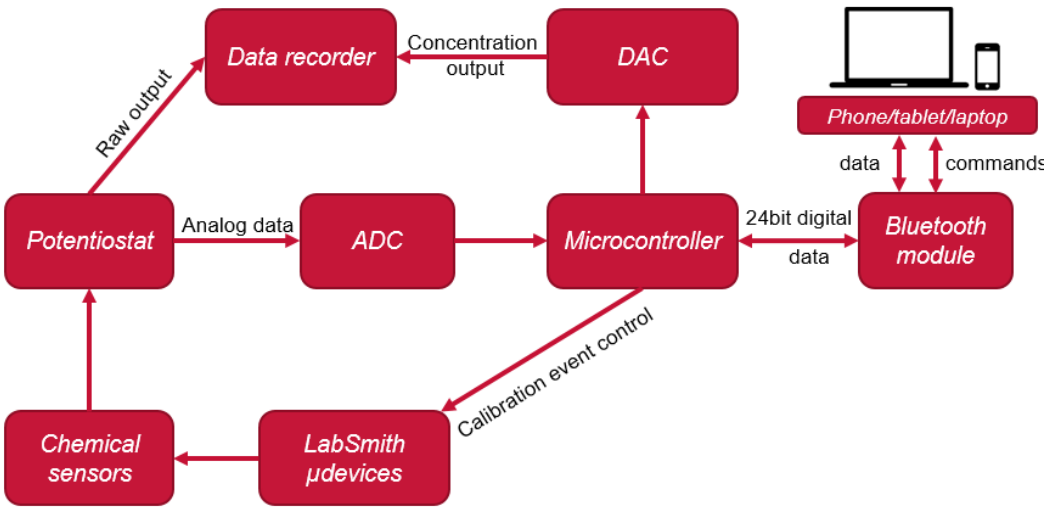

Figure 9.10: Flow diagram of the wireless controlling system

More specifically, the ADC used in this design is ADS1253, from Texas Instruments, which features as 4-channel 24-bit analog-to-digital converters. The external voltage reference chip is REF3040, from Texas Instruments, which provides stable 4.096V with ±0.2% variation. With the aid of de-coupling capacitors and low-pass filters, the performance of the voltage reference to the data converter can be optimised.

The DAC used in this design is DAC8564, from Texas Instruments, and it is a 4-channel 16-bit low-power DAC, with built-in reference voltage. As the DAC is used to output the processed concentration, which should always be a positive value, the chosen DAC is unipolar. The default reference voltage is 2.5V. In this design, the feature of the internal voltage reference has been disabled. In this design, ADS1253 and DAC8564 have the same reference voltage, such that the digital data in both devices represent the same analog voltage.

Another feature of this design is the power regulator. As the circuit board requires +12V to power the µdevices and the main power usage on board is 5V, a regulator is required to convert 12V to 5V. As mentioned, the heat dissipation is significant when dumping voltage in such a big range. The unwanted heat can be a major problem to affect the component's function as well as increase the noise level. Therefore, the regulator used in design was OKI-78SR, from Murata Power Solutions. It has ultra-wide DC input range, 7-36V, with built-in heatsink (Figure 9.11). The heatsink is capable of dissipate heat effectively, such that no extra thermal interference is introduced. In addition, it stays perpendicularly to the circuit board and maintain a better heat dissipation.

Figure 9.11: DC/DC converter with built-in heatsink

9.7.2 PCB layout

After selecting all the necessary electronic components, the PCB has been designed (Figure 9.12), and the overall size is 92mm × 41mm. The PCB has 4 functional layers: top signal layer, ground plane, power plane, and bottom signal layer. All the analog circuits, such as

amperometric circuit and potentiostat, have been placed on the left, while the digital circuits such as the microcontroller, the LabSmith, and the wireless module have been located on the right. The data converters have been placed in the middle of the board, where analog and digital ground planes are split. Following the techniques described in Chapter 3, all the analog inputs have been properly guarded and shielded.

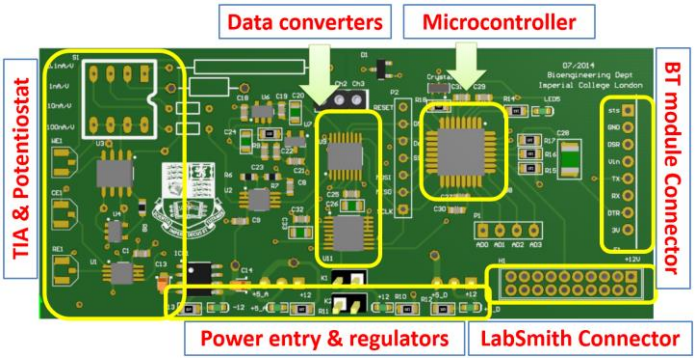

Figure 9.12: PCB layout of the circuit

9.7.3 Graphic user interface design

As the system is designed for clinical uses, an application-specific graphic user interface (GUI) is required. All the necessary functions can be implemented as different buttons on the GUI, such that the clinical members do not require to do any additional programming.

The relevant GUI has been implemented on PC via MATLAB, and it has also been compiled as an application software, which is downloaded to a 7-inch Android-based tablet[7]. The appearance and relevant experimental set-up is shown in Figure 9.13.

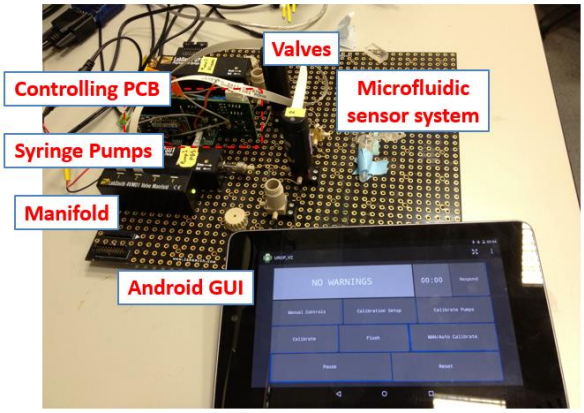

Figure 9.13: Experimental set-up of the wireless controlling system

[7] The main GUI design has been done by a master student, Mr. Thomas Watts, in the group under my supervision.

9.7.4 Experimental results[8]

As the first-version PCB has validated the relevant code, the experiments conducted for the second-version PCB are mainly for demonstrating its functionalities. The first experiment is about controlling a glucose sensor calibration process with ferrocene. 5 different concentration steps in the physiological range (from 0mM to 1mM, with 0.25mM step) are involved in the calibration. Two-channel recordings are shown in Figure 9.14. The upper graph shows the standard voltage output from the on-board potentiostat, which is similar to the data discussed in Chapter 4. The lower graph shows the corresponding concentration output, which is consistent with the concentrations in the upper graph. The sensitivity used for this conversion is acquired from the previous calibration event. Even the spikes that are due to the artefact of the syringe pump, can be observed at the same time on both channels.

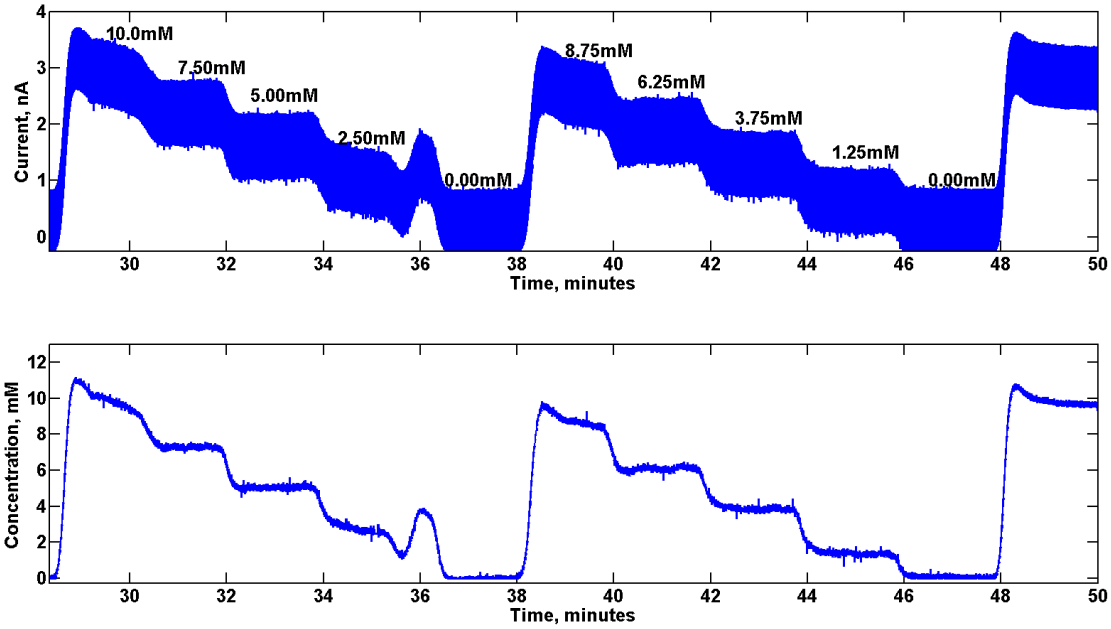

Figure 9.14: Concurrent outputs from the system

Simultaneous outputs from the system were recorded. The upper channel shows the raw data while the lower channel presents the processed glucose concentrations in this calibration event. The spikes were due to the artefact of the pumps, which can be seen on both channels.

After validating that the system can display real-time concentrations, another experiment has been conducted to check the degradation of a sensor's sensitivity over a long period. Figure 9.15 shows a 36-hour recording of a sensor's sensitivity. During this period, the calibration system has been configured in such a way that it calibrates the sensor every 3 hours and it

[8] The design, development, and results have been prepared to submit to the Journal of the Analyst in 2015. The paper has been named as "Wireless Microfluidic-Based Biosensor Auto-calibration System Development for Real-time Concentration Display".

shortens the period between two calibrations if the sensitivity drop is larger or the absolute sensitivity is smaller than a threshold.

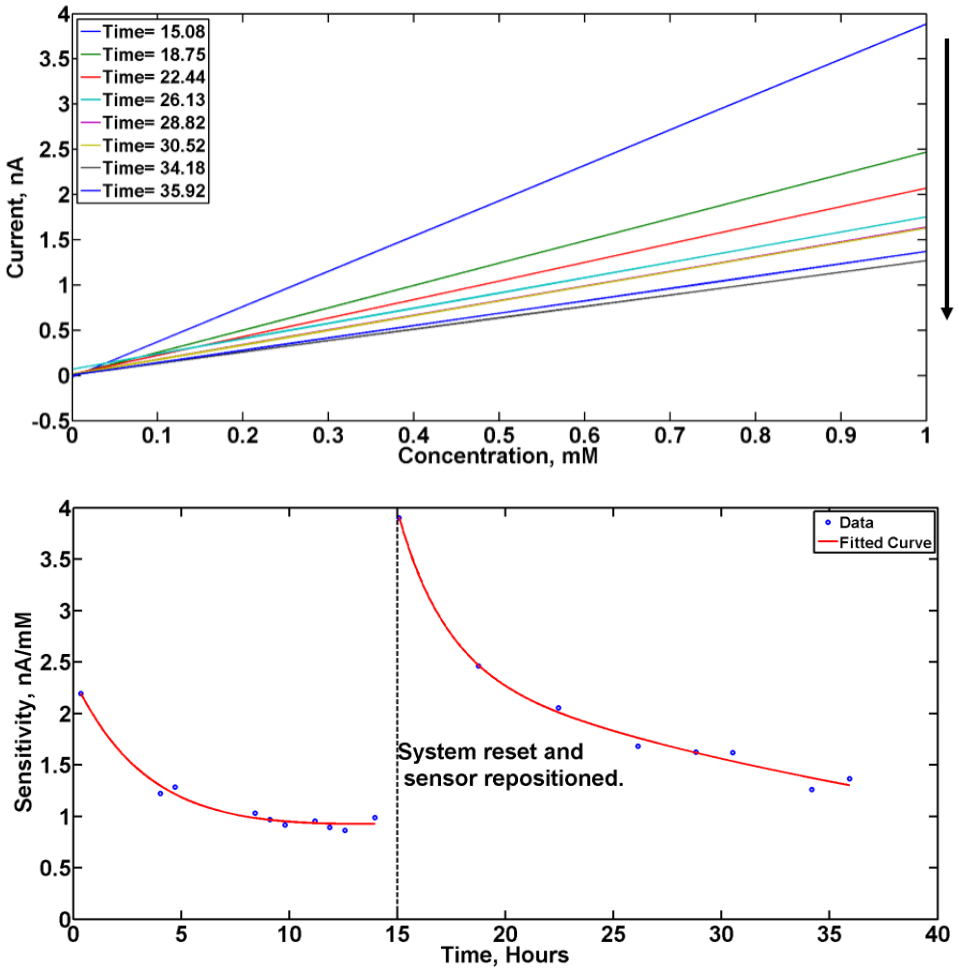

Figure 9.15: Long-term sensitivity degradation

The system was left running continuously for 36 hours. The system was only reset and the sensor was repositioned at hour 15, to achieve better sensitivity. The upper graph show the different current outputs from the sensor over time, from calibration 15 to 36. The sensitivity is the slope of each line, and it drops down from calibration 15 to 36. The lower graph shows the calibration changes over this 36 hour monitoring.

Numbers of factors, such as temperature, humidity, enzyme activity, sensor position, and system malfunctioning, may affect the sensitivity in a practical experiment. In this experiment, the initial sensitivity starts at 2.2nA/mM, and the next calibration event happens 3 hours later, which drops down to 1.2nA/mM. During hour 8 to 14, the sensitivity becomes very low. Therefore at hour 15, the system is reset, syringe pumps have been cleaned and refilled, and the sensor has been repositioned. The new sensitivity starts from 3.9nA/mM, followed by an exponential drop, and reach about 1.2nA/mM at hour 36.

9.8 Conclusion and further development

The sensor auto-calibration system has been validated to control the LabSmith µdevices and conduct different events for a microfluidic-based sensor experiment. Two different PCBs have been developed. The first PCB is used for testing the customised C++ code and the I^2C communication. The second design incorporates with high-precision data converters and the potentiostat, providing a monitoring system that can calculate sensitivity and display real-time concentrations.

A wireless Bluetooth module has been applied, such that the system is capable of being configured or controlled remotely by a PC or a tablet. The relevant GUI design, experimental set-up, and relevant results have been also discussed in this chapter. By operating on a GUI, the user does not require to understand the detailed controlling code in programming language.

The system has shown the capability of controlling LabSmith µdevices, conducting calibration events, calculating transient sensitivity, and outputting real-time concentration. The further development on this system is to design a case for the system, which can meet the medical safety regulation demonstrated in Chapter 6. After getting medical safety approval, the system can be used in hospital to perform clinical monitoring and provide real-time neurochemical concentrations to the clinical team.

Chapter 10: Conclusion and Further Development

10.1 Research achievement

Most of the work presented in this thesis are PCB design, relevant wireless embedded electronic system development, and realisation. The designs require considerable chip selections, schematic wiring, PCB layout and routing, sensor interface, noise elimination, and casing. This thesis is a very practical work, which aims at improving clinical monitoring standard, especially for TBI patient monitoring. Compared with pure lab-based experiment, this work requires extensive management skills to tackle practical issues, and implementation skills to convert a circuit board to a proper medical instrument.

Throughout the thesis, novel medical multimodal instruments for monitoring traumatic brain injury (TBI) patients and relevant wireless implementations have been demonstrated. Both lab-based and clinical data have been presented to validate the instrument and relevant electronic designs.

The TBI instrumentation box is capable of simultaneously recording 16-channel information from a TBI patient, which is sufficient for current clinical treatment and relevant research study. The information contains 8-channel electrocorticography (ECoG) data, to analyse spreading depolarisation (SD) events in the injured brain. 2 customised potentiostats have been designed and utilised to detect local glucose and lactate concentration changes, while one high-impedance instrumentation circuit board has been designed to detect potassium concentration changes. In addition, the instrument provides external connections to other monitoring devices, which are used for detecting other critical parameters from patients, such as blood pressure, intracranial pressure, blood oxygen, and temperature. An accelerometer is used to detect the patient movement, to eliminate any motion artefact during monitoring.

In addition, relevant wireless implementations, such as Zigbee-based potentiostat, Bluetooth-based wireless bio-signal acquisition system, wireless sensor auto-calibration system, and relevant user interface, have been also developed to facilitate the clinical team and improve the treatment standard.

The first three chapters are mainly about the introduction, literature review, common materials, and system design/operation considerations. In Chapter 1, the background of TBI

monitoring process and the current clinical set-up have been demonstrated. Fundamental electrochemical theory, operating principles, and relevant detection electronics are also illustrated in this Chapter. In Chapter 2, common materials, testing equipment, and technical terms are demonstrated. In Chapter 3, PCB routing techniques, system design considerations, relevant experimental set-up, and noise elimination methods have been discussed.

Chapter 4 to 9 are the main design and result chapters. In Chapter 4, 2 different types of potentiostats have been developed. In the first several sections of the chapter, a resistive potentiostat has been introduced. The design considerations, relevant advantages, and disadvantages have been also discussed. To achieve extra-low current detection (in pA level), a novel capacitive front-end current-to-voltage conversion system has been designed and developed. The comparative results with the resistive potentiostat are also presented.

In Chapter 5, a high-precision low-noise monitoring system is introduced to detect various bio-potentials. It is primarily designed for measuring ECoG signals in TBI patients, whereas it features internal programmable gains, which allows it to detect different bio-signals, such as ECG and EEG. The performance of the system has been compared with a commercial bio-potential acquisition system.

In Chapter 6, the construction principles and relevant engineering considerations of designing the TBI monitoring instrumentation box has been demonstrated. The electrical and mechanical properties of the box have been introduced. In addition, this chapter also discusses essential clinical safety requirements and regulations for medical devices.

After introducing different wired circuit designs for TBI monitoring, wireless implementations have been discussed from Chapter 7 to 9. Chapter 7 lists the features of different common wireless techniques in the ISM band, and discusses the possibilities of implementing in TBI instruments. In this chapter, a miniaturised Zigbee-based wireless potentiostat has been developed. In addition, a Zigbee-based wireless bio-potential acquisition system has also been developed, which is capable of monitoring 3-channel information.

In Chapter 8, a stacking modular system is introduced for universal prototyping. By featuring the same connector and pinout, different functional layers can be stacked together. In this chapter, a Bluetooth module has been used to implement an 8-channel wireless bio-potential

acquisition system. In addition, by connecting 2 ADS1298s in the cascaded mode, a 16-channel wired bio-potential monitoring system has been developed.

In Chapter 9, a wireless sensor auto-calibration system has been introduced, for long-term sensor sensitivity monitoring and real-time neurochemical concentration outputs. The system involves both hardware and software implementations. With customised graphic user interfaces, the data can be recorded from either a host computer or a smart phone/tablet. The system has been tested and validated with different chemical sensors.

Latest achievements

While writing up the thesis, several new designs have been achieved and validated:

a. The analog front-end IC, AFE91000, can be an alternative solution to support the amperometric sensors, discussed in Chapter 4. It integrates the three electrode system in one IC, with programmable bias voltages and transimpedance gains [114]. The chip achieves “bipolar” measurement by shifting up the reference voltage from ground to the middle point of the power rail. For example the reference voltage is set as +2.5V for a unipolar +5V supply. This avoids introducing a voltage inverter to supply the negative power, which significantly reduces the switching noise from a power inverter. The main disadvantage is the gain in the transimpedance phase, which is up to 350kΩ, 2.86µA/V. This is not large enough for biosensor applications (normal in nA level), and therefore second- or third-stage amplifications may be required.

b. Another analog front-IC, AFE91200, has been implemented for measuring ion-selective electrode (ISE). The chip features internal high-impedance buffers, which is able to reliably detect signal from ISEs [115]. Similar to AFE91000, this chip also shifts up the reference voltage, so it can detect “bipolar” changes. The standard deviation of the detected signal is only 0.23mV. In addition, the chip has been designed to connect with the Bluetooth module discussed in Chapter 9. Therefore, it can wirelessly transmit the signal to the host PC or a smart phone/tablet.

c. Another design is to combine the achievements discussed in Chapter 5 and 9 to make a miniaturised bed-side wireless ECoG, with the existing GUI system, and develop a customised ECoG GUI on the host PC or a smart phone/tablet. The design has been implemented and tested. The remaining task is to further develop the GUI and test it in a clinical environment.

10.2 Future development

Future mainstream developments in TBI monitoring applications are:

a. Updating state-of-the-art chips to improve the performance of the design.
b. Developing intelligent multifunctional ICs at chip-level design.

Regarding to the first option, the latest released high-performance microcontroller (2014), Edison from Intel (Figure 10.1), seems to be a good option. Compared with a traditional microcontroller, Edison works as a mini computer, which is slightly larger than a postage stamp. Edison utilises 22nm Intel SoC technology, and features with a dual core, dual threaded Intel Atom CPU, at 500MHz and a 32-bit Intel Quark microcontroller at 100MHz. The chip has 40 general purpose IO pins, and supports Wi-Fi and Bluetooth functions. Furthermore, the programming of the chip is relatively easy, as it is compatible with Arduino IDE and supports C/C++ language. This means most of the work demonstrated in this thesis are possible to be converted and controlled by this new chip.

Figure 10.1: Appearance of Edison from Intel

The figure is extracted from Intel website [116].

Another possible development field is to design a multifunctional intelligent IC, which is wearable and capable of monitoring all the parameters of TBI patients. It is so far called as "behind the ear" wireless TBI device, which integrates microfluidic sensors with relevant monitoring electronics. Both sensors and electronics are miniaturised and they can be combined as a monitoring device, which is also capable of transmitting signal wirelessly.

Reference

1. Sugerman, D.E., et al., *Patients with severe traumatic brain injury transferred to a Level I or II trauma center: United States, 2007 to 2009.* J Trauma Acute Care Surg, 2012. **73**(6): p. 1491-9.
2. Coronado, V.G., et al., *Surveillance for traumatic brain injury-related deaths--United States, 1997-2007.* MMWR Surveill Summ, 2011. **60**(5): p. 1-32.
3. Holmin, S., et al., *Intracerebral inflammation after human brain contusion.* Neurosurgery, 1998. **42**(2): p. 291-8; discussion 298-9.
4. Kurland, D., et al., *Hemorrhagic progression of a contusion after traumatic brain injury: a review.* J Neurotrauma, 2012. **29**(1): p. 19-31.
5. *http://labtestsonline.org/understanding/conditions/meningitis/*.
6. Sauaia, A., et al., *Epidemiology of trauma deaths: a reassessment.* J Trauma, 1995. **38**(2): p. 185-93.
7. Narayan, R.K., et al., *Clinical trials in head injury.* J Neurotrauma, 2002. **19**(5): p. 503-57.
8. Reilly, P.L. and S.B. Lewis, *Progress in head injury management.* J Clin Neurosci, 1997. **4**(1): p. 9-15.
9. Rocque BG, B.M., *Spontaneous acute subdural hematoma as an initial presentation of choriocarcinoma: A case report.* J Med Case Reports, 2008.
10. Novak, V. and I. Hajjar, *The relationship between blood pressure and cognitive function.* Nat Rev Cardiol, 2010. **7**(12): p. 686-98.
11. Asano, E., et al., *Origin and propagation of epileptic spasms delineated on electrocorticography.* Epilepsia, 2005. **46**(7): p. 1086-97.
12. Nakamura, H., et al., *Spreading depolarizations cycle around and enlarge focal ischaemic brain lesions.* Brain, 2010. **133**(Pt 7): p. 1994-2006.
13. Lauritzen, M., et al., *Clinical relevance of cortical spreading depression in neurological disorders: migraine, malignant stroke, subarachnoid and intracranial hemorrhage, and traumatic brain injury.* J Cereb Blood Flow Metab, 2011. **31**(1): p. 17-35.
14. Dohmen, C., et al., *Spreading depolarizations occur in human ischemic stroke with high incidence.* Ann Neurol, 2008. **63**(6): p. 720-8.
15. Strong, A.J., et al., *Treatment of critical care patients with substantial acute ischemic or traumatic brain injury.* Crit Care Med, 2005. **33**(9): p. 2147-9; author reply 2149.
16. Woitzik, J., et al., *Delayed cerebral ischemia and spreading depolarization in absence of angiographic vasospasm after subarachnoid hemorrhage.* J Cereb Blood Flow Metab, 2012. **32**(2): p. 203-12.
17. Hartings, J.A., et al., *Spreading depolarisations and outcome after traumatic brain injury: a prospective observational study.* Lancet Neurol, 2011. **10**(12): p. 1058-64.
18. Jeffcote, T., et al., *Detection of spreading depolarization with intraparenchymal electrodes in the injured human brain.* Neurocrit Care, 2014. **20**(1): p. 21-31.
19. Markus Riederer, O.L., Peter Fahrni, Rüdiger Vahldieck and Jürg Fröhlich, *Characterization of the Electronimagnetic Environment in a Hospital: Measurement Procedures and Results*, in *IEEE EMC Society Newsletter winter 2010*, J. O'Neil, Editor. 2010.
20. *IEC 60601-1: 3rd edition, "General Requirement for Basic Safety and Essential Performance".* International Electro technical Commission (www.iec.ch), 2008
21. Pallas-Areny, R., J. G. Webster, *Sensors and Signal Conditioning, 2nd edition.* 2001, New York: Wiley.
22. *http://www.microdialysis.se/*.

23. Kulagina, N.V., L. Shankar, and A.C. Michael, *Monitoring glutamate and ascorbate in the extracellular space of brain tissue with electrochemical microsensors.* Anal Chem, 1999. **71**(22): p. 5093-100.
24. Ewing, A.G. and R.M. Wightman, *Monitoring the stimulated release of dopamine with in vivo voltammetry. II: Clearance of released dopamine from extracellular fluid.* J Neurochem, 1984. **43**(2): p. 570-7.
25. Kuhr, W.G., et al., *Monitoring the stimulated release of dopamine with in vivo voltammetry. I: Characterization of the response observed in the caudate nucleus of the rat.* J Neurochem, 1984. **43**(2): p. 560-9.
26. Kishida, K.T., et al., *Sub-second dopamine detection in human striatum.* PLoS One, 2011. **6**(8): p. e23291.
27. Chang, S.Y., et al., *Wireless fast-scan cyclic voltammetry to monitor adenosine in patients with essential tremor during deep brain stimulation.* Mayo Clin Proc, 2012. **87**(8): p. 760-5.
28. Deeba, S., et al., *Use of rapid sampling microdialysis for intraoperative monitoring of bowel ischemia.* Diseases of the Colon & Rectum, 2008. **51**(9): p. 1408-1413.
29. Parkin, M.C., et al., *Dynamic changes in brain glucose and lactate in pericontusional areas of the human cerebral cortex, monitored with rapid sampling on-line microdialysis: relationship with depolarisation-like events.* Journal of Cerebral Blood Flow and Metabolism, 2005. **25**(3): p. 402-413.
30. Hopwood, S.E., et al., *Transient changes in cortical glucose and lactate levels associated with peri-infarct depolarisations, studied with rapid-sampling microdialysis.* Journal of Cerebral Blood Flow and Metabolism, 2005. **25**(3): p. 391-401.
31. Watson, C.J., B.J. Venton, and R.T. Kennedy, *In vivo measurements of neurotransmitters by microdialysis sampling.* Analytical Chemistry, 2006. **78**(5): p. 1391-1399.
32. Ungerstedt, U., *Microdialysis - Principles and Applications for Studies in Animals and Man.* Journal of Internal Medicine, 1991. **230**(4): p. 365-373.
33. Cashman, P.M.M., et al., *Automated Techniques for Visualization and Mapping of Articular Cartilage in MR Images of the Osteoarthritic Knee: A Base Technique for the Assessment of Microdamage and Submicro Damage.* Ieee Transactions on Nanobioscience, 2002. **1**(1): p. 42-51.
34. Jones, D.A., et al., *On-line monitoring in neurointensive care - Enzyme-based electrochemical assay for simultaneous, continuous monitoring of glucose and lactate from critical care patients.* Journal of Electroanalytical Chemistry, 2002. **538**: p. 243-252.
35. Shou, M.S., et al., *Monitoring dopamine in vivo by microdialysis sampling and on-line CE-laser-induced fluorescence.* Analytical Chemistry, 2006. **78**(19): p. 6717-6725.
36. M, C., *Über die Ursache der elektromotorischen Eigenschaften der Gewebe, zugleich ein Beitrag zur Lehre von Polyphasischen Elektrolytketten.* Z. Biol. 47 562, 1906.
37. Geddes, L.A., L.E. Baker, *Principles of Applied Biomedical Instrumentation, 3rd ed.* 1989, New York: John Wiley & Sons.
38. Bjerregaard, P. and I. Gussak, *Naming of the waves in the ECG with a brief account of their genesis.* Circulation, 1999. **100**(25): p. e148.
39. *Brain Waves (http://www.docgautham.com/causes/brain_waves.).*
40. Kirmizi-Alsan, E., et al., *Comparative analysis of event-related potentials during Go/NoGo and CPT: decomposition of electrophysiological markers of response inhibition and sustained attention.* Brain Res, 2006. **1104**(1): p. 114-28.

41. Kisley, M.A. and Z.M. Cornwell, *Gamma and beta neural activity evoked during a sensory gating paradigm: effects of auditory, somatosensory and cross-modal stimulation.* Clin Neurophysiol, 2006. **117**(11): p. 2549-63.
42. Vespa, P., et al., *Metabolic crisis without brain ischemia is common after traumatic brain injury: a combined microdialysis and positron emission tomography study.* J Cereb Blood Flow Metab, 2005. **25**(6): p. 763-74.
43. Strong, A.J., et al., *Spreading and synchronous depressions of cortical activity in acutely injured human brain.* Stroke, 2002. **33**(12): p. 2738-43.
44. Smith, J. and V. Hinson-Smith, *The potentiostat: electrochemistry's utility player.* Anal Chem, 2002. **74**(19): p. 539A-541A.
45. *http://www.ips-jaissle.de/en/projects.html.*
46. Heath, S., *Embedded System Design.*
47. Bober, B., *Altera and Xilinx Report: The Battle Contibues (http://seekingalpha.com/article/85478-altera-and-xilinx-report-the-battle-continues).* 2008.
48. Johnson, J., *List and comparison of FPGA companies (http://www.fpgadeveloper.com/2011/07/list-and-comparison-of-fpga-companies.html).* 2011.
49. *http://www.adtechmedical.com/cabrio-connection-system/.*
50. *PL3516 PowerLab 16/35 User Guide (http://www.dmt.dk/files/data_aquisition_systems/powerlab_16-35.pdf).*
51. *TI Application Notes: Auto-zero amplifiers ease the design of high-precision circuits (http://www.ti.com/lit/an/slyt204/slyt204.pdf).*
52. *Analog Devices Tutorial: Demystify Auto-zero Amplifiers (http://www.analog.com/library/analogDialogue/cd/vol34n1.pdf).*
53. *Analog Devices Tutorial: Chopper Stabilized (Auto-Zero) Precision Op Amps (http://www.analog.com/media/en/training-seminars/tutorials/MT-055.pdf).*
54. *https://en.wikipedia.org/wiki/Instrumentation_amplifier.*
55. *TI Application Notes: Understanding the Terms and Definitions of LDO Voltage Regulators (http://www.ti.com/lit/an/slva079/slva079.pdf).*
56. Guangyan Zhu, H.W., Chris Iannello, and Issa Batarseh, *A Study of Power Factor and Harmonics in Switched-Mode Power Supplies.* IEEE, 1999.
57. *I2C-bus specification and user manual (http://www.nxp.com/documents/user_manual/UM10204.pdf).*
58. Parris, C., *Design calculations for robust I2C communications (http://www.edn.com/design/analog/4371297/Design-calculations-for-robust-I2C-communications).*
59. *TI Application notes: Noise Analysis of FET Transimpedance Amplifier (http://www.ti.com/lit/an/sboa060/sboa060.pdf).*
60. *Analug Devices Tutorial: Op Amp Noise (MT-047) http://www.analog.com/media/en/training-seminars/tutorials/MT-047.pdf.*
61. *Maxim Appication Note 5450: Successful PCB Grounding with Mixed-Signal Chips Follw the Path of Least Impedance (http://www.maximintegrated.com/en/app-notes/index.mvp/id/5450).*
62. *LMP7721 datasheet (http://www.ti.com/lit/ds/symlink/lmp7721.pdf).*
63. *Analog Devices Tutorial: A Practical Guide to High-speed Printed-circuit-board Layout (http://www.analog.com/library/analogDialogue/archives/39-09/layout.pdf).*
64. *NI White Paper: Field Wiring and Noise Consideration for Analogue Signals (http://www.ni.com/white-paper/3344/en/).*
65. *iec-60601-1-medical-design-standards (http://www.cui.com/catalog/resource/iec-60601-1-medical-design-standards.pdf).*

66. John W. Clark, M.R.N., Walter H. Olson, Robert A. Peura, Frank R. Primiano, Melvin P. Siedband, John G. Webster, Lawrence A. Wheeler, *Medical Instrumentation: Application and Design*. 2010: JOHN WILEY & SONS, INC.
67. *Molex Product brochure: RF/Microwave Product (http://www.literature.molex.com/SQLImages/kelmscott/Molex/PDF_Images/987650-3232.pdf).*
68. Graeme, J.G., *Photodiode Amplifiers: OP AMP Solutions*. 1996: McGraw Hill Profession.
69. Johnson, J.B., *Thermal Agitation of Electricity in Conductors.* Phys. Rev., 1928. **32**(1): p. 97-109.
70. P N Bartlett, K.F.E.P., *A study of the kinetics of the reaction between ferrocene monocarboxylic acid and glucose oxidase using the rotating-disc electrode.* Journal of Electroanalytical Chemistry, 1995. **397**: p. 53-60.
71. *Linear Application Note 40: Take the Mystery Out of the Switched-Capacitor Filter, The System Designer's Filter Compendium (http://cds.linear.com/docs/en/application-note/an40f.pdf).*
72. *DDC114 data sheet (http://www.ti.com/lit/ds/symlink/ddc114.pdf).*
73. Takano, T., et al., *Cortical spreading depression causes and coincides with tissue hypoxia.* Nat Neurosci, 2007. **10**(6): p. 754-62.
74. *Bio Amp Owner Guide (http://cdn.adinstruments.com/adi-web/manuals/Bio_Amp_OG.pdf).*
75. *ADS1298 datasheet (http://www.ti.com/lit/ds/symlink/ads1298.pdf).*
76. *Si865x data sheet (http://www.silabs.com/Support%20Documents/TechnicalDocs/Si865x.pdf).*
77. *TPS7A7001 datasheet (http://www.ti.com/lit/ds/sbvs134/sbvs134.pdf).*
78. *LT1611 datasheet (http://cds.linear.com/docs/en/datasheet/1611f.pdf).*
79. *AD5362_5363 datasheet (http://www.analog.com/media/en/technical-documentation/data-sheets/AD5362_5363.pdf).*
80. *lpt50-m AC_DC_converter datasheet (http://www.artesyn.com/power/assets/lpt50-m_ds_06-03-2014_0f6e4b7707.pdf).*
81. *AD8628_8629_8630 data sheet (http://www.analog.com/static/imported-files/data_sheets/AD8628_8629_8630.pdf).*
82. *LT1611f data sheet (http://cds.linear.com/docs/en/datasheet/1611f.pdf).*
83. *TPS7A7001 data sheet (http://cds.linear.com/docs/en/datasheet/1611f.pdf).*
84. Feuerstein, D., et al., *Dynamic metabolic response to multiple spreading depolarizations in patients with acute brain injury: an online microdialysis study.* J Cereb Blood Flow Metab, 2010. **30**(7): p. 1343-55.
85. *PowerLab 35 Series Owner Guide (http://cdn.adinstruments.com/adi-web/manuals/PowerLab_35_Series_OG.pdf).*
86. Ungerstedt, U., *Microdialysis--principles and applications for studies in animals and man.* J Intern Med, 1991. **230**(4): p. 365-73.
87. Watson, C.J., B.J. Venton, and R.T. Kennedy, *In vivo measurements of neurotransmitters by microdialysis sampling.* Anal Chem, 2006. **78**(5): p. 1391-9.
88. Feuerstein, D., *Development and Use of Bioanalytical Instrumentation and Signal Analysis Methods for Rapid Sampling Microdialysis Monitoring of Neuro-intensive Care Patients*, in *Bioengineering Department*. 2010, Imperial College London.
89. *Guidance notes on the UK electrical equipment (safety) regulations 1994 (https://www.gov.uk/government/uploads/system/uploads/attachment_data/file/293397/07-616-product-standards-guidance-notes-electrical-equipment.pdf).*

90. Mathew, G., *Medical Devices Isolation - How safe is safe enough (Whitepaper).*
91. Sheng, C., et al., *[Design of portable 12-lead digital ECG with low power consumption].* Zhongguo Yi Liao Qi Xie Za Zhi, 2013. **37**(6): p. 417-20.
92. Massot, B., et al., *A wearable, low-power, health-monitoring instrumentation based on a Programmable System-on-Chip.* Conf Proc IEEE Eng Med Biol Soc, 2009. **2009**: p. 4852-5.
93. System, P.M., *Striving for cableless monitoring.* Philips Medical Perspective Magazine, 2005. **8**: p. 24-25.
94. *The MobiHealth Project (http://mobihealth.org/).*
95. Lo BPL, Y.G. *Key technical challenges and current implementations of body sensor networks*. in *the Second International Workshop on Wearable and Implantable Body Sensor Networks*. 2005.
96. *MyHeart project (http://www.hitech-projects.com/euprojects/myheart/).*
97. Eklund JM, H.T., Sprinkle J, Sastry S. *Information technology for assisted living at home: building a wireless infrastructure for assisted living*. in *the Twenty-Seventh Annual International Conference of the IEEE Engineering in Medicine and Biology Society*. 2005.
98. *Demystifying 802.15.4 and Zigbee (http://www.digi.com/pdf/wp_zigbee.pdf).*
99. NXP, *Co-existence of IEEE 802.15.4 at 2.4 GHz Application Note.* 2013.
100. *IEEE 802.11. standard for information technology - Telecommunications and information exchange between systems local and metropolitan area networks - Specific requirements Part 11: Wireless LAN Medium Access Control (MAC) and Physical Layer (PHY) Specifications. IEEE.* 2012.
101. *IEEE 802.15. standard for local and metropolitan area networks - Part 15.1: Wireless Medium Access Control (MAC) and Physical Layer (PHY) Specification for Wireless Personal Area Network (LR-WPANs). IEEE Std 802.15.1-2005* 2011.
102. *IEEE 802.15. standard for local and metropolitan area networks - Part 15.4: Low-Rate Wireless Personal Area Network (LR-WPANs). IEEE Std 802.15.4-2011* 2011.
103. Petrova M., R.J., Mahonen P., and Labella S., *Performance study of IEEE 802.15.4 using measurements and simulations*, in *Wireless Communications and Networking Conference*. 2006, IEEE: WCNC.
104. *The ZigBee Alliance (http://www.zigbee.org/).*
105. *Xbee user manumal (http://ftp1.digi.com/support/documentation/90000976_U.pdf).*
106. Javier Espina, T.F., Athanasia Panousopoulou, Lars Schmitt, Oliver Mulhens, and Guang-Zhong Yang, *Network Topologies, Communication Protocols, and Standards*, in *Body Sensor Networks*, G.Z. Yang, Editor. 2014, Springer: London.
107. *TI Application Notes: Using PWM Output as a Digital-to-Analog Converter on a TMS320F280x Digital Signal Controller (http://www.ti.com/lit/an/spraa88a/spraa88a.pdf).*
108. Amemiya, S. and A.J. Bard, *Scanning electrochemical microscopy. 40. Voltammetric ion-selective micropipet electrodes for probing ion transfer at bilayer lipid membranes.* Anal Chem, 2000. **72**(20): p. 4940-8.
109. Carl Nelson, J.W., *Boost Converter Operation, LT1070 Deisgn Manual.* 1986.
110. *Maxim Application Notes (3947): Daisy-Chaining SPI Devices (http://pdfserv.maximintegrated.com/en/an/AN3947.pdf).*
111. *DAC7634 datasheet (http://www.ti.com/lit/ds/symlink/dac7634.pdf).*
112. Intel, *USB3.0 Radio Frequency Interference Impace on 2.4 GHz Wireless Devices.* 2012.
113. *http://labsmith.com/.*
114. *LMP91000 datasheet (http://www.ti.com/lit/ds/symlink/lmp91000.pdf).*
115. *AFE91200 datasheet (http://www.ti.com/lit/ds/snas571c/snas571c.pdf).*
116. *http://www.intel.co.uk/content/www/uk/en/do-it-yourself/edison.html.*